Spectral Methods for Multi-Scale Feature Extraction and Data Clustering

by

Srinivas Chakra Chennubhotla

A thesis submitted in conformity with the requirements
for the degree of Doctor of Philosophy
Graduate Department of Computer Science
University of Toronto

Abstract

Spectral Methods for

Multi-Scale Feature Extraction and Data Clustering

Srinivas Chakra Chennubhotla

Doctor of Philosophy

Graduate Department of Computer Science

University of Toronto

2004

We address two issues that are fundamental to the analysis of naturally-occurring datasets: how to extract features that arise at multiple-scales and how to cluster items in a dataset using pairwise similarities between the elements. To this end we present two spectral methods: (1) Sparse Principal Component Analysis S-PCA — a framework for learning a linear, orthonormal basis representation for structure intrinsic to a given dataset; and (2) EigenCuts — an algorithm for clustering items in a dataset using their pairwise-similarities.

S-PCA is based on the discovery that natural images exhibit structure in a low-dimensional subspace in a local, scale-dependent form. It is motivated by the observation that PCA does not typically recover such representations, due to its single minded pursuit of variance. In fact, it is widely believed that the analysis of second-order statistics alone is insufficient for extracting multi-scale structure from data and there are many proposals in the literature showing how to harness higher-order image statistics to build multi-scale representations. In this thesis, we show that resolving second-order statistics with suitably constrained basis directions is indeed sufficient to extract multi-scale structure. In particular, S-PCA basis optimizes an objective function which trades off correlations among output coefficients for sparsity in the description of basis vector elements. Using S-PCA we present new approaches to the problem of constrast-invariant appearance

detection, specifically eye and face detection.

EigenCuts is a clustering algorithm for finding stable clusters in a dataset. Using a Markov chain perspective, we derive an eigenflow to describe the flow of probability mass due to the Markov chain and characterize it by its eigenvalue, or equivalently, by the halflife of its decay as the Markov chain is iterated. The key insight in this work is that bottlenecks between weakly coupled clusters can be identified by computing the sensitivity of the eigenflow's halflife to variations in the edge weights. The EigenCuts algorithm performs clustering by removing these identified bottlenecks in an iterative fashion. As an efficient step in this process we also propose a specialized hierarchical eigensolver suitable for large stochastic matrices.

Contents

Chapter 1

Introduction

1.1 Image Understanding

One of the goals in the study of computer vision is to devise algorithms that help us understand and recover useful properties of the scene from one or more images. This inverse problem is difficult because information is lost about the three-dimensional world when it is projected on to a two-dimensional image. However, our visual systems seem very adept at performing this task. For example, the objects (or well-defined parts of objects) in the scene are perceived as coherent *visual groups* in the image and the quality of the percept tends to be consistent across observers. Typically, subjects agree on the properties that they ascribe to objects in the scene, say in terms of colour, texture or shape attributes. Furthermore, if the objects are familiar, then they tend to get recognized as such. Thus, two processes: *perceptual grouping/organization* and *object recognition*, form the core of image understanding.

The importance of perceptual grouping and organization in visual perception has been laid out many years ago by the Gestaltist school [120]. For this thesis we motivate the grouping problem by inviting the reader to segment images shown in Fig. 1.1. Observers report perceiving two "things" – a foreground object occluding a textured background.

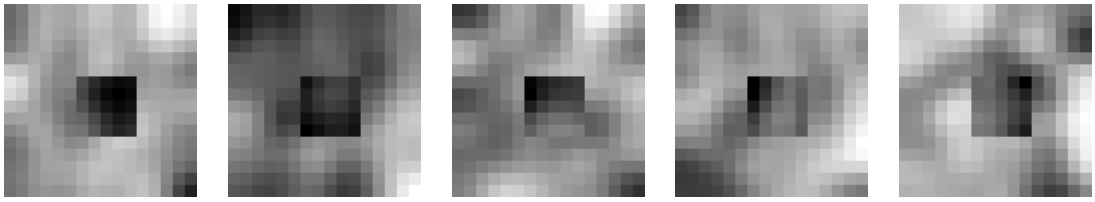

Figure 1.1: Images of a foreground occluder object against a textured background.

Figure 1.2: ORL database of face images [80].

A dominant cue perhaps is the difference in luminance between the occluder and the background. However, observe that in each image there is a portion of the occluder that blends into the background, but our visual systems appear to discount this information. One of our objectives in this thesis is to develop a computational process for segmenting images into plausible groups.

For object recognition, the groups thus segmented have to be associated with a stored representation (or memory) of the objects. For example, consider the problem of face recognition (see Fig. 1.2). A simple strategy is to first collect a database of face images viewed under roughly similar pose and illumination conditions, and then build a representation suitable for detection and matching. Clearly, the ensemble captures variations in the appearance of the whole (i.e., the overall face) and the parts (e.g., the forehead, nose, mouth, etc.) and this information can be useful for recognition. How might we represent these ensemble-specific multi-scale variations?

1.2 Contributions

In this thesis, we address two issues that we believe are fundamental to the analysis of high-dimensional, object-specific ensembles of visual, and other perceptual, data:

- how to extract features that arise at multiple-scales;
- how to cluster, or group, items in a dataset using pairwise similarities between the elements.

To this end, we present the following two spectral methods:

1. Sparse Principal Component Analysis (S-PCA) — a framework for learning a linear, orthonormal basis representation for structure intrinsic to a given dataset;
2. EigenCuts — an algorithm for clustering items in a dataset using their pairwise-similarities.

S-PCA is based on the discovery that natural images exhibit structure in a low-dimensional subspace in a local, scale-dependent form. It is motivated by the observation that PCA does not typically recover such representations. In fact, it is widely believed that the analysis of second-order statistics alone is insufficient for extracting multi-scale structure from data and there are many proposals in the literature showing how to harness higher-order image statistics to build multi-scale representations. In this thesis, we show that resolving second-order statistics with suitably constrained basis directions is indeed sufficient to extract multi-scale structure. The formulation of S-PCA is novel in that it successfully computes multi-scale representations for a variety of natural image ensembles including face images, images from outdoor scenes and a database of optical flow vectors representing a motion class.

Using S-PCA, we present new approaches to the problem of contrast-invariant appearance detection. The goal is to classify object-specific images (eg. face images) from

generic background patches. The novel contribution of this work is the design of a perceptual distortion measure for image similarity, i.e., comparing the appearance of an object to its reconstruction from the principal subspace. We demonstrate our approach on two different datasets: separating eyes from non-eyes and classifying faces from non-faces.

EIGENCUTS is a clustering algorithm for finding stable clusters in a dataset. Using a Markov chain perspective, we characterize the spectral properties of the matrix of transition probabilities, from which we derive eigenflows along with their halflives. An eigenflow describes the flow of probability mass due to the Markov chain, and it is characterized by its eigenvalue, or equivalently, by the halflife of its decay as the Markov chain is iterated. A ideal stable cluster is one with zero eigenflow and infinite half-life. The key insight in this work is that bottlenecks between weakly coupled clusters can be identified by computing the sensitivity of the eigenflow's halflife to variations in the edge weights. The EIGENCUTS algorithm performs clustering by removing these identified bottlenecks in an iterative fashion.

Also, in this thesis we propose a specialized eigensolver suitable for large stochastic matrices with known stationary distributions. In particular, we exploit the spectral properties of the Markov transition matrix to generate hierarchical, successively lower-dimensional approximations to the full transition matrix. The eigen problem is solved directly at the coarsest level of representation. The approximate eigen solution is then interpolated over successive levels of the hierarchy, using a small number of power iterations to correct the solution at each stage. To show the effectiveness of this approximation, we present a multi-scale version of the EIGENCUTS algorithm.

1.3 Overview

This thesis is organized in two parts. In the first part we discuss S-PCA and in the second we study spectral clustering.

We begin our discussion in Chapter 2 with the following question: how to identify object-specific multi-scale structure? We review the observation that natural images exhibit structure in a low-dimensional subspace in a sparse, scale-dependent form. Based on this discovery, we propose a new learning algorithm called S-PCA in Chapter 3. In particular, S-PCA basis optimizes an objective function which trades off correlations among output coefficients for sparsity in the description of basis vector elements. This objective function is minimized by a simple, robust and highly scalable algorithm consisting of successive planar rotations of pairs of basis vectors. We discuss the algorithm in detail and demonstrate results on a wide variety of ensembles.

In Chapter 4 we demonstrate an application of this model for appearance-based object detection using two different datasets: separating eyes from non-eyes and classifying faces from non-faces. We end the first part of this thesis in Chapter 5, with a discussion on two possible new directions that we can undertake with S-PCA.

We begin the second part of this thesis in Chapter 6 with an introduction to spectral clustering. In Chapter 7 we present a new clustering algorithm called EIGENCUTS based on a Markov chain perspective of spectral clustering. The significant time complexity of solving eigenvalue problems in spectral clustering motivated us to build a specialized eigensolver suitable for large stochastic matrices with known stationary distributions (Chapter 8). In particular, we exploit the spectral properties of the Markov transition matrix to generate hierarchical, successively lower-ranked approximations to the full transition matrix. To show the effectiveness of this approximation, we also present a multi-scale version of the EIGENCUTS algorithm. We conclude the second part of this thesis in Chapter 10.

Chapter 2

Identifying Object-Specific Multi-Scale Structure

2.1 Motivation

Our goal is to identify and represent structure inherent to high-dimensional object-specific ensembles of visual, and other perceptual, data. In this thesis we consider several different natural image ensembles: images sampled from outdoor environments (Fig. 2.1); face images acquired from roughly similar viewpoints (Fig. 1.2); images of a gesturing hand (Fig. 2.4); and vector-valued optical flow measurements collected from motion sequences. It is well known that natural image ensembles exhibit multi-scale structure. Typically, fine-scale structure is spatially localized while coarse-scale structure is spatially distributed. As an example, consider the database of face images acquired under roughly similar viewpoints and illumination conditions (Fig. 1.2). Here, we expect to see variations in the appearance of the whole (overall face), the parts (forehead, nose, mouth, etc.), and then perhaps some fine details (moles etc.). We are interested in representing these ensemble-specific multi-scale variations.

There are at least two approaches to take for building a multi-scale representation: (1)

Figure 2.1: Natural Image Ensemble.

use a basis set that is "predefined" or (fixed) as in 2-D Gabors (e.g., see [28,29] or wavelets (e.g., see [41, 69, 102]); (2) *learn* a representation that matches structure intrinsic to an ensemble (e.g., [10, 11]). A predefined basis is inflexible, and often awkward to define, so we pursue a learning framework instead.

For learning it is useful to begin with some knowledge of the ensemble statistics. Natural images form a highly constrained dataset when compared to random images. More important is the fact that natural images possess scale invariant statistics [19, 36, 94, 111, 113]. Scaling can be seen in the power spectrum $P(f)$ which takes the form of a power-law in the spatial frequency:

$$P\left(f\right) = C/f^{2-\alpha}, \tag{2.1}$$

where f is the magnitude of spatial frequency, α is a small number ≈ 0.2 and C is a constant determining the overall contrast. Scaling was also observed in higher-order statistics [94]. What might be the origin of scaling in natural images?

Images can be described in terms of primitive structural elements, such as *lines* and *edges* at various positions, scales and orientations (Fig. 2.2 and Fig. 2.3). This leads one to suspect that a power-law distribution of these structural elements might be the reason for scale-invariance [37] (for an alternate point of view see [47, 58, 93]). Interestingly, in mammalian striate cortex the response properties of simple cells involved in early stages of visual processing seem to fit the profiles of line and edge detectors at various positions, orientations, and scales. This raises the possibility that perhaps early cortical representation evolved to match the statistics of natural images [38].

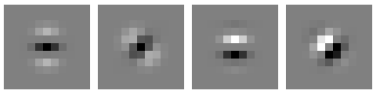

Figure 2.2: Spatial profiles of even ("line") and odd ("edge") wavelet filters. The filters shown here respond best to image structure oriented 0 and 45 degrees away from the horizontal, at a scale given by $\lambda = 4$ pixels [41].

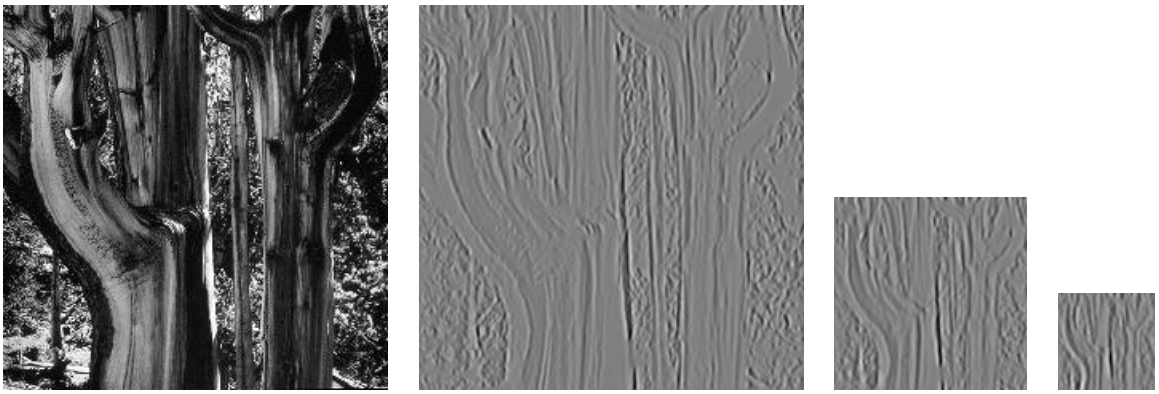

Image $\lambda = 4$ $\lambda = 8$ $\lambda = 16$

Figure 2.3: Multi-scale decomposition of a natural image using a "line" filter (Fig. 2.2). The results show responses from three different filters, each tuned to an angle of 90 degrees away from the horizontal and at scales $\lambda \in \{4, 8, 16\}$ pixels. The filter outputs at scales $\lambda \in \{8, 16\}$ have been sub-sampled.

While invariances may facilitate a direct understanding of the image structure, they are not always present, such as when the ensembles are object-specific. In a database of face images, the statistics are likely to be, at best, locally stationary. In fact, there is an important observation to be made about object-specific ensembles that is not apparent from studying the power spectrum alone; which is that in several object-specific ensembles multi-scale structure reveals itself in a sparse, scale-dependent form [85]. We will discuss this issue in considerable detail later in this chapter.

A typical learning strategy is then to combine knowledge of ensemble statistics with simple optimization principles, based on the hypothesis that images are caused by a linear combination of statistically *independent* components [10, 11]. The goal is to seek a representation that can reduce, if not eliminate, pixel redundancies. For example, we expect pixels that belong to the same object to have statistical dependencies and the statistics must be different if the pixels were to come from different objects. There were several specific optimization criteria put forth in the literature to achieve the goal of statistical independence in the derived representation: redundancy minimization or decorrelation [7–9, 34, 57, 61, 61, 66], maximization of information transmission [13, 14, 16, 27, 57, 64, 95, 114], or sparseness in encoding [38, 46, 79].

In this chapter, we will review three relevant algorithms: Principal Component Analysis (PCA) [49], sparse coding [46, 79] and Independent Component Analysis (ICA) [12–14, 27]. PCA uses second-order statistics to decorrelate the outputs of an orthogonal set of basis vectors. However, decorrelation alone does not guarantee statistical independence. Alternatively, sparse coding constrains outputs to be drawn from a low-entropy distribution to achieve, if not independence, at least a reduction in higher-order dependencies. Similarly, ICA is closely related to sparse coding and is based on an information-theoretic argument of maximizing the joint entropy of a non-linear transform of the coefficient vectors

The strategies of sparse coding and ICA were deemed successful because they extract

multi-scale, wavelet-like structure when applied on an ensemble of natural scenes (such as images of forests/outdoors). However, when the input ensemble is specific to an object (e.g. face images), sparse coding, ICA and PCA all lead to basis images that are *not* multi-scale, but rather appear *holistic* (or alternatively very local), lacking an obvious visual interpretation [12, 103, 112]. We will be discussing this issue in greater detail later in this chapter, where we identify object-specific structure and demonstrate that the learning algorithms such as PCA, sparse coding and ICA are not predisposed to converge to naturally occurring, object-specific, multi-scale structure.

2.2 Decorrelation, Sparsity and Independence

2.2.1 Datasets

In this chapter we train PCA, sparse coding and ICA on three different ensembles: a database of generic image patches sampled from images of outdoor environments [79] (Fig. 2.1), a database of gesturing hand images (Fig. 2.4) and a database of face images [80] (Fig. 1.2). We hope to extract multi-scale structure from these datasets. For example, in the hand image dataset we can observe that the back of the palm appears in all the images and hence pixels in that area should have large-scale, strong correlations across the ensemble. Also, the hand is undergoing transitions between stationary gestures and we expect the coordinated movement of the fingers in forming gestures to leave specific types of signatures. Thus, we seek a representation that depicts the multi-scale nature of this dataset.

The generic image patches were sampled from a database of outdoor images, which is the same database used in [79]. The patches are each of size: 16×16 pixels and we collected a total of 5000 patches. The hand images are each of size: 50×52 pixels and the database has 156 images in total. For the face database, we used the publicly available ORL database [80]. The face images are frontal-looking, but only roughly aligned. Each

Figure 2.4: Sample images from a database of a gesturing hand. Each sub-image is of size: 50×52 pixels. The database contains images of 6 stationary gestures, and also transition images between these gestures, for a total of 156 images.

image is of size: 112×92 pixels and the database contains 400 images in total.

2.2.2 Linear Synthesis Model

We begin with a linear synthesis model for an ensemble of images given by

$$\vec{t} = B\vec{c} + \vec{\mu} + \vec{\epsilon}, \tag{2.2}$$

where $\vec{t}$ is an N-element 1-D column vector obtained by scanning the image in a standard lexicographic order, B is a matrix of basis functions of size $N \times M$, $\vec{c}$ is a M-element coefficient vector and $\vec{\mu}$ is the mean of input ensemble. We take $\vec{\epsilon}$, an N-element vector, to represent noise sampled from a zero-mean, fixed variance Normal distribution. If M the number of basis vectors is equal to N the total number of pixels in the image, then the basis matrix B is considered to be *critical*, but if $M > N$ then it is called *overcomplete* [102].

2.2.3 Principal Component Analysis (PCA)

In PCA the goal is to construct a small set of basis functions (or images) that can characterize the majority of the variation in the training set. We take the standard view of PCA [49] (for a probabilistic treatment see [92, 109]). Here the data is assumed to be noise free (i.e., $\vec{\epsilon} = 0$) and the variation in the ensemble is characterized by the covariance matrix $\mathfrak{S}$ given by:

$$\mathfrak{S} = \mathcal{E}\left[(\vec{t} - \vec{\mu})(\vec{t} - \vec{\mu})^T\right], \tag{2.3}$$

where $\mathcal{E}$ represents the expectation over the image ensemble $\{\vec{t}_k\}_{k=1}^K$ and $\mathfrak{S}$ is a matrix of size $N \times N$. The eigenvectors of the covariance matrix given by

$$U = \begin{bmatrix} \vec{u}_1 & \vec{u}_2 & \cdots & \vec{u}_N \end{bmatrix}$$

form an orthonormal basis, that is

$$\vec{u}_k^T \vec{u}_j = \begin{cases} 1 & \text{if} \quad k = j, \\ 0 & \text{otherwise.} \end{cases} \tag{2.4}$$

The eigenvectors satisfy

$$\mathfrak{S}\vec{u}_j = \sigma_j^2 \vec{u}_j,$$

where σ_j^2 is the eigenvalue denoting the variance of the input data projected onto the basis direction $\vec{u}_j$ and

$$\sigma_1^2 \geq \sigma_2^2 \cdots \geq \sigma_n^2 \geq 0. \tag{2.5}$$

In a matrix form

$$\mathfrak{S}U = U\Sigma, \tag{2.6}$$

where Σ is a diagonal matrix with entries σ_j^2 arranged on the diagonal according to Eq. 2.5.

A low-dimensional representation for the input ensemble can be built if, for some M, the eigenvalues σ_k^2 are small for $k > M$. In particular, using a principal subspace U

containing the leading M eigenvectors associated with the largest M eigenvalues of the covariance matrix, namely

$$U = \left[\vec{u}_1 \quad \vec{u}_2 \quad \cdots \quad \vec{u}_M\right], \tag{2.7}$$

an approximation $\hat{\vec{t}}$ can be made to the input image $\vec{t}$,

$$\hat{\vec{t}} = U\vec{c} + \vec{\mu},$$

where the coefficient vector $\vec{c}$ is an M-element vector given by

$$\vec{c} = U^T(\vec{t} - \vec{\mu}). \tag{2.8}$$

There are two appealing properties to this eigenvector representation. One, for a given sub-space dimensionality M, the principal subspace defined by the leading M-eigenvectors is optimal in the sense of minimizing the mean squared reconstruction error [49]:

$$\mathcal{E}\left\|\vec{t} - \hat{\vec{t}}\right\|^2,$$

where $\mathcal{E}$ stands for the expectation operator. Two, the basis matrix U leaves the output coefficients *decorrelated*. In other words, the covariance matrix of the output coefficients is the diagonal matrix Σ,

$$\mathcal{E}\left[\vec{c}\,\vec{c}^T\right] = \Sigma.$$

This equation can be easily derived by combining Eq. 2.8, 2.6 and 2.3.

Additionally, we introduce two quantities, one to describe the fraction of the total input variance captured by a PCA basis image and the other to accumulate this fraction over principal subspaces for a given dimensionality s. First, we denote the relative variance captured by the m^{th} basis vector to be $d\mathcal{Q}_m$ given by:

$$d\mathcal{Q}_m = \frac{\sigma_m^2}{\sum_{k=1}^{M}\sigma_k^2}. \tag{2.9}$$

We use the variable $\overrightarrow{d\mathcal{Q}}$, a vector of length M, to represent the relative variances:

$$\overrightarrow{d\mathcal{Q}} = \left[d\mathcal{Q}_1 \quad d\mathcal{Q}_2 \quad \cdots \quad d\mathcal{Q}_M\right], \tag{2.10}$$

Second, we use $\mathcal{Q}_s$ to represent the fraction of total variance a *subspace* of a given dimensionality $s \leq M$ captures:

$$\begin{aligned} \mathcal{Q}_s &= \sum_{t=1}^{s} \frac{\sigma_t^2}{\sum_{k=1}^{M} \sigma_k^2}, \\ &= \sum_{t=1}^{s} d\mathcal{Q}_t. \end{aligned} \tag{2.11}$$

Similarly, $\overrightarrow{\mathcal{Q}}$ is a M-element vector representing the cumulative variances of a M-dimensional principal subspace:

$$\overrightarrow{\mathcal{Q}} = \begin{bmatrix} \mathcal{Q}_1 & \mathcal{Q}_2 & \cdots & \mathcal{Q}_M \end{bmatrix}. \tag{2.12}$$

Results from PCA

Our goal here is to use PCA to assess the intrinsic dimensionality's of the three image ensembles mentioned in §2.2.1 and evaluate if the PCA bases appear to match our intuition for object-specific structure. The datasets have been preprocessed to remove the mean (as in Eq. 2.3) and an eigendecomposition is performed on the covariance matrix of the mean-subtracted dataset. We then compute the relative variance $\overrightarrow{d\mathcal{Q}}$ (Eq. 2.10) and the cumulative variance $\overrightarrow{\mathcal{Q}}$ (Eq. 2.12) separately for each one of the datasets. The plots shown in Fig. 2.5 depict the variation in $\log(d\mathcal{Q}_m)$ and $\mathcal{Q}_m$ as we increase the subspace dimensionality m.

For the face and hand image ensemble, the $\overrightarrow{d\mathcal{Q}}$ plot shows eigen values dropping off rapidly at first, then decreasing roughly exponentially (linearly in $\log(d\mathcal{Q}_m)$ plot) for a large range in the subspace dimension m. This we find is typical for a wide variety of object-specific ensembles.

In comparison, for natural image ensembles we know the amplitude-spectrum has a power law dependency on spatial frequency (Eq. 2.1). This effect can be seen in the roughly linear fall-off that $\log(d\mathcal{Q}_m)$ plot exhibits (up to $m = 150$ or so). It is worth mentioning that the generic image patch dataset in [79] has been preprocessed by

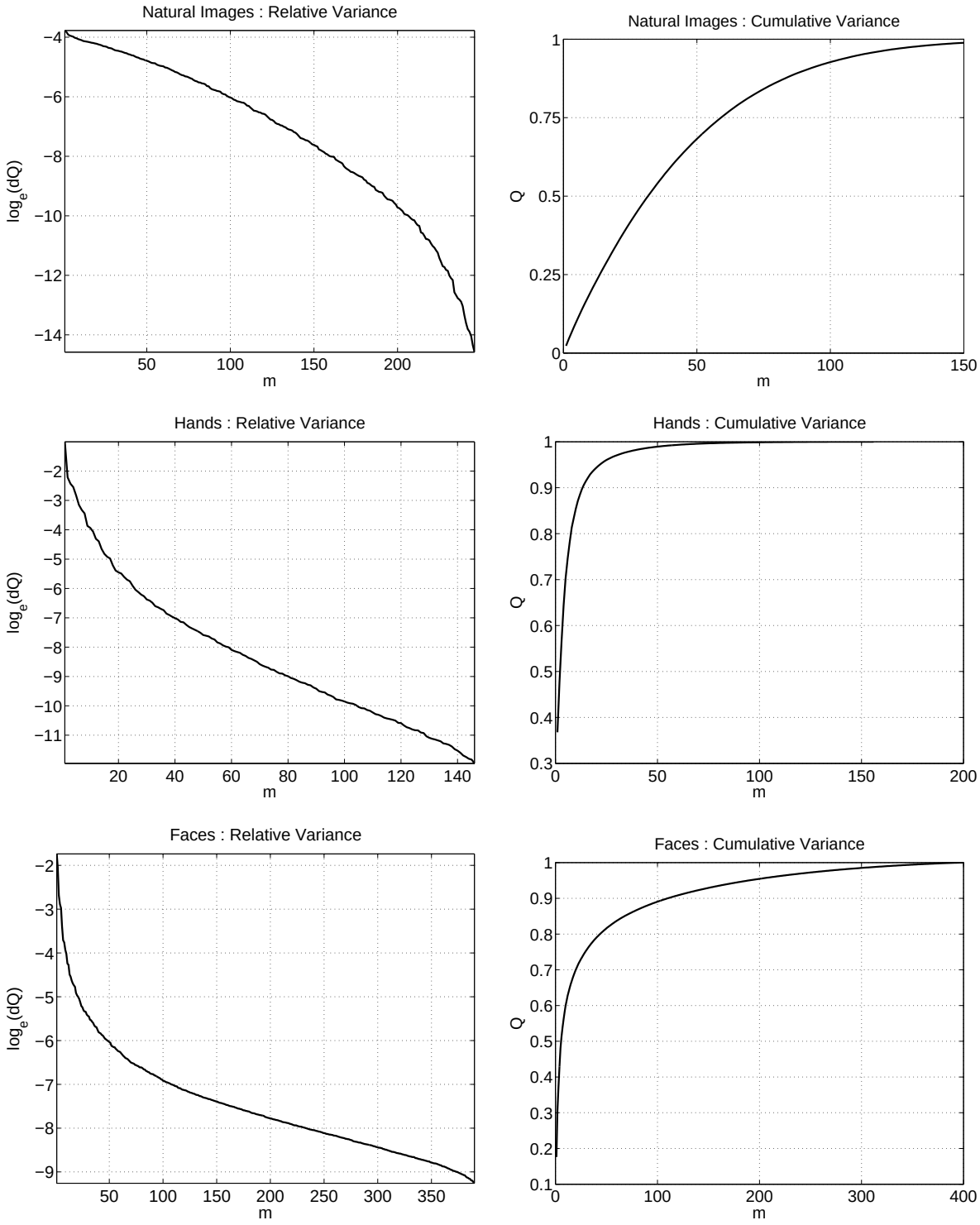

(a) (b)

Figure 2.5: Plots of relative variance (a) and cumulative variance (b) for three different datasets: (TOP) Natural Images (MIDDLE) Hand Images (BOTTOM) Face Images.

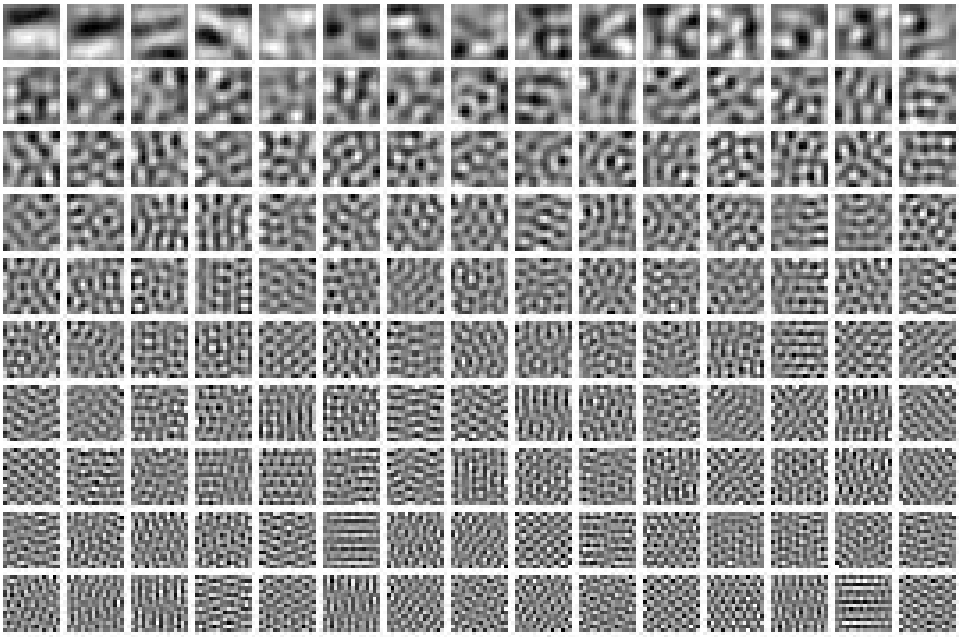

Figure 2.6: PCA basis for an ensemble of generic image patches. PCA basis are displayed in the decreasing order of the input variance they capture, beginning at the top left corner and going horizontally across the page. Observe that the fine-scale information captured by the high-order eigenbasis is spread spatially across the entire image.

a combined low-pass/variance-adjusting filter in the frequency domain, first to remove artifacts of rectangular sampling (that is to eliminate energies present in the corners of the 2-D frequency domain) and then to reduce the effect of large inequities in variance across frequency channels. The filtering effect can be seen in $\log(d\mathcal{Q}_m)$ plot, where the higher eigen bases report a sudden decrease in the accounted variance compared to what the linear fall-off predicts.

From the $\mathcal{Q}_m$ plot drawn for the generic image patch dataset, the first 50 bases account for more than 70% of the mean-subtracted ensemble variance. However, for the hand dataset, almost 95% of the variance is captured by a principal subspace of roughly 25 dimensions. The face database requires at least a 100 dimensional principal subspace to account for 90% of the input variance.

The PCA basis vectors for a generic image patch ensemble are shown in Fig. 2.6. The

PCA basis look similar to a set of discrete Fourier harmonics and the reason is as follows (see [38, 70]). If image statistics are stationary and the covariance information is mainly a function of the distance between pixels, then the covariance matrix exhibits a banded symmetry. If the images are assumed to be periodic, then the covariance matrix takes on a special form called a periodic Toeplitz matrix, where the elements along the diagonals are constant. Interestingly, complex exponentials are eigenvectors of periodic Toeplitz matrices. Hence, for generic image patches which have roughly stationary statistics, a discrete Fourier basis is a good approximation to the PCA directions.

From Fig. 2.6 we can see that the PCA basis are global and spatial frequency-specific. The leading eigenvectors appear to capture edge/line like structure at a coarse scale. However, the remaining PCA basis are not simultaneously local in space and frequency.

Now we analyze the PCA basis images shown in Figs. 2.7 and 2.8, for the hand and the face image ensembles, respectively. The first few basis vectors appear relatively smooth and hence they represent global correlations. In particular, for small values of the eigen vector index m the basis images seem to depict larger scales. An approximate measure of the scale, and hence the correlation length, can be inferred by estimating the size of a blob of one sign (either positive or negative) appearing in a basis image. As the index m for the principal component increases, the scale gets finer and hence the basis vectors appear to represent fine scale structure. However, they remain global in space. This clearly is not representative of the object-specific *local* structure that we believe these images to possess.

2.2.4 Sparse Coding and ICA

The goal in sparse coding is to seek a linear basis representation where each image is represented by a small number of active coefficients (e.g. [38, 46, 79]). The learning algorithm involves adapting a basis vector set, while imposing a *low-entropy* (or *sparse*) prior on the output coefficients. One example of a low-entropy prior is the double-sided

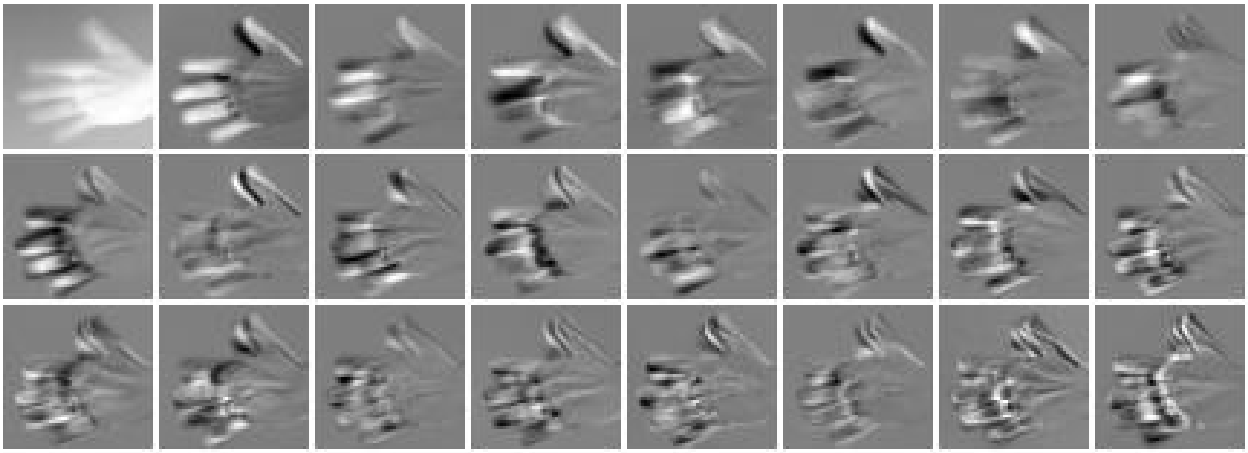

Figure 2.7: PCA results on the hand images. PCA basis are displayed in the decreasing order of the input variance they capture, beginning at the top left corner and going horizontally across the page. Note, fine-scale information represented by the high-order eigenvectors is spread across the entire image.

Laplacian,

$$p(c_j) \propto \exp\left(-\left|\frac{c_j}{\theta}\right|\right), \tag{2.13}$$

where $p(c_j)$ is the probability distribution on the j^{th} element of an output coefficient vector $\vec{c}$. For a discussion on low-entropy priors suitable for sparse coding see [46, 79]. Typically, these are uni-modal, long-tailed distributions with significant probability mass around the origin and having high-kurtosis.

The intuition for sparse priors comes from analyzing the statistics of natural scenes. In particular, evidence for sparse structure can be seen by processing images with wavelet-type filters (Fig. 2.2) and studying the histogram of the filter coefficients. It is clear from the wavelet processed image shown in Fig. 2.3 that smooth regions in an image typically provide negligible filter coefficients. But transition regions, e.g. image patches that appear line-like locally, and in the case of Fig. 2.3 oriented 90 degrees away from the horizontal, have high magnitudes. The resulting filter coefficient histograms show high kurtosis, which is taken to indicate sparse structure.

On the contrary, if the same image structure is filtered with global fine scale PCA

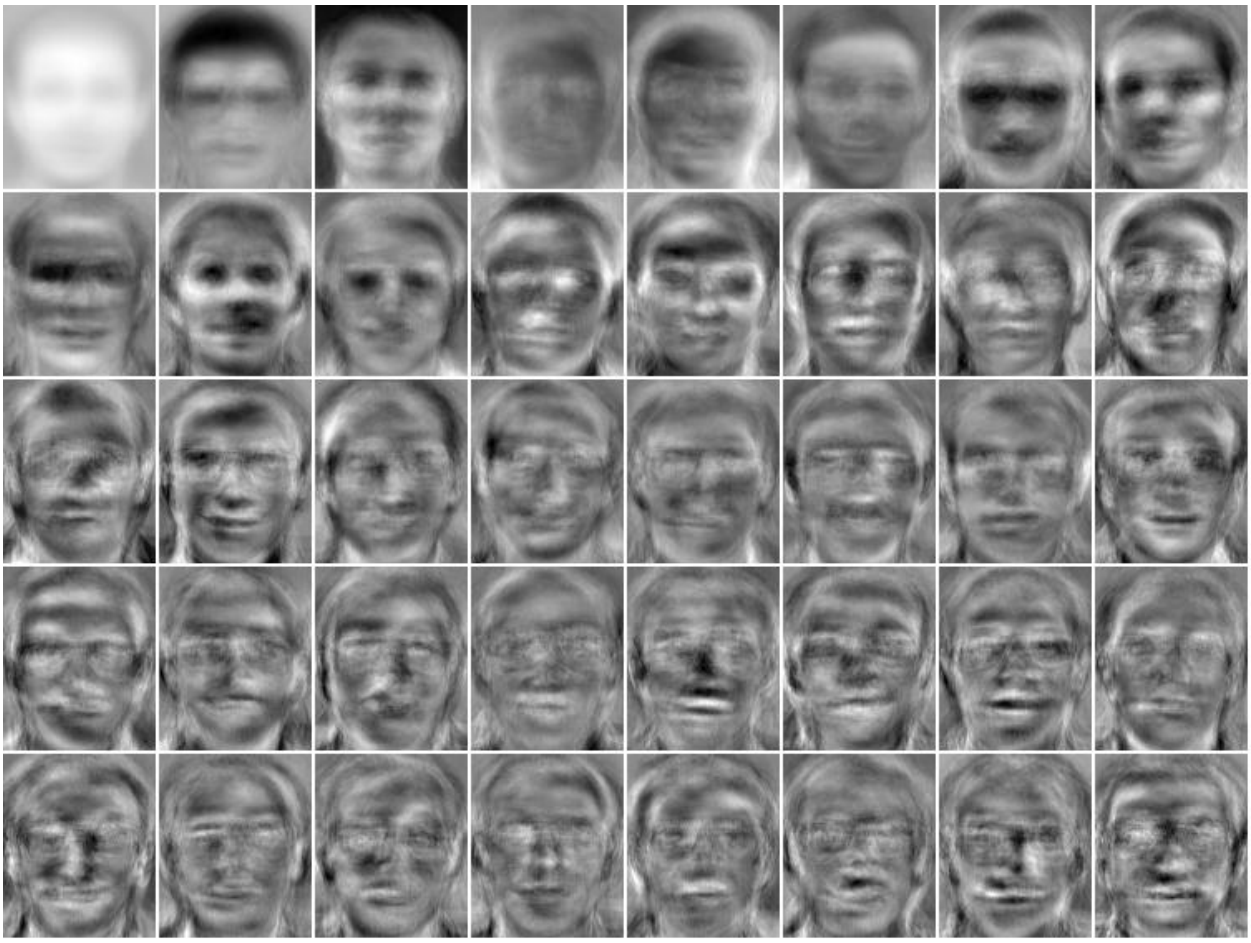

Figure 2.8: PCA basis vectors on face images from the ORL database [80]. The first 40 principal components are displayed in the decreasing order of the input variance they capture, beginning at the top left corner and going horizontally across the page. Observe the finer-scale information represented by the higher-order eigenvectors is spread across the entire image.

basis, then the coefficient histograms are more nearly Gaussian. This effect is due to the Central Limit Theorem, for which the sum of a larger number of independent random variables each of finite variance is approximately Gaussian, no matter what their individual distributions are. So, the hope in using a low-entropy prior for the coefficients is that the adapted basis vector set will acquire the shape and form of the naturally-occurring multi-scale structure.

For a given image ensemble $\left\{\vec{t}_i\right\}_{i=1..p}$ a sparse representation is learned by *minimizing* the following cost function [46, 79]:

$$E(\lambda) = \sum_i E_i(\lambda) = \sum_i \left[||\vec{t}_i - B\vec{c}_i||_2^2 + \lambda \sum_j \Omega(c_{ij}) \right]. \tag{2.14}$$

The cost function $E_i(\lambda)$ for each image $\vec{t}_i$ contains two terms: a reconstruction error term given by $||\vec{t}_i - B\vec{c}_i||_2^2$ and a regularization term given by $\lambda \sum_j \Omega(c_{ij})$. The reconstruction error term encourages B to span the subspace containing the input vectors $\left\{\vec{t}_i\right\}_{i=1..p}$. The regularization term is set up to favor solutions in which the responses c_{ij} match the prespecified prior distribution on the coefficients. In particular, the prior on the coefficients is assumed to be statistically independent, that is,

$$p(\vec{c}) = \prod_j p(c_j). \tag{2.15}$$

Then the penalty term $\Omega(c_j)$ can be expressed as

$$\Omega(c_j) = \log\left(p(c_j)\right). \tag{2.16}$$

The regularization parameter λ controls the weighting of the prior term in the cost function.

The overall cost function $E(\lambda)$ is minimized in two stages. In the inner loop for each image $\vec{t}_i$, the basis matrix B is held fixed and $E_i(\lambda)$ is minimized with respect to the coefficient vector $\vec{c}_i$. In the outer loop, after coding several training images, the accumulated $E(\lambda)$ is minimized with respect to B. The regularization parameter λ need not be held fixed [79].

Before initiating the sparse coding procedure, several decisions have to be made: choosing a functional form for the low-entropy prior (Eq. 2.16,2.13), fixing an appropriate value for λ or deciding to learn it from the data, and guessing a lower bound on the number of basis vectors needed to extract independent components in the images (Eq. 2.14). Our implementation follows the improved version of the sparse coding algorithm presented in [60].

Independent Component Analysis (ICA) is an algorithm based on maximizing the mutual information between the inputs and outputs of an information processing network [13]. ICA can be understood as solving a maximum-likelihood problem, similar to the one posed by sparse coding [67, 79, 83]. In particular, there are two assumptions made in ICA: the ensemble is assumed to be noise-free ($\vec{\epsilon} = 0$) and the basis matrix has a critical form where the number of basis vectors M is equal to the number of pixels N in the input image. Because the basis matrix is critical and the noise is zero, the reconstruction error term in Eq. 2.14 is also zero as long as the basis matrix is linearly independent. This leads to a simple formulation for the optimal basis:

$$B^{\dagger} = \arg\min_B \left[\lambda \sum_i \sum_j \Omega\big([B^{-1}\vec{t}_i]_j\big) - \log|\det(B^{-1})| \right]. \tag{2.17}$$

Instead of adapting the basis matrix B, in the ICA formulation a filter matrix D is learned, where

$$D = B^{-1}. \tag{2.18}$$

The rows of D act as filters and the filter coefficients are obtained by applying the filter matrix to the image $\vec{t}$:

$$\vec{c} = D\vec{t}. \tag{2.19}$$

The learning formulation specified in Eq. 2.17 for the optimal basis matrix B can be easily rewritten to obtain update equations for an optimal filter matrix D. This is precisely the formulation given in the ICA algorithm [13], under the condition that the output of

the ICA network be equal to the cumulative density function of the sparse prior on the coefficients.

As argued in [13] maximizing the mutual information between the inputs and outputs of an information processing network promotes independence in the distribution of the output coefficients. However, a transformation that minimizes the entropy of the individual outputs also promotes their statistical independence (see [46] or Sec 2.5 in [45]).

To get a better understanding of this issue, consider the mutual information $I\left(\vec{c};\,\vec{t}\,\right)$ between the output $\vec{c}$ and input $\vec{t}$ of an information processing system. We will assume the dimensionalities of the input signal $\vec{t}$ and the output coefficient $\vec{c}$ are the same. The mutual information $I\left(\vec{c};\,\vec{t}\,\right)$ can be written as the difference between the joint entropy of the output coefficients $H\left(\vec{c}\right)$ and the conditional entropy of the output given the input given by $H\left(\vec{c}\,|\,\vec{x}\right)$. If the system is assumed to be noiseless, then the conditional entropy in the output given the input $H\left(\vec{c}\,|\,\vec{x}\right)$ is zero. In this case, maximizing the mutual information between the input and output is equivalent to maximizing the overall output entropy. Furthermore, the output entropy is given by the sum of the individual output element entropies minus any mutual information between them:

$$H(\vec{c}) = \sum_i H(a_i) - \sum_i I(c_i; c_{i-1}, \cdots, c_1)$$

. In attempting to maximize the output entropy, we can simultaneously minimize the mutual information term if the individual entropies $\sum_i H(a_i)$ are suitably constrained, either by applying some upper bound or by placing a downward pressure on the sum of the output entropies, as is done in low-entropy or sparse coding. In this way, the mutual information between the output elements is reduced, thus promoting statistical independence among outputs. In fact, in much of the literature the term "independent", as applied to the study of low-level structure in images, is abused when they really mean "low-entropy" (e.g., [14]). We continue this tradition when we refer to the "independent components".

Results from Sparse Coding

The strategies of sparse coding and ICA were deemed successful because they extract multi-scale, wavelet-like structure when applied to an ensemble of natural scenes (such as the images from outdoors/forests) [14,46,79]. This result was seen to be insensitive to the exact functional form of the low-entropy prior [46, 79]. However, for object-specific ensembles we observe that it can be difficult to extract object-specific structure by imposing a low-entropy prior on the output coefficients.

In Figures 2.9 and 2.10 we show results of sparse coding on the hand image dataset. As shown in Fig. 2.5, this ensemble has a low-dimensional description in that the eigen spectrum decays rapidly. So we assume independent components, if any, will reside within a low-dimensional sub-space. Our experience with sparse coding suggests that this procedure has difficulty finding the correct low-dimensional subspace and resolving the independent components within [23]. During optimization, perturbations to the basis matrix B will cause the representation to move away from the spanning space. Optimization steps mainly cause the updates to move the basis matrix B to the spanning space, instead of modifying the representation so it can come closer to capturing the structure within the spanning space. Assuming this to be the case, we split the problem into two sub-problems, namely the restriction to the subspace and the representation within the subspace.

The restriction to the subspace is achieved by principal component analysis (PCA). Images are projected to a low-dimensional subspace spanned by an *orthogonal* set of principal component vectors:

$$\vec{q} = U^T \vec{t},$$

where $\vec{t}$ is the input image, U is a basis matrix with a small number of principal components, U^T is the PCA matrix transposed and $\vec{q}$ is the resulting low-dimensional coefficient

vector. We then search for the sparse structure matrix B' in the projected space:

$$\vec{q} = B'\vec{c},$$

where a low-entropy prior is placed on $\vec{c}$ and B' resolves the sparse structure in the set of low-dimensional data points $\vec{q}$. These two equations can be combined to give the independent components matrix B:

$$\begin{aligned}\vec{t} &= U\vec{q}, \\ &= UB'\vec{c}, \\ &= B\vec{c}.\end{aligned}$$

So to facilitate sparse coding, we first project the data into the space spanned by the first 10 principal components. We can see from Fig. 2.5 that the first ten principal components account for more than 90% of the input variance. However, in this 10-dimensional principal subspace it is not clear how many independent components one should search for. Recall in the sparse coding framework we have the freedom to set the basis matrix to be overcomplete. In Figures 2.9 and 2.10 we show the results from extracting 10 and 15 independent components respectively. The overall appearance of the basis vectors is global and edge-like (alternating dark and bright regions). They cannot be simply interpreted in terms of object parts, i.e. fingers of a hand. We also applied the ICA algorithm in [13] but the results are not very different from the ones shown for sparse coding.

For sparse coding/ICA results on the face images the reader is referred to the thesis in [12], where the filter matrix shows some resemblance to facial features, but the resulting basis matrix appears "holistic". Thus, we have demonstrated that PCA, sparse coding and ICA do not necessarily extract object-specific, multi-scale, local structure. Either our intuition is wrong and the datasets do not contain such structure or the three algorithms have failed to extract it. We next turn our attention to characterizing object-specific structure and discuss how this may impose novel constraints on a learning algorithm.

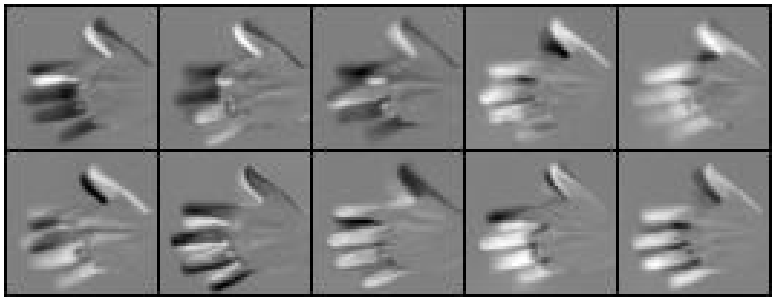

Figure 2.9: Sparse coding results after projecting the data into a 10-dimensional subspace and then searching for 10 basis directions. The mean component of the ensemble is removed prior to the analysis.

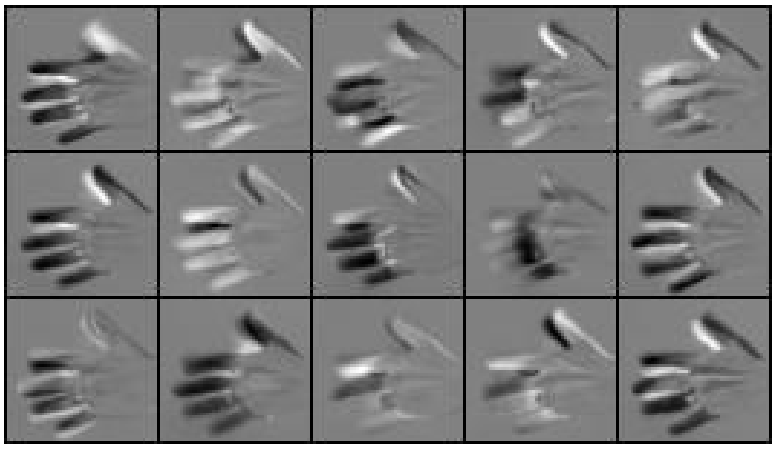

Figure 2.10: Sparse coding results after projecting the data into a 10-dimensional subspace and then searching for 15 basis directions. The mean component of the ensemble is removed prior to the analysis.

2.3 Object-Specific Multi-Scale Structure

What is the structure one can expect to find in an object-specific ensemble? We show that object-specific ensembles exhibit structure in a low-dimensional subspace in a sparse, scale-dependent, local form. In particular, there is large-scale structure correlated across the entire image and fine-scale structure that is spatially localized. Although we study a database of gesturing hand images (Fig. 2.4), the following argument holds true for other object-specific ensembles as well. Once the structure is made explicit, it is easier to conclude whether PCA, sparse coding or ICA was successful in extracting the object-specific structure.

We review the observations made by Penev and Atick in [85]. Here we extend their results to highlight object-specific multi-scale properties. We begin with a linear low-dimensional representation for the ensemble, which can be readily obtained by PCA. As we discussed earlier, the principal components characterize the second-order statistical variation in the ensemble. The associated variance spectrum, for a majority of object-specific ensembles, shows a rapid drop at first, then starts to decrease roughly exponentially (Fig. 2.5). The images in the ensemble can be approximated using a small number of principal components.

We assume each input image $\vec{t}$ that is N-pixels long is approximated by M leading principal components to give:

$$\hat{\vec{t}} = U_{1:M} U_{1:M}^T \vec{t}, \tag{2.20}$$

where U is the principal component matrix spanning the image space, $U_{1:M}$ is a sub-matrix with M leading principal components and $M << N$, the size of the input image. Notice that $U_{1:M} U_{1:M}^T$ is the projection/reconstruction operator for the M-dimensional subspace approximating the image ensemble.

To understand structure, we ask what it means to reconstruct the intensity at a pixel position r in $\hat{\vec{t}}$? It involves the r^{th} row of the projection operator: $U_{1:M} U_{1:M}^T$. We

rearrange the data in the r^{th} row of the matrix $U_{1:M}U_{1:M}^T$, so it can be seen as an image of the same size as the input. As we show in Fig. 2.11, the r^{th} row of $U_{1:M}U_{1:M}^T$ varies with M. Observe that with increasing M, the appearance of the r^{th} row changes from being global to very local. We interpret the projection operator in the following way:

- $U_{1:M}U_{1:M}^T$ captures correlations, not in the raw image space, but in the *whitened* space. For each image $\vec{t}$ there is a whitened image $\vec{j}$ given by:

$$\begin{aligned} \vec{j} &= U_{1:M}\Sigma^{-1/2}U_{1:M}^T\vec{t}, \\ &= U_{1:M}\Sigma^{-1/2}\vec{q}, \\ &= U_{1:M}\vec{d}, \end{aligned}$$

  where $\vec{q} = U_{1:M}^T\vec{t}$ is the vector of PCA coefficients for input image $\vec{t}$, Σ is a diagonal matrix providing the variance in each element of the coefficient vector $\vec{q}$ across the ensemble, and $\vec{d}$ is a rescaling of $\vec{q}$ such that it can be treated as a sample from a zero-mean unit-variance Gaussian distribution (assuming the dataset is zero mean). The image $\vec{j}$ is considered whitened because the covariance matrix of $\vec{d}$ is the identity matrix. Hence, the covariance of the whitened image ensemble is given by:

$$\begin{aligned} < \vec{j}\vec{j}^T > &= U_{1:M} < \vec{d}\vec{d}^T > U_{1:M}^T, \\ &= U_{1:M}U_{1:M}^T. \end{aligned}$$

- The correlation in the space of whitened images $< \vec{j}\vec{j}^T >$ provides a measure of how appropriate it was to use M global models in representing the image ensemble. If the correlations are large, global models such as PCA are appropriate. Otherwise, at least some spatially local models (and perhaps some global models) would be more appropriate. This is clearly the case for $M = 12$ and higher in Fig. 2.11.

In Fig. 2.12 we show how the correlation map at each pixel appears to have a shape, characteristic of a part of the object (i.e. the hand and its fingers) and the correlation

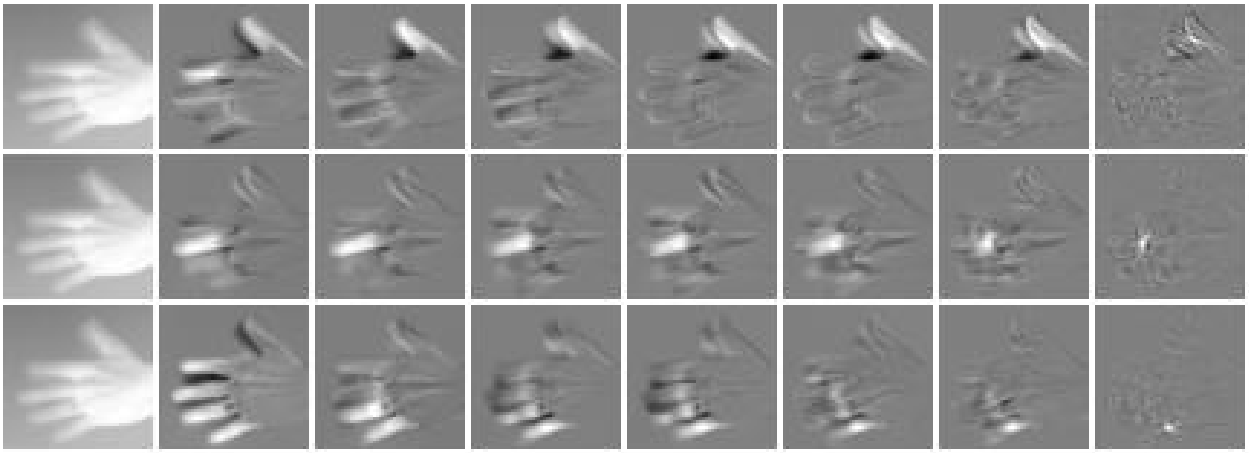

Figure 2.11: The appearance of the projection/reconstruction matrix $U_{1:M}U_{1:M}^T$, for the hand image ensemble, at three different pixel locations centered on the thumb (Top), middle (Center) and the last finger (Bottom), each corresponding to a different row in the matrix: $U_{1:M}U_{1:M}^T$. Each column in the figure corresponds to a different value of M ranging in: $\{1, 4, 8, 12, 16, 20, 40, 156\}$, where $M = 1$ is the left most column. Sub-images are rescaled to have the zero value correspond to a gray level of 127. Observe that fine scale structure caused by the moving fingers is spatially localized.

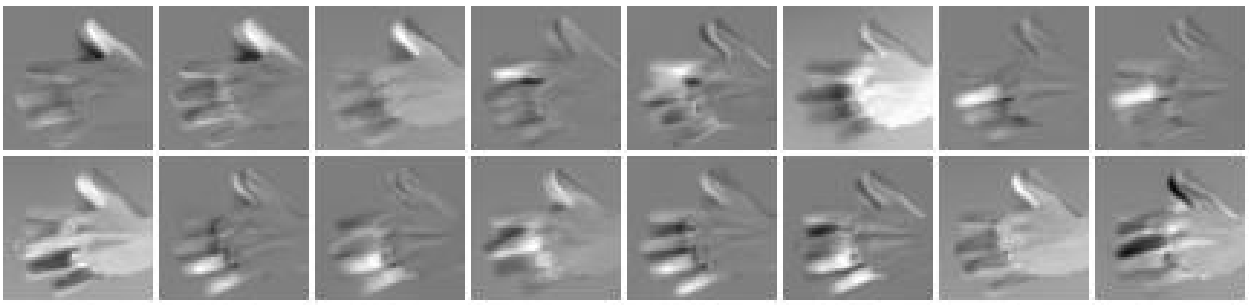

Figure 2.12: A sample of rows from the projection matrix $U_{1:M}U_{1:M}^T$, with $M = 10$. Depending on the row selected, sub-images clearly exhibit structure characterizing parts of the hand. Sub-images are rescaled to have zero value correspond to a gray level of 127.

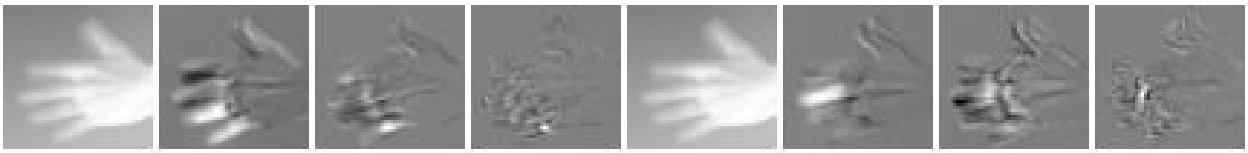

Figure 2.13: Multi-scale structure in the hand image ensemble measured at two different pixel locations, corresponding to the last finger (Cols 1–4) and the middle finger (Cols 5–8). The first, and last, four columns each correspond to a row location in the projection matrix created by grouping four different sets of principal eigenvectors: $[U_{1:1}U_{1:1}^T]$, $[U_{2:5}U_{2:5}^T]$, $[U_{6:24}U_{6:24}^T]$ and $[U_{25:99}U_{25:99}^T]$. Each of these projection operators can be interpreted as denoting a different scale for the correlation lengths between pixels.

maps vary smoothly between adjacent pixels. For pixels in large coherent regions, such as the back of the hand, the extent of the correlation is large. At other points the correlation maps appear sparse by being dominant only in local regions. PCA ignores this sparse form, coalescing local structure to form global basis vectors.

Moreover, by considering projections of the form $U_{k:m}U_{k:m}^T$ we can demonstrate the local nature of spatial correlations at specific scales (also see Sec 5.4 in [84]). Suppose the principal components are grouped into consecutive bands of roughly equal energy. Energy here is measured as the total amount of input variance captured. Let $U_{k:m}$ be one such matrix band having principal components numbered consecutively from k to m. As shown in Fig. 2.13, each banded projection operator indicates a different scale for the correlation lengths between pixels.

We will not pursue this analysis in too much detail because we propose a new algorithm in the following chapter which gives us a clearer understanding of the relationship between scale and correlation length in such datasets.

To summarize, we have shown that in object-specific ensembles there is a large-scale structure correlated across the entire image and fine-scale structure that is localized spatially. The learning algorithms based on PCA, sparse coding and ICA did not capture

this structure. As we demonstrate in the next chapter, placing a sparse prior on the basis elements, instead of output coefficients, is a powerful way to predispose a learning mechanism to converge to this naturally-occurring, sparse, multi-scale, local structure. In particular, we demonstrate that when eigenvalues are pooled into bands of roughly equal values, the corresponding eigenvectors within each band possess many rotational degrees of freedom that can be utilized.

Chapter 3

Sparse Principal Component Analysis: S-PCA

3.1 Introduction

A primary contribution of this thesis is to show how multi-scale representations emerge, for a variety of image ensembles, by trading off redundancy minimization for sparsity maximization in a basis matrix. We base our strategy *Sparse Principal Component Analysis* (S-PCA) on the observation we made in the previous chapter, that natural images exhibit structure in a low-dimensional subspace in a sparse, scale-dependent form. S-PCA learns an orthonormal basis by rotating the basis vectors that span the principal subspace. Rotation achieves sparsity in the basis vectors at the cost of introducing small correlations in the output coefficients. If the input ensemble is a multi-dimensional Gaussian with widely separated variance distribution (that is the ratio of successive values in the eigen spectrum is large) , then S-PCA returns a redundancy minimizing solution, namely the basis vectors of PCA. On the other hand, if the input ensemble is devoid of any structure (i.e. i.i.d. pixel intensities), then S-PCA returns a maximally sparse representation, with each basis vector representing the brightness at a single pixel. As

our examples show, this property of returning a sparse representation, when possible, provides a much more intuitive representation of the ensemble than a standard PCA based representation.

Besides this theoretical advantage of providing a better intuitive model of an ensemble, the computation of the basis coefficients is more efficient because of the presence of zero valued weights in the sparse basis vectors. The speed-up obtained from this sparsity will depend on both the ensemble and on the number of basis vectors used. In particular, for all the natural data sets we have considered, the S-PCA basis vectors tend to get increasingly sparse as the corresponding variances decrease. Therefore the speed-up due to sparsity can be very significant when many basis vectors are used, but less significant when only a few are used.

3.2 Encouraging Sparsity

To illustrate the basic idea of S-PCA, consider 2-pixel image ensembles generated from a multi-dimensional Gaussian distribution. Each image is a point in a 2-dimensional space. In Fig. 3.1, we show two such datasets, one with a dominant orientation (a) and the other essentially isotropic (b).

PCA determines an orthonormal set of basis vectors with the property that the basis expansion coefficients are decorrelated. The idea of PCA in this 2D example is to rotate the pixel basis, $\left[\begin{smallmatrix}1 & 0\\ 0 & 1\end{smallmatrix}\right]$, until the variance of the projected data is maximized for one component and is minimized for the other. In Fig. 3.1, the PCA directions for the distributions are shown in blue. For the correlated dataset in Fig. 3.1a, the PCA vectors are aligned with the oriented structure underneath. For the uncorrelated dataset in Fig. 3.1b, the specific directions that PCA selects are dictated by sampling noise. For such datasets we prefer basis vectors that are sparse (and orthonormal), that is, have few non-zero entries. In this 2D example, this is just the pixel basis, $\left[\begin{smallmatrix}1 & 0\\ 0 & 1\end{smallmatrix}\right]$, as shown in red in Fig. 3.1b.

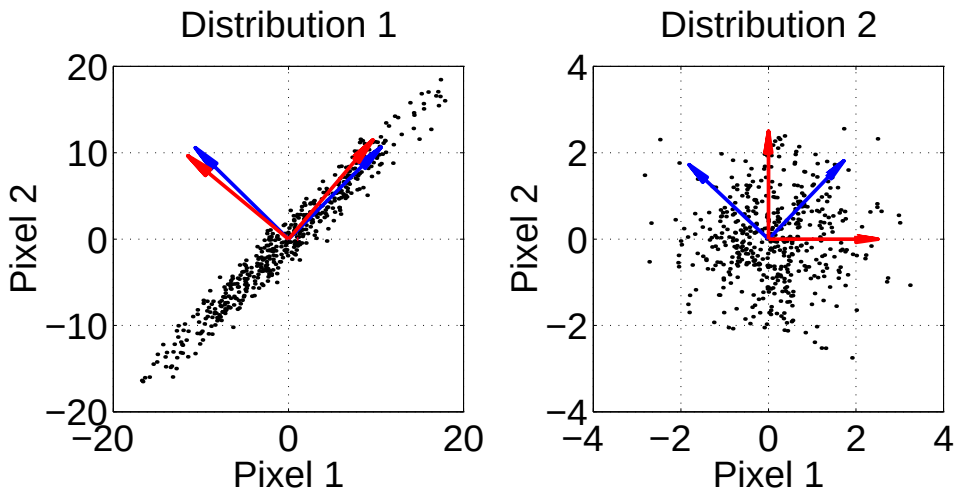

(a) (b)

Figure 3.1: What is PCA good for? Distributions 1 and 2 (black dots) are 2-pixel image ensembles sampled from multi-dimensional Gaussian priors. (a) Distribution 1 has a dominant orientation indicated by the PCA basis (blue). (b) Distribution 2 has no orientational structure, and the PCA basis (blue) reflects sampling noise. In both cases the preferred S-PCA basis vectors are obtained by rotating PCA directions. In (a) the rotation is minimal, while in (b) the rotation maximizes sparsity in the basis vector description by aligning them with the pixel basis.

Note the sparse basis can be achieved by simply *rotating* the PCA basis by an amount depending on the degree of correlation in the underlying dataset.

3.3 S-PCA Pairwise Rotation Algorithm

The idea behind S-PCA is to retain the PCA directions when there is correlational structure in the data set, and otherwise rotate them to be as sparse as possible. We propose a cost function

$$C(\lambda) = C_1 + \lambda C_2, \tag{3.1}$$

where C_1 is a function of the variances of the data projected onto the individual basis vectors, and C_2 is a function of the elements of the basis vectors themselves. The exact form for C_1 and C_2 are not so important, so long as C_1 is designed to retain the PCA directions while C_2 promotes sparsity. The λ parameter in the cost function provides the relative importance of the sparsity term, and we choose it to make the contributions from C_1 and C_2 have the same scale. See the next section for the actual forms of C_1, C_2 and how λ was selected to keep the scale of C_1 and C_2 the same in all the examples used in this thesis.

The learning algorithm of S-PCA is very simple. The basis vectors are initialized to be the principal components or any other convenient orthonormal basis. The dimensionality of this principal subspace is chosen beforehand. Selecting a maximal dimension basis is also possible. Every pair of these basis vectors defines a hyperplane, and we successively select suitable rotations within these hyperplanes to minimize $C(\lambda)$. We sweep through every possible basis vector pair doing these rotations, and these sweeps are repeated until the change in $C(\lambda)$ is below a threshold. The product of the pairwise rotations provides a composite rotation matrix which, when applied to the PCA vectors generates the S-PCA basis. In particular, the S-PCA and PCA bases are orthonormal representations for the same subspace and are related to each by other by this rotation matrix. A typical implementation of this algorithm is given in the next section.

The PCA basis is used as the starting point since it identifies the principal subspace best suited to recovering correlational structure. The job of the S-PCA algorithm is then simply to resolve the range of the spatial correlations. Note that the S-PCA basis is always a rotation of the original basis, so some care should be taken in choosing this starting basis. In cases for which we want a complete representation (that is the basis matrix is square), we have found that the trivial basis (i.e. provided by the columns of an identity matrix), and also random orthonormal matrices, can be used as a starting point for the S-PCA algorithm.

3.3.1 Details

A typical implementation of S-PCA is given in ALGORITHM 1. We chose a entropy-like measure for the two terms C_1 and C_2 in the cost function. It is also possible to have a probabilistic treatment for the cost function, and we present this in a later chapter.

Let $U = \left[\vec{u}_1\, \vec{u}_2\, \cdots\, \vec{u}_M\right]$ be a basis matrix spanning an $M-$dimensional subspace, with $\vec{u}_m = \left(u_{1,m}, \ldots, u_{N,m}\right)^T$ and $\vec{u}_m^T \vec{u}_k = \delta_{m,k}$ (the Kronecker delta). Let σ_m^2 be the variance of the data projected onto the direction $\vec{u}_m$. Using Eq. 2.10 we set up a relative variance vector

$$\overrightarrow{d\mathcal{Q}} = \left[d\mathcal{Q}_1 \quad d\mathcal{Q}_2 \quad \cdots \quad d\mathcal{Q}_M\right]$$

where

$$d\mathcal{Q}_m = \frac{\sigma_m^2}{\sum_{k=1}^{M} \sigma_k^2}.$$

The first term of the cost function, namely $C_1\left(\overrightarrow{d\mathcal{Q}}\right)$, is defined as

$$C_1\left(\overrightarrow{d\mathcal{Q}}\right) = \sum_{m=1}^{M} -d\mathcal{Q}_m \log(d\mathcal{Q}_m). \tag{3.2}$$

It can be shown that $C_1\left(\overrightarrow{d\mathcal{Q}}\,;\, U\right)$ is minimized if and only if the basis vectors U are PCA directions [32].

The second term in the cost function, namely $C_2(U)$, is defined as

$$C_2(U) = \sum_{m=1}^{M} \sum_{n=1}^{N} -u_{n,m}^2 \log(u_{n,m}^2). \tag{3.3}$$

Notice that this is just the sum of the entropies of the distributions defined by the square of the elements for each basis vector $\vec{u}_m$ (recall the basis vectors have unit norm). If the elements of the basis vector have a Gaussian-like distribution, as in PCA, entropy is high and so is the cost function C_2. If the basis vectors form an identity matrix, entropy is minimal, i.e. zero. Thus, $C_2(U)$ promotes sparsity. We have also experimented with other concave objective functions that can promote sparsity in $C_2(U)$, e.g. $\sum_{mn} \log\left[\alpha + \beta \exp\left(-\left|u_{n,m}/\gamma\right|\right)\right]$ where α, β and γ are the parameters of the sparsity driving function, and observed qualitatively similar results with S-PCA.

We choose the λ parameter such that the contributions from C_1 and C_2 to the overall cost function C will be on the same scale. For this we need to know the range of values C_1 and C_2 take for a typical dataset. For example, the cost term C_2 is a function of the elements of the basis vectors (Eq. 3.3) and is independent of any other properties of the input data. In particular, for an identity basis (or any permutation thereof), which is the sparsest matrix, the contribution from C_2 is 0, but for an orthonormal matrix of size $N \times M$ having entries each of size $1/\sqrt{N}$, C_2 contributes a maximum value of $M \log(N)$.

Similarly, the term C_1 measures the entropy of a variance distribution (Eq. 3.2). The entropy is minimal when the basis vectors are PCA directions and maximal if the variance is spread uniformly across all the basis directions. The upper-bound is clearly $\log(M)$ but how do we get an estimate for the lower-bound set by the PCA basis? One simple approach is to assume scale-invariant statistics in the dataset (Fig. 2.5 Top) where the power spectrum is inversely proportional to the square of the spatial frequency Eq. 2.1. Following the discussion in §2.2.3, we can replace the spatial frequency index f in Eq. 2.1 by the eigenbasis index m and develop an analytical form for the variance spectrum:

$$\sigma_m^2 \propto 1/m^2.$$

We use this expression to empirically evaluate C_1 for various values of M, the dimensionality of the principal subspace. With increasing M, the maximum value C_1 can take changes as $\log(M)$ but we observe a much slower growth in the lower-bound, with C_1 approaching an asymptotic value of 2.3626. Also, from the analysis presented in Fig. 3.1 we expect the variance spectrum returned by S-PCA basis to be 'close' to the spectrum obtained by PCA directions. In fact we show this to be the case for a wide variety of ensembles. Thus it makes sense to set a value for λ that scales C_2 to match the lower-bound of C_1. We use the following expression for λ for all the datasets used in this thesis:

$$\frac{1}{\lambda} = M \log(N). \tag{3.4}$$

In choosing λ we have ignored the size of the dataset, which obviously affects the com-

putation of the variance spectrum. Also, not all datasets have scale-invariant statistics and we may have to adjust the λ parameter accordingly.

Additionally, there are two implementation details that are worth mentioning. First, the optimization problem reduces to a sequence of rotations involving pairs of basis vectors, $[u_i\, u_j]$. One trick is to not consider every basis pair. For example, if the variances on the corresponding basis pair are widely different, then they are likely to correspond to the situation shown in Fig. 3.1a. In this case, there should be no significant rotation. A simple way to disregard a basis pair $[u_i\, u_j]$ is to check if the log ratio of the corresponding variances: $\max\left(\sigma_i^2, \sigma_j^2\right)/\min\left(\sigma_i^2, \sigma_j^2\right)$, is less than a threshold. We use a threshold of 7.0 on all the datasets reported in this thesis. However, we found S-PCA results not to be overly sensitive to the actual setting of this threshold. Secondly, there is a search done for the correct rotation angle θ_{ij}. The gradient of the cost function with respect to the rotation angle θ_{ij} is easy to derive and hence, can be used while searching for the optimal solution. However, we find the results are as good if we take the less expensive option, which is to use optimization routines that do not use gradient information (eg. routines `mnbrak` in conjunction with `brent` from [89]).

As we discuss next, the iterative algorithm converges to a stationary point of the cost function $C(\lambda)$. We select a basis pair and search for a suitable rotation in the hyperplane defined by the basis pair that minimizes $C(\lambda)$. Because the rotation is within the hyperplane, contribution to the overall cost function $C(\lambda)$ by the remaining basis vectors, and their variances, does not change. We use this fact in setting up the optimization problem (Algorithm 1, lines $16 - 18$). Because the rotation angle, selected for every basis pair, minimizes the cost function, and a rotation update to the basis directions, and the corresponding variances, is applied before picking the next basis pair (Algorithm 1, lines $19 - 20$), the algorithm either continuously descends or remains stationary. Thus, at the end of every sweep the overall cost function has either been reduced or is left at a stationary point.

Algorithm 1 Function $U = \text{Sparse-PCA}(U, \Sigma, \lambda)$

1: INPUT

2: $U \Leftarrow \{U \text{ is a } N \times M \text{ matrix with orthonormal columns, } M \leq N\}$

3: $\Sigma \Leftarrow \{\text{Variance matrix for data projected onto } U\text{: } \Sigma_{ii} = \sigma_i^2;\ \Sigma_{ij} = \Sigma_{ji} = \sigma_{ij}^2\ \}$

4: $\lambda \Leftarrow \{\text{Sparsity factor which can be a function of } N \text{ and } M \text{ as in Eq. 3.4}\}$

5: OUTPUT

6: $U \Leftarrow \{\text{Sparse PCA basis matrix}\}$

7: CONSTANTS

8: $\theta_{\text{init}} = 0; \quad \theta_{\text{tol}} = 1.0e{-}4; \quad \epsilon = 1.0e{-}8$

9:

10: $d_m = \dfrac{\sigma_m^2}{\sum_{k=1}^{M} \sigma_k^2} \quad \forall m = 1 \cdots M; \quad \vec{d} = \big(d_1, \ldots, d_M\big)^T$

11: $C_{\text{new}} = C_1(\vec{d}) + \lambda C_2(U)$ {Eq. 3.2 and 3.3}

12: **while** not converged **do**

13: $C_{\text{old}} = C_{\text{new}}$

14: **for** $i = 1$ to M-1 **do**

15: **for** $j = i + 1$ to M **do**

16: $\widetilde{U} \Leftarrow \big[\vec{u}_i\, \vec{u}_j\big]; \quad \widetilde{D} \Leftarrow \begin{bmatrix} \frac{\sigma_i^2}{\sum_{k=1}^{M} \sigma_k^2} & \frac{\sigma_{ij}^2}{\sum_{k=1}^{M} \sigma_k^2} \\ \frac{\sigma_{ij}^2}{\sum_{k=1}^{M} \sigma_k^2} & \frac{\sigma_j^2}{\sum_{k=1}^{M} \sigma_k^2} \end{bmatrix}$

17: $\theta_{ij} = \theta_{\text{init}}; \quad R(\theta_{ij}) = \begin{bmatrix} \cos(\theta_{ij}) & -\sin(\theta_{ij}) \\ \sin(\theta_{ij}) & \cos(\theta_{ij}) \end{bmatrix}$

18: $\theta_{ij} \Leftarrow \text{MINIMIZE}\Big\{ C_1\Big(\text{diag}(R^T \widetilde{D} R)\Big) + \lambda C_2\Big(\widetilde{U} R\Big) \Big\} \text{ for } \theta_{ij}$

19: $U\big(:, [i\, j]\big) = \widetilde{U} R(\theta_{ij}) \quad \text{if } \theta_{ij} > \theta_{\text{tol}}$ {Update the i and j columns of U}

20: $\begin{pmatrix} \sigma_i^2 & \sigma_{ij}^2 \\ \sigma_{ji}^2 & \sigma_j^2 \end{pmatrix} = R(\theta_{ij})^T \begin{pmatrix} \sigma_i^2 & \sigma_{ij}^2 \\ \sigma_{ji}^2 & \sigma_j^2 \end{pmatrix} R(\theta_{ij}) \quad \text{if } \theta_{ij} > \theta_{\text{tol}}$ {Update entries in Σ}

21: **end for**

22: **end for**

23: $C_{\text{new}} = C_1(\vec{d}) + \lambda C_2(U)$ {Compute $\vec{d}$ as in Line 10 above (Eq. 3.1)}

24: converged $= \left(\left| \frac{C_{\text{old}} - C_{\text{new}}}{C_{\text{old}}} \right| < \epsilon \right)$

25: **end while**

3.4 S-PCA on Datasets With Known Structure

We demonstrate results from applying S-PCA on datasets where the structure is known *a priori*. Consider an image ensemble generated by convolving Gaussian white-noise vectors with a filter kernel and adding small amounts of noise to the filtered signals (Fig. 3.2). The generative model can be written as:

$$\vec{y} = \vec{g} \otimes \vec{x} + \kappa \vec{n}, \tag{3.5}$$

where $\vec{x}$ and $\vec{n}$ are samples from a zero-mean, unit-variance Gaussian distribution, $\otimes$ is the convolution operator, $\vec{g}$ is a filter kernel, $\vec{y}$ is the noisy version of the filtered signal $\vec{g} \otimes \vec{x}$ and finally, κ is the standard deviation of the noise distribution chosen to be 2% of the maximum absolute value in the ensemble. This translates to about 5 gray levels for an image with a peak intensity value of 255 gray levels. In Fig. 3.2(a & b) we also show the filter kernels which are low-pass and band-pass respectively. The filters are modeled after a Gaussian function and its second derivative. The standard deviation of the Gaussian was chosen to be 1 pixel and the filters were designed to be 7-tap long. The ensemble contains 10000 samples of the filtered signal $\vec{y}$.

3.4.1 Low-Pass Filtered Noise Ensemble

We begin our analysis with a low-pass filtered noise ensemble. We expect to see correlations in spatially local neighborhoods of the output signal $\vec{y}$ because of the Gaussian smoothing. We now show that S-PCA provides a representation which highlights this structure.

A Principal Component Analysis (PCA) of such a data set provides a basis representation which is global and spatial frequency specific. The PCA basis vectors are shown in Fig. 3.3 and a Fourier transform of each individual basis vector is shown in Fig. 3.4. The variance spectrum resulting from the PCA basis is shown in Fig. 3.7. Notice that

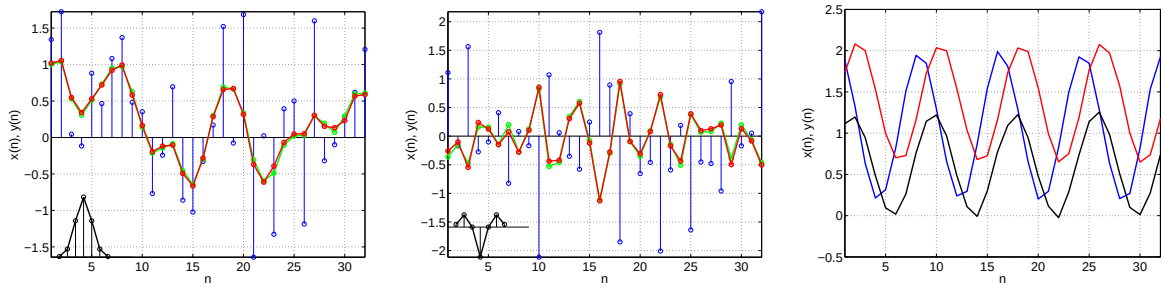

Figure 3.2: (LEFT & MIDDLE) Stem plots in blue are Gaussian noise signals, which are filtered by a low-pass kernel (drawn as an inset figure (LEFT)) and a band-pass kernel (also drawn as an inset figure (MIDDLE)). The filtered signals are shown in green and their noisy versions are drawn in red. (RIGHT) Noisy versions of sine waves each initialized with a random phase/amplitude and a random DC value. Signals are 32 pixel long vectors.

the PCA representation does not highlight the spatially localized structure introduced by Gaussian smoothing.

In comparison, the S-PCA basis derived for the low-pass filtered noise ensemble provides structure at multiple scales, evident from the spatial domain plot in Fig. 3.3 and the frequency domain plot in Fig. 3.4. The first few basis vectors appear as low-pass filters in the spatial domain, whose size is indicative of the Gaussian kernel used to introduce the correlations between pixels. While these basis vectors are spread evenly over the pixel space, they cannot significantly overlap due to the orthogonality constraint. Instead, basis vectors at the next scale exhibit entries with multiple signs, but still remain local.

To confirm if there is a good match between the correlation lengths depicted by the multi-scale basis vectors and the scale of the low-pass kernel used to generate the ensemble (Fig. 3.2), we overlay a (circularly) shifted and scaled version of the low-pass kernel on each of the S-PCA basis vectors as shown in Fig. 3.5. Visually, the scales appear to be in good agreement and we confirm this numerically by computing a scale value for each

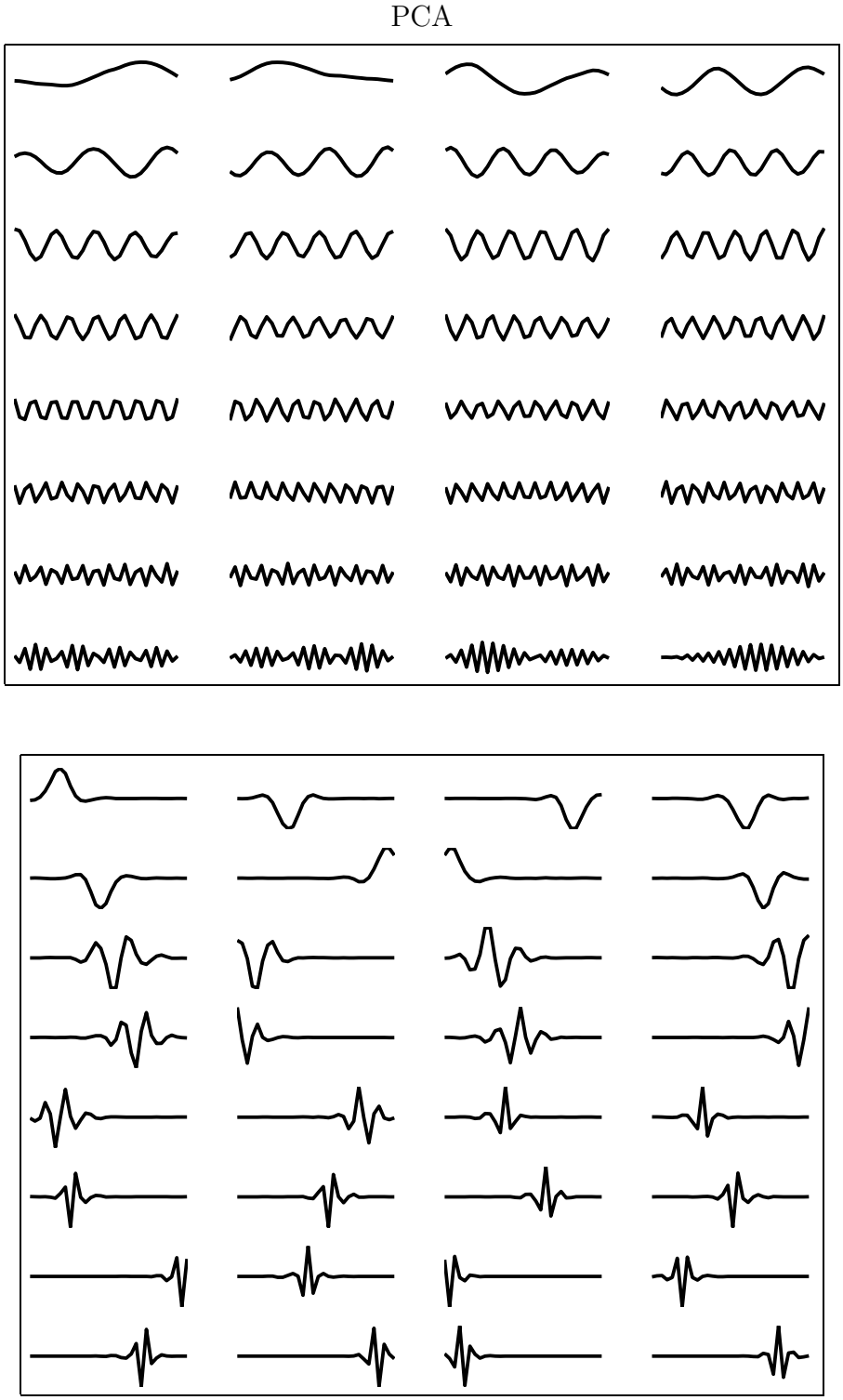

Figure 3.3: Representing Gaussian filtered noise ensemble using PCA (Top) and S-PCA (Bottom). Each waveform is 32 pixels long. In each waveform the zero line is near the median value of the waveform. Zero valued weights in S-PCA results indicate a sparse basis matrix.

PCA Basis in Fourier Domain

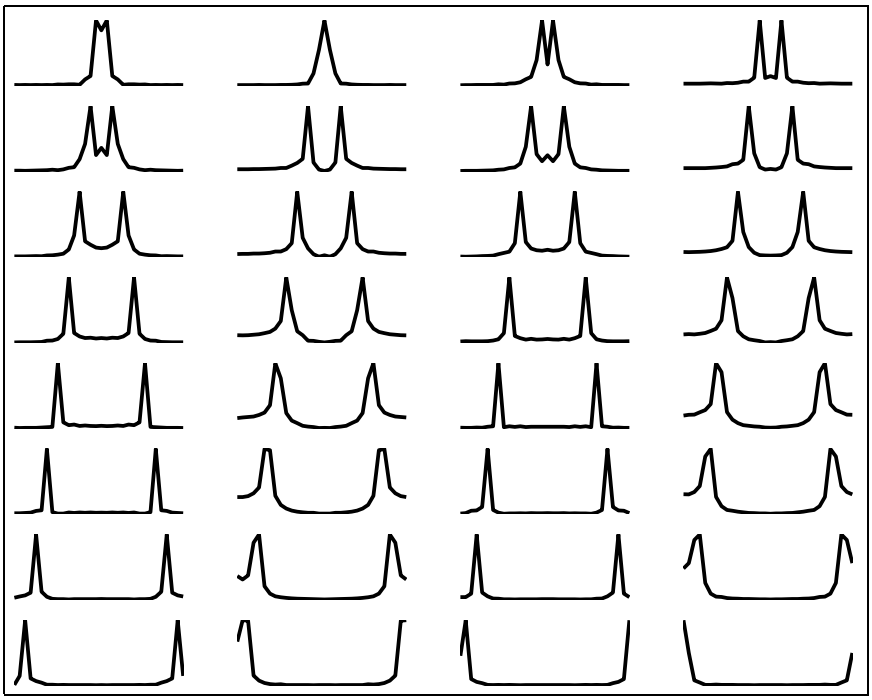

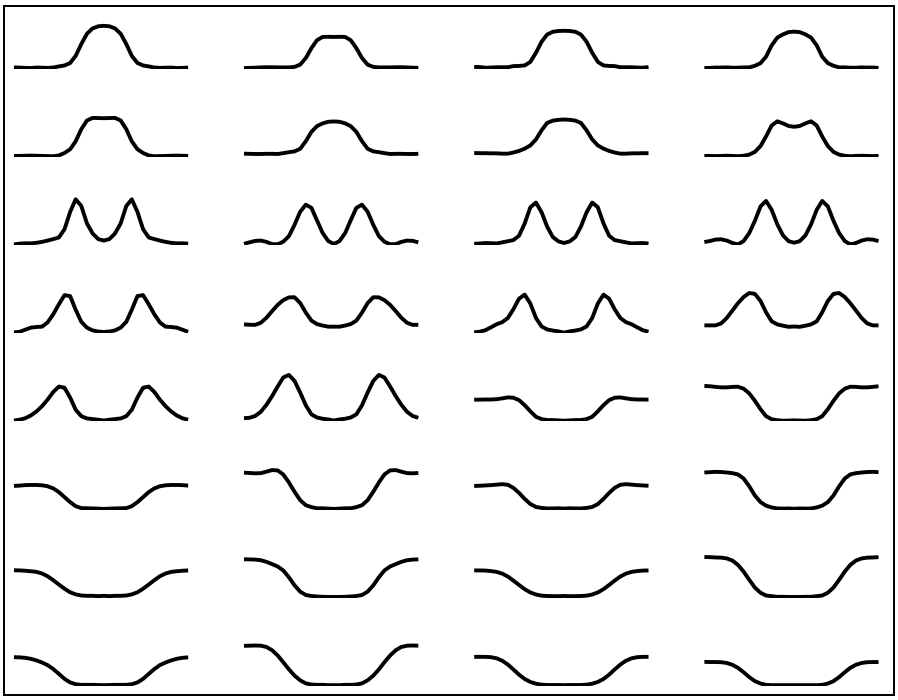

S-PCA Basis in Fourier Domain

Figure 3.4: Representing Gaussian filtered noise ensemble (contd). Fourier transform of the PCA basis (Top) and S-PCA basis (Bottom). Plots depict the amplitude in the Fourier domain. PCA basis are frequency-specific but S-PCA basis have multi-scale band-pass character.

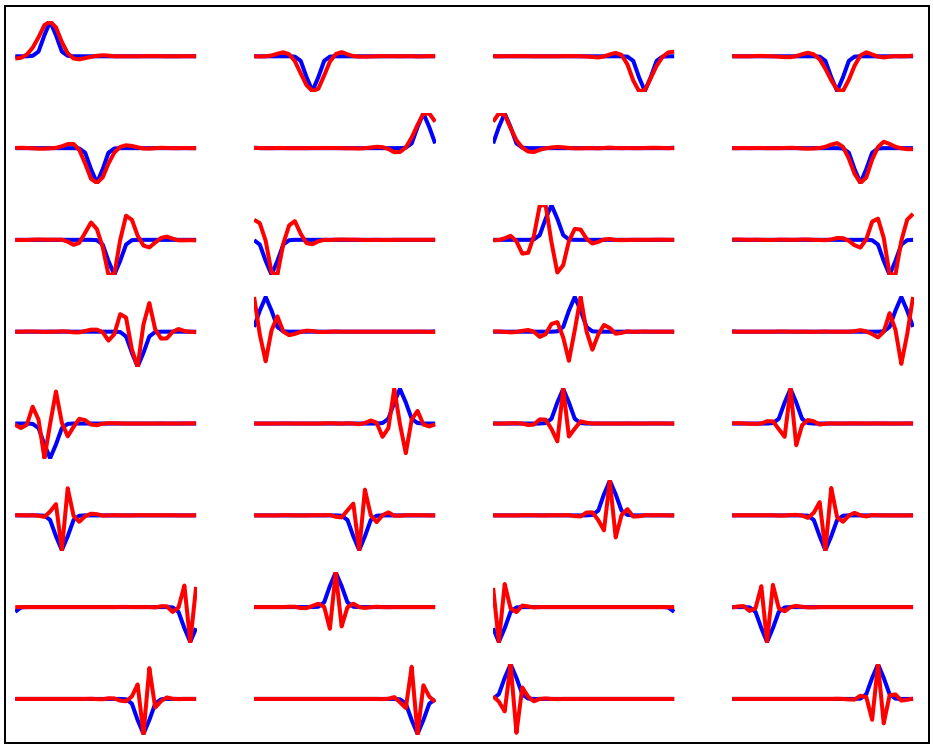

Figure 3.5: Overlay of a circularly shifted, scaled version of the low-pass kernel (blue) on the multi-scale basis (red).

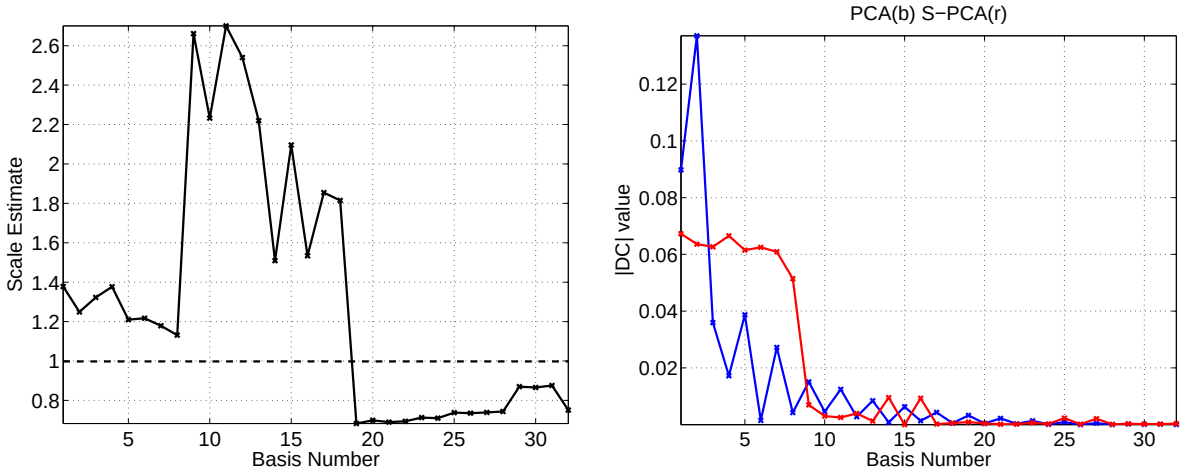

Figure 3.6: Representing Gaussian filtered noise ensemble (contd). (LEFT) Estimate of the scale for each S-PCA basis vector. For comparison the scale of the low-pass kernel is drawn as a dashed horizontal line at 1.0. (RIGHT) Absolute of the DC value for each PCA (blue) and S-PCA (red) basis vectors.

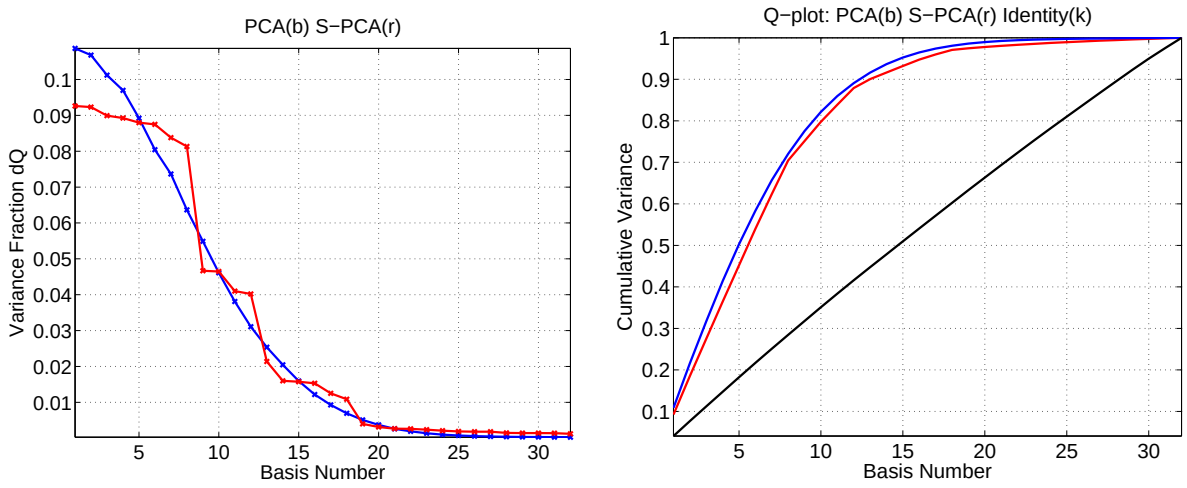

Figure 3.7: Representing Gaussian filtered noise ensemble (contd). (LEFT) Smoothly decaying variances of PCA (blue) reshaped to locally flat portions by S-PCA (red) (RIGHT) Fraction of the total variance captured by m-dim subspaces as m varies from 1 to 32: PCA (blue), S-PCA (red), Identity matrix (maximally sparse) (black).

basis vector as given below:

$$\mu_i = \frac{\sum_{p=1}^{N} p \times |\vec{u}_i(p)|}{\sum_{p=1}^{N} |\vec{u}_i(p)|}, \tag{3.6}$$

$$s_i = \frac{\sum_{p=1}^{N} (p - \mu_i)^2 \times |\vec{u}_i(p)|}{\sum_{p=1}^{N} |\vec{u}_i(p)|}, \tag{3.7}$$

where $\vec{u}_i$ is the i^{th} basis vector, index p runs over the pixel locations, N is the length of the basis vector, μ_i is weighted mean of the absolute values of the basis vector $\vec{u}_i$ and finally, s_i is the scale we are after. For the Gaussian kernel used to generate the ensemble, this computation would return a value of 1.0 (which is how the kernel is designed). We plot the scales computed for the S-PCA basis set in Fig. 3.6. Indeed, the leading S-PCA basis and the basis vectors higher in the hierarchy have scales close to 1, but basis vectors in the middle of the multi-scale hierarchy exhibit somewhat larger scales. Overall, we think this distribution of scales supports our argument that the structure in this ensemble is spatially localized.

On a closer inspection of the multi-scale basis in Fig. 3.3, we observe that the leading

S-PCA basis functions appear to have "small" side lobes that are typically associated with band-pass filters, although the lobes are not as prominent as they are in basis vectors down the multi-scale hierarchy. Moreover, for band-pass filters in the frequency domain we expect a 'dip' in the amplitude spectrum at the zero frequency, but from Fig. 3.4 the leading basis vectors appear to be low-pass filters. The reason is that the leading basis vectors have a significant non-zero DC value. This can be seen from the plot in Fig. 3.6. Obviously a non-zero DC component in any basis vector adds power to the zero frequency in the Fourier domain, potentially washing away any dip in the amplitude spectrum.

S-PCA thus generates spatially localized, bandpass orthonormal functions as basis vectors, thereby achieving a joint space and frequency description in a manner similar to a wavelet basis. The separation in scales can be also seen in the plot of the variances as a function of the basis index (Fig. 3.7). Notice that the smoothly decaying variances for the PCA basis have been reshaped by S-PCA to locally flat portions. Each flat portion corresponds to basis functions at a particular scale.

There are two other properties of S-PCA worth noting. First, when λ is non-zero, the fraction of input variance captured by the first m-dimensional subspace is always higher in PCA (blue curve in Fig. 3.7(Right)) than S-PCA (red curve in Fig. 3.7(Right)). We know this must be the case from the corresponding optimality property of the PCA basis (see § 2.2.3). However, the difference between these two curves is relatively small, compared to the increased sparsity of the basis vectors (see Fig. 3.3). Note that the ranges of constant variance for S-PCA basis vectors correspond to linear segments in the $\overrightarrow{\mathcal{Q}}$ (Fig. 3.7 Left).

As λ is increased, the sparsity of the S-PCA basis is increased, with a corresponding decrease in the variance captured by S-PCA. At extremely large values of λ, the S-PCA basis becomes maximally sparse, with each basis function representing an individual pixel. The variance captured by the maximally sparse basis is given by the single black line in Fig. 3.7.

3.4.2 Band-Pass Filtered Noise Ensemble

Can S-PCA resolve structure that is *local* in both *space* and *frequency*? We investigate this issue by analyzing a noise ensemble that has been convolved with a band-pass filter. The generative model is similar to the one discussed in Eq. 3.5. A sample of this dataset, along with the band-pass kernel, is shown in Fig. 3.2. The filter kernel is the second-derivative of a Gaussian. The Gaussian function has a standard deviation of 1 pixel and the filter kernel is 7-tap long. The ensemble contains 10000 samples.

Due to band-pass filtering we expect the correlations to be local both in space and frequency. The PCA basis shown in Fig. 3.8 buries this structure but S-PCA basis clearly indicate the range, and specificity, of correlation lengths in space and frequency. Fourier descriptions of the PCA and S-PCA basis shown in Fig. 3.9 make this point clear. In fact, from Fig. 3.8 it appears as if the first few S-PCA basis vectors approximate the band-pass filter used on the noisy ensemble. To confirm this we use Eq. 3.7 to estimate the extent of the filter kernel (which is ≈ 1.5609) and the S-PCA basis vectors. From the plot shown in Fig. 3.11, we can see that the leading S-PCA basis functions have extents that match the filter kernel. The variance spectrum and the cumulative distribution for the subspace variance are shown in Fig. 3.10. Again, it is clear that S-PCA basis fits a multi-scale description to the band-pass filtered ensemble.

3.4.3 Noisy Sine Waves

Can S-PCA resolve structure that is *global* in space? We investigate this issue by analyzing an ensemble of noisy single-frequency sinusoids generated by randomizing the phase and amplitude. In particular, we used the following generative model:

$$\vec{y} = d + a \times \sin\left(\frac{8\pi}{N}\vec{x} + \theta\right) + \kappa\vec{n},$$

where $\vec{x}$ is a position vector of length N ranging between $[0, N-1]$, N is 32, $\vec{n}$ is N-element noise vector whose elements are sampled from a zero-mean, unit-variance

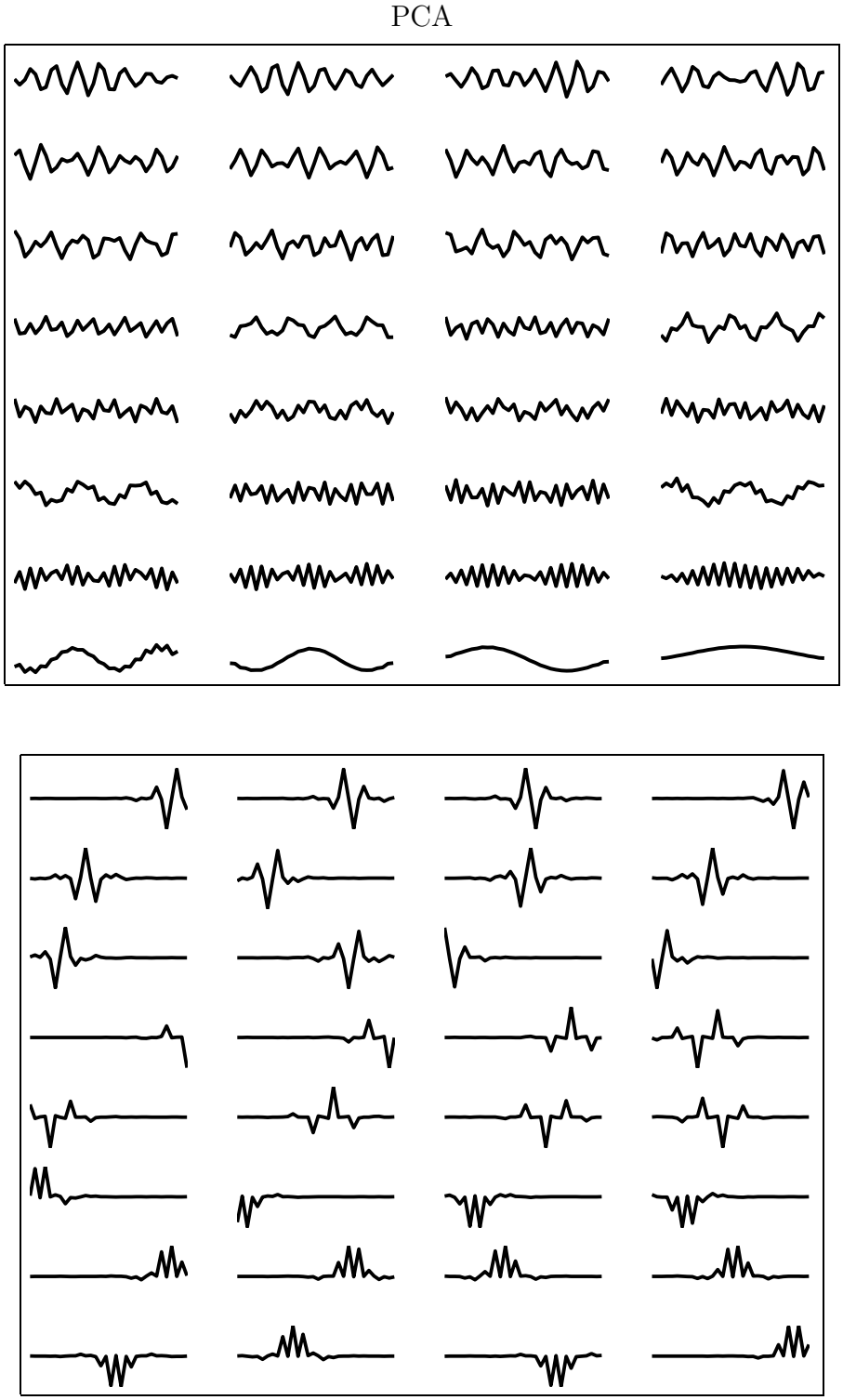

Figure 3.8: Representing band-pass filtered noise ensemble using PCA (Top) and S-PCA (Bottom). Each waveform is 32 pixels long. In each waveform the zero line is near the median value of the waveform. Zero valued weights in S-PCA results indicate a sparse basis matrix.

PCA Basis in Fourier Domain

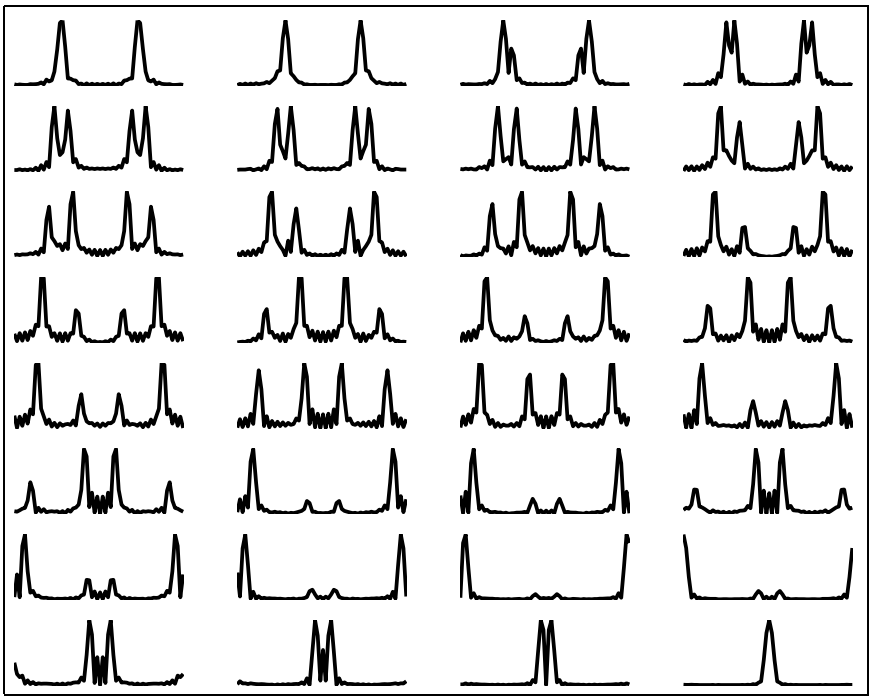

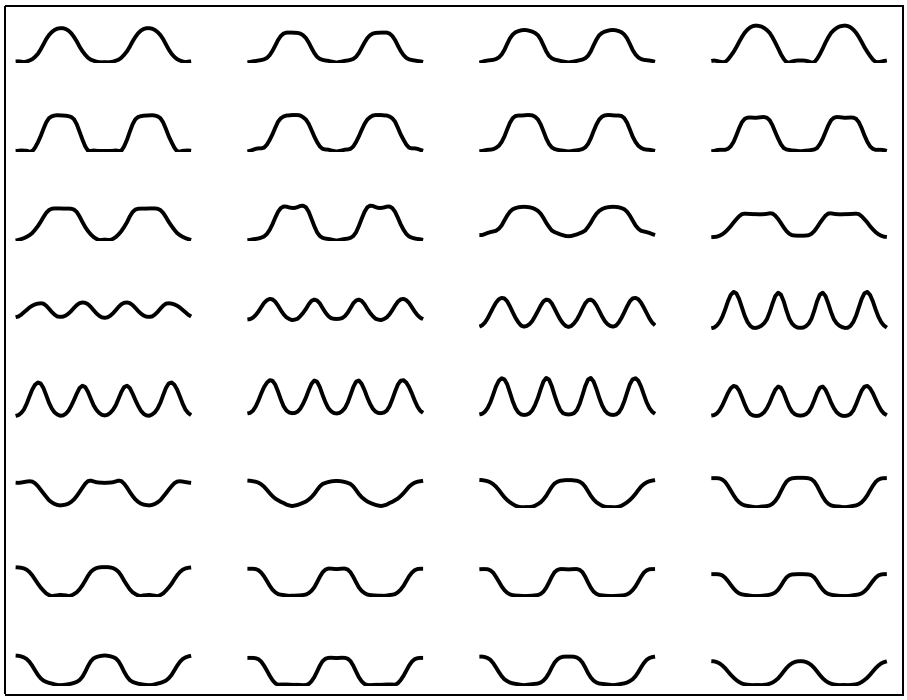

S-PCA Basis in Fourier Domain

Figure 3.9: Representing band-pass filtered noise ensemble (contd). Fourier transform of the PCA basis (Top) and S-PCA basis (Bottom). Plots depict the amplitude in the Fourier domain. PCA basis are frequency-specific but S-PCA basis have multi-scale band-pass character.

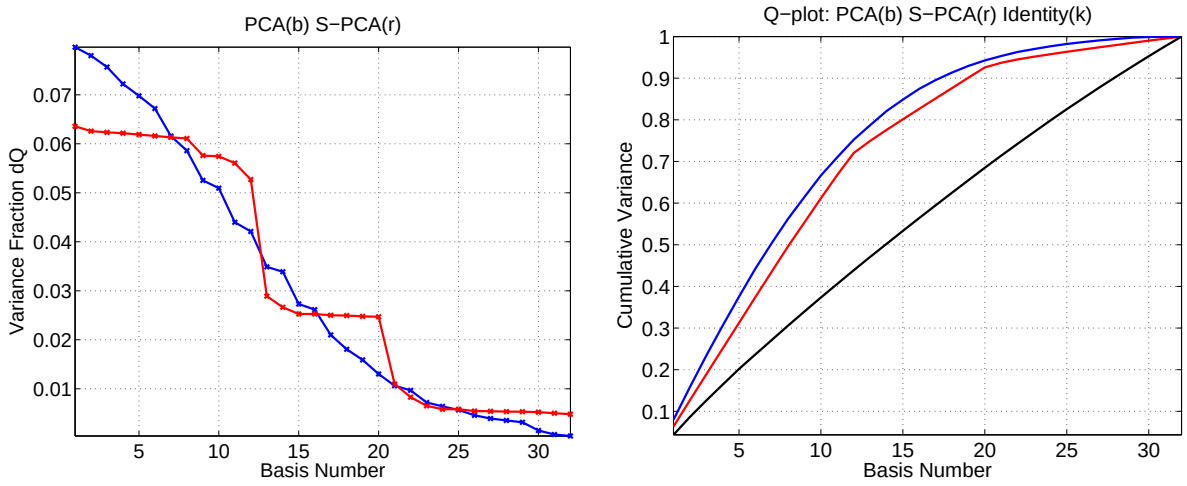

Figure 3.10: Representing band-pass filtered noise ensemble (contd). (LEFT) Smoothly decaying variances of PCA (blue) reshaped to locally flat portions by S-PCA (red) (RIGHT) Fraction of the total variance captured by m-dim subspaces as m varies from 1 to 32: PCA (blue), S-PCA (red), Identity matrix (maximally sparse) (black).

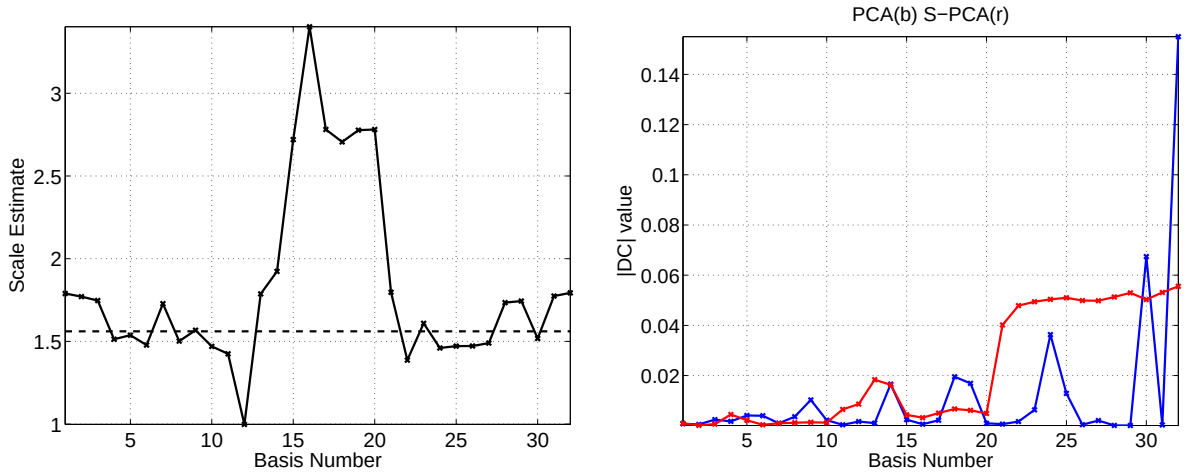

Figure 3.11: Representing band-pass filtered noise ensemble (contd). (LEFT) Estimate of the scale for each S-PCA basis vector. For comparison the scale of the band-pass kernel is drawn as a dashed horizontal line at ≈ 1.5609. (RIGHT) Absolute of the DC value for each PCA (blue) and S-PCA (red) basis vectors.

Gaussian distribution, d and a represent the DC and the amplitude values respectively both drawn from a zero-mean, unit-variance Gaussian distribution and finally, θ is the random phase between $[-\pi, \pi]$. The noise variance κ is chosen to be 2% of the maximum absolute value in the ensemble. The ensemble is generated with 10000 noisy sinusoids and a sample of them is shown in Fig. 3.2.

Because of the sinusoid we expect the correlations to be global and in fact, sinusoidal. Indeed both PCA and S-PCA retrieve the sine and cosine basis functions from the data along with a DC vector (see Fig. 3.12). However, unlike PCA, the basis vectors from S-PCA clearly indicate that the remaining correlations are spurious because of noise and hence the most appropriate basis vectors are small variations of the trivial basis so that orthogonality with respect to the leading basis functions can be preserved.

3.4.4 Garbage In, "Garbage" Out?

What happens if the ensemble is *white noise*? To make this problem interesting, we take a small number of white noise vectors (sampled from zero-mean, unit-variance Gaussian) and perform PCA/S-PCA analysis. The data lies in a 32 dimensional space but we use only 100 samples.

As shown in Fig. 3.15, the PCA directions cannot resolve the fact that the ensemble is really garbage. However, the S-PCA pays attention to the lack of correlations and returns a trivial basis set as a suitable representation. Consequently, the variance spectrum returned by S-PCA basis is roughly flat (Fig. 3.14).

3.5 S-PCA on Natural Ensembles

We next apply S-PCA on ensembles of natural images. For each ensemble, we present our guess for the inherent structure and show that S-PCA confirms our intuition.

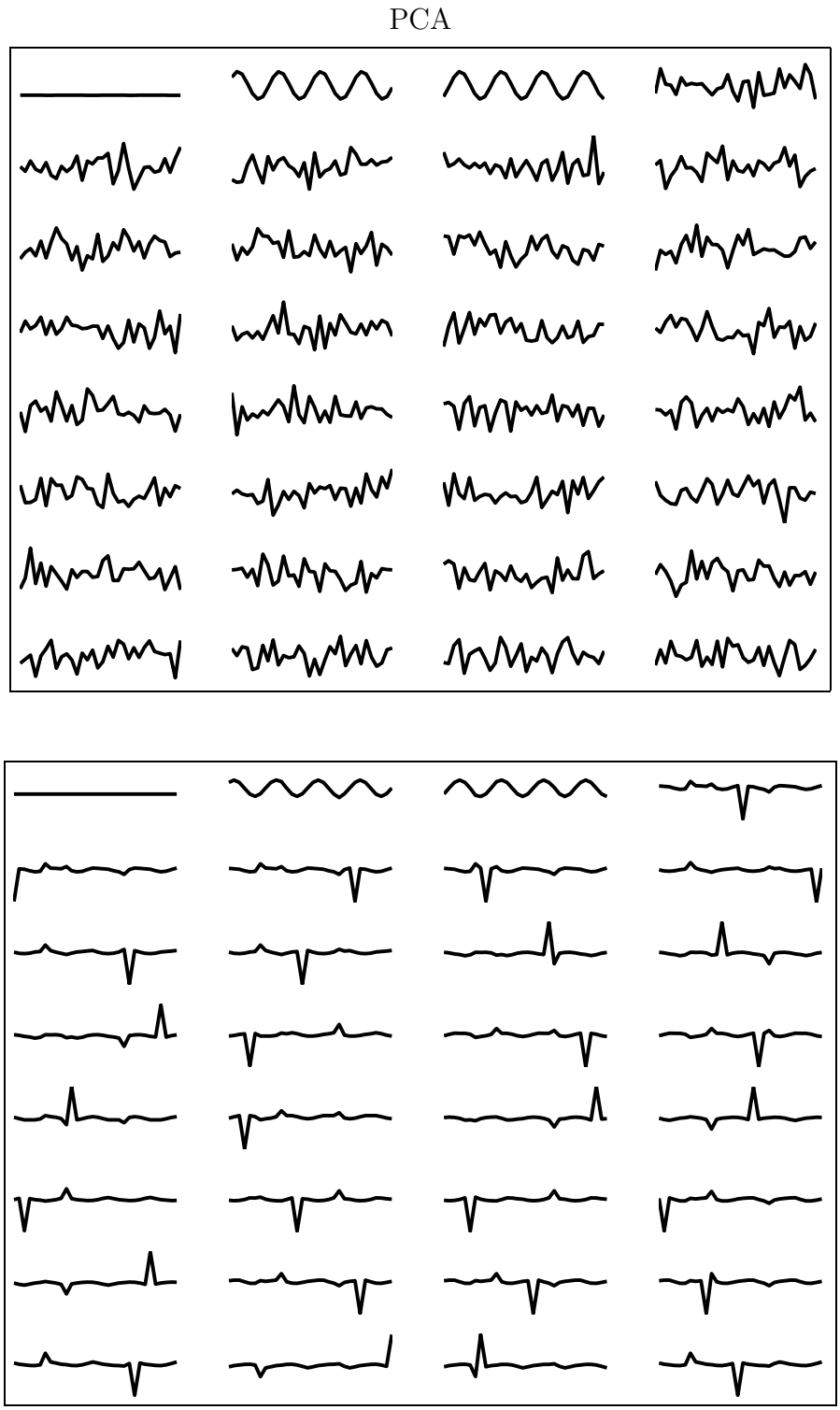

Figure 3.12: Representing noisy-sinusoid ensemble using PCA (Top) and S-PCA (Bottom). Each waveform is 32 pixels long. In each waveform the zero line is near the median value of the waveform.

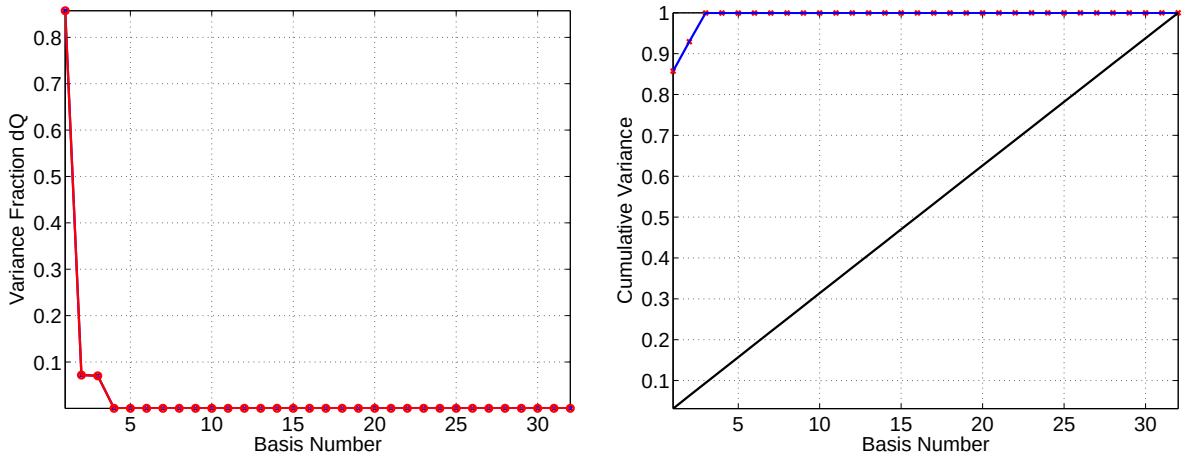

Figure 3.13: Representing noisy-sinusoid ensemble (contd). (LEFT) The variance spectra are identical for both PCA and S-PCA. (RIGHT) Fraction of the total variance captured by m-dim subspaces as m varies from 1 to 32: PCA (blue), S-PCA (red), Identity matrix (maximally sparse) (black).

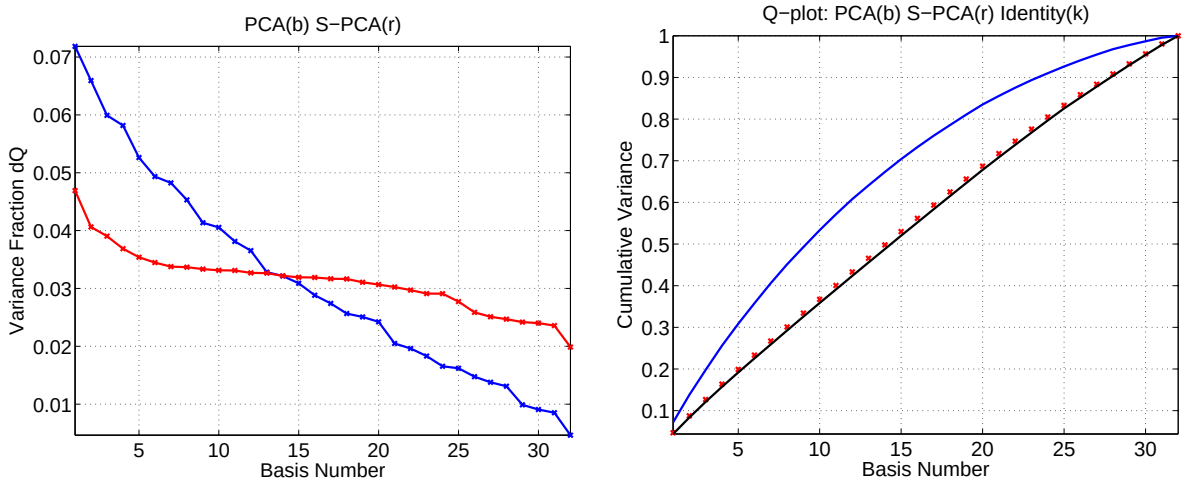

Figure 3.14: Representing white noise ensemble. (LEFT) Smoothly decaying variances of PCA (blue) reshaped by S-PCA to be roughly flat (red). (RIGHT) Fraction of the total variance captured by m-dim subspaces as m varies from 1 to 32: PCA (blue), S-PCA (red), Identity matrix (maximally sparse) (black).

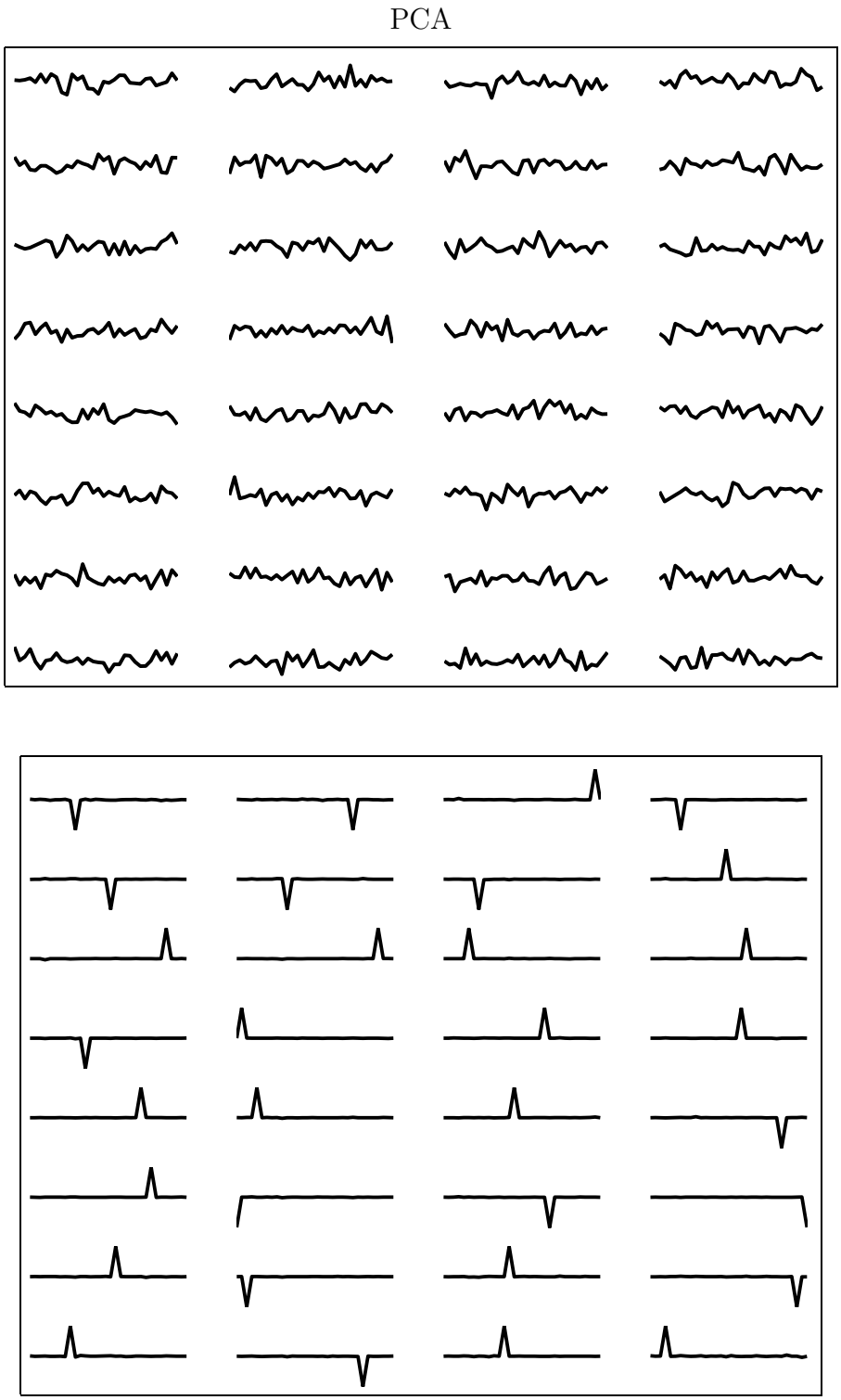

Figure 3.15: Representing white noise ensemble (contd). (Top) PCA and (Bottom) S-PCA. Each waveform is 32 pixels long. In each waveform the zero line is near the median value of the waveform.

3.5.1 Facelets

We represent face images that have been acquired under roughly similar viewing conditions with a varying degree of pose change [80]. For such an image collection we argue that the ensemble can be decomposed using a multi-scale, local basis. Each basis vector represents a spatially coherent image blob. The spatial coherence is caused by the consistency in the overall shape of the object and in the shape of its parts across the ensemble.

The PCA representation displayed in Fig. 2.8 is typical of the results obtained for object specific image ensembles. In particular, the first few principal vectors are relatively smooth and represent global correlations. As the index m increases (i.e. the variance of the component decreases), the basis vectors represent finer spatial structure but remain global in space. This is apparent in Fig. 2.8 from the relative sizes of the individual regions in which the basis functions are of one sign, which get increasingly smaller with increasing index. Unfortunately, it is impossible to tell from the PCA basis whether or not such fine scale structure is correlated across the entire image.

The first few basis vectors for the S-PCA results on the face ensemble represent correlations across the whole image (see Fig. 3.16). However, as the index increases, the basis vectors become quite sparse, indicating that the information at finer spatial scales is not strongly correlated across the entire image.

3.5.2 Handlets

In Fig. 3.17 we show results from applying S-PCA on the hand image ensemble. The first few basis vectors represent correlations across the whole image. In particular, for pixels in large coherent regions, such as the back of the hand, the extent of the correlation is large. However, as the basis index increases, the basis vectors become quite sparse by being dominant only in local regions. This indicates that the information at finer spatial

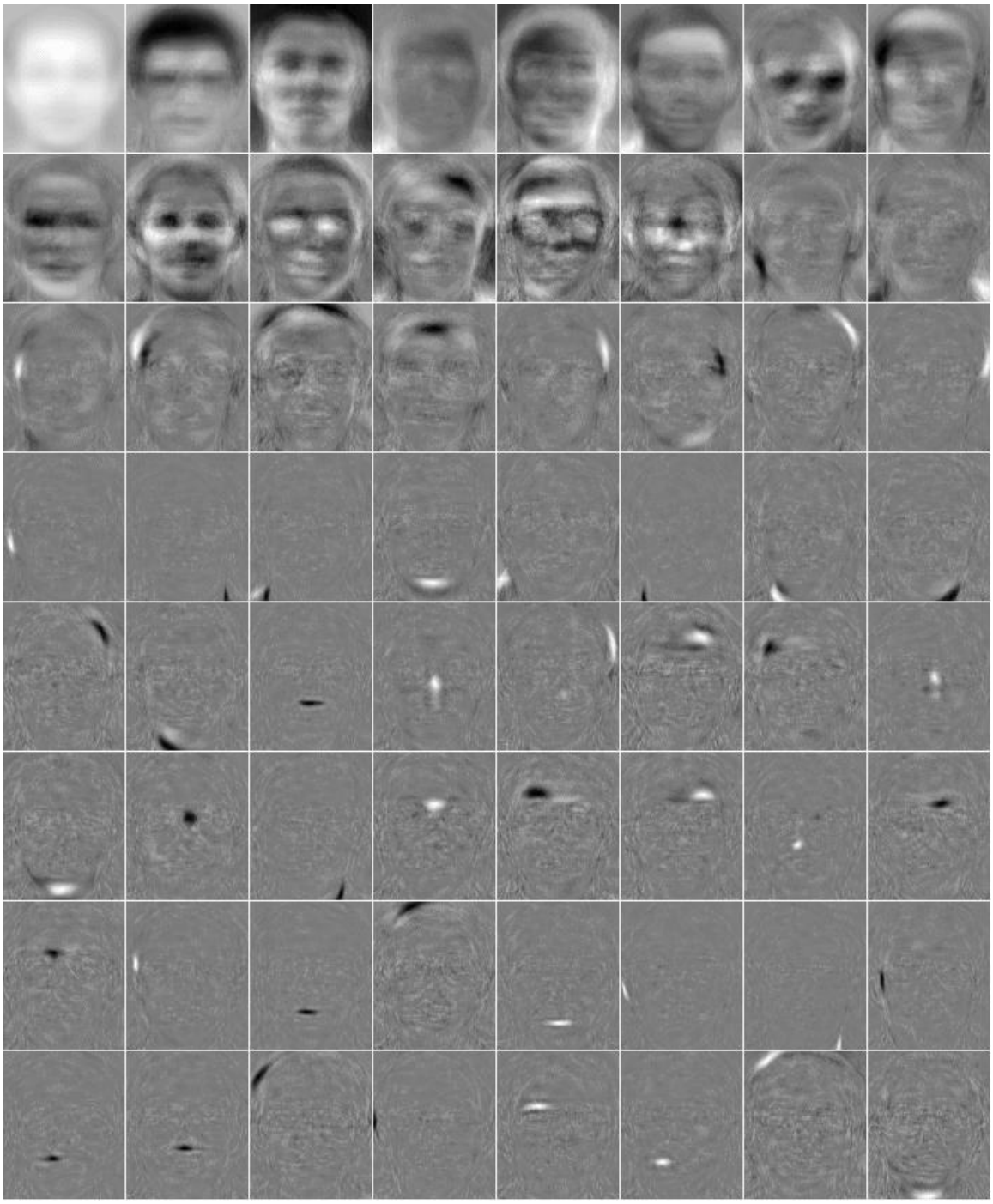

Figure 3.16: Sparse-PCA results on the face images. Each basis image is of size: 112×92 pixels. Subimages are rescaled to have zero value correspond to a gray level of 127. Only the first 64 basis vectors are displayed here. Unlike PCA, here the basis vectors representing fine-scale information are spatially localized. Compare this with the result from PCA shown in Fig. 2.8.

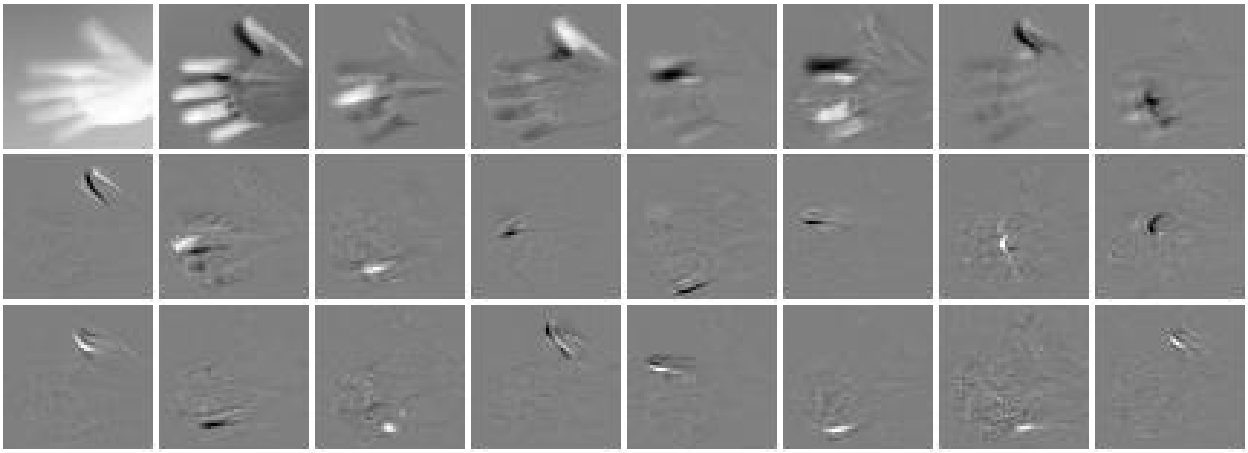

Figure 3.17: Sparse-PCA results on the hand images. Each basis image is of size: 50×52 pixels. Only the first 24 basis vectors are displayed here. The basis vectors representing fine-scale information are spatially localized. Compare this with the result from PCA shown in Fig. 2.7.

scales is not strongly correlated across the entire image, as was anticipated in §2.3. PCA clearly ignores this sparse form, coalescing local structure to form global basis vectors (Fig. 2.7).

3.5.3 Wavelets

The results of PCA and S-PCA on a set of 5000 image patches each of size 16×16 pixels drawn from natural images show the same general results (Fig. 3.18). We sampled the patches from the database of natural images used in [79], where the natural images were preprocessed to remove artifacts of rectangular sampling (corner frequencies in the Fourier spectrum). We see that the PCA results provide global basis vectors which represent variations on increasingly fine spatial scales as the basis index increases (see Fig. 3.18a). Again, the PCA analysis leaves open the question of whether or not this fine scale spatial structure is correlated across the image patch. However, S-PCA reveals that the fine grain structure is not significantly correlated over large spatial regions. Rather,

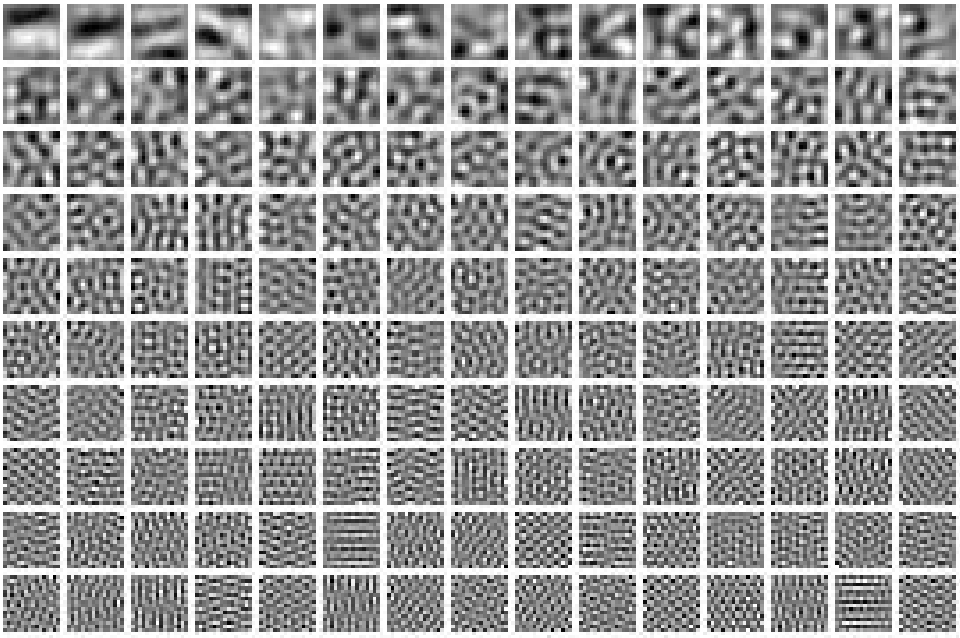

(a) PCA

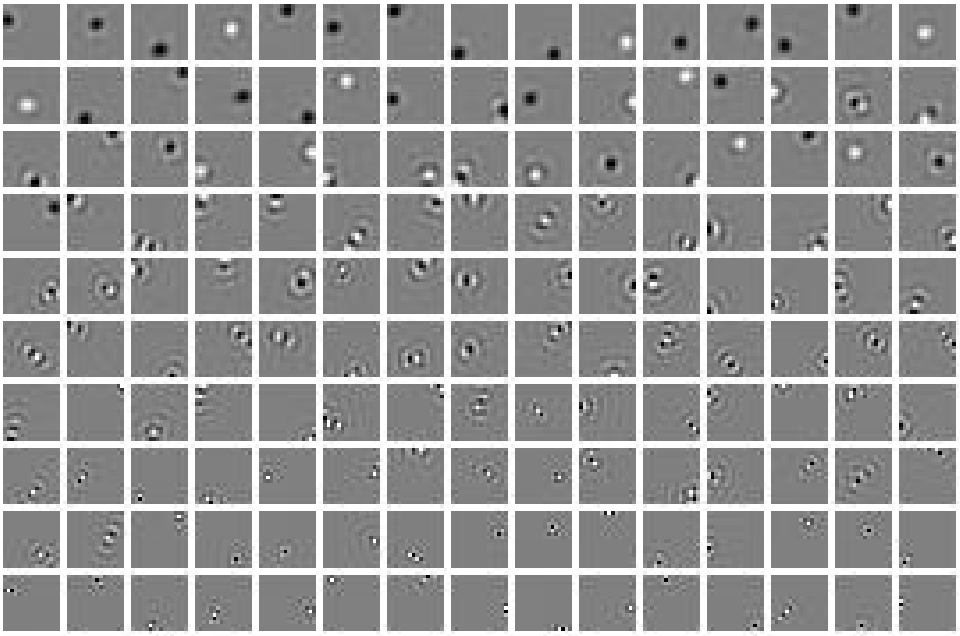

(b) S-PCA

Figure 3.18: *Wavelets* represent images from outdoor scenes. The ensemble is a collection of image patches, each of size 16×16, randomly sampled from natural scenes. (a) PCA basis vectors are global while (b) S-PCA learns a sparse, multi-scale representation.

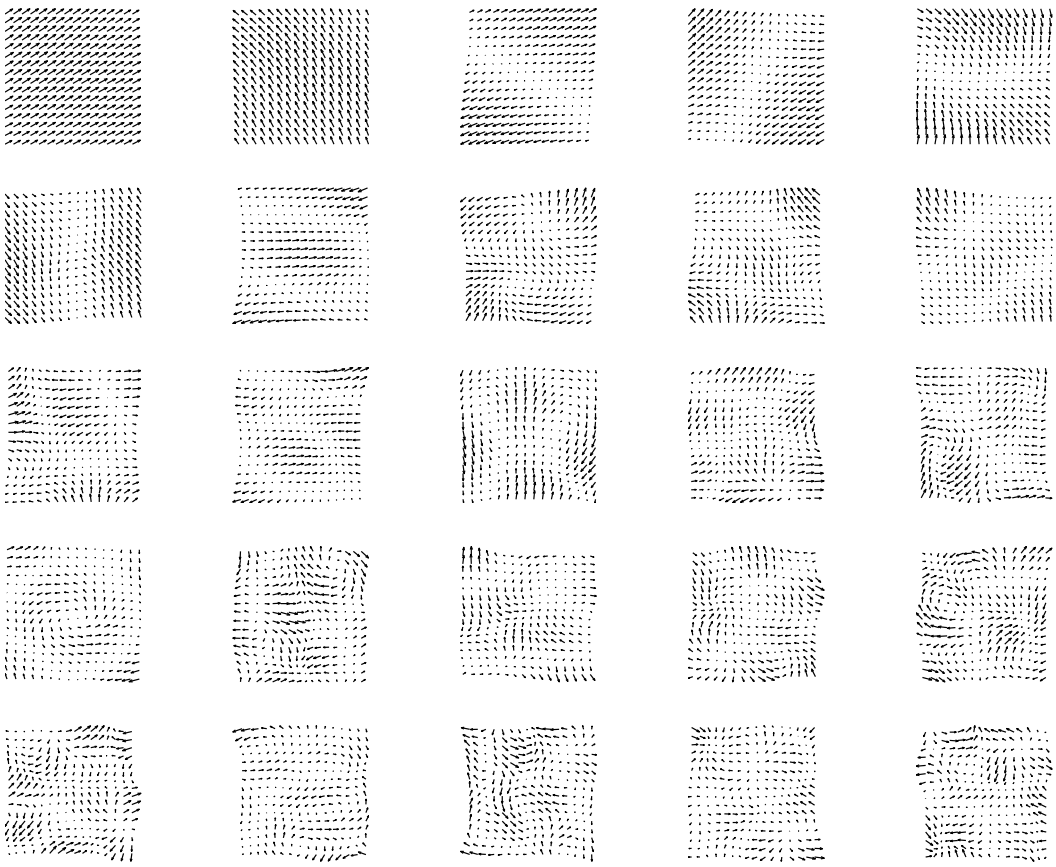

Figure 3.19: PCA results on the optical flow fields measured from an image sequence of a bush moving in the wind. The flow fields are sampled in 16×16 pixel blocks.

as the basis index increases, the S-PCA basis vectors exhibit increasingly local structure (Fig. 3.18b). Here the fine scale basis vectors appear to have either a center-surround structure or are similar to orientation tuned, scale-specific filter kernels.

3.5.4 Flowlets

The results from training PCA and S-PCA on a set of 5000 flow fields obtained from an outdoor motion sequence are presented in Figs. 3.19 and 3.20. The flow fields are sampled in 16×16 pixel blocks[1]. We see that the PCA results provide global vector

[1]We thank Michael Black for the motion sequence and the optical flow fields (`http://www.cs.brown.edu/~black/images.html`).

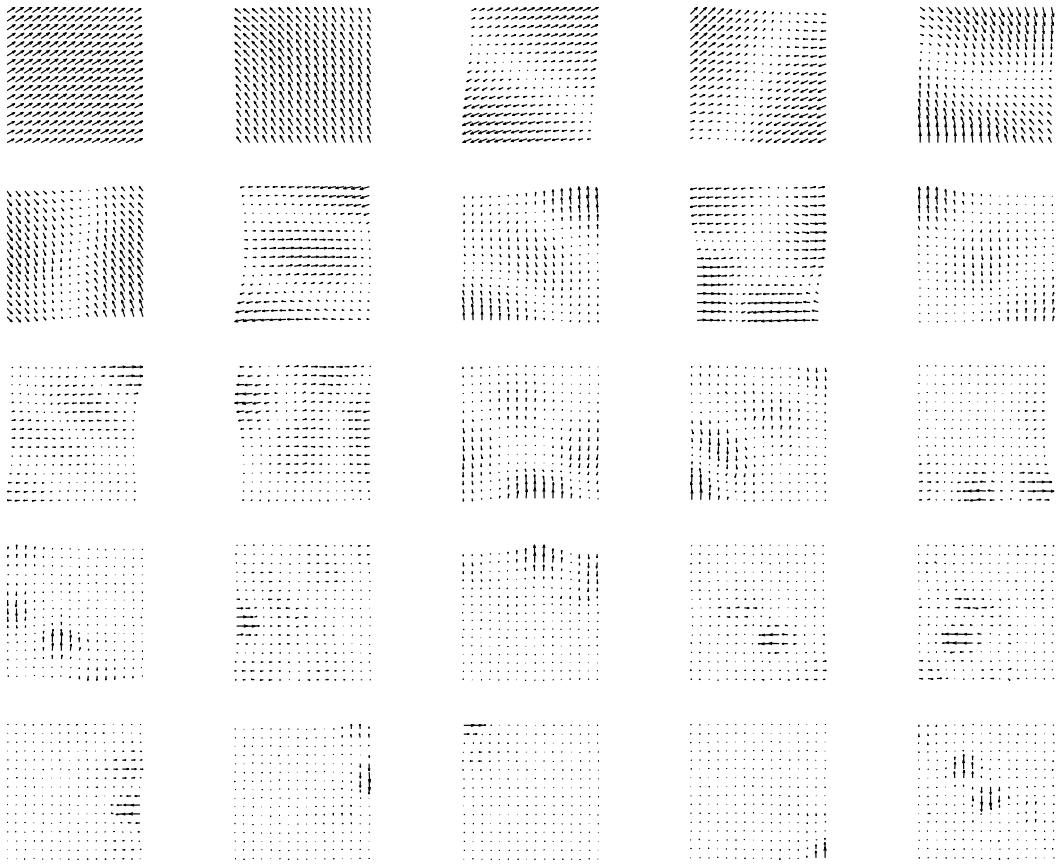

Figure 3.20: *Flowlets* represent optical flow fields measured from an image sequence of a bush moving in the wind. The flow fields are sampled in 16×16 pixel blocks.

fields which vary on increasingly fine scales as the basis index increases (Fig. 3.19). The PCA analysis leaves open the question of whether or not the fine scale structure of the flow is correlated across the image patch. However, S-PCA reveals multi-scale structure in a way similar to the ensembles considered so far.

3.6 Enforcing Sparsity by Coring

In deriving the S-PCA basis, we encourage sparsity, which means the basis elements may be close to zero but need not be exactly zero. If the basis elements were to be exactly zero, then we can avoid doing extra arithmetic operations. How might we achieve this? One idea is to apply a "sharper" prior while learning the S-PCA basis, that is to use a probability model with a large mass at the origin. In the extreme case, the prior could take the shape of a mixture model, e.g. a impulse function with unit area at the origin suitably mixed with a large-scale Gaussian. The problem with such a prior is that the impulse function makes the optimization difficult.

Adopting a mixture model form for the sparse prior is a good idea, and we discuss this later in the thesis. Here we overcome the problem of basis elements not being exactly zero by simply coring them, i.e., basis elements that are "small" are reset to zero. However, there is a problem: coring destroys the orthogonality property of the S-PCA basis. The non-orthogonality is annoying because the basis coefficients can no longer be obtained by simple projections and the energy along one basis direction depends on all the others. For an optimal coefficient set, we need to use the (pseudo–) inverse of the non-orthogonal basis. Moreover, this pseudo-inverse is unlikely to be a sparse matrix, i.e. the zeroes we introduce in coring are filled again with non-zero values in the corresponding elements of the pseudo-matrix. Obviously, we would like to avoid computing the inverse and we show how to do this next. For demonstration we pick the task of reconstructing an image.

3.6.1 Iterative Image Reconstruction

Consider the following linear model for an image $\vec{x}$

$$\vec{x} = B\vec{c},$$

where the coefficient vector $\vec{c}$ is obtained by projecting the image onto the orthonormal S-PCA basis B,

$$\vec{c} = B^T\vec{x}.$$

Let $\widetilde{B}$ represent the cored S-PCA basis,

$$\widetilde{B} = \lfloor B \rfloor, \tag{3.8}$$

where for a given threshold ϵ, the basis elements in $B = \{b_{i,j}\}$ are cored to $\widetilde{B} = \{\tilde{b}_{i,j}\}$ based on their sizes "relative" to the maximum absolute value in B:

$$\tilde{b}_{i,j} = \begin{cases} b_{i,j} & \text{if } \frac{|b_{i,j}|}{\max_{k,l}|b_{k,l}|} > \epsilon, \\ 0 & \text{otherwise.} \end{cases} \tag{3.9}$$

Once the bases are cored, there is no reason for $\widetilde{B}$ to be orthogonal. Hence, a simple projection of $\vec{x}$ onto the basis $\widetilde{B}$ would be insufficient to produce the exact coefficients $\vec{c}$ that can represent $\vec{x}$. The optimal coefficient vector using the cored basis,

$$\vec{c} = \arg\min_{\vec{c}} \left\| \vec{x} - \widetilde{B}\vec{c} \right\|_2 \tag{3.10}$$

requires a pseudo-inverse

$$\vec{c} = \left(\widetilde{B}^T\widetilde{B}\right)^{-1} \widetilde{B}^T\vec{x}. \tag{3.11}$$

Note the matrix-vector operations: $\widetilde{B}\vec{c}$ and $\widetilde{B}^T\vec{x}$, are sparse but the pseudo-inverse $\left(\widetilde{B}^T\widetilde{B}\right)^{-1}$ is unlikely to be sparse and hence we wish to avoid this computation. So consider the following iterative procedure to build the coefficients:

$$\begin{aligned} \vec{c}_0 &= \vec{0}, \\ \vec{c}_{n+1} &= \vec{c}_n + \widetilde{B}^T(\vec{x} - \widetilde{B}\vec{c}_n). \end{aligned} \tag{3.12}$$

The idea is to repeatedly project the residual vector $\vec{r}_n = \vec{x} - \widetilde{B}\vec{c}_n$ onto the cored basis and accumulate the coefficients. Notice that if this iteration converges then

$$\vec{c}_\infty = \vec{c}_\infty + \widetilde{B}^T(\vec{x} - \widetilde{B}\vec{c}_\infty), \tag{3.13}$$

implying

$$\widetilde{B}^T(\vec{x} - \widetilde{B}\vec{c}_\infty) = 0, \tag{3.14}$$

and therefore

$$\vec{c}_\infty = \left(\widetilde{B}^T\widetilde{B}\right)^{-1}\widetilde{B}^T\vec{x}. \tag{3.15}$$

as desired.

How do we find the rate of convergence of this expression? If the cored bases $\widetilde{B}$ are the same as the un-cored basis B, then the above iteration converges in a single step. Otherwise, consider the following analysis:

$$\begin{aligned}
\vec{c}_{n+1} &= \vec{c}_n + \widetilde{B}^T(\vec{x} - \widetilde{B}\vec{c}_n), \\
&= \vec{c}_n - \widetilde{B}^T\widetilde{B}\vec{c}_n + \widetilde{B}^T\vec{x}, \\
&= \left(\mathcal{I} - \widetilde{B}^T\widetilde{B}\right)\vec{c}_n + \widetilde{B}^T\vec{x},
\end{aligned} \tag{3.16}$$

where $\mathcal{I}$ is the identity matrix of an appropriate dimension. Define the change in the coefficient vector between successive iterations as

$$\vec{\mathfrak{d}}_{n+1} = \vec{c}_{n+1} - \vec{c}_n, \tag{3.17}$$

which, from Eq. 3.16, can be expressed recursively as

$$\vec{\mathfrak{d}}_{n+1} = \left(\mathcal{I} - \widetilde{B}^T\widetilde{B}\right)\vec{\mathfrak{d}}_n \tag{3.18}$$

The rate of convergence is therefore determined by the spectral radius ρ, which is the maximum absolute eigenvalue of the matrix $(\mathcal{I} - \widetilde{B}^T\widetilde{B})$. In particular, the magnitude of the update vector $\vec{\mathfrak{d}}_n$ decays as $|\rho|^n$.

There are two user-defined thresholds implicit in the iterative process. The first one is the constant ϵ used in Eq. 3.9 to enforce sparsity on the S-PCA basis vectors. We chose a value of $\epsilon = 0.05$, which means all the S-PCA basis elements that are below 5% of the maximum absolute value in the basis matrix get suppressed to zero. We need an additional constant to help terminate the iterative process. For this we compare in each iteration the magnitude of the error vector $\vec{\delta c}_n$ with the norm of the coefficient

$$\|\vec{\mathfrak{d}}_n\|_1 < \nu \|\vec{c}_n\|_1.$$

We set the tolerance parameter ν to a value 10^{-2}. We apply this analysis for reconstructing images in a database of eye images, which we discuss next.

3.6.2 EYELETS

We train S-PCA on a database of eye images. The training images have been cropped from the FERET database [87]. The original face images were scaled and rotated so that, in the warped image, the left and right eyes have a horizontal separation of 40 pixels. These warped images were then cropped to 20×25 regions around each eye, resulting in a database of 2392 eye images (Fig. 4.1). Furthermore, these images were contrast-normalized to minimize the effects of shading and specularity. We defer the actual details of this normalization to the next chapter.

The PCA and the S-PCA basis, called EYELETS, are shown in Figs. 3.21 and 3.22, respectively. We use both PCA and S-PCA representations to do the reconstruction. For a given subspace dimensionality, on the training set PCA has to do better than S-PCA in minimizing the reconstruction error. However, with sparsity enforced via coring and the iterative procedure just outlined for computing a coefficient vector, the S-PCA basis vectors must be computationally more efficient for reconstruction.

In Fig. 3.22 we see that as the basis index increases the S-PCA bases appear increasingly sparse. In fact, coring basis elements which are less than 5% of the maximum

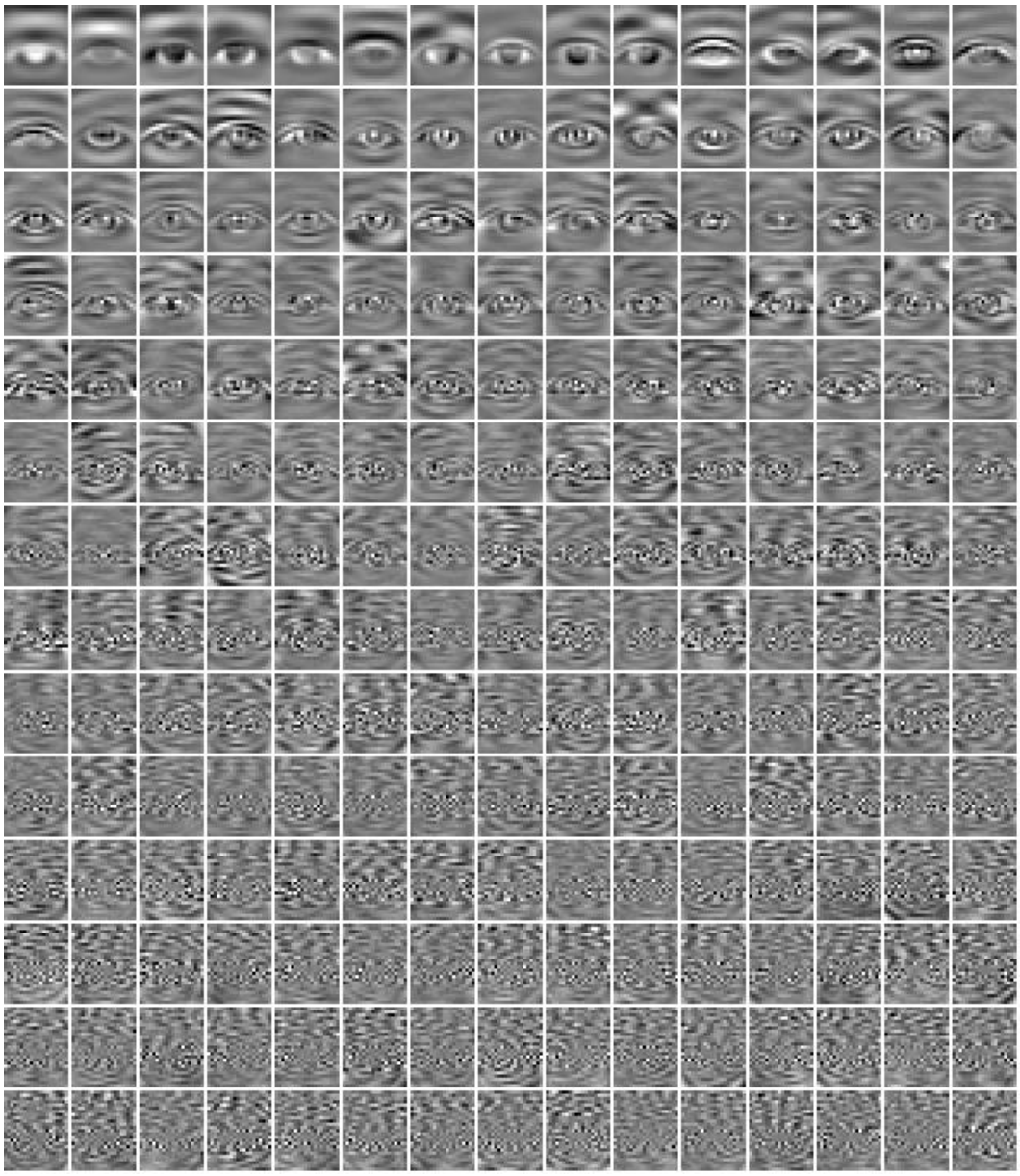

Figure 3.21: The leading 200 PCA bases for eye images, displayed in the decreasing order of the input variance they capture, beginning at the top left corner and going horizontally across the page. Observe the fine-scale information, captured by the high-order eigenvectors, is spread across the entire image.

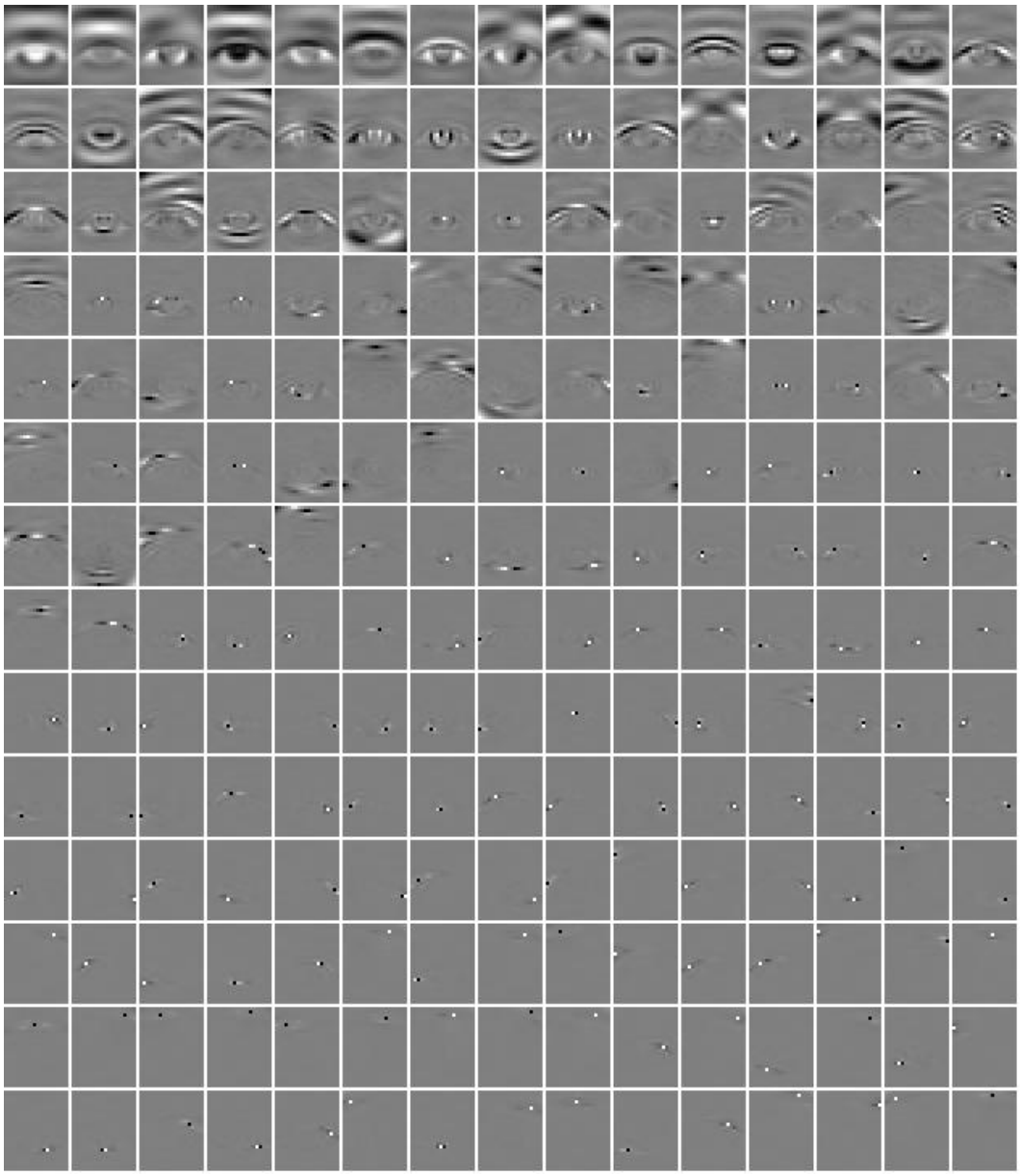

Figure 3.22: The leading 200 S-PCA bases for eye images. Each basis image is 25×20 (pixels) in size. Subimages are rescaled to have zero value correspond to a gray level of 127. Unlike the PCA basis (Fig. 3.21), here the basis vectors capture fine-scale information in spatially localized regions.

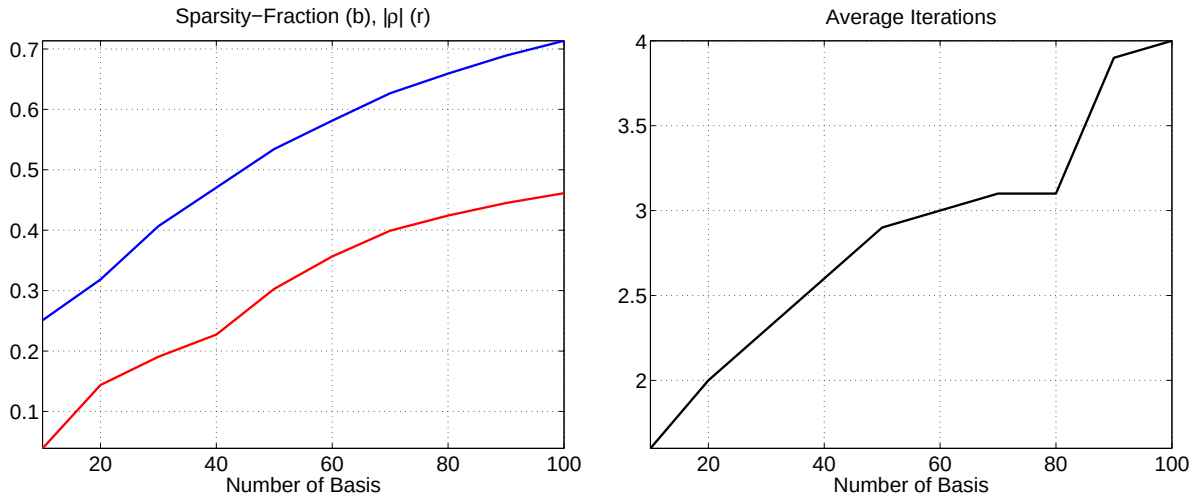

Figure 3.23: (LEFT) Sparsity Fraction (blue) and the magnitude of the leading eigenvalue λ (red). (RIGHT) Average Number of Iterations taken to compute the coefficient vector.

absolute value, causes the S-PCA matrix, constructed from the leading 100 basis vectors, to be over 70% sparse. In Fig. 3.23 we measure this sparsity fraction, which is the ratio of the number of zeros in the matrix to the total size of the matrix, as a function of the subspace dimensionality.

Coring however causes the S-PCA basis to be non-orthogonal. A measure of this non-orthogonality is given by the magnitude of the leading eigenvalue $|\rho|$ for the matrix: $\left(\mathcal{I} - \widetilde{B}^T \widetilde{B}\right)$. If the cored basis are orthogonal, then we expect ρ to be zero. From Fig. 3.23 we observe that there is a steady increase in ρ as a function of the subspace dimensionality.

As we noted earlier, the rate of convergence of the iterative process, for computing coefficients of the cored basis, is proportional to $|\rho|^n$ – the higher the magnitude of ρ, the slower is the decay rate. From Fig. 3.23, we can see that the average number of iterations it takes to converge is small even for a 100 dimensional subspace.

We also measure the relative error between the norm of the reconstruction error and the norm of the input image, as a function of the subspace dimensionality. From Fig. 3.24 we can see that PCA and S-PCA offer similar relative error values when the

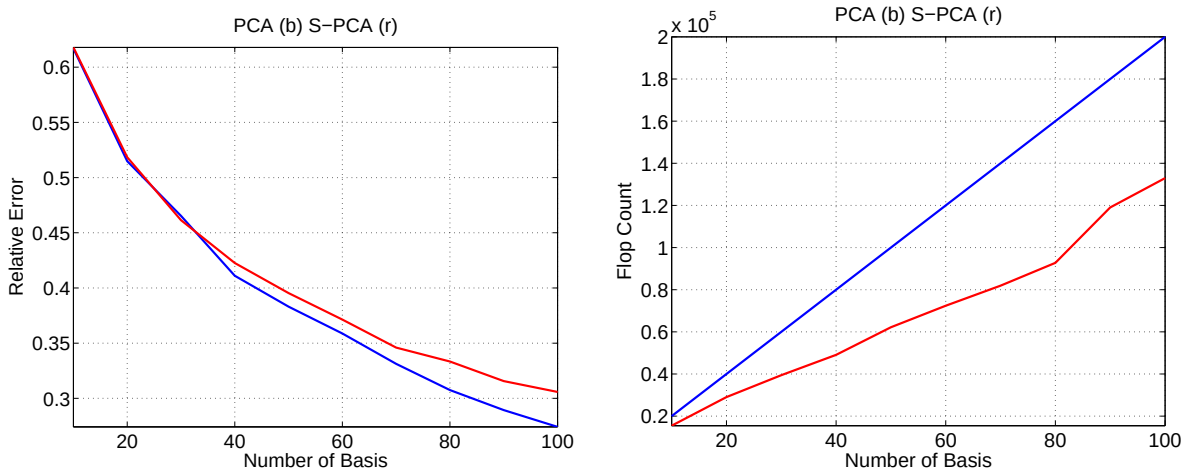

Figure 3.24: (LEFT) Reconstruction Error from PCA (blue) S-PCA (red). (RIGHT) Average Flop Count with PCA (blue) and S-PCA (red).

subspace dimensionality is small. However, with increasing index PCA gives a much better performance. Also in Fig. 3.24 we plot the average number of flops used for reconstruction from the cored S-PCA basis and compare it with the PCA basis. The flop count by S-PCA basis for a 50-dimensional subspace indicates it is about 40% faster than the PCA basis. To achieve even better performance, we would need to decrease the spectral radius of $\left(\mathcal{I} - \widetilde{B}^T \widetilde{B}\right)$, perhaps by encouraging the S-PCA coefficients to be closer to zero while still maintaining orthogonality so that coring is less severe. We return to this issue later in the thesis.

Finally, we show how distorted the reconstructions can be from the cored basis. We discuss a perceptual distortion measure in the following chapter, but here we perform a simple visual comparison of the reconstruction results from PCA, cored S-PCA and the pseudo-inverse computation (Eq. 3.11). Given the cored basis, the result from pseudo-inverse computation is the optimal. In Fig. 3.25 we show reconstruction results for a sample of random images in the eye database. The top row contains the input images and within each sub-figure, the top row is the result from S-PCA basis, the middle row from the pseudo-inverse computation and the last row is the PCA result. The results

validate the iterative reconstruction approach we have taken with the cored S-PCA basis. However, as we mentioned earlier, we can improve the flop count with S-PCA basis by driving hard on sparsity, while learning the basis directions.

3.7 Related Work

The relationship to sparse coding and ICA has already been discussed in the previous chapter. With sparse coding (or ICA) the optimization process can be expensive, so it is often the case that basis functions are learned on sub-images (say 16×16 image patches) extracted from a larger image. As a consequence, spatial structure larger than an image block may never be captured. In this context, it is worth mentioning that the image size is much less of a restriction for S-PCA. For example, the images in the face database have a size of 112×92 pixels and the database has 400 images. S-PCA has been successful in highlighting the multi-scale structure in this ensemble.

Varimax is one of the earliest known references for rotating principal components so that the basis vectors are more interpretive [50]. The rotation is performed to increase the variance of the elements that describe the basis vectors. In our framework this increase in variance will also increase the cost term C_2. As we have shown, for basis directions to provide a meaningful representation for naturally-occurring ensembles, we found it useful to draw the basis elements from a low-entropy distribution.

The idea of applying a sparse constraint on the weights of a neural net appears in [78, 122]. The networks are non-linear and the learning has not shown the ability to extract multi-scale structure. Recently, such sparsity constraints were extended to both the basis matrix and the coefficients as in [48] but this algorithm is likely to have problems with the size of the input image. Our learning algorithm has a flavor similar to the one used in [20] where the tensor properties of the cumulants for the coefficient densities are exploited using a rotation based Jacobi algorithm. For the application of

(a) Eye Images

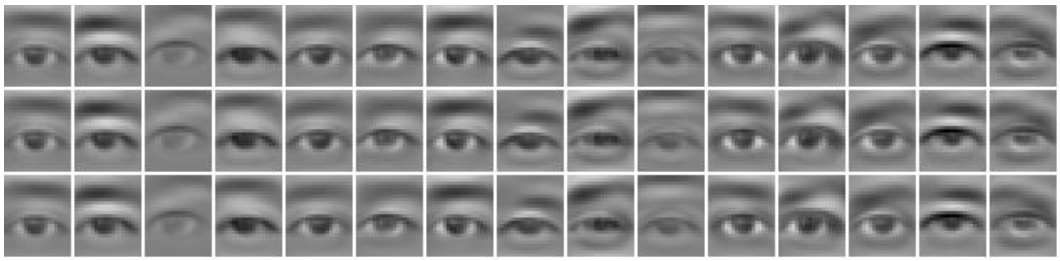

(b) Reconstruction with 10-dimensional subspace.

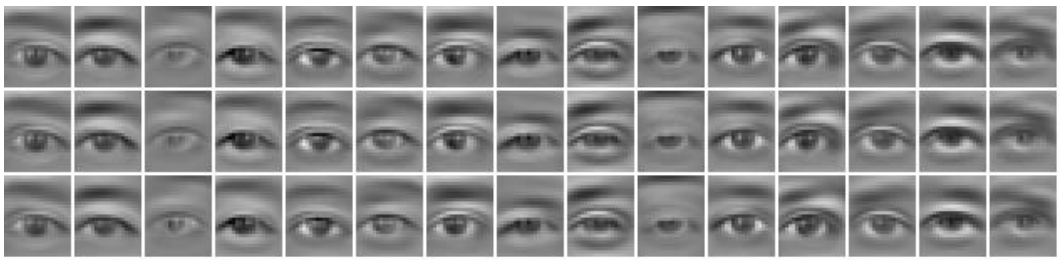

(c) Reconstruction with 20-dimensional subspace.

(d) Reconstruction with 50-dimensional subspace.

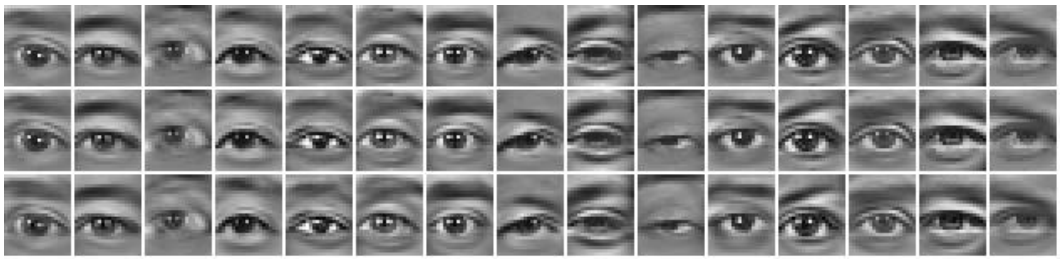

(e) Reconstruction with 100-dimensional subspace.

Figure 3.25: Reconstruction of input eye images in (a) as a function of the subspace dimensionality. With in each subfigure the results are: (Top) iterative reconstruction from cored S-PCA, (Middle) pseudo-inverse with cored S-PCA and (Bottom) PCA.

sparsity in regression and kernel analysis see [76, 106, 108].

The notion of sparsity also appears in the basis selection literature. The idea is to have a dictionary of basis functions, possibly multi-scale, and pick a small number of them to represent the input image [22]. The basis functions are either predefined, as in wavelets, or specific to a class, as in correlation-based kernels [81, 85]. Unfortunately, determining coefficients for each image is formulated as a quadratic programming problem and this can be computationally very expensive. In [44, 59, 91] a constraint of positiveness on the basis elements, called non-negative matrix factorization (NMF), appears to lead to facial features at a single scale. Finally, a Bayesian treatment of Sparse-PCA is given in [116], which postdates our original publication of S-PCA [24].

Chapter 4

Contrast-Invariant Appearance-Based Detection

4.1 Introduction

In this chapter we propose two different models for contrast-invariant appearance detection. The contrast signal, which is the intensity variation around a mean brightness value, can be measured in two ways, either by an object-specific, global model or a generic, local method. Once the dataset is adjusted for contrast, a representation is built using the principal subspace (*within-space*) and its orthogonal complement (*out-of-subspace*). We experiment with principal subspaces obtained by PCA and S-PCA basis vectors. An important feature of our system is a *perceptual distortion measure* that we designed to compare the appearance of an object to its reconstruction from the principal subspace. By distortion we mean the reconstruction error caused by not including the out-of-subspace signal. We show how to use S-PCA basis trained on generic background patches to decide if two images are perceptually similar.

Our work builds upon four key observations on subspace-based representations. First, subspace methods involve least squares approximations which are notoriously sensitive

to large outliers. Hence, it is important to account for outliers in training, and testing, subspace methods [17, 30]. A related issue is one of variation in the image contrast. In general, images with higher contrasts have larger variance. If some images have variance much larger than others then these images can potentially skew the estimation of the object-specific subspace. Often a contrast normalization step is performed, either by histogram equalization or by normalizing the variance (or the power) of an image so that it is of unit length. We offer two alternative normalization strategies which we feel are more appropriate for object-specific ensembles.

Second, S-PCA amounts to a rotation of input coordinate axes and, as such, it does not define a probability density model for the input data. However, subspaces can also be derived from the perspective of density estimation [75, 92, 109]. The advantage in estimating the input density is that it allows for the design of probabilistic methods to detect, recognize and/or classify test images as appearances of known objects. In particular, one strategy for object representation is to divide the signal space into a principal subspace and its orthogonal complement and then build probability models separately for the two subspaces. Then the detection strategy is to apply a threshold on the likelihood assigned by the combined density model to a test image [75].

The third key observation, as noted in [25, 74], is that the variance estimate *per–pixel* given by the subspace density models for the residual signal in the out–of–subspace is overly conservative [75, 109]. We defer the actual details of variance estimation used in our appearance-based detector to a later section.

Finally, the detection problem can be posed as one of assessing image similarity, where the issue is to develop a measure that captures the notion that two images are *perceptually* similar. It is well known that standard error norms, such as the mean-squared-error (MSE), are unsuitable for measuring perceptual distortion. Recent successes in formulating perceptual distortion norms (e.g., [105]) have come from analyzing the psychophysics of spatial pattern detection, particularly contrast and orientation masking, and under-

standing the functional properties of neurons in the primary visual cortex. A typical perceptual distortion model consists of a linear transformation of images by a "hand-crafted" wavelet representation that is tuned to different spatial orientations and scales, followed by a divisive normalization mechanism. The normalization scheme involves pooling information in adjacent wavelet channels (that is in neighbouring spatial locations, orientations and scales, eg. [18]). Normalization provides a context for local significance, in that a high sensor channel (wavelet) response is down-weighted if the adjacent channels are equally active but upgraded otherwise. The full set of normalized sensors tuned for different spatial positions, spatial frequencies, orientations and contrast discrimination bands provide a basis for assessing the perceptual similarity between two images. Our work generalizes this normalization scheme to object-specific multi-scale representations derived from S-PCA.

While we concentrate on sub-space methods, much work has also been done in building feature-based object detectors [98, 104], in particular systems where the features are simple to compute and hence the objects are fast to detect [3, 39, 82, 117].

4.2 Datasets

We investigate two different image datasets: eyes/non-eyes [25] and faces/non-faces [6]. The eye images are regions cropped from the FERET face database [87]. The face images were first scaled and rotated such that, in the warped image, the centers of left and right eyes have a horizontal separation of 40 pixels. From these warped images, we crop image regions around the eyes, each of size 20×25 pixels, to generate a database of 2392 eye patches (Fig. 4.1).

For non-eyes, we construct a generic background patch ensemble by running an interest point detector [97] on several different natural images and collecting image patches with detector responses above a certain threshold (Fig. 4.2). The interest point detector

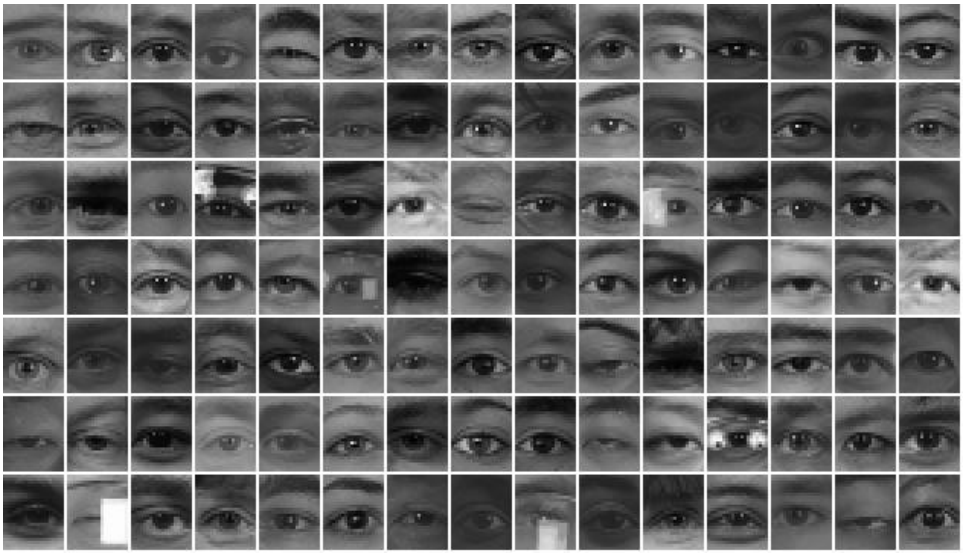

Figure 4.1: Eye images cropped from the FERET database [87]. Each image is of size 20×25 pixels.

can be seen as a first step in the detection hierarchy in that it eliminates blank, textureless regions from further consideration. To populate the 500 dimensional input space with a sufficiently large number of positive and negative examples, we symmetrize the ensemble. In particular, the eye images were flipped to generate mirror-symmetric pairs for a total of (2×2392) images. We take more liberties with the generic background patches, reflecting them about the x-/y-axis and around the origin, to make the original database of 3839 images four times as large. The datasets were randomly split in half to train and test the detection algorithm proposed here. We defer the details of the MIT face database [6] to the results section of this chapter.

4.3 Detection Model – I

The approach we take here is to use a global, object-specific model to normalize the ensemble for contrast variation and then build a low-dimensional description for the data. We then measure two statistics that we show are relevant for appearance detection.

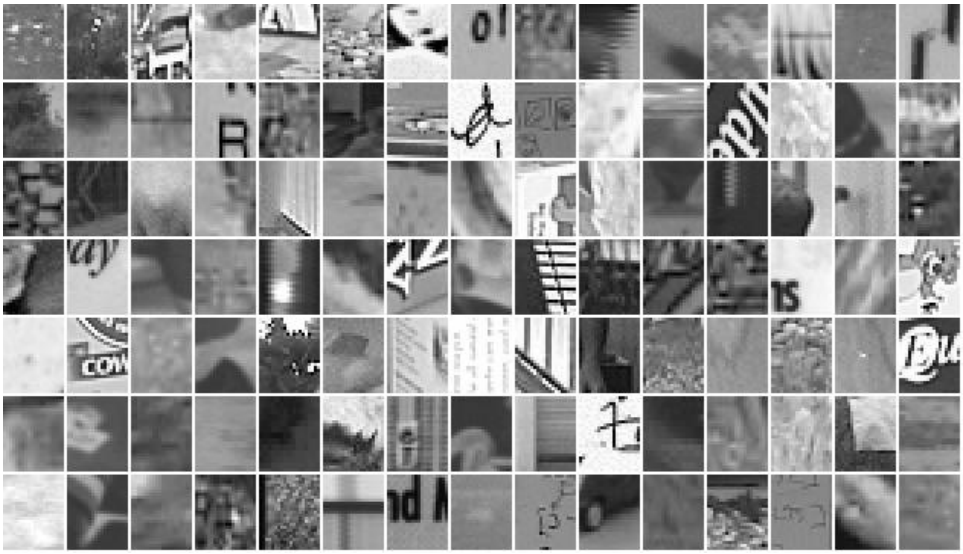

Figure 4.2: Generic background patches detected by an interest point detector [97]. The image size is 20×25.

4.3.1 Contrast Model for an Object-Specific Ensemble

Contrast is defined as the variation in image intensities around a mean brightness value. We can extend this contrast model to be global and explicit for an object-specific ensemble by using two basis vectors, namely a constant "DC" basis vector and a vector in the direction of the mean of the training set after removing the contribution from the DC basis. We define the training set as $\{\vec{t}_k\}_{k=1}^{K}$ where K is the total number of training images and $\vec{t}_k$ is the k^{th} training image stored in a column format. Each element of the DC vector $\vec{\xi}$ is given by

$$\xi_i = 1/\sqrt{N}, \tag{4.1}$$

where N is the total number of pixels in the image, and $\vec{\xi}$ is of unit length. The mean image $\vec{\mu}$ is derived from the training set after removing the DC contribution, that is

$$\vec{\mu} \propto \frac{1}{K} \sum_{k=1}^{K} \left[\vec{t}_k - \vec{\xi} \left(\vec{\xi}^T \vec{t}_k \right) \right], \tag{4.2}$$

and $\vec{\mu}$ is normalized to be of unit length. We define the components of $\vec{t}_k$ in the directions of the DC and the mean vector as

$$d_k = \vec{\xi}^T \vec{t}_k \tag{4.3}$$

and

$$m_k = \vec{\mu}^T \vec{t}_k \tag{4.4}$$

respectively.

The goal here is to generate a subspace representation for the spatial structure of the eye images that is insensitive to contrast changes. We wish to capture the spatial structure by a basis matrix B given by

$$B = \left[\vec{b}_1 \quad \vec{b}_2 \quad \cdots \quad \vec{b}_N \right]. \tag{4.5}$$

It is possible that the spatial structure of eye images, and thus the basis matrix B, changes as the mean component m_k increases. Alternatively, these basis images may stay roughly the same and only the variation of their coefficients increases with the mean component m_k. The coefficient $c_{k,j}$ in the direction of j^{th} basis vector for the k^{th} image is given by,

$$c_{k,j} = \vec{b}_j^T \vec{t}_k. \tag{4.6}$$

Indeed, if the variation of the mean component is primarily due to lighting and imaging effects, then we might assume that the underlying signal, i.e. the spatial structure of eye images, is invariant to contrast. In this case we would expect the basis images $\vec{b}_j$ to be independent of m_k and only the variance of coefficients $c_{k,j}$ to scale as a function of m_k.

We test this hypothesis by analyzing the relationship between the mean component m_k and the contrast variance l_k, given by

$$l_k = \frac{1}{N} \left\| \vec{t}_k - d_k \vec{\xi} - m_k \vec{\mu} \right\|_2^2, \tag{4.7}$$

where $\|\cdot\|_2^2$ is the expression for the square of the two-norm and l_k determines the variance-per-pixel that remains unaccounted for, after using the DC and the mean vectors to describe the ensemble. In Fig. 4.3(LEFT) we plot the contrast variation $\sqrt{l_k}$ as a function

of the mean coefficient m_k for each eye image. Notice that there are a large range of variances in the training images, with those images with larger values of the mean coefficient having significantly larger variances. As a rough approximation this relationship can be modeled by a straight line fit to the data, shown by the black line going through the origin in Fig. 4.3(LEFT). Note, the straight line fit is biased by the constraint that it passes through the origin (denoting perfect contrast invariance). From Fig. 4.3(LEFT) there appears to be a trend away from the line for smaller values of the mean coefficient. We suspect this is due to the use of a single mean image, which may not model the lower contrast images particularly well.

To balance the variances across different image contrasts, we rescale the training images to get

$$\vec{q}_k = \frac{\left[\vec{t}_k - d_k\vec{\xi} - m_k\vec{\mu}\right]}{s(m_k)}, \tag{4.8}$$

where $s(m_k)$ is a scaling factor for training image $\vec{t}_k$ with mean coefficient m_k. It is convenient to assume a minimum value for the left-over variance, say due to independent pixel noise, and use this in the estimate for scaling:

$$s(m_k) = \sqrt{\sigma_{\min}^2 + f(m_k)}. \tag{4.9}$$

The red curve in Fig. 4.3(LEFT) is a plot of $s(m_k)$ with $f(m_k) = p \times m_k^2$, where p is the slope of the straight line fit (the black line in Fig. 4.3(LEFT)), and $\sigma_{\min} = 8$. After normalization, all the scaled images falling on the red curve shown in Fig. 4.3(RIGHT) will have a left-over-variance value of one. We discuss next how to use the rescaled images for training a principal subspace.

4.3.2 Principal Subspace and its Complement

Once the images are rescaled into $\vec{q}_k$ for $k = 1, \cdots, K$, we first trim the database by removing extreme images that either have a low or negative mean image coefficient (≤ 20) and/or very large left-over variances per pixel (> 25). Most of these extreme images have

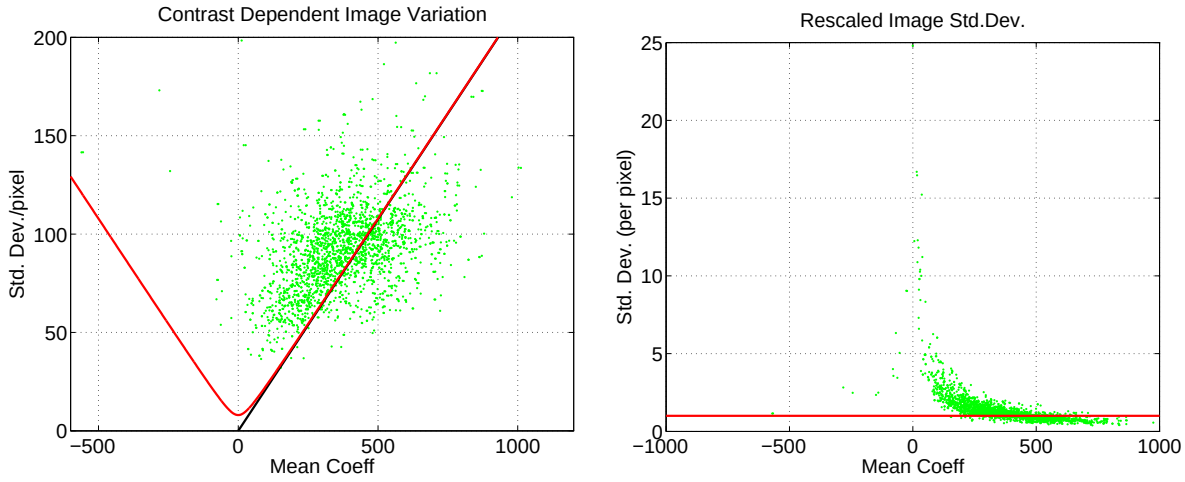

Figure 4.3: Contrast dependency of the Eye Dataset.

identifiable problems, such as the eye being closed, not centered, having a different scale, or having reflections from glasses. For the database we consider here they constitute only a small fraction of the input data: 46 out of 2392 eye images in the training set. We then use singular value decomposition (SVD) to perform principal component analysis. The PCA bases are shown in Fig. 4.4. The PCA basis in turn are used as a starting point for training the S-PCA representation. The S-PCA basis is trained for a complete representation of the input space, that is, the basis matrix is square. The resulting S-PCA basis are shown in Fig. 4.5.

Let $\vec{b}_j$ denote the basis images obtained either by PCA or S-PCA and σ_j^2 the variance obtained by projecting the data onto the basis direction $\vec{b}_j$. Suppose we approximate the normalized images $\vec{q}_k$ with just the M leading basis images. We can compute the residual signal $\vec{e}_k$ in the complement space as

$$\vec{e}_k = \vec{q}_k - \sum_{j=1}^{M} c_{k,j}\vec{b}_j, \tag{4.10}$$

where the expansion coefficient is given by

$$c_{k,j} = \vec{b}_j^T \vec{q}_k, \tag{4.11}$$

and M is taken to be much less than the total number of training images K and the total

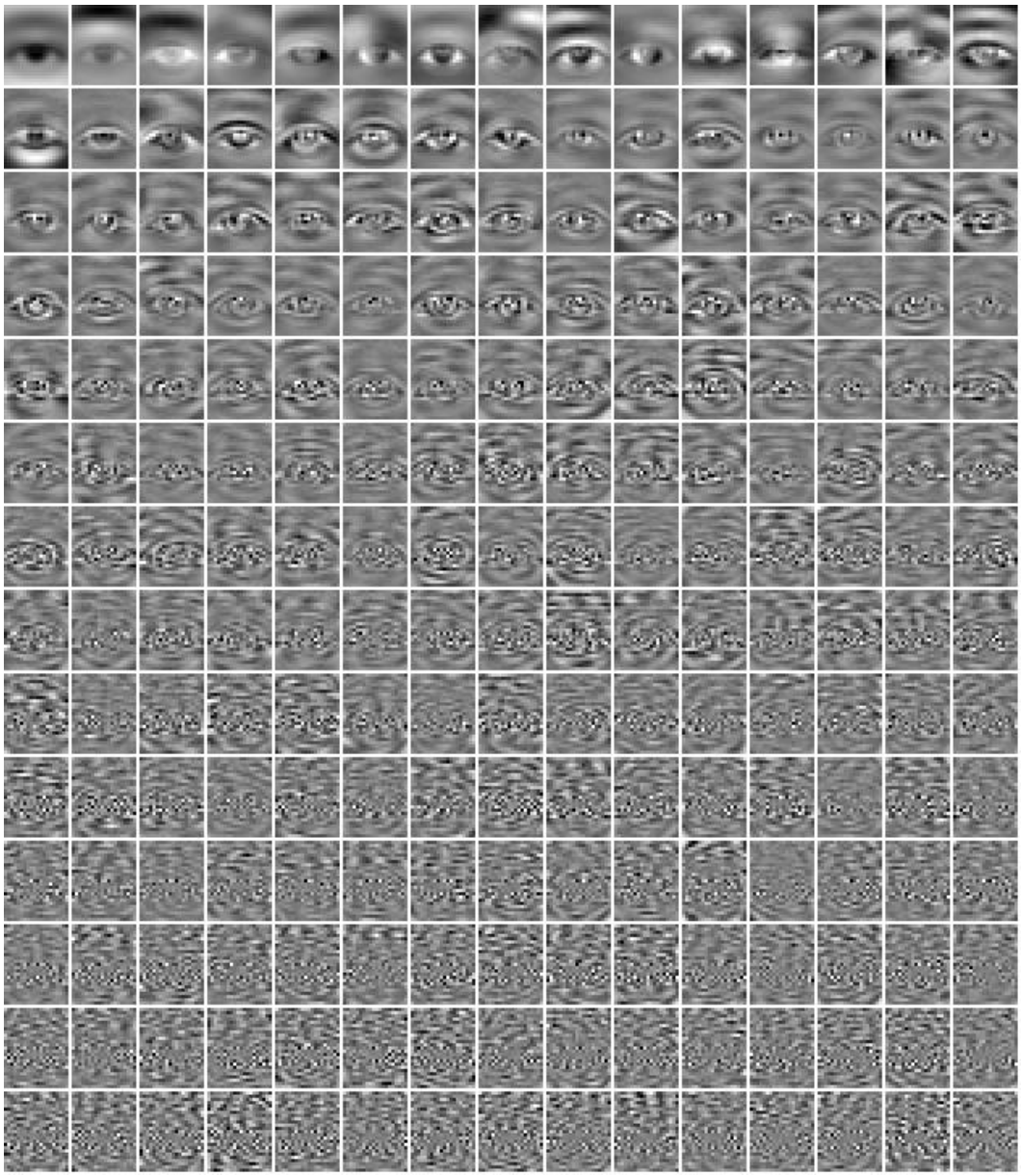

Figure 4.4: PCA basis for the eye space, arranged from left to right in decreasing order of the input variance captured. The first sub-image on the left is the mean image.

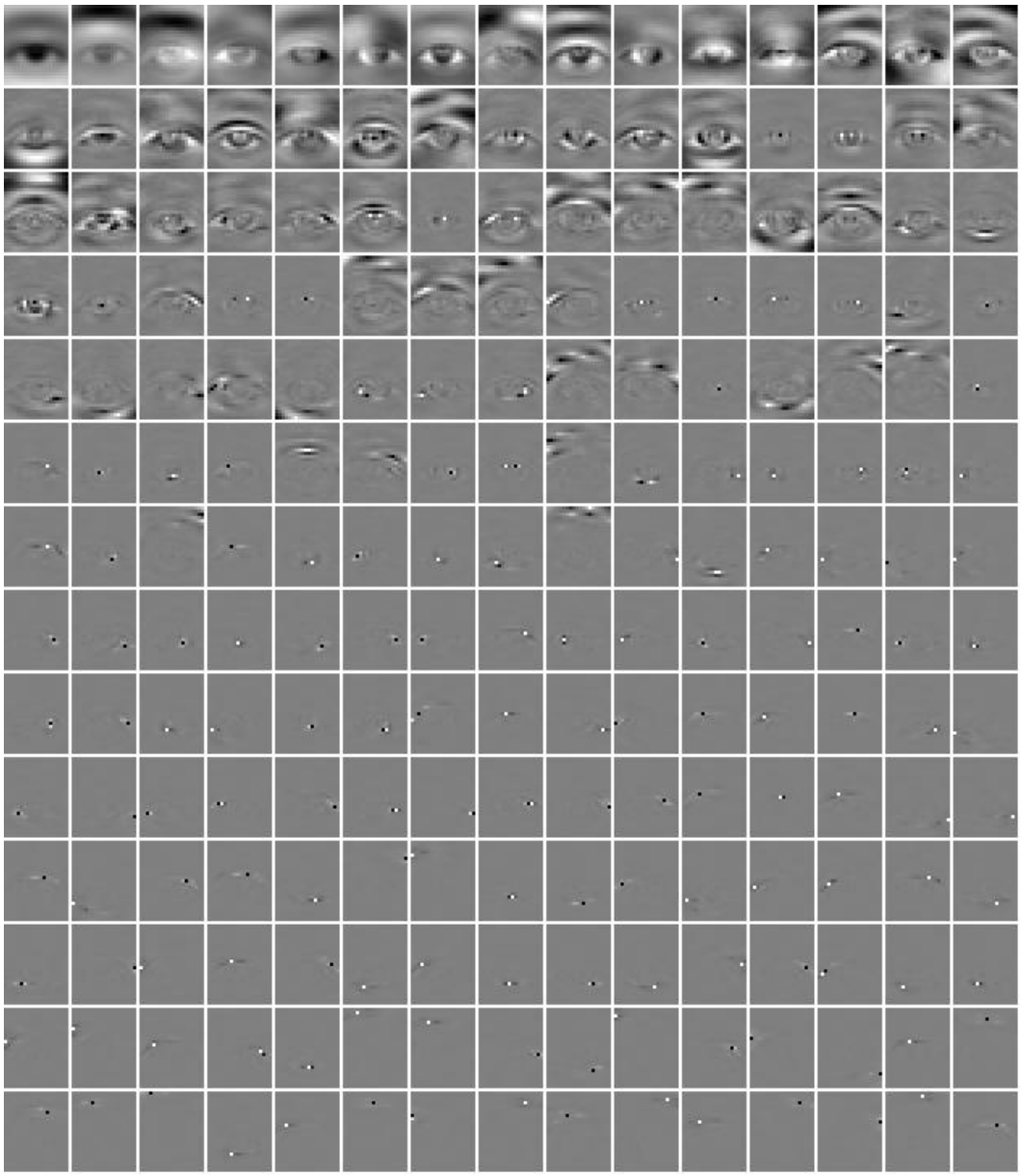

Figure 4.5: S-PCA basis for the eye space, arranged from left to right in decreasing order of the input variance captured. The first sub-image on the left is the mean image.

number of pixels N. We can now define the residual variance to be

$$v_M(\vec{x}) = \frac{1}{K}\sum_{k=1}^{K} e_k^2(\vec{x}), \tag{4.12}$$

where $v_M(\vec{x})$ denotes the variance at pixel $\vec{x}$ resulting from approximating the input with the leading M-dimensional subspace. This expression is exact for PCA on the training set, that is the residual variance at pixel $\vec{x}$ after projecting out the first M basis directions (along with the DC and the mean images) in the training set is just $v_M(\vec{x})$. The residual variances at nearby pixels are likely to be correlated. We ignore this correlation issue for now, but this is an important issue and we will return to it in a future section.

4.3.3 Detection Strategy

The detection strategy is to expand test images in terms of the DC and mean images, along with the first M leading basis images and measure two statistics namely, m_k and S_k^{oos}. Here m_k is the coefficient of the mean image, and

$$S_k^{\text{oos}} = \frac{1}{N}\sum_{\vec{x}} \frac{\left[\vec{t}_k(\vec{x}) - d_k\vec{\xi}(\vec{x}) - m_k\vec{\mu}(\vec{x}) - \sum_{j=1}^{M} c_{k,j}\vec{b}_j(\vec{x})\right]^2}{\vec{v}_M(\vec{x})}, \tag{4.13}$$

measures the variance of the residual error in expanding the test image $\vec{t}_k$ by the leading M-dimensional basis images (along with $\vec{\xi}$ and $\vec{\mu}$), as compared to the residual variance $\vec{v}_M$ obtained by expansions of the same form over the training set.

The variance plot drawn in Fig. 4.6(LEFT) shows $\sqrt{S_k^{\text{oos}}}$ computed with just the DC and the mean images (i.e. $M = 0$) and it is clear from the figure that the feature spaces of S_k^{oos} and m_k are amenable to a simple classification strategy. In particular, we use the constraint that

$$m_k > m_{\min} \tag{4.14}$$

where $m_{\min}$ is a small positive value ($= 20$). Negative values of m_k correspond to contrast reversals and small positive values for m_k generate a mean image component which varies

only by a few gray levels. Additionally, we apply a simple contrast invariant threshold of the form

$$\arctan(m_k, \sqrt{S_k^{\text{oos}}}) \leq \tau_{\text{oos}}, \tag{4.15}$$

which requires that the distribution of the eye dataset be underneath a line drawn through the origin at an angle τ_{oos} for successful detection. A particular detector is then defined by the number of basis vectors used for the principal subspace and the choice of the parameter τ_{oos}.

4.3.4 Results

We first discuss results from using the PCA basis and then show the improvement in performance obtained by the S-PCA basis. While the eye data is split into training and testing sets, the generic background patch ensemble is considered as one large test dataset.

In Figs. 4.6 and 4.7 we show the separation of the test datasets: eyes (green) and non-eyes (red), in the feature space of $\sqrt{S_k^{\text{oos}}}$ vs m_k, as a function of the increasing subspace dimensionality ($M = 0, 20, 50,$ and 100). The detection threshold lines drawn as black lines in each one of the plots generate roughly 5% false positives. The true detection/rejection rates and the corresponding ROC curve obtained by changing the value of the τ_{oos} parameter can be seen in more detail in Fig. 4.8. The simplest strategy of using just the DC and the mean images (i.e. $M = 0$) results in a detection rate of 93% and a false target rate of 7%. With increasing subspace dimensionality, the datasets appear to be more separable visually, however the improvement in the ROC curves is marginal. In particular, a 50-dimensional PCA subspace is suitable for describing the eye manifold, as the true detection rate grows to 95% and the false positive rate reduces to $\approx 5.5\%$ and increasing M further causes over-fitting on the training set, as seen from the ROC plots in Fig. 4.9.

The discriminative ability of the PCA representation is not high. Is there any im-

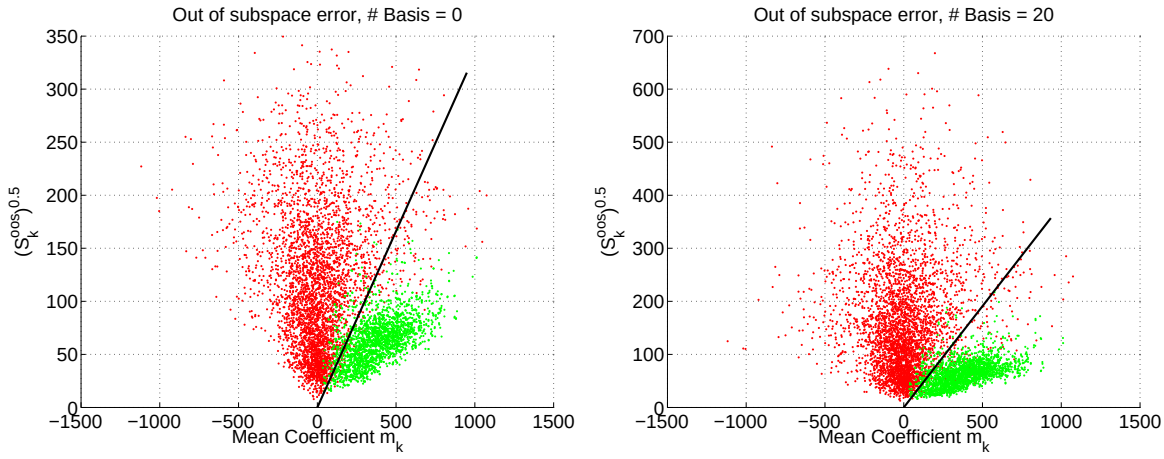

Figure 4.6: Separation of the eye and the non-eye clouds in the feature space of $\sqrt{S_k^{\text{oos}}}$ vs m_k with the addition of 0 (LEFT) and 20 (RIGHT) PCA basis.

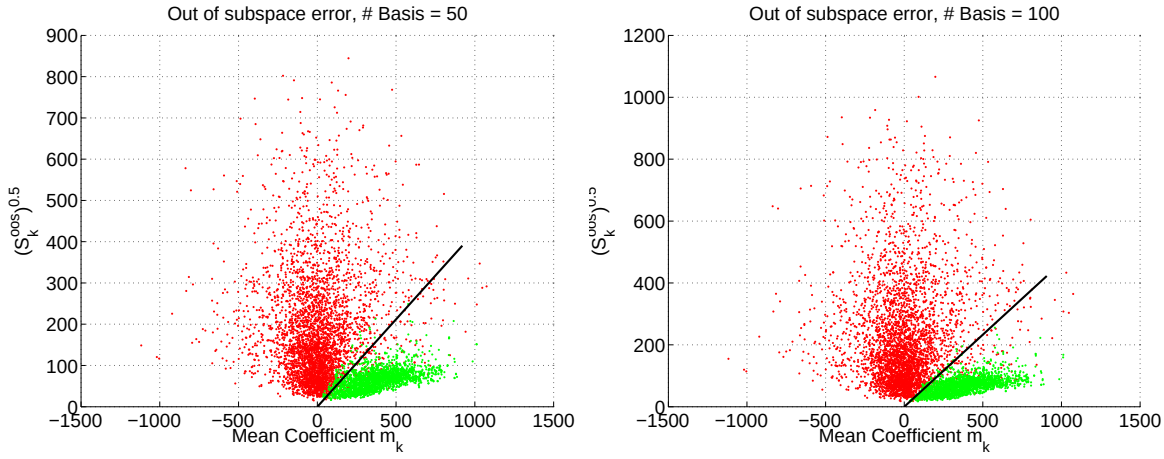

Figure 4.7: Separation of the eye and the non-eye clouds in the feature space of $\sqrt{S_k^{\text{oos}}}$ *vs* m_k with the addition of (LEFT) 50 and (RIGHT) 100 PCA basis.

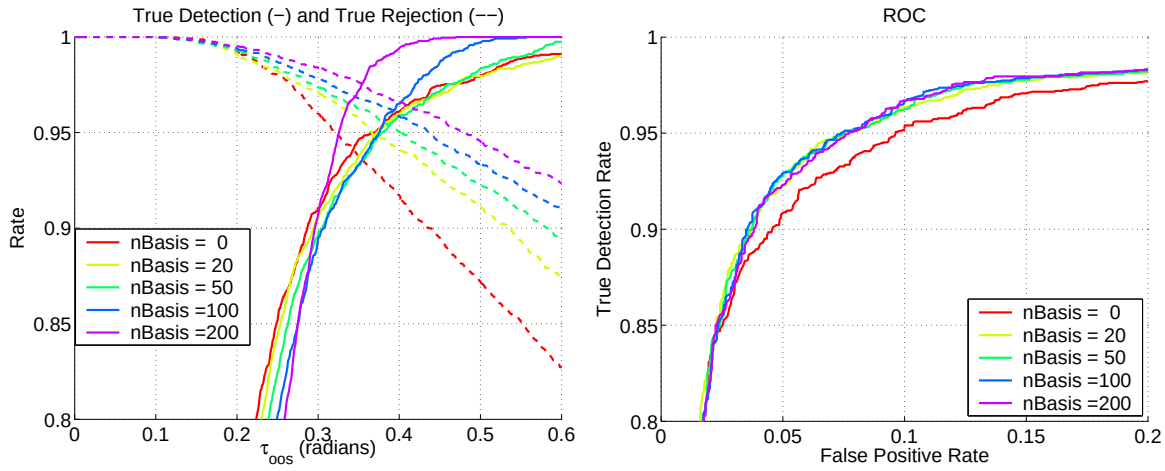

Figure 4.8: PCA basis applied to the test dataset. (LEFT) True detection and rejection rates. (RIGHT) ROC curve.

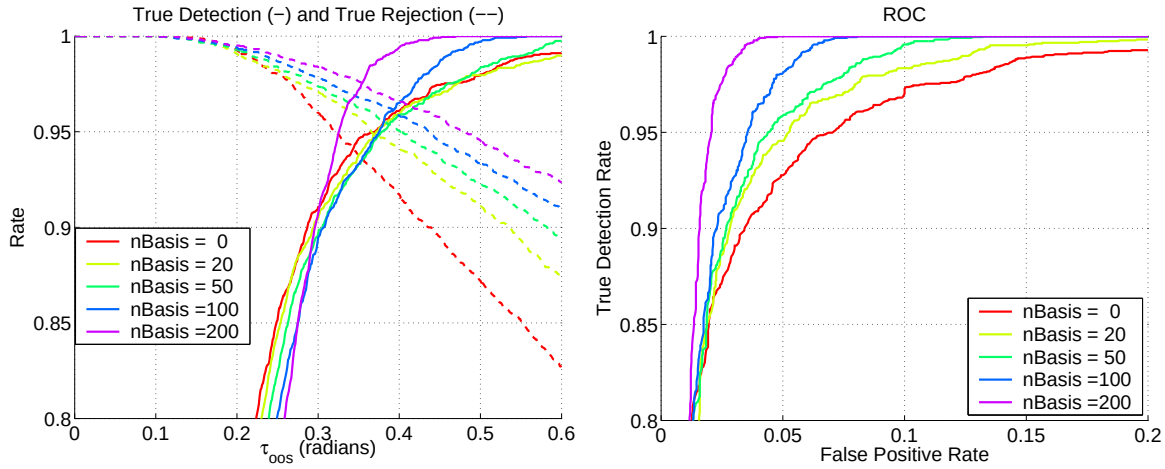

Figure 4.9: PCA basis applied to the training dataset. (LEFT) True detection and rejection rates. (RIGHT) ROC curve. Note the difference from Fig. 4.8 in the curves for nBasis = 100 and 200, indicating overfitting.

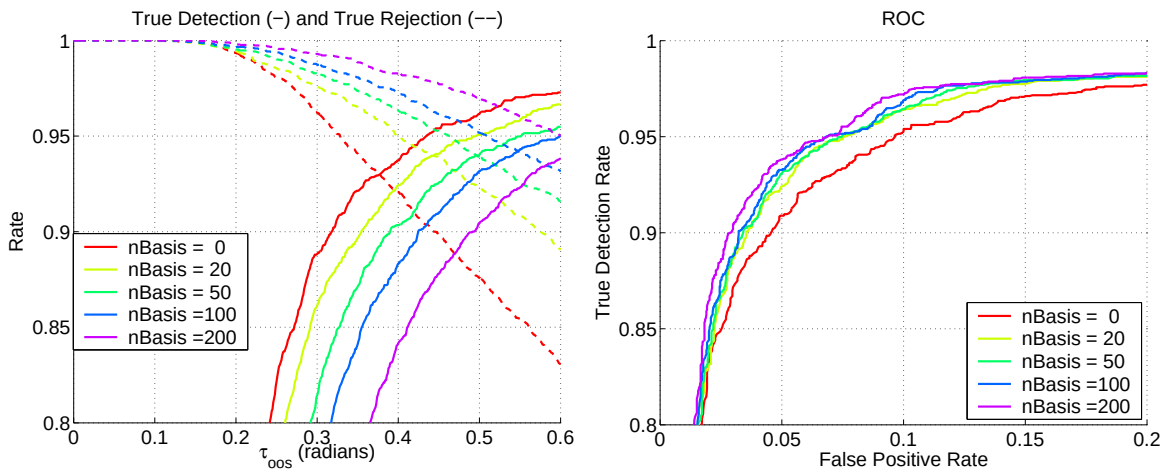

Figure 4.10: S-PCA basis applied to the test dataset. (Left) True detection and rejection rates. (Right) ROC curve.

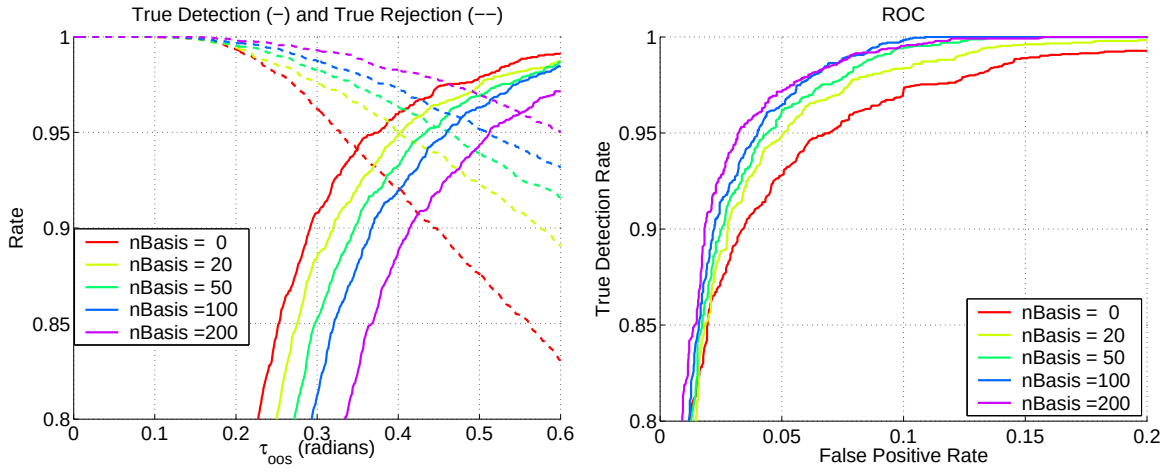

Figure 4.11: S-PCA basis applied to the training dataset. (Left) True detection and rejection rates. (Right) ROC curve.

provement in using the S-PCA basis? The results from applying the S-PCA basis on the test datasets is shown in Fig. 4.10. Compared with the results obtained from using the PCA basis, as shown in Fig. 4.8, the improvement with S-PCA basis is at most a few percentage points. It is not surprising that PCA and S-PCA do about the same because the reconstruction errors are roughly the same. While there is an advantage in using S-PCA basis, in that they facilitate fast detection (see § 3.6), the recognition rates for both PCA and S-PCA are less than satisfactory.

A closer inspection of the eyes rejected as false negatives shows that these are images that look extreme, in that many have highlights caused by the specularities from the eye glasses or pixel outliers such as the hair falling over the eye brows etc. It is possible to improve on the false negative rates by taking into account only relevant portions of an image in detecting eyes, as we have done in [25]. However, the high false positives rates are a major cause for concern and we present a vastly improved detection model next.

4.4 Detection Model – II

The problem of detecting known appearances is analogous to the problem of measuring image similarity, in that we need a perceptual error norm for meaningful results. In § 4.3 we used a mean-squared-error (MSE) norm for measuring image distortions and we ignored the fact that the residual errors in the out-of-subspace signal may be correlated spatially. Thus, the detector model we proposed earlier is unlikely to capture perceptual distances between image pairs.

Motivated by the work in [105], we propose a new detector model outlined in Fig. 4.12. For this new detector model, we find it convenient to employ a generic, local contrast-normalization scheme, so that there is no bias introduced by the object-specific mean image into the dataset (Eq. 4.2). There are five steps involved: (1) contrast-normalize ($\mathcal{WCN}$) the test image $\vec{y}$ to obtain $\vec{t}$; (2) project $\vec{t}$ onto the wavelet-like space W derived

$$
\begin{array}{ccccc}
\vec{t} & \xleftarrow{\mathcal{WCN}} & \vec{x} & & \\
\downarrow{\scriptstyle W^T} & & & & \\
\vec{d} & \xrightarrow{B^T} & \vec{b} & \xrightarrow{B} & \hat{\vec{d}} \\
\downarrow{\scriptstyle \mathcal{PDN}} & & & & {\scriptstyle \mathcal{PDN}}\downarrow \\
\vec{z} & & & & \hat{\vec{z}}
\end{array}
$$

Figure 4.12: Detector Model – II with perceptual distance normalization ($\mathcal{PDN}$). See § 4.4 for more details.

from training S-PCA on generic background patches and obtain $\vec{d}$ as the coefficient vector; (3) build a low-dimensional approximation $\hat{\vec{d}}$ to the coefficient vector $\vec{d}$ using S-PCA basis B constructed for the object-specific ensemble in the "wavelet" space; (4) apply perceptual distance normalization $\mathcal{PDN}$ on the coefficient vector $\vec{d}$ and its reconstruction $\hat{\vec{d}}$ to obtain normalized vectors $\vec{z}$ and $\hat{\vec{z}}$; and finally (5) apply a simple detection strategy to $\vec{z}$ and $\hat{\vec{z}}$. We explain these details next.

4.4.1 Weber-Contrast Normalization

Weber-contrast is a measure of the relationship between the response of a pixel and that of its neighborhood. In particular, if x_i is the response of a pixel at location i and μ_i is an estimate of the mean response value in its neighborhood, then the Weber contrast signal c_i is defined as:

$$c_i = \frac{x_i - \mu_i}{\mu_i}. \tag{4.17}$$

The mean signal value μ_i can be obtained by convolving the image with a two-dimensional radially-symmetric Gaussian filter $G(i\,;\,\sigma)$. The neighborhood size is determined by the standard deviation σ of the Gaussian function. While this contrast computation removes shading variations, there are pixel outliers, such as the specularities from the eye glasses or the hair falling over the eye brows, that can bias the computation (Fig. 4.1). To reduce

Figure 4.13: Weber-contrast normalized eye dataset. Compare this with Fig. 4.1.

the effect of outliers we normalize the contrast values using the following expression:

$$\begin{aligned} t_i &= \mathcal{F}(c_i\,;\,\beta), \\ &= \frac{1-\exp(-\beta c_i)}{1+\exp(-\beta c_i)}, \end{aligned} \tag{4.18}$$

where β is chosen such that for a predefined contrast value $c_i = c_{\text{def}}$, the normalized contrast t_i takes a value of 0.5.

The contrast normalization results on a subset of the eye and the non-eye datasets are shown in Figs. 4.13 and 4.14 respectively. We set $\sigma = 3$ for estimating the contrast and $c_{\text{def}} = 0.3$ for normalization. In Fig. 4.15 we show histograms of the pixel intensities for the two datasets before and after normalization. The normalization removes the DC signal for generic background patches. But for the eye ensemble, we see a small non-zero average, caused by pixel intensities being brighter than their neighbors more often than not. The range of intensities after normalization is compressed, that is the tails of the distributions are clipped. In general, we observe larger values of σ improve the performance of the detector, but the detector is less susceptible to the actual setting of c_{def}.

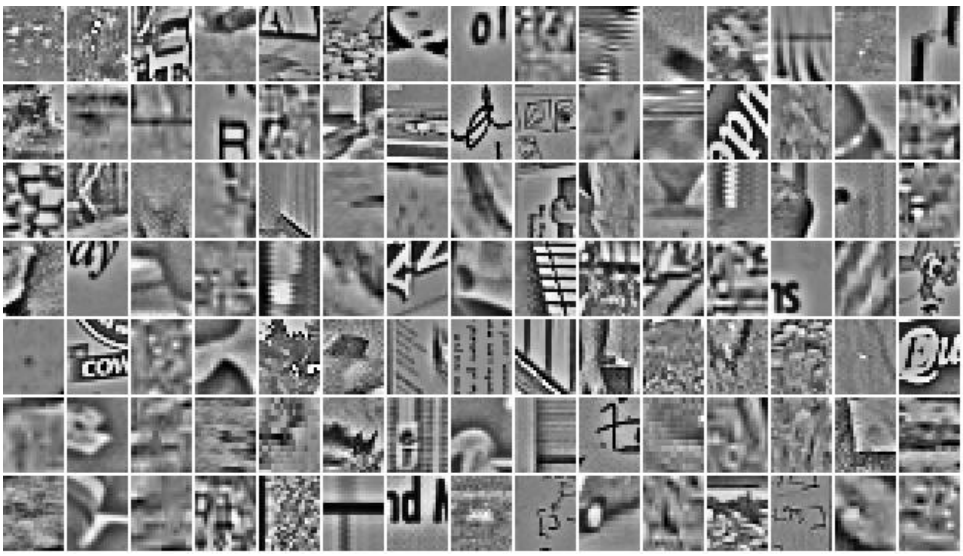

Figure 4.14: Weber-contrast normalized non-eye images (compare with Fig. 4.2).

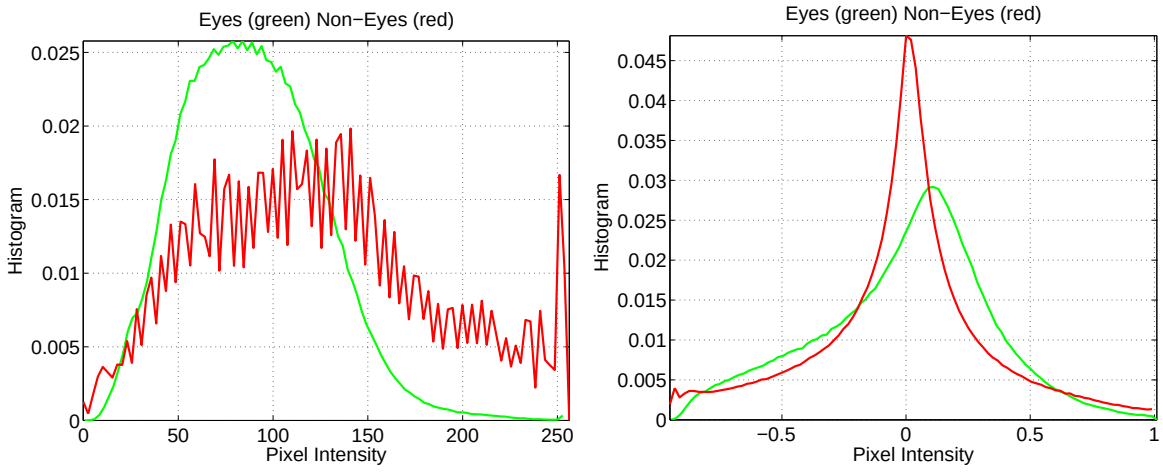

Figure 4.15: Weber-contrast normalization: histograms of the pixel intensities in the eye (green) and non-eye (red) datasets before (Left) and after normalization (Right).

4.4.2 S-PCA Representation: W, B

The S-PCA basis matrix trained on generic background patches is given by W, an $N \times N$ matrix, shown in Fig. 4.16. For an N-dimensional contrast-normalized image $\vec{t}$ the N-dimensional S-PCA coefficient vector is given by

$$\vec{d} = W^T \vec{t}.$$

Because the S-PCA basis look like wavelets, we abuse the notation slightly to call $\vec{d}$ a wavelet coefficient vector. Next, S-PCA is trained separately on the wavelet coefficients generated for the images in the object-specific ensemble (eg. eyes). For the following step, we build a low-dimensional representation for the wavelet coefficient vector using the leading M object-specific S-PCA basis vectors. In particular let B be the object-specific S-PCA basis matrix of size $N \times M$, then projecting the wavelet coefficient $\vec{d}$ gives

$$\vec{b} = B^T \vec{d}$$

and the wavelet coefficient vector can be reconstructed as

$$\begin{aligned} \hat{\vec{d}} &= B\vec{b} \\ &= BB^T \vec{d}, \end{aligned}$$

which is again N-dimensional. Because the basis matrix B resides in the wavelet space, it is hard to interpret it and hence in Fig. 4.17 we show the matrix: $W \times B$ obtained by pre-multiplying object-specific S-PCA basis B by the generic background patch S-PCA basis W. Notice, the basis $W \times B$ is sparse, spatially local and multi-scale.

4.4.3 Perceptual Distance Normalization

The coefficient vectors $\vec{d}$ and $\hat{\vec{d}}$ are now subjected to a perceptual distance normalization process. The idea is to normalize each wavelet coefficient by the pooled amplitude of wavelet coefficients tuned to similar spatial frequencies and similar spatial neighborhoods

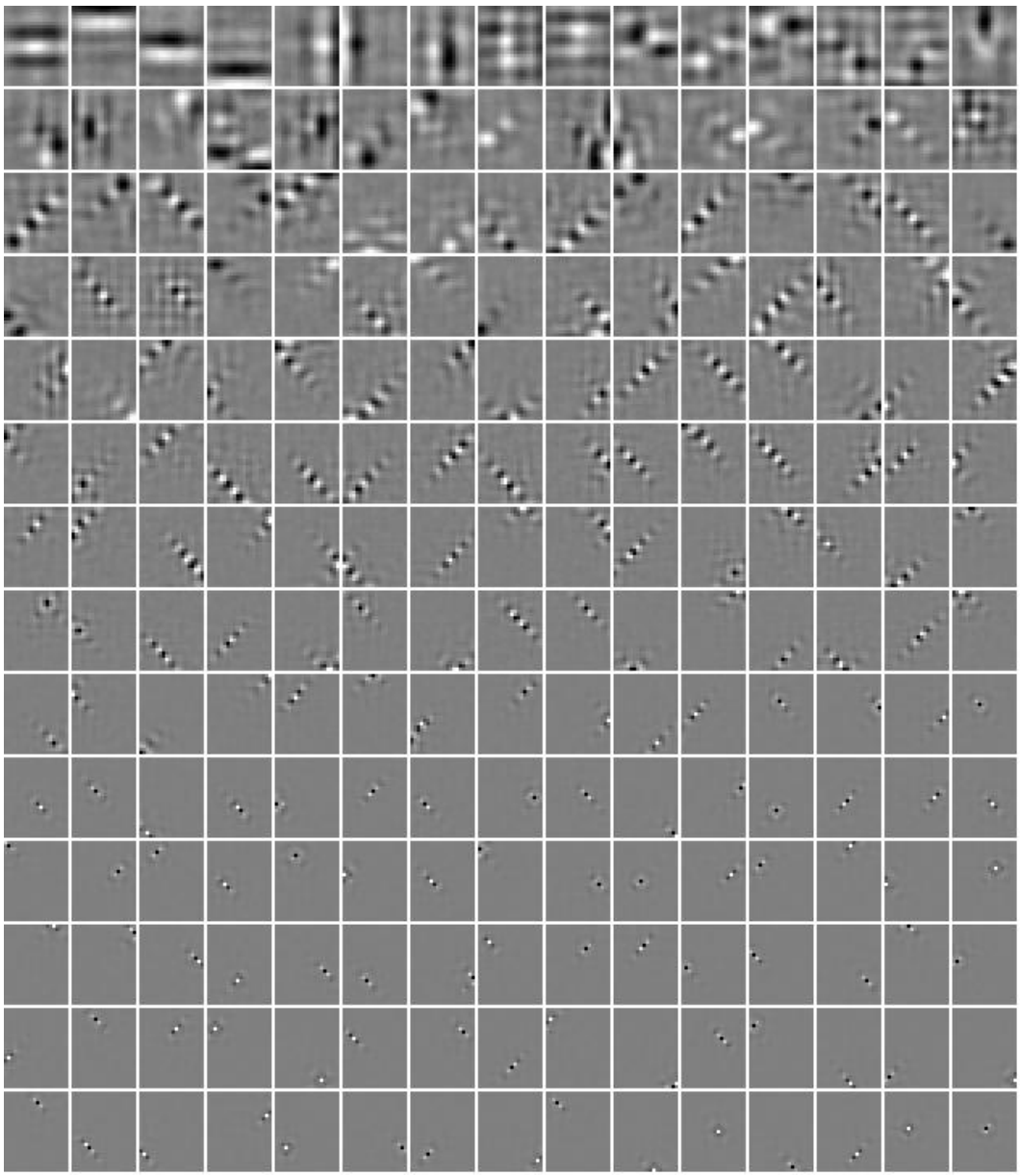

Figure 4.16: S-PCA basis for Weber-contrast normalized generic background patches.

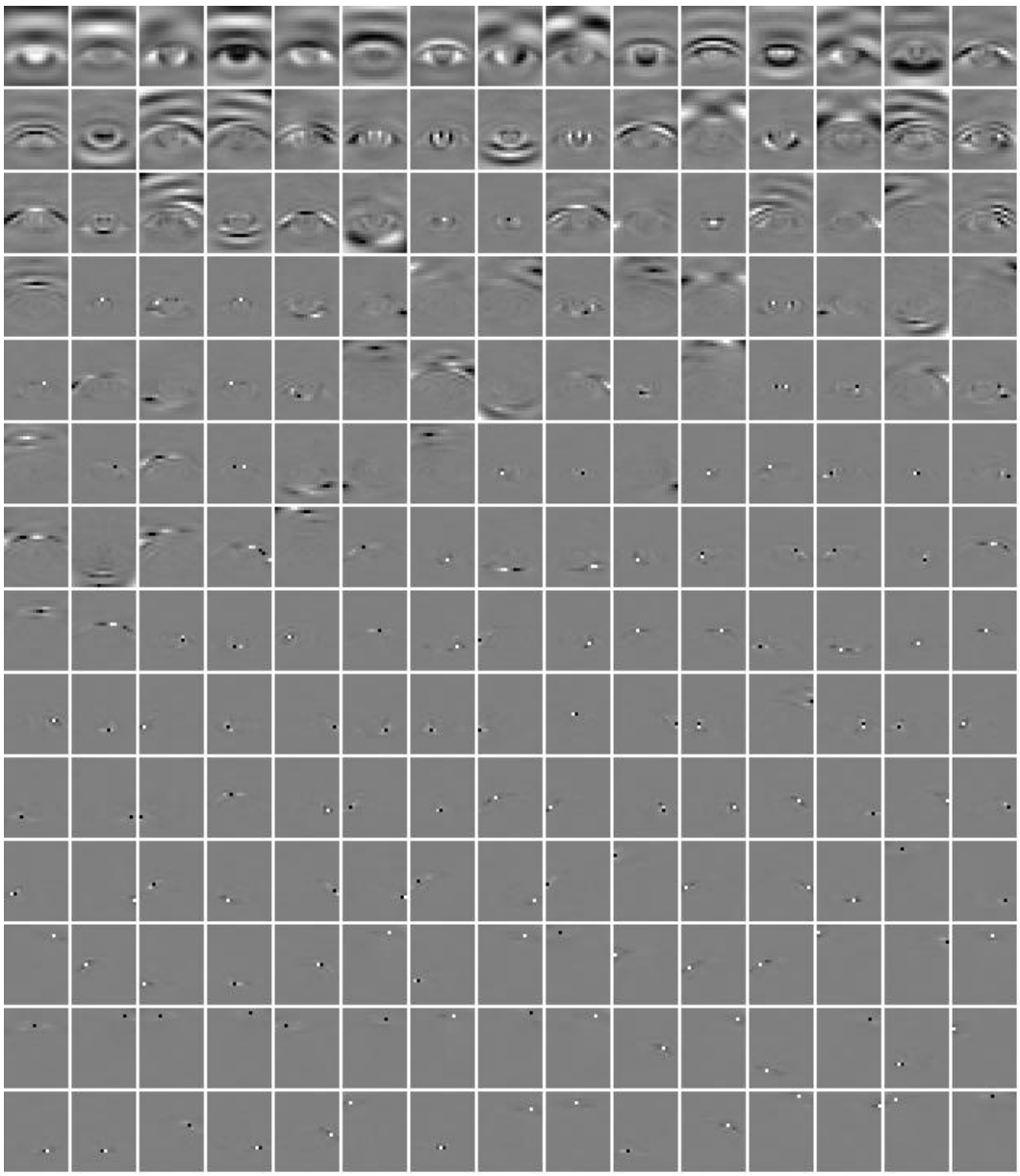

Figure 4.17: S-PCA basis for Weber-contrast normalized eye images.

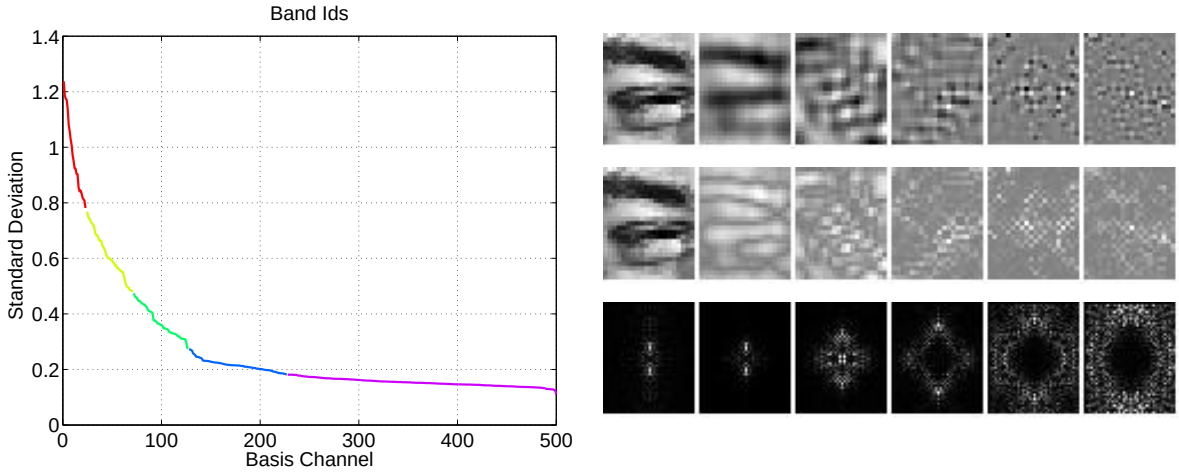

Figure 4.18: (LEFT) Partitioning the variance spectrum into five different subsets (shown here in different colors) each tuned to roughly similar spatial frequencies. (RIGHT) An eye image and its bandpass components from the five different basis bands (TOP), the corresponding amplitude maps (MIDDLE) and the corresponding Fourier magnitude maps for the bandpass images (BOTTOM).

[18, 105]. Because S-PCA basis are learned from the data, as opposed to being hand-crafted, we need to find what the adjacent scales and orientations are for each S-PCA basis function in an automatic fashion. We outline a simple strategy next.

The spatial frequency tuning of the wavelets in W was observed to be related to the variance of the wavelet coefficients over the training set. Therefore by partitioning the variance spectrum we obtain subsets of wavelets tuned to roughly similar spatial frequencies. We automated this partitioning using K-means on the log variance spectrum. The result is shown in Fig. 4.18(LEFT), where the spectrum is partitioned into 5 groups, each drawn in a different color for the generic background patch ensemble.

To identify the local amplitude of image structure in each frequency band we form the amplitude image using a band of S-PCA basis indexed from l to h,

$$\vec{p} = \left| \sum_{l \leq k \leq h} \vec{w}_k d_k \right| . \tag{4.21}$$

Here $\vec{w}_k$ denotes the k^{th} basis vector, d_k is the corresponding wavelet coefficient value. In

Fig. 4.18(RIGHT, TOP) we show an eye image and the bandpass images that result from the summation in Eq. 4.21 in each of the five different basis bands. In Fig. 4.18(RIGHT, MIDDLE) we show the eye image along with its amplitude maps that result from the absolute operation over the bandpass images shown before, as given in Eq. 4.21. To provide a better intuition for the bandpass images, the images in Fig. 4.18(RIGHT, BOTTOM) show the Fourier magnitudes of the bandpass images. To estimate the portion of this amplitude image within the spatial support of the k^{th} wavelet $\vec{w}_k$, we compute:

$$s_k = \left|\vec{w}_k^T\right| \vec{p}. \tag{4.22}$$

It can be shown that $s_k \geq |d_k|$ with the equality holding when $d_j = 0$ for $j \neq k$.

We can finally express the perceptual distance normalization ($\mathcal{PDN}$) of the k^{th} element of the coefficient vector as

$$z_k = \frac{d_k}{(s_k + \upsilon_{lh})}. \tag{4.23}$$

The constant υ_{lh} is a saturation parameter for the basis band indexed from l to h. It is determined empirically by processing random images with a predetermined noise level (= 4 gray levels) and measuring the statistics of the resulting S-PCA coefficients. In particular, the random images are contrast normalized and for each wavelet band a corresponding amplitude map is generated. The amplitude maps are then projected back into the wavelet space and the saturation constant υ_{lh} is set to the median value of the coefficients of the amplitude map in each wavelet band. The perceptual distance normalized coefficients of a wavelet coefficient vector $\vec{d}$ and its reconstruction $\hat{\vec{d}}$ are given by vectors $\vec{z}$ and $\hat{\vec{z}}$ respectively.

4.4.4 Detection Strategy

For the purpose of detection we measure two numbers: (1) the wavelet norm given by the L_1 norm of $\vec{z}$; and (2) the error norm given by the L_1 norm of the error vector $\vec{z} - \hat{\vec{z}}$.

We study the variation of these two numbers as a function of the increasing subspace dimensionality M, the number of columns in the basis matrix B shown in Fig. 4.13 (for relevant discussion see §4.4.2). We expect the error norm to be high for generic image patches because the subspace was built for the object-specific ensemble. Also, we expect that the higher the wavelet norm, the higher will be the error norm for generic image patches. In fact, as we discuss next, what we observe is that the generic background patches and the object-specific ensemble appear as two distinguishable clouds with a small amount of overlap. We next present results using a straightforward detection strategy.

4.4.5 Results

Eyes/Non-Eyes:

In Figs. 4.19 and 4.20, we show the results of applying the new detection method on the test set of eyes/non-eyes by varying $M = \{20, 50, 100, 200\}$. For clarity the plots have been scaled in such a way as to show all of the eye images (green points) at the expense of omitting a portion of the non-eye images (red points). As a detection strategy, we adopted a very simple approach of using a line aligned with the principal axis of the generic image patch cloud as shown in Fig. 4.21(LEFT) for the test set and Fig. 4.22(LEFT) for the training set. Points below the line are taken as positive detections. The ROC curve for a given M is obtained by adjusting the y-intercept of the line and these are shown for both the test and train sets. For example, in Fig. 4.21(LEFT) the two black lines correspond to two different points on the ROC curve ($M = 50$) shown in Fig. 4.21(RIGHT).

The ROC curve in Fig. 4.21(RIGHT) for the test set makes one thing very clear: the false positives can be kept very low, namely a value less than 0.8%, for a true acceptance rate of $\approx 95\%$ in a $M = 50$ dimensional subspace. This is a significant improvement over the previously reported detection model results (see Figs. 4.8 and 4.10). For comparison,

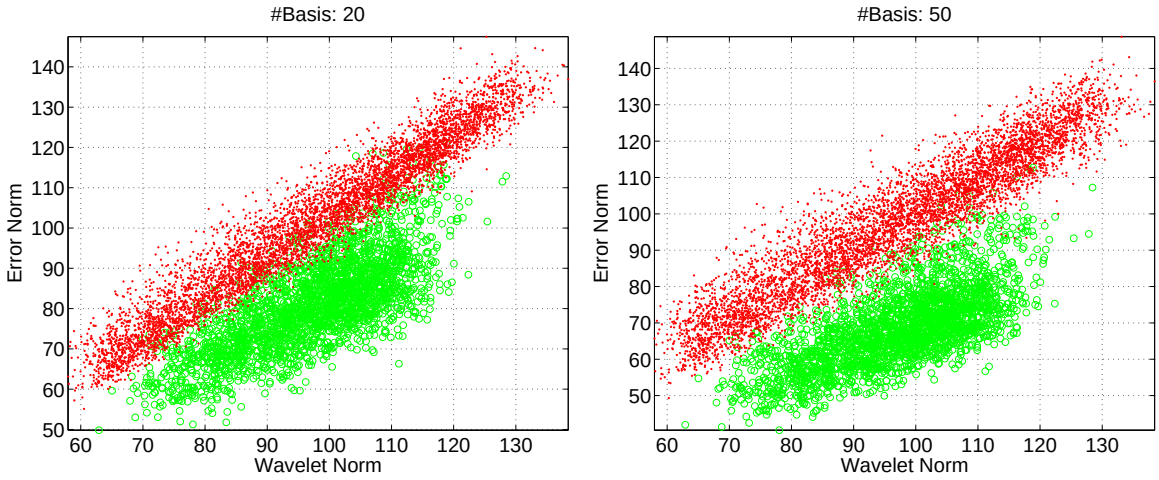

Figure 4.19: Separation of the eye and the non-eye clouds in the test set with the addition of (LEFT) 20 and (RIGHT) 50 SPCA basis.

the ROC curve with $M = 50$ from Fig. 4.8 is reproduced here as a black line. In particular, for $M = 50$ the gain in false positive rate with $\mathcal{PDN}$ is nine-fold for a true detection rate of 95% and is 24-times better for a true detection rate of 90%. Some of the false positives admitted by the detection algorithm are shown in Fig. 4.23. The false positives were collected over the training and testing datasets and displayed in a single figure for convenience.

Faces/Non-Faces:

The MIT face database [6] consists of 2429/472 training/testing face images and 4548/23573 training/testing non-face images. Informally, most of the images in the training set are: cropped above the eyebrows, cropped just below the bottom lip, centered, roughly frontal views, and relatively well exposed. However, very few of the images in the test set appear to satisfy all these properties. We therefore created "mixed" training and testing sets by merging all these face images, adding the mirror symmetric versions, then randomly selecting half the dataset for mixed-training and the other half for mixed-testing. In Fig. 4.24(LEFT) we plot the perceptually normalized space for the newly created mixed-

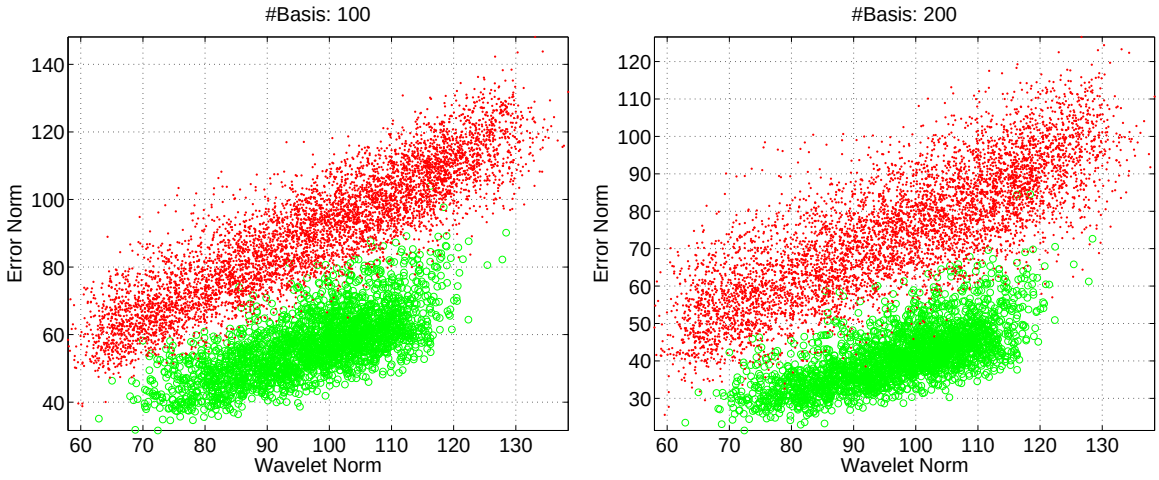

Figure 4.20: Separation of the eye and the non-eye clouds in the test set with the addition of (LEFT) 100 and (RIGHT) 200 SPCA basis.

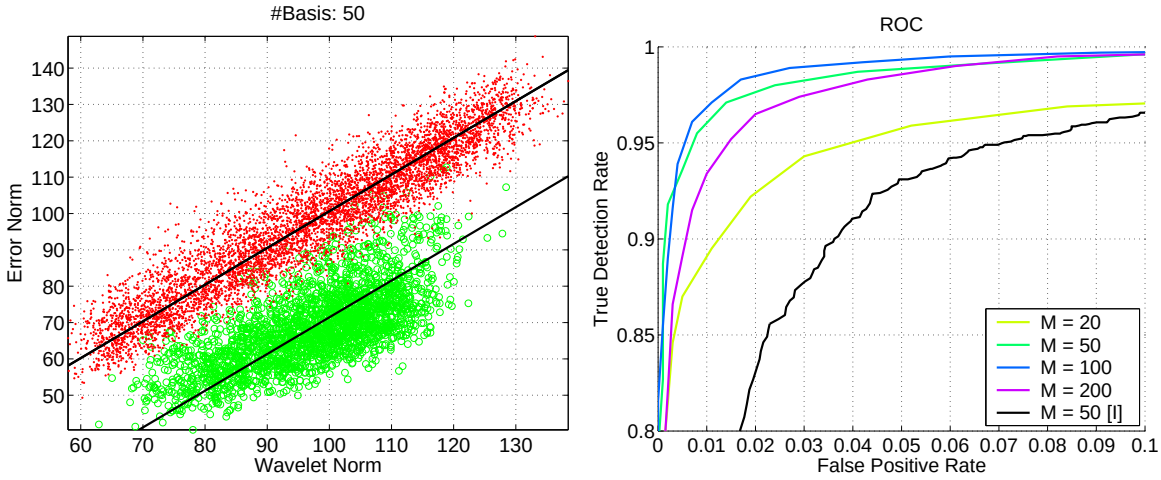

Figure 4.21: Detection results on the test set. (LEFT) Strategy is to adjust the y-intercept of a line aligned with the principal axis of the non-eye cloud (red). Points below the line are taken as positive detections. The two black lines correspond to two different points on the ROC curve for $M = 50$ (green) shown on the (RIGHT). For comparison, the ROC curve for detector model I with $M = 50$ (from Fig. 4.8) is reproduced here on the (RIGHT) as a black line (labeled $M = 50$ (I)).

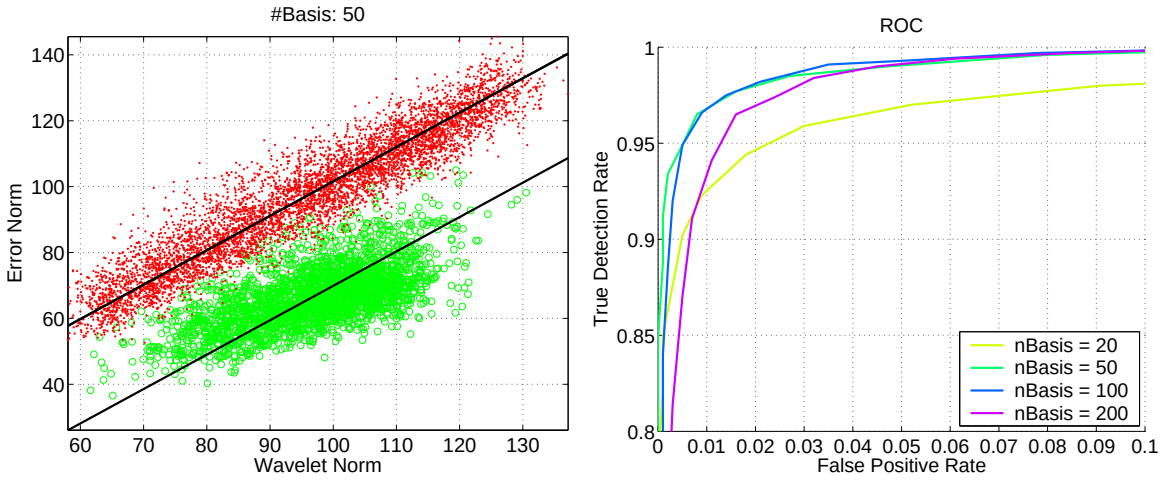

Figure 4.22: Detection results on the training set. (LEFT) Strategy is to adjust the y-intercept of a line aligned with the principal axis of the non-eye cloud (red). Points below the line are taken as positive detections. The two black lines correspond to two different points on the ROC curve for $M = 50$ shown in the (RIGHT).

testing set, where the non-faces are indicated by red dots and the faces by the blue and green dots. In particular, the green dots indicate faces from the original training set and blue dots indicate faces from the original testing set. Using a subspace of $M = 50$ dimensions, for a false positive rate of 0.1% we observe 16% false negatives, out of which 96% belong to the original testing set. In fact, the face images in the original testing set make up 16% of the mixed dataset and, given the separation between the original training and original testing face images in the perceptually normalized space, this is not a surprise. In Fig. 4.24(RIGHT) the black curve denotes the recognition rates obtained using just the original training set, and omitting the original test set, in a $M = 50$ dimensional subspace. The recognition rates are near perfect.

Comparison with Support Vector Machine (SVM)

We compare the performance of our detector with a *support vector machine* (SVM) classifier [115]. SVM is parameterized by a kernel function and a C value which is the cost

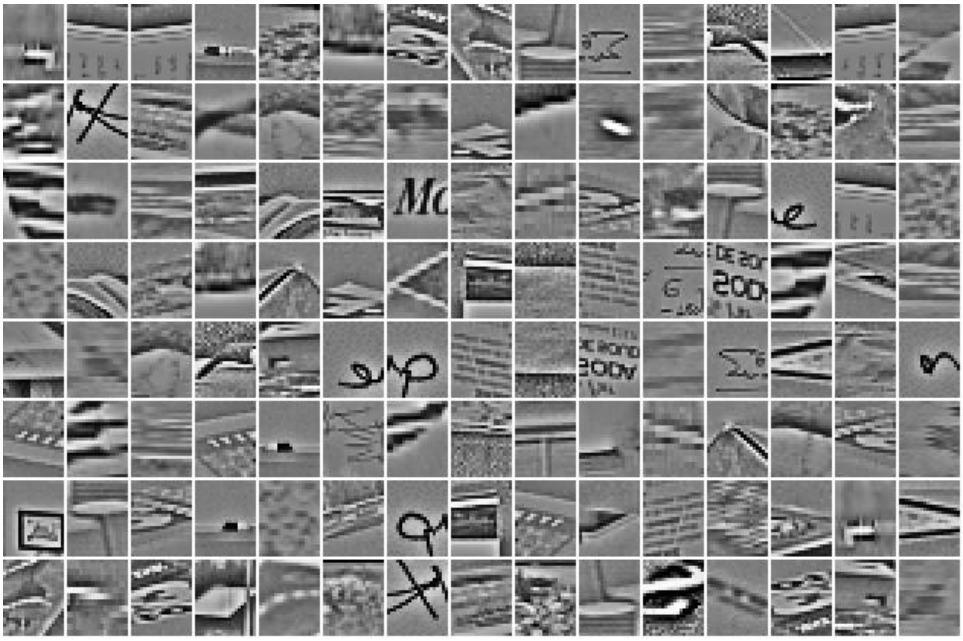

(a) False positives

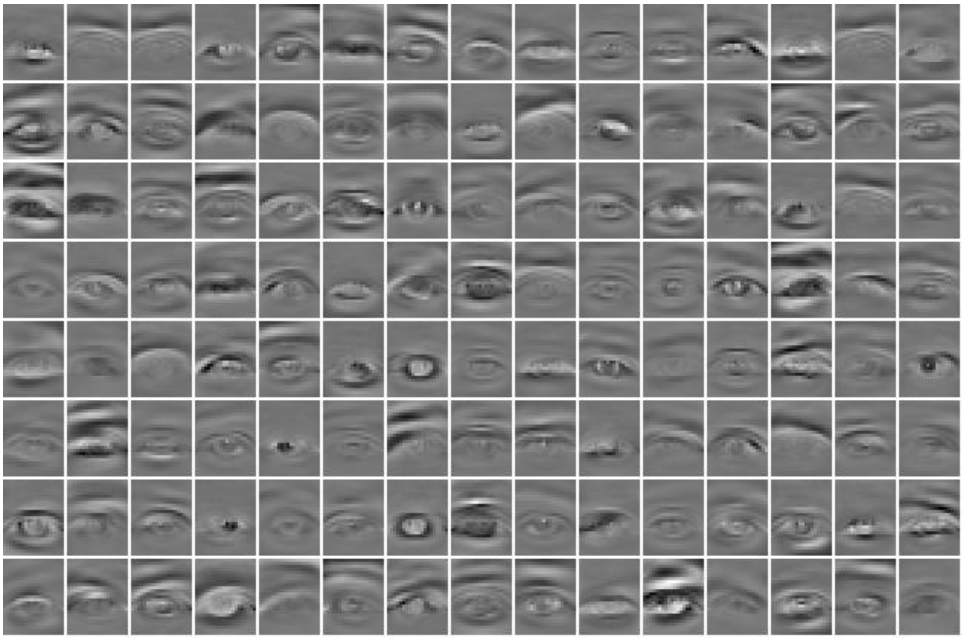

(b) Reconstruction from a 50 dimensional subspace

Figure 4.23: (Top) False positives collected over the training and testing sets and displayed in one figure. (Top) Reconstruction results from a 50 dimensional subspace.

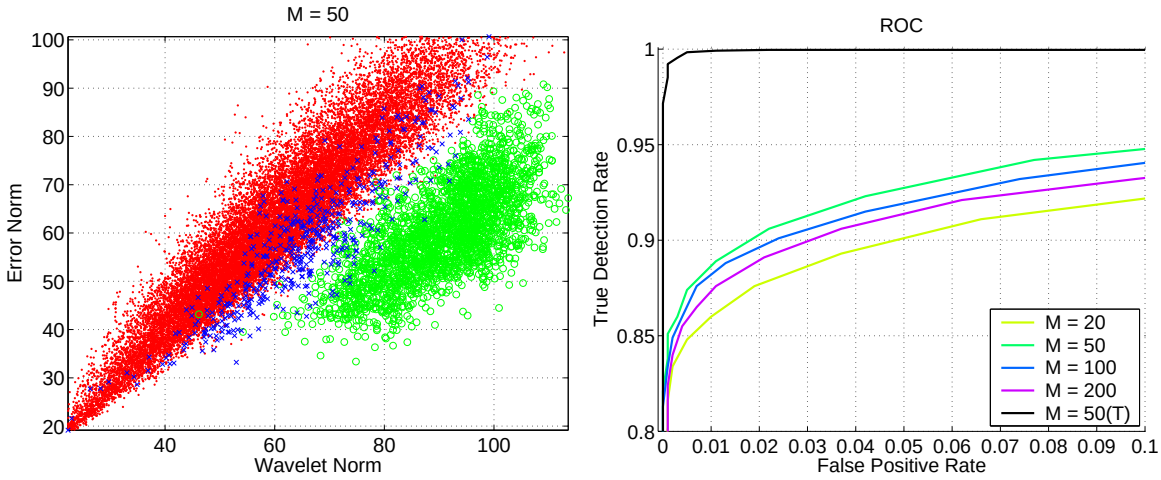

Figure 4.24: Detection results on the MIT face database. (LEFT) Characterizing test-faces (blue), train-faces (green) (which together constitute the mixed-test set) and non-faces in the test set (red) in the perceptually normalized space. (RIGHT) ROC curves for the "mixed" test set. The black curve denotes recognition rate for just the train-faces in the "mixed" test set.

per unit violation of the classifier margin. We used a publicly available implementation of SVM [6]. We chose a Gaussian kernel and varied the σ parameter. The C value was set to 1, other values were tried but did not have a significant effect on the classifier.

On the eye dataset for different values of σ we observed a large variation in the total number of support vectors returned. In particular, for $\sigma = [3, 5, 10, 20]$ the number of support vectors returned on the training set are $[5267, 1564, 1140, 1616]$ respectively. Each support vector involves a dot product and hence, for a fair comparison the number of support vectors returned should be comparable to the number of inner products performed with the $\mathcal{PDN}$ model for a suitable choice of M. Thus, we selected $\sigma = [5, 10]$ and $M = [50, 100]$.

In Fig. 4.25(LEFT) we compare the detection results from SVM to our $\mathcal{PDN}$ model on the eye dataset. The green and the blue curves denote the use of $M = [50, 100]$ dimensional subspaces with the $\mathcal{PDN}$ model. The $\mathcal{PDN}$ graphs are identical to the

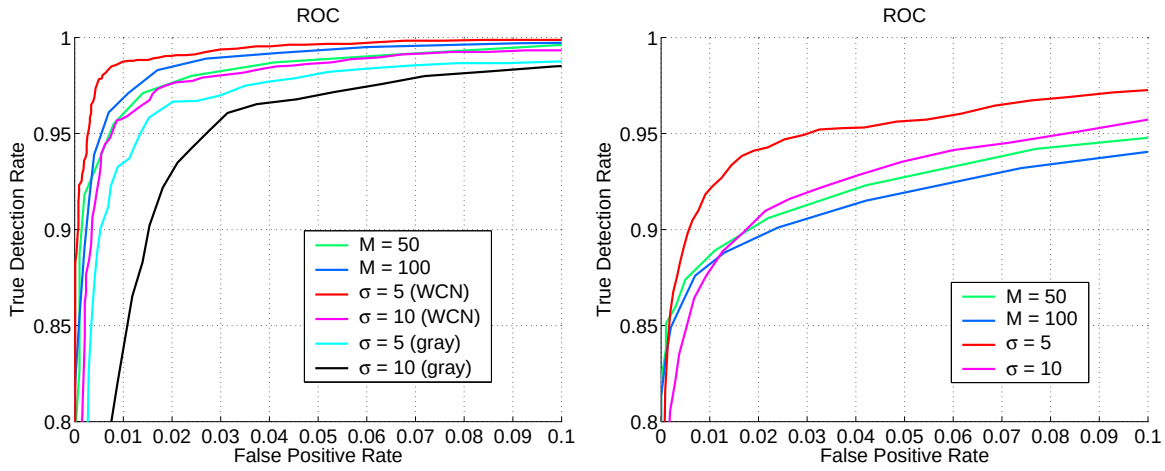

Figure 4.25: Comparing SVM with $\mathcal{PDN}$. (LEFT) ROC curves for the eye test set. The green and the blue curves correspond to $M = [50, 100]$ dimensional subspaces with the $\mathcal{PDN}$ model. The $\mathcal{PDN}$ graphs are identical to the ones shown in Fig. 4.21. The red and magenta curves show results from SVM, with $\sigma = [5, 10]$, on the contrast normalized ($\mathcal{WCN}$) dataset. The SVM performance on unnormalized images (gray) is given by the black and cyan curves. (RIGHT) ROC curves for the "mixed" face testing set. The green and the blue curves correspond to $M = [50, 100]$ dimensional subspaces with the $\mathcal{PDN}$ model. The $\mathcal{PDN}$ graphs are identical to the ones shown in Fig. 4.24. The red and magenta curves show results from using SVM with $\sigma = [5, 10]$.

ones shown in Fig. 4.21. The red and magenta curves show results from using SVM with $\sigma = [5, 10]$. The performance of SVM with $\sigma = 10$ is similar to using $\mathcal{PDN}$ with $M = 50$. Increasing the total number of support vectors, i.e. reducing σ from 10 to 5, improves the performance of SVM. In addition, we tested the performance of the SVM on the original gray-level images (i.e. without $\mathcal{WCN}$), and the results are given by the black and cyan curves in Fig. 4.25(LEFT). It is clear that contrast normalization causes a significant improvement in the performance of SVM.

We ran a similar experiment on the mixed training and testing sets that we created for the MIT face database. The number of support vectors obtained on the mixed training set for $\sigma = [5, 10]$ are $[1549, 1434]$ respectively. In Fig. 4.25(RIGHT) we compare the detection results from SVM to our $\mathcal{PDN}$ model on the mixed testing set. The green and the blue curves denote the use of $M = [50, 100]$ dimensional subspaces with the $\mathcal{PDN}$ model. The $\mathcal{PDN}$ graphs are identical to the ones shown in Fig. 4.24. The red and magenta curves show results from using SVM with $\sigma = [5, 10]$. The performance of SVM with $\sigma = 10$ is similar to using $\mathcal{PDN}$ with $M = 50$. The best detection result we obtained was for $\sigma = 5$, which required 1549 support vectors.

A detailed comparison of the different methods is beyond the scope of this thesis, for several reasons: (1) The $\mathcal{PDN}$ normalization is *not* optimal in terms of computational efficiency. It was designed for simplicity. The normalization of each wavelet should depend only on a few "neighbouring" wavelets, and there is likely to be a more efficient way to do this than by generating the amplitude map; (2) It is not clear that the SVM implementation we have used is optimal (e.g. see [107]). If neither method is optimal, a detailed comparison may not be very revealing. Perhaps, most interesting is the use of several detectors (e.g. an eye, a nose, a mouth, and a face detector) within a single system. For such a system the wavelet transform used in our approach is common to all detectors, and hence the cost of the wavelet transform, in terms of the underlying hardware, can be amortized.

4.5 Conclusion

Using PCA models, in place of S-PCA, we have observed detection results similar to the ones shown in Fig. 4.21 for both the object-specific and background ensembles with the same $\mathcal{PDN}$ formulation as provided in Eq. 4.21–4.23. The improved performance with $\mathcal{PDN}$ comes with a price, in that the images have to be represented in the full N-dimensional wavelet domain. However, we expect wavelet decomposition of signals to be a standard pre-processing tool. The simplicity of the detector in the wavelet domain is striking. In particular, after applying a linear model of eyes and doing perceptual normalization we can simply use the L_1 norm to separate classes.

Chapter 5

S-PCA: Conclusions and Future Work

We presented a novel framework, Sparse Principal Component Analysis (S-PCA), for extracting multi-scale structure from data. We showed how introducing a sparsity constraint on the elements of a basis matrix recovers structure in spatially coherent image blobs and provides a multi-scale representation for the ensemble. The principal advantages of S-PCA over a standard PCA based representation include an intuitive understanding of the features underlying the ensemble and efficiency in computations resulting from a sparse basis representation.

Sparsity in the basis matrix is best understood as saving computations over the lifetime of a representation system. However, in encoding images there are a few extra bits spent because S-PCA coefficients are correlated slightly. The learning algorithm of S-PCA is very simple, consisting of successive planar rotations of pairs of basis vectors. We have demonstrated the suitability of this algorithm for large-dimensional spaces.

The formulation of S-PCA is novel in that multi-scale representations emerge for a wide variety of ensembles using just the second-order correlations. We believe the feasibility of extracting multi-scale structure from second-order statistics is a point overlooked

in the literature.

We briefly outline two proposals for future work. First, in learning the basis directions the S-PCA formulation presented here does not take into account the presence of noise in the dataset. For a recent attempt in this direction see [116]. In the next section (§ 5.1.1), we sketch a well-known information-theory based algorithm called Infomax [63] that takes into account the effect of noise in the input and show how to modify it to provide a sparse representation. Second, in deriving the S-PCA basis we encourage sparsity, which means a majority of the basis elements may be close to zero, but they need not be exactly zero. If the basis element values were indeed zero, then we can save lots of arithmetic operations. So we briefly consider the possibility of driving sparsity harder by using a mixture-of-Gaussian prior in § 5.1.2.

5.1 Future Work

5.1.1 Sparse-Infomax

Linsker's Infomax principle states that a network is optimal if the mutual information between its input and output is maximal [63]. The network is considered noisy. In particular, the input to the network $\vec{t}$ comes from an unknown source signal $\vec{s}$ that has been corrupted by (photon) noise $\vec{p}$, as in

$$\vec{t} = \vec{s} + \vec{p}.$$

We will assume that the source vectors have an unknown covariance C given by

$$\mathcal{E}\left(\vec{s}\vec{s}^T\right) = C,$$

where $\mathcal{E}$ is the expectation operator, and the noise vectors are uncorrelated in directions each with a σ_p^2 variance,

$$\mathcal{E}\left(\vec{p}\vec{p}^T\right) = \sigma_p^2 I,$$

where I is an identity matrix of appropriate dimension. Combining these two equations gives the covariance Q for the observables $\vec{t}$

$$\begin{aligned}\mathcal{E}\left(\vec{t}\vec{t}^{T}\right) &= C + \sigma_p^2 I \\ &= Q\end{aligned}$$

The network is assumed to be linear, where the input image $\vec{t}$ is represented by a coefficient vector $\vec{c}$ given by simple projection onto the basis direction matrix W

$$\vec{c} = W^T \vec{t}.$$

It is easy to show that

$$\mathcal{E}\left(\vec{c}\vec{c}^{T}\right) = W^T Q W.$$

Also, there is quantization noise at the output which is modelled as uncorrelated additive noise $\vec{q}$ with variance

$$\mathcal{E}\left(\vec{q}\vec{q}^{T}\right) = \sigma_q^2 I,$$

and hence the output $\vec{z}$ is given by

$$\vec{z} = \vec{c} + \vec{q}.$$

The covariance of the output signal can be expressed as

$$\mathcal{E}\left(\vec{z}\vec{z}^{T}\right) = W^T Q W + \sigma_q^2 I$$

The INFOMAX criterion is to find a basis matrix W that maximizes the mutual information between the unknown source input and the quantized output given by:

$$\mathsf{MI}(\vec{s};\, \vec{z}) = \log\left|W^T Q W + \sigma_q^2 I\right| - \log\left|\sigma_p^2 W^T W + \sigma_q^2 I\right|.$$

If σ_p^2 is zero, then there is an analytical solution to the basis matrix, which is given by

$$W = R \times F,$$

where R is a matrix of eigenvectors for the covariance matrix C and F is a diagonal matrix inversely proportional to the square root of the eigenvalues of C. Hence, F acts as a whitening filter in the limit of zero noise in the input. But if the input noise is non zero, then F sets elements on the diagonal to zero in directions where the signal power is less than the power of noise [8, 63].

We can modify the INFOMAX framework to accommodate a sparsity term on the basis elements and we call this procedure SPARSE-INFOMAX. In particular, we can continue to assume a simplified form for the basis matrix $W = R \times F$ as given above, but introduce a sparse prior on the elements of the R matrix.

The objective function in SPARSE-INFOMAX will be set up to maximize the mutual information between the input and the output of the network, while promoting sparsity via a regularization term on the basis elements. Additionally, a pre-specified bit budget can be imposed on the outputs, just as in the INFOMAX framework. For sparsity, the following functional form can be applied on the basis elements r_{ij}:

$$\sum_{ij} \log p(r_{ij}) \propto \sum_{ij} \log \left(\alpha + \beta \times \exp \left(- \left| \frac{r_{ij}}{\gamma} \right| \right) \right),$$

where α, β and γ are the parameters of the sparsity driving function. The constraint of bit budget K can be incorporated into the cost function in the following way:

$$\sum_{i} \left(\log \left[\mathcal{E}(z_i^2) \right] - \log \sigma_q^2 \right) - K = 0,$$

where $\mathcal{E}(z_i^2)$ is the variance in each output channel.

5.1.2 Encouraging Sparsity with a Mixture-of-Gaussian Prior

We briefly consider a Gaussian mixture model to drive sparsity in the basis directions. In particular, elements of a basis vector $\vec{b}_k$ are driven by a two-component Gaussian mixture,

$$p(b_{ik}) = m_{nk} \mathcal{N}(b_{ik}\,;\, \sigma_n^2) + (1 - m_{nk}) \mathcal{N}(b_{ik}\,;\, \sigma_{bk}^2),$$

where b_{ik} is the i^{th} element of the k^{th} basis vector $\vec{b}_k$, $p(b_{ik})$ is the prior probability distribution on the basis elements and $\mathcal{N}(\cdot\,;\,\cdot)$ represents a Gaussian distribution. There are two Gaussian distributions here, one that is *narrow* with variance σ_n^2 and the other component is *broad* with variance σ_{bk}^2.

The narrow Gaussian has a mixing coefficient m_{nk}, which is also a function of the basis vector index k. This dependency is natural as we expect the mixing coefficient for coarse-scale S-PCA basis functions to be close to zero, but a lot higher for the fine-scale basis vectors. In comparison, for the PCA basis or a pixel basis (identity matrix) we expect m_{nk} to be independent of the basis index k. For example, we expect the higher-order PCA basis to have $m_{nk} = 0$ and the identity matrix (or the pixel basis) to have $m_{nk} = \frac{N-1}{N}$, accounting for the fact that there is only one pixel on in each basis vector.

The mixture model has several independent parameters but there is a constraint binding them all, as we show next. The S-PCA representation is orthonormal and hence the basis vectors have unit length,

$$\sum_i b_{ik}^2 = 1.$$

The variance computation on the basis elements leads to

$$\frac{1}{N}\sum_i b_{ik}^2 = \frac{1}{N},$$

and this in turn gives rise to a linear constraint on the variance of the mixture model:

$$m_{nk}\sigma_n^2 + (1 - m_{nk})\sigma_{bk}^2 = \frac{1}{N},$$

where N is the length of the basis vector $\vec{b}_k$. Given m_{nk} this is a linear equation in the parameters σ_n^2 and σ_{bk}^2, so there is a one-parameter family of solutions for each mixing coefficient m_{nk}. The goal here is to drive sparsity hard. We achieve this by annealing the parameter σ_n^2 that is independent of the basis index k.

In each sweep of the S-PCA rotations, we hold the mixture model parameters constant for each basis vector, and update the basis directions. Then, in iteration $t+1$, the variance

parameter σ_n^2 is lowered by setting

$$\sigma_n^2(t+1) = \rho \times \sigma_n^2(t).$$

Using the new value of $\sigma_n^2(t+1)$ and the old value of $\sigma_{bk}^2(t)$ we fit $m_{nk}(t+1)$ for each basis vector $\vec{b}_k$ using a typical EM procedure. Finally, given the new value of $m_{nk}(t+1)$ and $\sigma_n^2(t+1)$, we can use the linear constraint mentioned above to update σ_{bk}^2:

$$\sigma_{bk}^2 = \frac{1}{(1-m_{nk})}\left(\frac{1}{N} - m_{nk}\sigma_n^2\right).$$

For initialization of this new process, it seems convenient to use the S-PCA basis produced by the algorithm proposed earlier in the thesis.

Chapter 6

Spectral Clustering

6.1 Visual Grouping

The importance of perceptual grouping and organization in visual perception was laid out many years ago by the Gestaltist school [120]. For this thesis we motivate the grouping problem by inviting the reader to segment images shown in Fig. 6.1. Observers report perceiving two "things" – a foreground object occluding a textured background. A dominant cue perhaps is the difference in luminance between the occluder and the background. However, observe that in each image there is a portion of the occluder that blends into the background, but our visual systems appear to discount this information. One of our objectives in this thesis is to develop a computational process for segmenting images into plausible groups. We approach this partitioning problem with a graph-theoretic formulation.

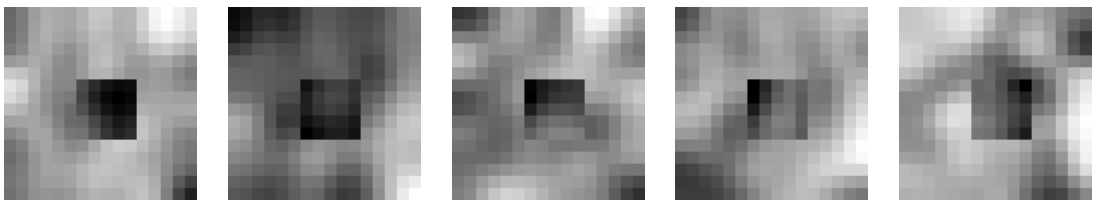

Figure 6.1: Images of a foreground occluder object against a textured background.

6.2 Graph-Theoretic Partitioning

We consider partitioning a weighted undirected graph G into a set of discrete clusters. Each node in the graph corresponds to a pixel in the image, and the edges correspond to the strength (or affinity) with which two nodes belong to one group. Ideally, the nodes in each cluster should be connected with high-affinity edges, while different clusters are either disconnected or are connected only by a few edges with low affinity. The practical problem is to identify these tightly coupled clusters, and cut the inter-cluster edges.

6.2.1 Graph Formulation

For illustration purposes we consider an ensemble of random test images formed from two independent samples of 2D Gaussian filtered white noise (see Fig. 6.1). One sample is used to form the 16×16 background image, and a cropped 5×5 fragment of a second sample is used for the foreground region. A small constant bias is added to the foreground region.

A graph clustering problem is formed where each pixel in the test image is associated with a vertex in the graph G. The edges in G are defined by the standard 8-neighbourhood of each pixel (with pixels at the edges and corners of the image only having 5 and 3 neighbours, respectively). A weight is associated with each edge based on some property of the pixels that it connects. For example, the affinities between pixels (or nodes) $\vec{x}_i$ and $\vec{x}_j$ will correspond to how much the two pixels agree in luminance, color, texture *etc.* and how far apart they are in the image. The affinities are captured in a symmetric $n \times n$ matrix A with $a_{i,j} \geq 0$ and $a_{i,j} = a_{j,i}$. For the images considered in this thesis, we use intensities at pixels $\vec{x}_i$ and $\vec{x}_j$ denoted by $I(\vec{x}_i)$ and $I(\vec{x}_j)$ and define affinity as

$$a_{i,j} = \begin{cases} \exp\left\{ \frac{-\left[I(\vec{x}_i) - I(\vec{x}_j)\right]^2}{(2\sigma^2)} \right\} & \text{for } \vec{x}_j \text{ in the 8-neighbourhood of } \vec{x}_i, \\ 0 & \text{otherwise,} \end{cases} \tag{6.1}$$

where σ is a grey-level standard deviation. We use

$$\sigma = \rho \times g,$$

where g is the median absolute difference of gray levels between all neighbouring pixels and $\rho = 1.5$. It is worth mentioning that for the clustering algorithms that we propose later in this thesis, ρ can be set anywhere between 1 and 2.

We make note of one other property of the graph, which is the *degree* d_j of a node j. It is defined to be

$$d_j = \sum_{i=1}^{n} a_{i,j} = \sum_{i=1}^{n} a_{j,i}, \tag{6.2}$$

and consider a diagonal matrix D which is stacked with the degrees of the nodes as in

$$D = \text{diag}\begin{bmatrix} d_1 & d_2 & \dots & d_n \end{bmatrix}. \tag{6.3}$$

This generative process provides an ensemble of clustering problems that we feel are representative of the structure of typical image segmentation problems. In particular, due to the smooth variation in gray-levels, there is some variability in the affinities within both foreground and background regions. Moreover, due to the use of independent samples for the two regions, there is often a significant step in gray-level across the boundary between the two regions. Finally, due to the small bias used, there is also a significant chance for pixels on opposite sides of the boundary to have similar gray-levels, and thus high affinities. This latter property ensures that there are some edges with significant weights between the two clusters in the graph associated with the foreground and background pixels.

The affinity matrices for images in Fig. 6.1 may be less intuitive to interpret, so we show datasets that have a simple distribution in two-dimensional space as in Figure 6.2a. The affinities were designed to fall off rapidly as a function of the Euclidean distance between points. Because the dataset is well separated in space, the corresponding affinity matrix, shown in Fig. 6.2b, has a pronounced block structure. For convenience, the

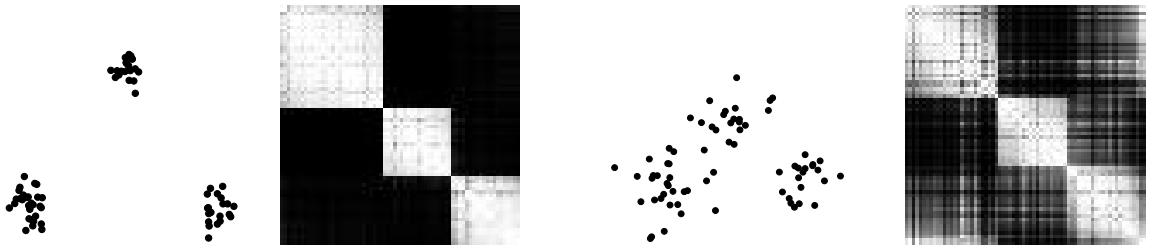

(a) Well separated (b) Affinities (c) Weakly separated (d) Affinities

Figure 6.2: Two sets of points in a plane and the corresponding affinity matrices. The affinities are designed to fall off rapidly as a function of the Euclidean distance between points.

affinity matrix has been arranged to have the points appear sorted. Specifically, the points are sorted based on the angle made by the lines joining each of the points in the dataset to the overall mean of the dataset. Because we know the generative model for the dataset, we also know the overall cluster center. The angle sorting procedure groups all the points in a cluster together and makes the block diagonal structure of the affinity matrix obvious. For comparison, we show a weakly coupled dataset and its affinity matrix in Fig. 6.2c and Fig. 6.2d respectively. Observe the cross-talk, or the weak coupling, between clusters in the affinity matrix in Fig. 6.2d.

6.2.2 Cut Measures / Criterion

To partition the graph we need a *cut measure* and a *cut criterion*. For now, consider segmenting the image (graph) into two clusters, a foreground object F and a background object B. Define a corresponding cut measure A_{FB} to be the sum of the affinities for all the edges that begin in the foreground cluster and end in the background object:

$$A_{FB} = \sum_{i \in F, j \in B} a_{i,j}.$$

	Foreground F	Background B	Complete Graph G
Foreground F	$A_{\mathrm{FF}} = \sum_{i \in F, j \in F} a_{i,j}$	$A_{\mathrm{FB}} = \sum_{i \in F, j \in B} a_{i,j}$	$A_{\mathrm{FG}} = A_{\mathrm{FF}} + A_{\mathrm{FB}}$
Background B	$A_{\mathrm{BF}} = \sum_{i \in B, j \in F} a_{i,j}$	$A_{\mathrm{BB}} = \sum_{i \in B, j \in B} a_{i,j}$	$A_{\mathrm{BG}} = A_{\mathrm{BF}} + A_{\mathrm{BB}}$

Table 6.1: A summary of cut measures. A_{FB} and A_{BF} summarize the connections between the foreground and the background objects. Observe A_{FB} has the same value as A_{BF} because the affinity matrix A is symmetric. A_{FG} and A_{BG} summarize the connections from the foreground and the background to the complete graph.

Similarly, define A_{BF} to be the sum of the affinities for all the edges that begin in the background object and end in the foreground cluster:

$$A_{BF} = \sum_{i \in B, j \in F} a_{i,j}.$$

Because the affinity matrix is symmetric, $A_{FB} = A_{BF}$. In Table 6.1 we list several possible cut measures that arise when the graph is partitioned into two groups. In particular, we have:

$$A_{FF} = \sum_{i \in F, j \in F} a_{i,j},$$

$$A_{BB} = \sum_{i \in B, j \in B} a_{i,j},$$

$$A_{FG} = A_{FF} + A_{FB},$$

$$A_{BG} = A_{BB} + A_{BF}.$$

There are many possible alternatives for a cut criterion, but here we will discuss a recent proposal, called *Normalized Cut* [101]. We will also show how this criterion leads us to a random walk perspective for graph partitioning, which we investigate in depth in the following chapter. The goal with normalized cut (NCut) is to minimize the following criterion:

$$\mathrm{NCut} = \frac{A_{\mathrm{FB}}}{A_{\mathrm{FG}}} + \frac{A_{\mathrm{BF}}}{A_{\mathrm{BG}}}, \tag{6.4}$$

	Cut Criterion
Normalized Cut [101]	$\frac{A_{\mathrm{FB}}}{A_{\mathrm{FG}}} + \frac{A_{\mathrm{BF}}}{A_{\mathrm{BG}}}$
Foreground Cut [86]	$\frac{A_{\mathrm{FB}}}{A_{\mathrm{FF}}}$
Min-Max Cut [33]	$\frac{A_{\mathrm{FB}}}{A_{\mathrm{FF}}} + \frac{A_{\mathrm{BF}}}{A_{\mathrm{BB}}}$
Conductance [51]	$\frac{A_{\mathrm{FB}}}{\min\left(A_{\mathrm{FG}}, A_{\mathrm{BG}}\right)}$

Table 6.2: A summary of cut criteria based on the measures given in Table 6.1.

over all possible foreground and background partitions (F, B). Minimizing NCut means identifying two tightly coupled clusters with relatively small affinities between the two clusters. NCut is also an attempt to remove any biases that are in favor of cutting small isolated modes in the graph (as in [123]). In Table 6.2 we list several possible cut criteria, where each criterion was shown to be optimal for a particular distribution of points in a dataset [33, 51, 86]. Not surprisingly, optimizing the NCut criterion is NP hard [26, 101].

We now turn to spectral-based methods for an approximate way of solving the NCut criterion. We will then discuss a recent proposal for partitioning the graph into K (> 2) clusters. Finally, we will discuss very briefly a random walk view of spectral clustering. We will also highlight an important assumption underlying the spectral methods.

6.3 Spectral-based Methods

Spectral graph methods have gained popularity in a variety of application domains including segmenting images [68, 96]; clustering parallel scientific computation tasks [88] and circuit layouts [4, 21] among others. Here we explore how spectral methods provide an approximate solution to the NCut problem.

6.3.1 NCut algorithm

The minimization of NCut criterion has an approximate solution and it is based on solving a generalized eigenvalue problem [101]. The NCut algorithm uses the *Laplacian* matrix

$$Q = D - A \tag{6.5}$$

where A is the affinity matrix (Eq. 6.1) and D is the diagonal matrix of degree values (Eq. 6.3). The algorithm consists of solving the generalized eigen problem:

$$Q\vec{u} = \lambda D\vec{u}. \tag{6.6}$$

The solution consists in analyzing the structure of the eigenvector associated with the second smallest eigenvalue of (6.6). In particular, it is shown in [101] that when there is a partitioning of the image into the foreground F and background B such that

$$u_i = \begin{cases} \alpha, & i \in F \\ \beta, & i \in B \end{cases} \tag{6.7}$$

then (F, B) is the optimal NCut and the value of the cut itself is $\text{NCut}(F, B) = \lambda$. A vector $\vec{u}$ satisfying condition Eq. 6.7 is called *piecewise* constant with respect to the partition (F, B). The partitioning of the second smallest eigenvector can be done by thresholding its elements. This in turn induces a partitioning of the graph into (F, B). To obtain K clusters where $K > 2$ we have to proceed recursively. It is conceivable that using more eigenvectors and directly computing a K way partitioning is perhaps a better option [5].

6.3.2 K–Means Spectral Clustering

While much of the earlier work in spectral graph partitioning dealt with finding just two partitions [26], here we consider one particular proposal for finding a K-way partitioning.

This proposal builds on the prior work of using K eigenvectors simultaneously to perform K-way partitioning of the data (e.g. [21, 77, 99, 101, 119]).

1. From the affinity matrix A construct a symmetric normalized matrix

$$L = D^{-1/2} A D^{-1/2}.$$

2. Find a matrix U of eigenvectors: $U = [\vec{u}_1, \vec{u}_2, \cdots, \vec{u}_K]$, associated with the K largest eigenvalues of L.

3. Form a matrix V by re-normalizing each row of U to be unit length:

$$v_{i,j} = \frac{u_{i,j}}{\left(\sum_j u_{i,j}^2\right)^{1/2}}.$$

4. Treat each row of V as a point in $\mathbb{R}^K$. Cluster them into K clusters via K-means (or any algorithm that minimizes distance to K centers).

5. Assign node i to cluster k if and only if row i of the matrix V was assigned to cluster k.

For K well separated clusters, it was shown in [77] that the rows of matrix V form tight clusters around K well separated points that are orthogonal to each other on the surface of a K sphere. As we discuss next, this property is related to having *piecewise constancy* in the form of the leading K eigenvectors i.e., elements of the eigenvectors have approximately the same value within each cluster.

6.3.3 Random Walks and Normalized Cuts

We can convert the affinity matrix A into a stochastic matrix M by a simple normalization via the inverse of the degree matrix D [72]:

$$M = AD^{-1}. \tag{6.8}$$

This normalization causes the column sums of the matrix M to add up to 1. This is a slight change from the notation used in [72], where they use a normalization of the form $D^{-1}A$, which causes the row sums of the resulting stochastic matrix to be 1. We chose the formulation in Eq. 6.8 to suit the analysis we provide in later chapters.

From the theory of Markov random walks [52] the element $M_{i,j}$ represents the probability of moving from node j to i in one step, given a particle is in node j. We will discuss this formulation in greater depth in the next chapter but for now we establish the connection to the spectral problem of NCut. In particular we can show that the NCut formulation (6.6) and the matrix M share eigenvectors, and eigenvalues, that are *similar*. Assuming eigenvector $\vec{u}$ and eigenvalue λ satisfy the generalized eigenvalue problem in 6.6, we can write

$$Q\vec{u} = \lambda D\vec{u}.$$

Substituting from Eq. 6.5 for the Laplacian Q gives

$$(D - A)\vec{u} = \lambda D\vec{u}.$$

Simplifying further using Eq. 6.8

$$\begin{aligned}(D - MD)\vec{u} &= \lambda D\vec{u},\\ D\vec{u} - MD\vec{u} &= \lambda D\vec{u},\\ MD\vec{u} &= (1 - \lambda)D\vec{u}.\end{aligned}$$

Thus the NCut formulation (Eq.6.6) and the stochastic matrix M share an eigenvector that has a simple relationship: $\vec{u}$ and $D\vec{u}$. Because D is a diagonal matrix, $D\vec{u}$ is an element-wise normalization of the vector $\vec{u}$. Similarly the eigenvalues are λ and $1 - \lambda$ respectively. The key aspect we focus on is the result, shown in [72], that the leading K eigenvectors of the stochastic matrix M are piecewise constant. In this context, the K-means spectral clustering can be seen as a method that can identify the appropriate

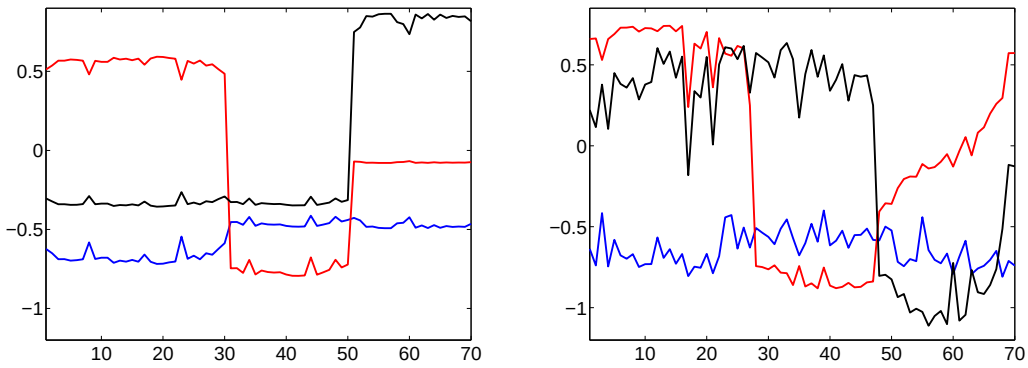

(a) Well separated (b) Weakly coupled

Figure 6.3: The three leading eigenvectors for (a) well separated and (b) weakly coupled datasets shown in Fig. 6.2. Eigenvectors are drawn in colors: first (blue), second (red) and third (black). For the well separated cluster the eigenvectors appear roughly piecewise constant but not so when the cluster is weakly coupled.

piecewise constant regions in the leading K eigenvectors. We demonstrate this on datasets that are well separated and also show how the assumption breaks down when the clusters are not that well separated.

6.3.4 Assumption of piecewise constancy

For the dataset shown in Figure 6.2a we display the leading eigenvectors of the corresponding stochastic matrix M (Eq. 6.8) in Fig. 6.3a. It is clear from the plot that the eigenvectors are piecewise constant, i.e., the elements of the eigenvectors have approximately the same value within each cluster. However we can also see from Fig. 6.3b that this assumption breaks down for weakly coupled clusters in that the eigenvectors do not display the piecewise constant form.

What is the form of the eigenvectors for the occluder data? First, we show a well separated cluster in Fig. 6.4 where the foreground occluder has structure clearly differentiable from the background. Indeed the first and the second eigenvectors have the piecewise constant form (Fig. 6.4b,c) and when K-means spectral algorithm is initiated

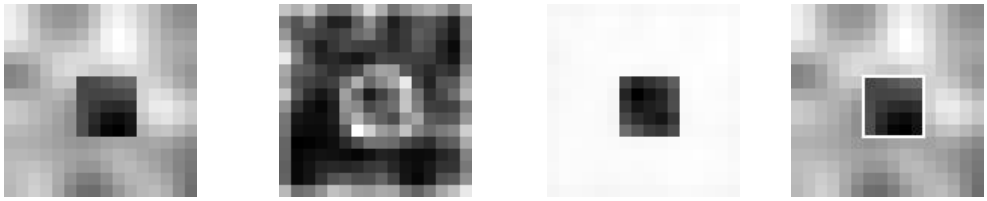

(a) Occluder Data (b) Eigenvector 1 (c) Eigenvector 2 (d) $K = 2$

Figure 6.4: K-means spectral clustering on well separated clusters. The first eigenvector is roughly constant while the second eigenvector is clearly piecewise constant. Initializing the K-Means procedure with K set to 2 partitions the image into foreground and background regions.

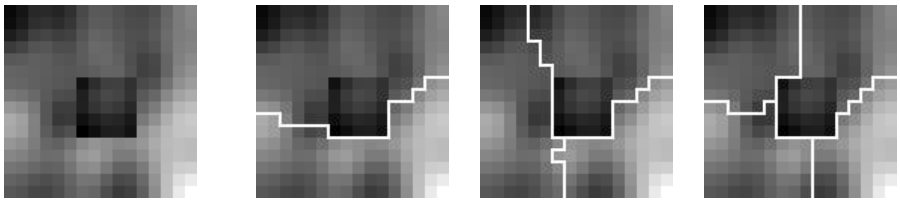

(a) Occluder Data (b) $K = 2$ (c) $K = 3$ (d) $K = 4$

Figure 6.5: K-means spectral clustering on weakly separated clusters with several different initializations for K. The occluder data is weakly coupled because the boundary between the foreground occluder and the background texture is not always distinguishable.

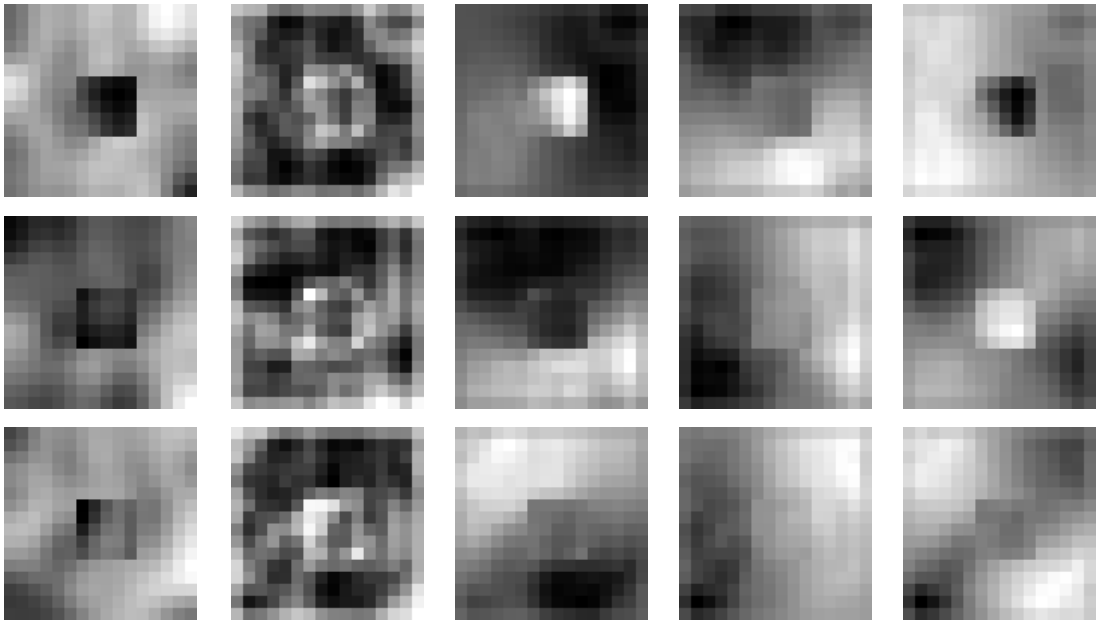

Occluder Data Eigenvector 1 Eigenvector 2 Eigenvector 3 Eigenvector 4

Figure 6.6: Eigenvectors piecewise constant? Compare with Fig. 6.4b,c.

to search for 2 clusters, it finds the right partition (Fig. 6.4d).

In comparison, for a weakly coupled dataset shown in Fig. 6.5 a variety of initializations for K-means spectral clustering fail to separate the occluder from the background. Comparing figures 6.6 and 6.4, we can see that the eigenvectors in Fig. 6.6 do not appear to be piecewise constant. Obviously, lack of piecewise constancy is affecting the performance of the K-means spectral algorithm.

Chapter 7

EigenCuts: A Spectral Clustering Algorithm

7.1 Introduction

In the previous chapter we investigated the form of the leading eigenvectors of the stochastic matrix. Using some simple image segmentation examples we confirmed that the leading eigenvectors are roughly piecewise constant when the clusters are well separated. However, we observed that for several segmentation problems that we wish to solve, the coupling between the clusters is significantly stronger and, as a result, the piecewise constant approximation breaks down.

Unlike the piecewise constant approximation, a perfectly general view that we introduce in this chapter is that the eigenvectors of the Markov transition matrix determine particular flows of probability along the edges in the graph. We refer to these as *eigenflows* and characterize the rate of decay of these flows in terms of their *half-lives*.

We show that from the perspective of eigenflows, a graph representing a set of weakly coupled clusters produces eigenflows between the various clusters which decay with long half-lives. In contrast, the eigenflows within each cluster decay much more rapidly. In

order to identify clusters we therefore consider the eigenflows with long half-lives.

Given such a slowly decaying eigenflow, we identify particular bottleneck regions in the graph which critically restrict the flow (cf. [110]). To identify these bottlenecks we propose computing the sensitivity of the flow's half-life with respect to perturbations in the edge weights. Intuitively, this sensitivity arises because the flow across a bottleneck will have fewer alternative routes to take and therefore will be particularly sensitive to changes in the edge weights within the bottleneck. In comparison, the flow between two vertices in a strongly coupled cluster will have many alternative routes and therefore will not be particularly sensitive on the precise weight of any single edge.

We introduce a simple spectral graph partitioning algorithm, called EIGENCUTS, which is based on these ideas. We first compute the eigenvectors for the Markov transition matrix, and select those with long half-lives. For each such eigenvector, we identify bottlenecks by computing the sensitivity of the flow's half-life with respect to perturbations in the edge weights. We then cut edges within the bottleneck for each eigenvector, simultaneously enforcing a step of non-maximal suppression. The algorithm then recomputes the eigenvectors and eigenvalues for the modified graph, and continues this iterative process until no further edges are cut.

7.2 From Affinities to Markov Chains

7.2.1 Notation and basic parameters

For the sake of continuity, we reintroduce the notation for graph partitioning. Following the formulation in [72], we consider an undirected graph G with vertices v_i, for $i = 1, \ldots, n$, and edges $e_{i,j}$ with non-negative weights $a_{i,j}$. Here the weight $a_{i,j}$ represents the affinity of vertices v_i and v_j. The edge affinities are assumed to be symmetric, that is, $a_{i,j} = a_{j,i}$. In matrix notation the affinities are represented by a symmetric $n \times n$ matrix

A with elements $a_{i,j}$. The degree of a node j is defined as:

$$d_j = \sum_{i=1}^{n} a_{i,j} = \sum_{i=1}^{n} a_{j,i}. \tag{7.1}$$

We will use $\vec{d}$ for the vector of degrees:

$$\vec{d} = (d_1, \ldots, d_n). \tag{7.2}$$

In matrix notation the degree vector $\vec{d}$ is obtained by

$$\vec{d} = A\mathbf{1}, \tag{7.3}$$

where $\mathbf{1}$ is a column vector of all ones. We represent D for a diagonal matrix of degrees:

$$D = \text{diag}(d_1, \ldots, d_n) = \text{diag}(\vec{d}). \tag{7.4}$$

7.2.2 Markov Chain

A Markov chain is defined using these affinities by setting the transition probability $m_{i,j}$ from vertex v_j to vertex v_i to be proportional to the edge affinity, $a_{i,j}$. That is, $m_{i,j} = d_j^{-1} a_{i,j}$ where d_j gives the normalizing factor which ensures $\sum_{i=1}^{n} m_{i,j} = 1$. In matrix notation, the affinities are represented by a symmetric $n \times n$ matrix A, with elements $a_{i,j}$, and the transition probability matrix $M = \{m_{i,j}\}$ is given by:

$$M = AD^{-1}, \tag{7.5}$$

where the columns of M sum to 1. While the affinity matrix A is symmetric, the Markov matrix M is not necessarily symmetric. Also, note that while the underlying graph G is weighted and undirected, the graph induced by M, say G_{M}, is weighted but directed. In particular, if in G there is a path between any pair of nodes i and j, then in G_{M} there will be a path from $i \to j$ and another path from $j \to i$. Also, if G is *connected*, that is there is a path between every pair of nodes, then the corresponding graph G_{M} is *strongly*

connected. A strongly connected graph is also called *irreducible* and these notions will be used to explore the eigen properties of the Markov matrix.

The transition probability matrix M defines the random walk of a particle on the graph G. Suppose the initial probability of the particle being at vertex v_j is p_j^0, for $j = 1, \ldots, n$. Then, the probability of the particle being initially at vertex v_j and taking edge $e_{i,j}$ is $m_{i,j}p_j^0$. In matrix notation, the probability of the particle ending up any of the vertices $\vec{v} = (v_1, v_2, \cdots, v_n)$ after one step is given by the distribution $\vec{p}^1 = M\vec{p}^0$, where $\vec{p}^k = (p_1^k, \ldots, p_n^k)$. Clearly this process can be iterated, so after β steps we have

$$\vec{p}^\beta = M^\beta \vec{p}^0, \tag{7.6}$$

For analysis it is convenient to consider the normalized affinity matrix L given by,

$$L = D^{-1/2} M D^{1/2}. \tag{7.7}$$

Observe L is *similar* to M and therefore matrix L has the same spectrum as M. Also, by relating L to the affinity matrix A as shown below, it is easy to see that L is symmetric:

$$\begin{aligned} L &= D^{-1/2} M D^{1/2}, \\ &= D^{-1/2} A D^{-1} D^{1/2}, \\ &= D^{-1/2} A D^{-1/2}. \end{aligned}$$

The advantage of considering the matrix L over M is that the symmetric eigenvalue problem is more stable to small perturbations, and is computationally much more tractable. Since the matrix L is symmetric it has an orthogonal decomposition of the form:

$$L = U \Lambda U^T, \tag{7.8}$$

where $U = [\vec{u}_1, \vec{u}_2, \cdots, \vec{u}_n]$ are the eigenvectors and Λ is a diagonal matrix of eigenvalues $[\lambda_1, \lambda_2, \cdots, \lambda_n]$ sorted in decreasing order. While the eigenvectors have unit length, $\|\vec{u}_k\| = 1$, the eigenvalues are real and have an absolute value bounded by 1, $|\lambda_k| \leq 1$.

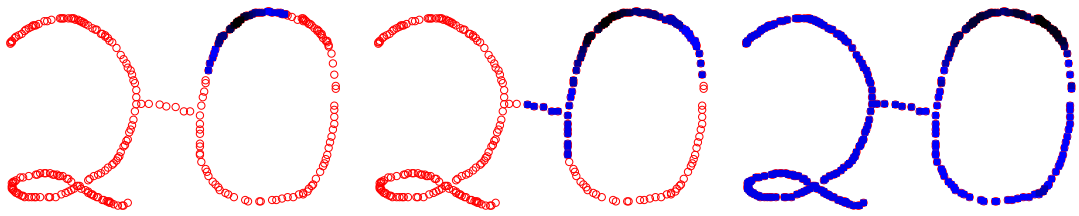

$\beta = 10$ $\beta = 100$ $\beta = 1000$

Figure 7.1: Markov chain propagation on a point dataset distributed in the shape of numerals 2 and 0 connected by a bridge. Affinity between points i and j is proportional to $e^{-\frac{s_{i,j}^2}{2\sigma^2}}$, where $s_{i,j}$ is the Euclidean distance between the two points. Initial distribution $\vec{p}^0$ evolves to $\vec{p}^\beta = M^\beta \vec{p}^0$ after β iterations. The probability mass is shown in shades of blue: the darker the hue, the higher is the probability. The figures each correspond to a different β value: 10, 100 and 1000 respectively.

We will return shortly to characterize the first eigenvector and show why the eigenvalues are bounded by 1. Because L and M are similar we can perform an eigendecomposition of the Markov transition matrix as:

$$\begin{aligned} M &= D^{1/2} L D^{-1/2}, \\ &= \underbrace{D^{1/2} U}\ \Lambda\ \underbrace{U^T D^{-1/2}}. \end{aligned} \tag{7.9}$$

Thus an eigenvector $\vec{u}$ of L corresponds to an eigenvector $D^{1/2}\vec{u}$ of M with the same eigenvalue λ.

7.2.3 Markov Chain Propagation

The eigenvector representation provides a simple way to capture the Markovian relaxation process described by Eq. 7.6. For example, consider propagating the Markov chain for β iterations as shown in Fig. 7.1. The transition matrix after β iterations, namely M^β,

can be represented as:

$$M^\beta = D^{1/2} U \Lambda^\beta U^T D^{-1/2}. \tag{7.10}$$

Therefore the probability distribution for the particle being at vertex v_i after β steps of the random walk, given that the initial probability distribution was $\vec{p}^0$, is

$$\vec{p}^\beta = D^{1/2} U \Lambda^\beta \vec{r}^0, \tag{7.11}$$

where $\vec{r}^0 = U^T D^{-1/2} \vec{p}^0$ provides the expansion coefficients of the initial distribution $\vec{p}^0$ in terms of the eigenvectors of M.

In Fig. 7.1 we show the results from propagating a random walk on a point cloud, which is in the shape of numerals 2 and 0 coupled by a bridge. The dataset is first converted into a weighted undirected graph. The weights are designed to fall off rapidly as a function of the Euclidean distance between points. For each data point the distances are computed only within a small neighborhood. Then, a Markov transition matrix is computed before initializing a random walk with a unit probability mass on a random data point. In Fig. 7.1 shown in shades of blue is the evolution of the probability distribution of the random walk under the operation of M for several different values of β; darker the hue, higher is the probability mass of the random walk at the datapoint. After a large number of iterations, the random walk achieves a stationary distribution. Because the graph is assumed to be connected, the stationary distribution will be the same regardless of the starting point.

In the next section, we see that the stationary distribution has an analytical form. With the stationary distribution known it becomes convenient to interpret the Markovian relaxation process as *perturbations* to the stationary distribution [65].

7.2.4 Perturbations to the Stationary Distribution

All weighted, connected, undirected graphs have a stationary distribution $\vec{\pi}$ given by:

$$\vec{\pi} = \frac{\vec{d}}{\sum_{i=1}^n d_i}, \tag{7.12}$$

where d_i denotes the degree of node i, as defined in Eq. 7.1. Stationary distributions satisfy the property

$$M\vec{\pi} = \vec{\pi},$$

and this can be verified by a simple substitution:

$$\begin{aligned} M\vec{\pi} &= AD^{-1}\vec{\pi}, \\ &= A\left(\text{diag}(\vec{d})\right)^{-1}\frac{\vec{d}}{\sum_{i=1}^{n} d_i}, \\ &= A\frac{\mathbf{1}}{\sum_{i=1}^{n} d_i}, \\ &= \frac{\vec{d}}{\sum_{i=1}^{n} d_i}, \\ &= \vec{\pi}. \end{aligned}$$

Here we have used the fact that $M = AD^{-1}$, $\mathbf{1}$ is a vector of all 1's and $A\mathbf{1} = \vec{d}$.

There are two questions worth asking about the stationary distribution $\vec{\pi}$. While the distributions $\vec{p}^0, \vec{p}^1, \ldots, \vec{p}^\beta$ are different in general, do they converge to $\vec{\pi}$ as $\beta \to \infty$? It can be shown that for bipartite graphs the stationary distribution will never be reached starting at a general $\vec{p}^0$. But the graphs we are interested in are not bipartite. Is the stationary distribution unique? Again, for undirected graphs it can be shown that the stationary distribution is indeed unique. While the graphs we are interested in are weighted and undirected, they need not be connected. So if the graph can be partitioned into disconnected (non bipartite) components, then there will be a unique, separate stationary distribution associated with each connected component.

We now explore the eigenvalue connection to the stationary distribution. Since $M\vec{\pi} = \vec{\pi}$, we have $\vec{\pi}$ as an eigenvector of M with an eigenvalue 1. Therefore by Eq. 7.7, there is an eigenvector $\vec{u}$ for L given by

$$\vec{u} = \kappa D^{-1/2}\vec{\pi},$$

with an eigenvalue 1 and $\kappa > 0$ is a constant set by enforcing $\vec{u}^T\vec{u} = 1$. Since this eigenvector is positive and has an eigenvalue of 1, it follows from Perron-Frobenius theorem

(see Ch.8 in [73]) for non-negative matrix L, for which the underlying graph is assumed to be connected and non-bipartite, the leading eigenvector $\vec{u}_1$ is indeed the vector $\vec{u}$ and the leading eigenvalue is 1. Also, the remaining eigenvalues are bounded by

$$\lambda_1 = 1 > \lambda_2 \geq \lambda_3 \cdots \lambda_n > -1.$$

It also follows that the Markov chain iterated β times would give:

$$\begin{aligned}
M^\beta &= D^{1/2} U \Lambda^\beta U^T D^{-1/2}, \\
&= D^{1/2} \vec{u}_1 \vec{u}_1^T D^{-1/2} + \sum_{k=2}^{n} \lambda_k^\beta D^{1/2} \vec{u}_k \vec{u}_k^T D^{-1/2}, \\
&= D^{1/2} \frac{\sqrt{\vec{d}}}{\left(\sum_{i=1}^n d_i\right)^{1/2}} \frac{\sqrt{\vec{d}}^T}{\left(\sum_{i=1}^n d_i\right)^{1/2}} D^{-1/2} + \sum_{k=2}^{n} \lambda_k^\beta D^{1/2} \vec{u}_k \vec{u}_k^T D^{-1/2}, \\
&= \frac{\vec{d}}{\left(\sum_{i=1}^n d_i\right)^{1/2}} \frac{\mathbf{1}^T}{\left(\sum_{i=1}^n d_i\right)^{1/2}} + \sum_{k=2}^{n} \lambda_k^\beta D^{1/2} \vec{u}_k \vec{u}_k^T D^{-1/2}, \\
&= \frac{\vec{d}}{\sum_{i=1}^n d_i} \mathbf{1}^T + \sum_{k=2}^{n} \lambda_k^\beta D^{1/2} \vec{u}_k \vec{u}_k^T D^{-1/2}, \\
&= \vec{\pi} \mathbf{1}^T + \sum_{k=2}^{n} \lambda_k^\beta D^{1/2} \vec{u}_k \vec{u}_k^T D^{-1/2}. \qquad (7.13)
\end{aligned}$$

Because $|\lambda_k| < 1$ for $k = 2, \ldots, n$, as $\beta \to \infty$ the Markov chain approaches a unique stationary distribution $\vec{\pi}$:

$$M^\infty = \vec{\pi} \mathbf{1}^T. \qquad (7.14)$$

Hence it is convenient to interpret the Markovian relaxation process as *perturbations* to the stationary distribution:

$$\begin{aligned}
\vec{p}^\beta &= M^\beta \vec{p}^0, \\
&= \vec{\pi} \mathbf{1}^T \vec{p}^0 + \sum_{k=2}^{n} \lambda_k^\beta D^{1/2} \vec{u}_k \vec{u}_k^T D^{-1/2} \vec{p}^0, \\
&= \vec{\pi} + \sum_{k=2}^{n} \lambda_k^\beta D^{1/2} \vec{u}_k \vec{u}_k^T D^{-1/2} \vec{p}^0, \qquad (7.15) \\
&= \vec{\pi} + \sum_{k=2}^{n} r_k \lambda_k^\beta \vec{q}_k, \qquad (7.16)
\end{aligned}$$

where $\lambda_1 = 1$ is associated with the stationary distribution $\vec{\pi}$, $\vec{q}_k$ are the eigenvectors of the transition matrix M given by $\vec{q}_k = D^{1/2}\vec{u}_k$ and r_k are the expansion coefficients of the initial distribution in terms of the eigenvectors $\vec{u}_k$: $r_k = \vec{u}_k^T D^{-1/2}\vec{p}^0$.

If we relax the assumption of the graph G being connected, that is, there are multiple connected components in G, then we have to allow for a multiplicity of eigenvalues at 1, that is $|\lambda_k| \leq 1$. For every λ_k that is 1, there is a distinct stationary distribution $\vec{\pi}_k$ associated with one connected component in the graph. The perturbation argument presented above is then applicable to each distinct connected component. Next, we explore the fact that the eigenvectors of the Markov transition matrix determine particular flows of probability along the edges in the graph, which we refer to as *eigenflows*.

7.3 EigenFlows and Perturbation Analysis

7.3.1 EigenFlows

Let $\vec{p}^0$ be an initial probability distribution for a random particle to be at the vertices of the graph G. By the definition of the Markov chain, recall that the probability of making the transition from vertex v_j to v_i is the probability of starting in vertex v_j, times the conditional probability of taking edge $e_{i,j}$ given that the particle is at vertex v_j, namely $m_{i,j}p_j^0$. Similarly, the probability of making the transition in the reverse direction is $m_{j,i}p_i^0$. The net flow of probability mass along edge $e_{i,j}$ from v_j to v_i is therefore the difference $m_{i,j}p_j^0 - m_{j,i}p_i^0$. It then follows that the net flow of probability mass from vertex v_j to v_i is given by $F_{i,j}(\vec{p}^0)$, where $F_{i,j}(\vec{p}^0)$ is the (i,j)-element of the $n \times n$ matrix

$$F(\vec{p}^0) = M\text{diag}(\vec{p}^0) - \text{diag}(\vec{p}^0)M^T. \tag{7.17}$$

Notice that $F = E - E^T$ for $E = M\text{diag}(\vec{p}^0)$, and therefore F is antisymmetric (i.e. $F^T = -F$). This expresses the fact that the flow $F_{j,i}$ from v_i to v_j is just the opposite sign of the flow in the reverse direction. Furthermore, it can be shown that for a connected

component in the graph with a stationary distribution $\vec{\pi}$ the net probability flow is zero:

$$\begin{aligned} F(\vec{\pi}) &= M\text{diag}(\vec{\pi}) - \text{diag}(\vec{\pi})M^T, \\ &= AD^{-1}\text{diag}\left(\frac{\vec{d}}{\sum_{k=1}^n d_k}\right) - \text{diag}\left(\frac{\vec{d}}{\sum_{k=1}^n d_k}\right)D^{-1}A^T, \\ &= \frac{A}{(\sum_{k=1}^n d_k)} - \frac{A^T}{(\sum_{k=1}^n d_k)}, \\ &= 0. \end{aligned}$$

Therefore, in the perturbations to the stationary distribution, as given by Eq. 7.16 and reproduced below for convenience,

$$\vec{p}^{\,\beta} = \vec{\pi} + \sum_{k=2}^{n} r_k \lambda_k^\beta \vec{q}_k,$$

nonzero flow is caused by the eigenvectors $\vec{q}_k$ of the transition matrix M given by $\vec{q}_k = D^{1/2}\vec{u}_k$ with $\lambda_k \neq 1$. Here, r_k is the expansion coefficient of the initial distribution in terms of the $\vec{u}_k$ eigenvector: $r_k = \vec{u}_k^T D^{-1/2}\vec{p}^{\,0}$. Given the fact that the nonzero flow in $F(\vec{p}^{\,\beta})$ is caused by the terms $r_k\lambda_k^\beta F(\vec{q}_k)$, we call $F(\vec{q}_k)$ the *eigenflows*.

In Figure 7.2 we plot several different eigenvectors $\vec{q}_k$ of the matrix M along with their eigenflows, $F(\vec{q}_k)$. As discussed earlier, the eigenmodes are in general not piecewise constant. For all but the stationary distribution, it is clear from Figure 7.2 that there is a significant net flow between neighbours, especially in regions where the magnitude of the spatial gradient of the eigenmode is larger. We will return to this gradient idea in the following section. For now, consider the rate of decay of these eigenflows $F(\vec{q}_k)$. While λ_k specifies the flow's overall rate of decay, we find it more convenient to use the flow's *half-life* β_k, which is simply defined by $|\lambda_k|^{\beta_k} = 1/2$. Here β_k is the number of Markov chain steps needed to reduce the particular eigenflow $F(\vec{q}_k)$ to half its initial value.

From the perspective of eigenflows, a graph representing a set of weakly coupled clusters produces eigenflows between the various clusters which decay with long half-lives. In contrast, the eigenflows within each cluster decay much more rapidly. In order

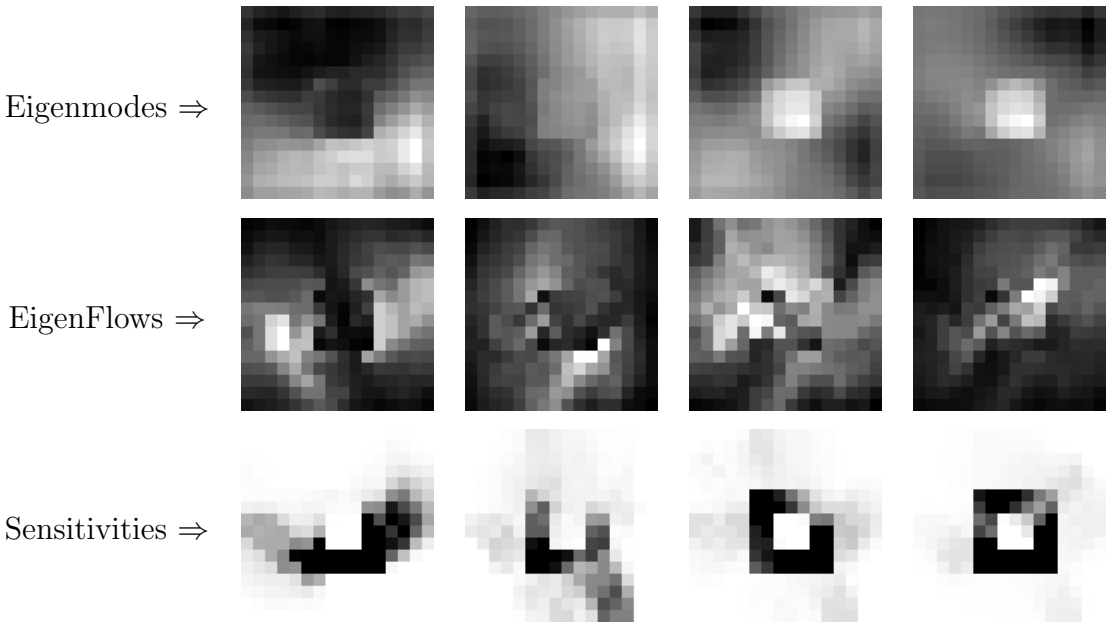

Figure 7.2: (TOP) Eigenmodes of the Markov matrix generated for Fig. 7.4b shown in order, from second to the fifth, and (MIDDLE) the corresponding eigenflows. The eigenflow depicted by a gray value at pixel (or vertex) v_j corresponds to $F_{i,j}$ where $i = \text{argmax}_i |F_{i,j}|$. Because the eigenflow of the stationary distribution is zero, this vector is not displayed here. (BOTTOM) Half-life sensitivities. Gray value at each pixel corresponds to the maximum of the absolute sensitivities obtained by perturbing the weights on the edges connected from each pixel to all of its neighbours (not including itself). Dark pixels indicate high absolute sensitivities.

to identify clusters we therefore consider the eigenflows with long half-lives. Given such a slowly decaying eigenflow, we have to identify particular bottleneck regions in the graph which critically restrict the flow (cf. [110]). To identify these bottlenecks we propose computing the sensitivity of the flow's half-life with respect to perturbations in the edge weights.

7.3.2 Perturbation Analysis

As just discussed, we seek to identify bottlenecks in the eigenflows associated with long half-lives. This notion of identifying bottlenecks is similar to the well-known max-flow, min-cut theorem. In particular, for a graph whose edge weights represent maximum flow capacities between pairs of vertices, the bottleneck edges can be identified as precisely those edges across which the maximum flow is equal to their maximum capacity. For the graphs we consider the capacities are indeed given by the single-step transition probabilities, but the flow we use is a conditional probability which is maximal only in the extreme cases for which the initial probability of being at one of the edge's endpoints is equal to one, and zero at the other endpoint. Thus the max-flow criterion is not directly applicable here.

Instead, we show that the desired bottleneck edges can be conveniently identified by considering the sensitivity of the flow's half-life to perturbations of the edge weights (see Fig. 7.2). Intuitively, this sensitivity arises because the flow across a bottleneck will have fewer alternative routes to take and therefore will be particularly sensitive to changes in the edge weights within the bottleneck. In comparison, the flow between two vertices in a strongly coupled cluster will have many alternative routes and therefore will not be particularly sensitive on the precise weight of any single edge.

In order to pick out larger half-lives, we will use one parameter, β_0, which is a rough estimate of the smallest half-life that one wishes to consider. Since we are interested in perturbations which *significantly* change the current half-life of a mode, we choose to use a logarithmic scale in half-life. A simple choice for a function that combines these two effects is:

$$H(\beta;\beta_0) = \log(\beta + \beta_0), \tag{7.18}$$

where β is the half-life of the current eigenmode.

Suppose we have an eigenvector $\vec{u}$ of L, with eigenvalue λ, such that $L\vec{u} = \lambda\vec{u}$, where

L is the modified affinity matrix (see Eq. 7.8). This eigenvector decays with a half-life of

$$\beta = -\log(2)/\log(\lambda). \tag{7.19}$$

Consider the effect on $H(\beta;\beta_0)$ of perturbing the affinity $a_{i,j}$, for the (i,j)-edge, to $a_{i,j}+\alpha_{i,j}$. Define the sensitivity with respect to weight $a_{i,j}$ as

$$S_{i,j} \equiv \frac{\partial H(\beta;\beta_0)}{\partial \alpha_{i,j}}. \tag{7.20}$$

It follows from Eq. 7.19 that

$$\frac{\partial \log(\beta+\beta_0)}{\partial \alpha_{i,j}} = \frac{\log(2)}{\lambda \log(\lambda)\log(\lambda^{\beta_0}/2)}\frac{\partial \lambda}{\partial \alpha_{i,j}}. \tag{7.21}$$

The previous equation requires that we compute $\frac{\partial \lambda}{\partial \alpha_{i,j}}$. To do this we differentiate

$$L\vec{u} = \lambda \vec{u},$$

with respect to $\alpha_{i,j}$ to obtain

$$\frac{\partial L}{\partial \alpha_{i,j}}\vec{u} + L\frac{\partial \vec{u}}{\partial \alpha_{i,j}} = \frac{\partial \lambda}{\partial \alpha_{i,j}}\vec{u} + \lambda\frac{\partial \vec{u}}{\partial \alpha_{i,j}}. \tag{7.22}$$

We can evaluate this at $\alpha_{i,j}=0$. Because $\vec{u}$ is a unit vector, it is also a point on an n-dimensional hypersphere. Small perturbations of the direction vector $\vec{u}$ amount to computing a direction that is tangent to the sphere and hence orthogonal to $\vec{u}$. Thus the product:

$$\vec{u}^T\frac{\partial \vec{u}}{\partial \alpha_{i,j}} = 0,$$

holds true. Alternatively, differentiating $\vec{u}^T\vec{u}=1$ with respect to $\alpha_{i,j}$ gives the same result. To use this fact we multiply both sides of the Eq. 7.22 by $\vec{u}^T$:

$$\begin{aligned}
\vec{u}^T\frac{\partial L}{\partial \alpha_{i,j}}\vec{u} + \vec{u}^T L\frac{\partial \vec{u}}{\partial \alpha_{i,j}} &= \vec{u}^T\frac{\partial \lambda}{\partial \alpha_{i,j}}\vec{u} + \vec{u}^T\lambda\frac{\partial \vec{u}}{\partial \alpha_{i,j}}, \\
&= \frac{\partial \lambda}{\partial \alpha_{i,j}}\vec{u}^T\vec{u} + \lambda\vec{u}^T\frac{\partial \vec{u}}{\partial \alpha_{i,j}}, \\
&= \frac{\partial \lambda}{\partial \alpha_{i,j}}
\end{aligned}$$

Finally, using the fact that $\vec{u}^T L = \lambda \vec{u}^T$ gives

$$\begin{aligned}\vec{u}^T L \frac{\partial \vec{u}}{\partial \alpha_{i,j}} &= \lambda \vec{u}^T \frac{\partial \vec{u}}{\partial \alpha_{i,j}}, \\ &= 0.\end{aligned}$$

Hence the effect on λ of perturbing the affinity is:

$$\frac{\partial \lambda}{\partial \alpha_{i,j}} = \vec{u}^T \frac{\partial L}{\partial \alpha_{i,j}} \vec{u}. \tag{7.23}$$

As $L = D^{-1/2} A D^{-1/2}$ and D is given by Eqs. 7.3,7.4, we can write for all $i \neq j$:

$$\frac{\partial L}{\partial \alpha_{i,j}} = D^{-1/2}\big[Z_{ij} + Z_{ji}\big] D^{-1/2} - PAD^{-1/2} - D^{-1/2} AP, \tag{7.24}$$

where Z_{gh} is a matrix of all zeros except for a value of 1 at location (g, h); (d_i, d_j) are degrees of the nodes i and j (stacked as elements on the diagonal matrix D, see Sec 7.2.1); and

$$P = \big[\frac{d_i^{-3/2}}{2} Z_{ii} + \frac{d_j^{-3/2}}{2} Z_{jj}\big]$$

having non-zero entries only on the diagonal. Susbtituiting the expression in Eq. 7.23, we get

$$\begin{aligned}\vec{u}^T \frac{\partial L}{\partial \alpha_{i,j}} \vec{u} = \vec{u}^T D^{-1/2}\big[Z_{ij} + Z_{ji}\big] D^{-1/2} \vec{u} - \vec{u}^T P D^{1/2}\big[D^{-1/2} A D^{-1/2}\big]\vec{u} \\ - \vec{u}^T\big[D^{-1/2} A D^{-1/2}\big] D^{1/2} P \vec{u}.\end{aligned} \tag{7.25}$$

Using the fact that $D^{-1/2} A D^{-1/2} \vec{u} = L\vec{u} = \lambda \vec{u}$, $\vec{u}^T L = \lambda \vec{u}^T$ and $D^{1/2} P = P D^{1/2}$ as both P and D are diagonal, the above equation reduces to:

$$\begin{aligned}\vec{u}^T \frac{\partial L}{\partial \alpha_{i,j}} \vec{u} &= \vec{u}^T D^{-1/2}\big[Z_{ij} + Z_{ji}\big] D^{-1/2} \vec{u} - 2\lambda \vec{u}^T P D^{1/2} \vec{u} \\ &= \vec{u}^T D^{-1/2}\big[Z_{ij} + Z_{ji}\big] D^{-1/2} \vec{u} - \lambda \vec{u}^T\big[d_i^{-1} Z_{ii} + d_j^{-1} Z_{jj}\big]\vec{u}.\end{aligned} \tag{7.26}$$

Hence the derivative of $H(\beta(\alpha_{i,j}))$ with respect to $\alpha_{i,j}$, evaluated at $\alpha_{i,j} = 0$, satisfies

$$S_{i,j} \equiv \frac{\partial \log(\beta + \beta_0)}{\partial \alpha_{i,j}} = \frac{1}{\big[\beta_0 \log(\lambda) - \log(2)\big]} \frac{\log(2)}{\lambda \log(\lambda)} \times \ldots$$
$$\vec{u}^T \Big[D^{-1/2} \big[Z_{ij} + Z_{ji} \big] D^{-1/2} - \lambda \big[d_i^{-1} Z_{ii} + d_j^{-1} Z_{jj} \big] \Big] \vec{u}. \qquad (7.27)$$

Here Z_{ij} is the matrix with 1 for the (i, j) element, and zeros everywhere else. A scalar form of the perturbation equation reveals some structure:

$$S_{i,j} = \frac{\log(2)}{\lambda \log(\lambda) \log(\lambda^{\beta_0}/2)} \left[-\left(\frac{u_i}{\sqrt{d_i}} - \frac{u_j}{\sqrt{d_j}} \right)^2 + (1 - \lambda) \left(\frac{u_i^2}{d_i} + \frac{u_j^2}{d_j} \right) \right], \qquad (7.28)$$

where (u_i, u_j) are the (i, j) elements of eigenvector $\vec{u}$ and (d_i, d_j) are degrees of nodes (i, j). In particular, the perturbation expression is partly influenced by the difference between the values of the normalized eigenvector $D^{-1/2}\vec{u}$ at vertices v_i and v_j. A similar observation was made with eigenflows, in the previous section, where significant net flow occurs between neighbors especially in regions where the magnitude of the spatial gradient of the eigenmode is large (see Fig. 7.2).

What do half-life sensitivities reveal? In particular, do these sensitivities exhibit a structure that can be used to identify the bottlenecks? We discuss these issues next.

7.3.3 What do half-life sensitivities reveal?

In Figure 7.2, we plot the maximum of the absolute sensitivities obtained by perturbing the weights on the edges connected from each pixel to all of its neighbours (not including itself), as in Eq. 7.28. Note that the sensitivities are large in the bottlenecks at the border of the foreground and background, especially where the values of the eigenvector differ significantly on either side of the border.

In Fig. 7.3 we plot a histogram of half-life sensitivities resulting from images, each of size $N \times N$, formed by Gaussian smoothing of i.i.d noise. The affinities are computed as in Eq. 6.1. The affinity matrix is then normalized so that the median value for the degree d_i of any node i in the underlying graph is 1 (see Sec. 7.4 for more discussion).

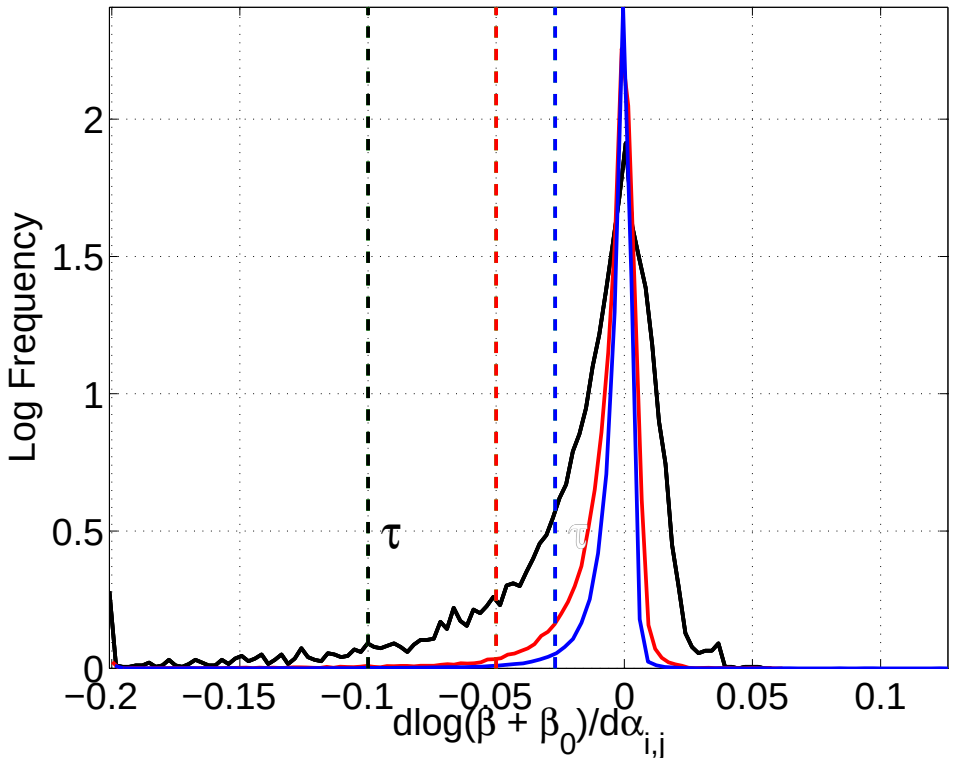

Figure 7.3: What do half-life sensitivities reveal? We analyze half-life sensitivities resulting from images (of size $N \times N$) formed by Gaussian smoothing of i.i.d noise. The affinities are computed as in Eq. 6.1. The affinity matrix is then normalized so that the median value for the degree d_i of any node i in the underlying graph is 1 (see Sec. 7.4 for more discussion). For computing half-life sensitivities, $S_{i,j}$, only those eigenvectors of the Markov transition matrix that have half-lives above a certain threshold ($> \epsilon\beta_0$) are used. We chose $\beta_0 = 40$ and $\epsilon = 1/4$. The three curves show histograms of half-life sensitivities for three different image sizes: $N = 16$ (black), 32 (red) and 48 (blue). Sensitivities were clamped to have a minimum value of -0.2. Observe that the tails are long on the negative side in the graphs, which indicates that by decreasing affinity $a_{i,j}$ the half-life β will increase relative to β_0. We turn this observation into an algorithm for clustering by cutting a link $a_{i,j} \to 0$ whenever $S_{i,j} < \tau$. The threshold $\tau < 0$ is chosen by inspection, so that relatively few edges are cut in such examples. A suitable τ is drawn as a dashed vertical line for each of the image sizes: $N = 16$ (black), 32 (red) and 48 (blue).

For computing half-life sensitivities $S_{i,j}$ only those eigenvectors of the Markov transition matrix that have half-lives above a certain threshold ($> \epsilon\beta_0$) are used. We chose $\beta_0 = 40$ and $\epsilon = 1/4$. The three curves show histograms of half-life sensitivities for three different image sizes: $N = 16$ (black), 32 (red) and 48 (blue). Sensitivities were ceiled to have a minimum value of -0.2.

It is clear that for many links the perturbation results in values around zero and hence they can be considered stable. However, observe that the graphs have long tails on the negative side, which means decreasing the affinities that are non-negative, we can increase the half-life. To reiterate, tightly coupled clusters have eigenflows with long half-lives and if by decreasing the affinities we can increase the half-life then we are a step closer to partitioning the graph. How much can the affinities be decreased? As the minimum value for affinities is zero, we select a threshold $\tau < 0$ (drawn as vertical dashed lines in Fig. 7.3) to sever all those links with sensitivities $\frac{d\log(\beta+\beta_0)}{d\alpha_{i,j}}$ that are less than τ. We next show how to turn this intuition into a clustering algorithm, which we call EIGENCUTS.

7.4 EigenCuts: A Basic Clustering Algorithm

We select a simple clustering algorithm to test our proposal of using the derivative of the eigenmode's half-life for identifying bottleneck edges. Given a value of β_0, which is roughly the minimum half-life to consider for any eigenmode, we iterate on the following steps:

1. Form the symmetric $n \times n$ affinity matrix A, and initialize $A^c = A$.

2. Set D to be a diagonal $n \times n$ matrix with $D_{i,i} = \sum_{j=1}^{n} A^c_{i,j}$, and set a scale factor δ to be the median of $D_{i,i}$ for $i = 1, \ldots, n$. Form the symmetric matrix $L^c = D^{-1/2} A^c D^{-1/2}$.

3. Compute eigenvectors $[\vec{u}_1, \vec{u}_2, \cdots, \vec{u}_n]$ of L^c, with eigenvalues $|\lambda_1| \geq |\lambda_2| \ldots \geq |\lambda_n|$.

4. For each eigenvector $\vec{u}_k$ of L^c with half-life $\beta_k > \epsilon\beta_0$, compute the half-life sensitivities, $S^k_{i,j} = \frac{d\log(\beta_k+\beta_0)}{d\alpha_{i,j}}$ for each edge in the graph using Eq. 7.28. Here we use $\epsilon = 1/4$.

5. Do non-maximal suppression within each of the computed sensitivities. That is, suppress the sensitivity $S^k_{i,j}$ if there is a strictly more negative value $S^k_{m,j}$ or $S^k_{i,n}$ for some vertex v_m in the neighbourhood of v_j, or some v_n in the neighbourhood of v_i.

6. Cut all edges (i,j) in A^c (i.e. set their affinities to 0) for which $S^k_{i,j} < \tau/\delta$ and for which this sensitivity was not suppressed during non-maximal suppression. The weights of the links that are cut, are moved into the diagonal of the affinity matrix A^c, i.e., before setting $a_{i,j} \to 0$ we do $a_{i,i} \leftarrow a_{i,i} + a_{j,i}; a_{j,j} \leftarrow a_{j,j} + a_{i,j}$ and then set $a_{i,j} \to 0; a_{j,i} \to 0$.

7. If any new edges have been cut, go to 2. Otherwise stop.

Here steps $1-3$ are as described previously, other than computing the scaling constant δ, which is used in step 6 to provide a scale invariant (i.e. invariant with respect to rescaling A to νA for some $\nu > 0$) threshold on the computed sensitivities. We chose to perform a scale-invariant sensitivity analysis because for many applications the edge weights on the underlying graphs need not correspond to probabilities. In fact, the affinities can take on arbitrary values and may not be confined to the range $[0, 1]$. To tackle such problems, we scale the affinities $a_{i,j}$ by an adaptive constant δ determined in each iteration of the algorithm. This gives rise to a new value $b_{i,j}$, where $b_{i,j} = a_{i,j}/\delta$. What we would like then is to apply a threshold on the sensitivity $\frac{d\log(\beta+\beta_0)}{db_{i,j}}$. Instead, what we have computed is the sensitivity $\frac{d\log(\beta+\beta_0)}{da_{i,j}}$. It is easy to show that checking $\frac{d\log(\beta+\beta_0)}{db_{i,j}} < \tau$ is the same thing as confirming $\frac{d\log(\beta+\beta_0)}{da_{i,j}} < \tau/\delta$, as is done in step 6.

In step 4 we only consider eigenmodes with half-lives larger than $\epsilon\beta_0$, with $\epsilon = 1/4$ because this typically eliminates the need to compute the sensitivities for many modes with tiny values of β_k and, because of the β_0 term in $H(\beta_k; \beta_0) = \log(\beta_k + \beta_0)$, it is very rare for eigenvectors with half-lives β_k smaller than $\epsilon\beta_0$ to produce any sensitivity less than τ.

In step 5 we perform a non-maximal suppression on the sensitivities for the k^{th} eigenvector. We have observed that at strong borders the computed sensitivities can be less than τ in a band a few pixels thick along the border. This non-maximal suppression allows us to thin this region. Otherwise, many small isolated fragments can be produced in the neighbourhood of such strong borders.

In step 6, once the links $\{i, j\}$ and $\{j, i\}$ are removed the weights of these cut links are moved to the diagonal, to avoid adversely affecting the transition probabilities $m_{i,k}$ and $m_{k,i}$ for all other nodes k. Thus, the transition probablities on the uncut links will remain the same from one iteration to the next.

This iterative cutting process must eventually terminate since, except for the last iteration, edges are cut in each iteration and any cut edges are then never uncut. When the process does terminate, the selected succession of cuts provides a modified affinity matrix A^c which may have one or more well separated clusters. For the final clustering result, we use a connected components algorithm [43].

7.4.1 Iterative Cutting Process

We now illustrate the various steps of the iterative cutting process. For demonstration purpose we apply EIGENCUTS on the image shown in Fig. 7.4a. The affinities are computed as in Eq. 6.1. The affinity matrix is then normalized so that the median value for the degree d_i of every node i in the underlying graph is 1. For computing half-life sensitivities $\frac{d\log(\beta+\beta_0)}{d\alpha_{i,j}}$ only those eigenvectors of the Markov transition matrix that have half-lives above a certain threshold ($> \epsilon\beta_0$) are used. We chose $\beta_0 = 80$ and $\epsilon = 1/4$.

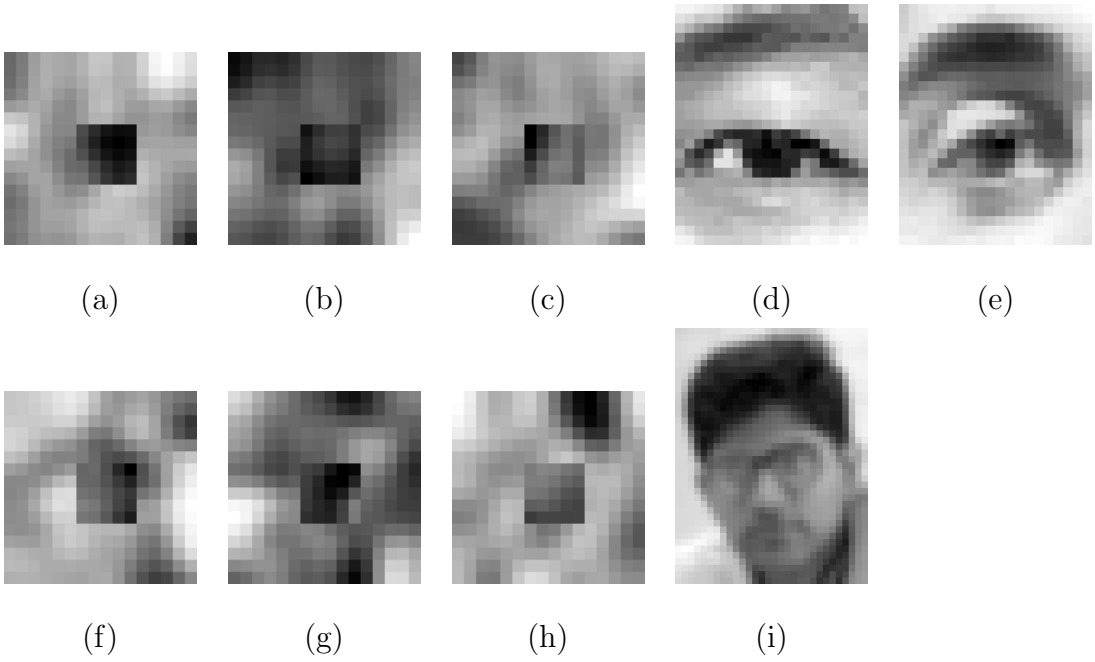

Figure 7.4: (a-c,f-h) Random images with a textured background and an occluder object in front. Image size: 16×16 pixels (d-e) A pair of eye images each of size: 25×20 pixels. (i) A face image of size 30×40 pixels.

The image that is being tested upon requires five iterations of the cutting procedure and the results are documented in Figs. 7.5 to 7.9.

Consider the results from the first iteration shown in Fig. 7.5. Each row represents information derived from a separate eigen mode, with labels attached to reveal the identity of the mode. The first column depicts the eigen modes of the normalized affinity matrix. In iteration 1 only three eigenmodes pass the $> \epsilon\beta_0$ threshold. The first eigenmode is related to the stationary distribution of the Markov matrix and stationary distributions, or equivalently eigenvectors with long half-lives, have zero eigenflows and hence induce no cuts.

The second column shows half-life sensitivities. Gray values correspond to the maximum of the absolute sensitivities, resulting from perturbation of the weights on all the out-going links from a pixel (excluding the self-links $a_{i,i}$). Dark pixels indicate high

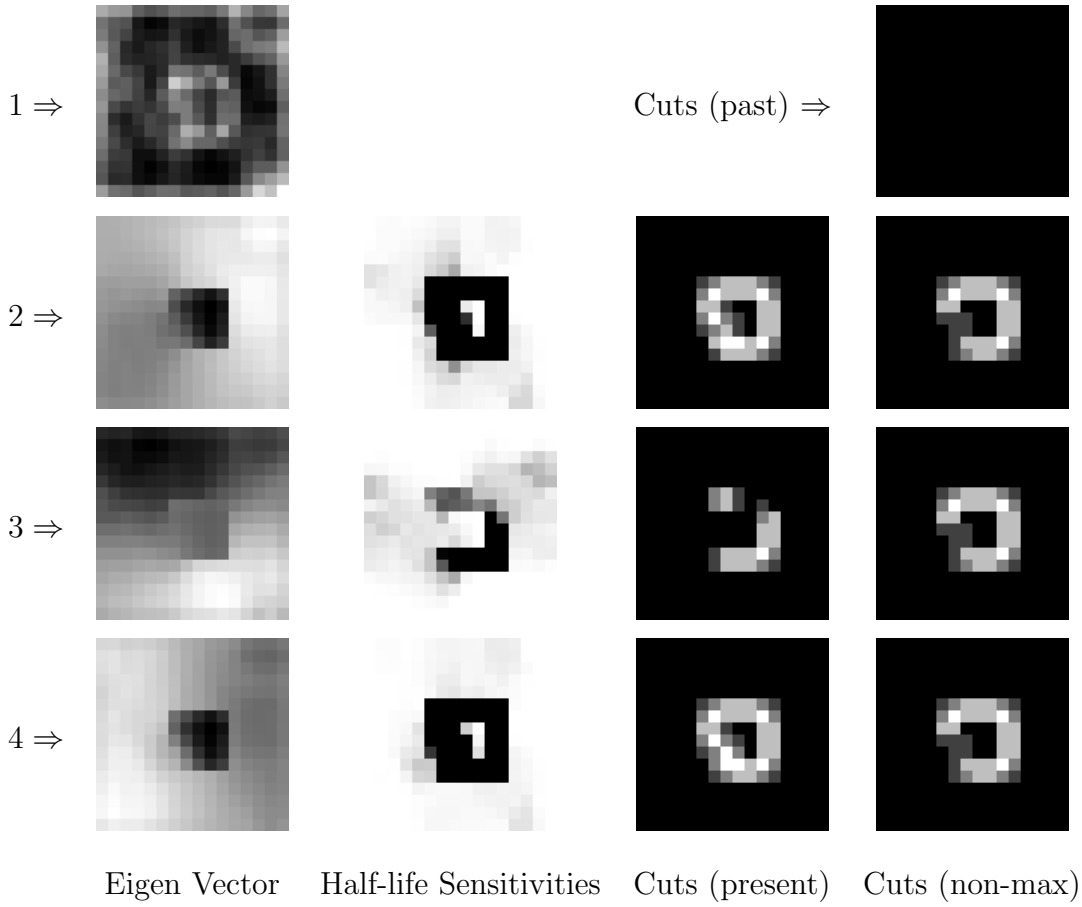

Figure 7.5: Iteration 1 of the EIGENCUTS algorithm for segmenting the image shown in Fig. 7.4a.

absolute sensitivities. Roughly speaking, whereever the spatial gradient in the normalized eigenmode is significant (see Eq. 7.28), we should expect a sensitive link. For the convenience of display, sensitivities are ceiled to have a minimum value of -0.2.

The third column reveals a map of the proposed cuts for the current eigenmode in the current iteration. The cuts are caused by applying a threshold τ $(= -0.1)$ on the sensitivities. The map should be interpreted as follows: the gray level at each pixel represents the total number of links that were cut at that pixel, so the brighter the pixel the higher the number of links cut. The fourth column reveals the cuts that survive the non-maxima suppression. If the map appears the same for different modes, then that means the additional eigenmodes are not adding any new cuts. Each link that is cut

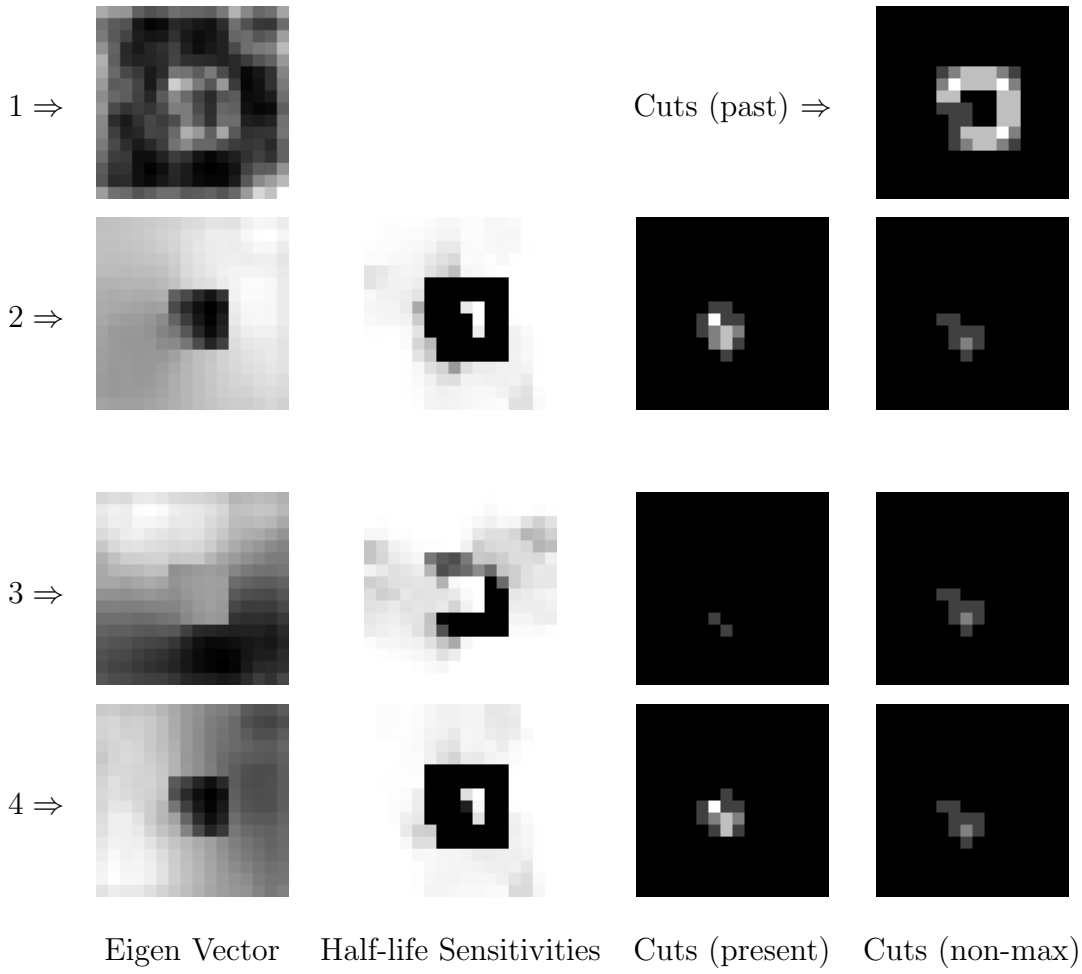

Figure 7.6: Iteration 2 of the EigenCuts algorithm for segmenting the image shown in Fig. 7.4a.

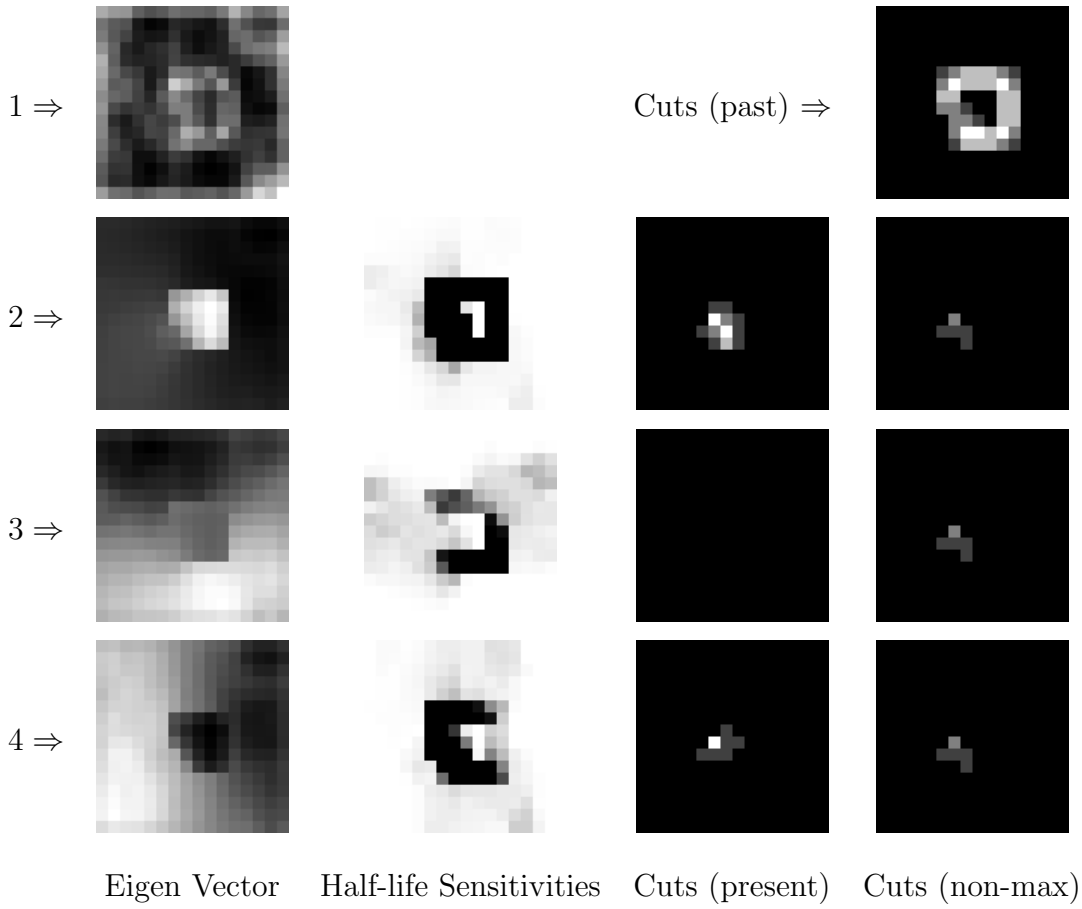

Figure 7.7: Iteration 3 of the EigenCuts algorithm for segmenting the image shown in Fig. 7.4a.

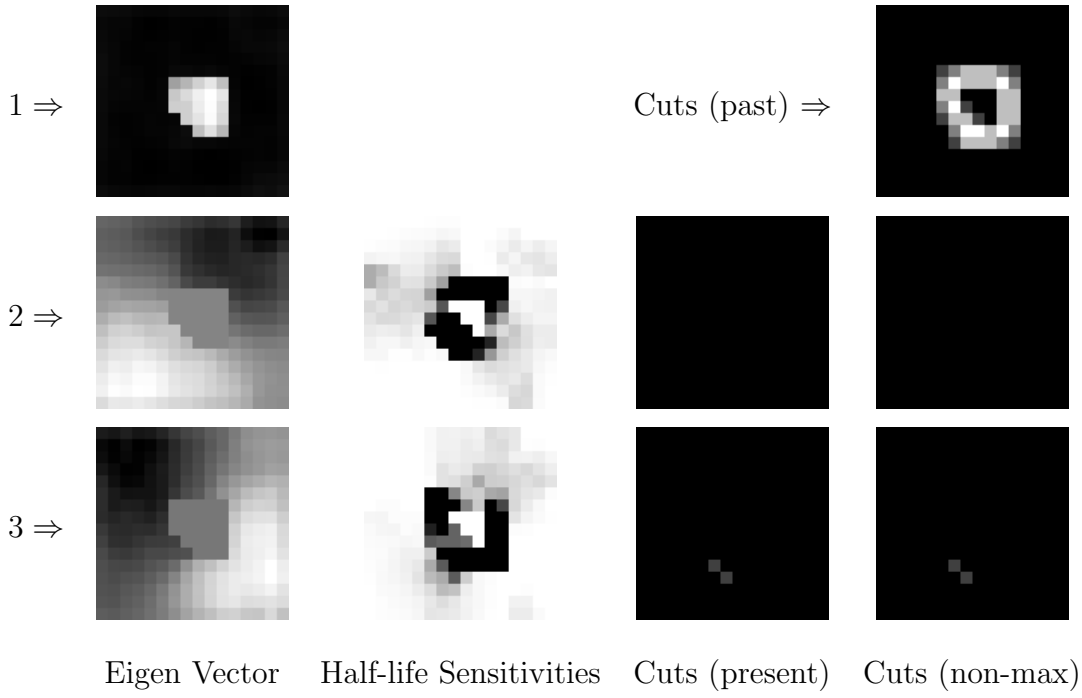

Figure 7.8: Iteration 4 of the EigenCuts algorithm for segmenting the image shown in Fig. 7.4a.

increments a cut counter for each of the two attached nodes. With this in mind, it easy to see that the three brightest pixels in this column correspond to the two corners at the top and the corner at the bottom right of the occluder square in Fig. 7.4a.

At the top of column 4, "Cuts (past)", we record all the actual cuts made so far in the affinity matrix. The last column changes only at the beginning of each iteration, hence there is nothing to report in iteration 1.

Similarly, in iterations 2 (Fig. 7.6) and 3 (Fig. 7.7) cuts are mainly caused by the second eigenmode. The fourth column incorporates all the cuts and can be seen to evolve over the three iterations. It can be seen by the fourth iteration (Fig. 7.8) that sufficient cuts have been made in the affinity matrix, such that two leading eigenvectors emerge each giving rise to a separate stationary distribution (only one of which is displayed in Fig. 7.8). In effect, the graph now has been partitioned into two independent components. While a few more cuts are made in the fourth iteration, by the following iteration (Fig. 7.9) the

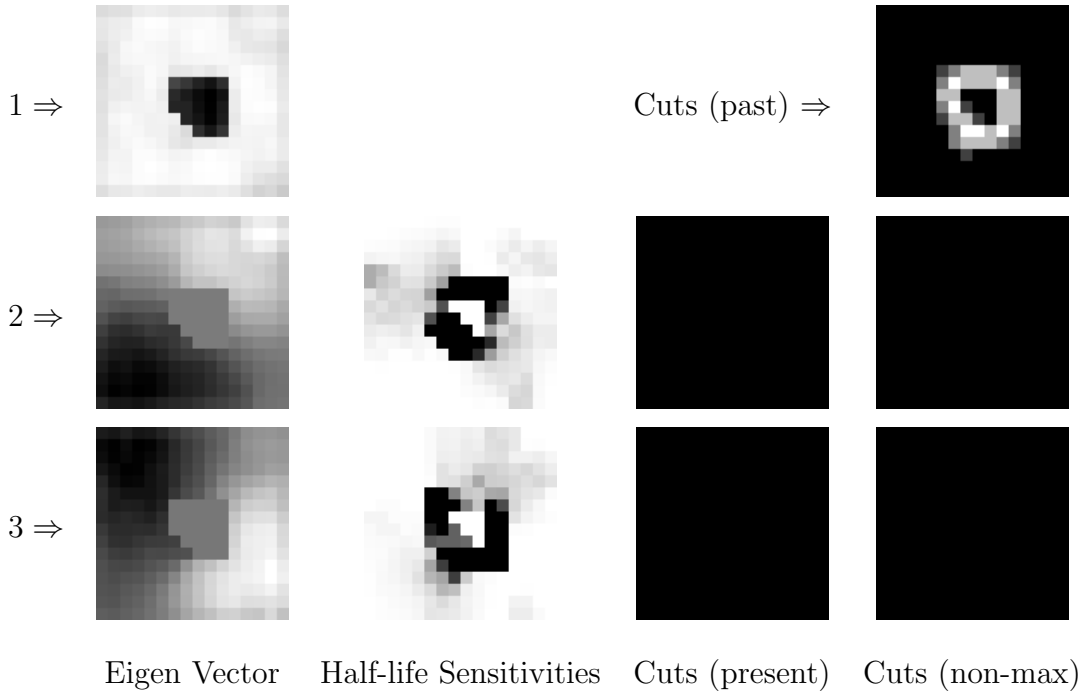

Figure 7.9: Iteration 5 of the EigenCuts algorithm for segmenting the image shown in Fig. 7.4a.

procedure stabilizes in that no new cuts can be seen. Thus, having made no new cuts the iterative cutting process terminates.

7.5 Experiments

We compare the quality of EigenCuts with two other methods: the K-means based spectral clustering algorithm [77] and an efficient segmentation algorithm proposed in [35] based on a pairwise region comparison function. Our strategy was to select thresholds that are likely to generate a small number of stable partitions. We then varied these thresholds to test the quality of partitions. To allow for comparison with K-means spectral, we needed to determine the number of clusters K a priori. We therefore set K to be the same as the number of clusters that EigenCuts generated. The cluster centers were initialized to be as orthogonal as possible [77].

The first two rows in Fig. 7.10 show results using EIGENCUTS with $\rho = 1.5, \epsilon = 0.25, \tau = -0.1$ and $\beta_0 = 80$ (Row 1) and 60 (Row 2). Here ρ is a constant used in derivation for affinities (Eq.6.1), ϵ helps to decide which eigenmodes to perturb, τ is a threshold for cutting links and β_0 is the minimum half-life we are interested in. We observed the performance of the EIGENCUTS to be stable for a wide range of these threshold settings.

A crucial observation with EIGENCUTS is that, although the number of clusters changed slightly with a change in β_0, the regions they defined were qualitatively preserved across the thresholds. Notice in the random images the occluder is seen as a cluster clearly separated from the background. The performance on the eye images is also interesting in that the largely uniform regions around the center of the eye remain as part of one cluster.

For comparison we ran the K-means spectral clustering (rows 3 & 4 in Fig. 7.10) and also an efficient image segmentation algorithm proposed by Falsenszwalb & Huttenlocher [35] (rows 5 & 6). The K-means spectral algorithm was constrained to give the same number of segments as EIGENCUTS. In other words, because EIGENCUTS returns 4 segments for the image shown in (row 1, column 2), the K-means spectral clustering is run on the same image with K set to 4. The result is shown in (row 3, column 2 in Fig. 7.10).

The segmentation algorithm in [35] is designed based on the intuition that there should be evidence for a boundary between each pair of distinct segments. The algorithm uses a region comparison function that compares the minimum edge weight between two regions to the maximum edge weight in the minimum spanning tree of each region. The region comparison function requires a single user defined threshold k, which controls the degree to which the differences in measures beween inside and outside a region are considered significant. The method runs in $O(m \log m)$ time for m graph edges. Again our strategy was to select a threshold that would return a small number of partitions and check if

the partitions are stable for small variations in the threshold. The results are shown in Fig. 7.10 with k set to 70 (row 5) and 50 (row 6).

From the results shown in Fig. 7.10, both the K-means spectral algorithm and the image segmentation algorithm in [35] show a tendency to divide uniform regions and give partitions that are not necessarily stable nor intuitive, despite multiple restarts. We show more results in Fig. 7.11. It is worth mentioning that increasing K in K-means spectral clustering does sometime segment the occluder object. However, what we also observed is that the region boundaries are not typically preserved across changes in K (see Fig. 6.5).

7.6 Discussion

We have demonstrated that the common piecewise constant approximation to eigenvectors arising in spectral clustering problems limits the applicability of previous methods to situations in which the clusters are only relatively weakly coupled. We have proposed a new edge cutting criterion which avoids this piecewise constant approximation. Bottleneck edges between distinct clusters are identified through the observed sensitivity of an eigenflow's half-life on changes in the edges' affinity weights. The basic algorithm we propose is computationally demanding in that the eigenvectors of the Markov matrix must be recomputed after each iteration of edge cutting. On average the procedure requires about $5 - 12$ iterative cutting steps for most of the datasets shown in Fig. 7.4, but up to 40 iterations for the face image. While this process is computationally expensive, our goal in this chapter was to demonstrate that the partitioning of a graph can be achieved through the computation of the sensitivity of eigenflow half-lives to changes in edge weights. In the following chapter, we propose a reduced-rank multi-scale representation for large stochastic matrices and use this representation to design an efficient algorithm for computing the leading eigenvalues, and the corresponding eigenvectors of

such matrices. To show the effectiveness of this algorithm, we also present a multi-scale version of the EigenCuts algorithm.

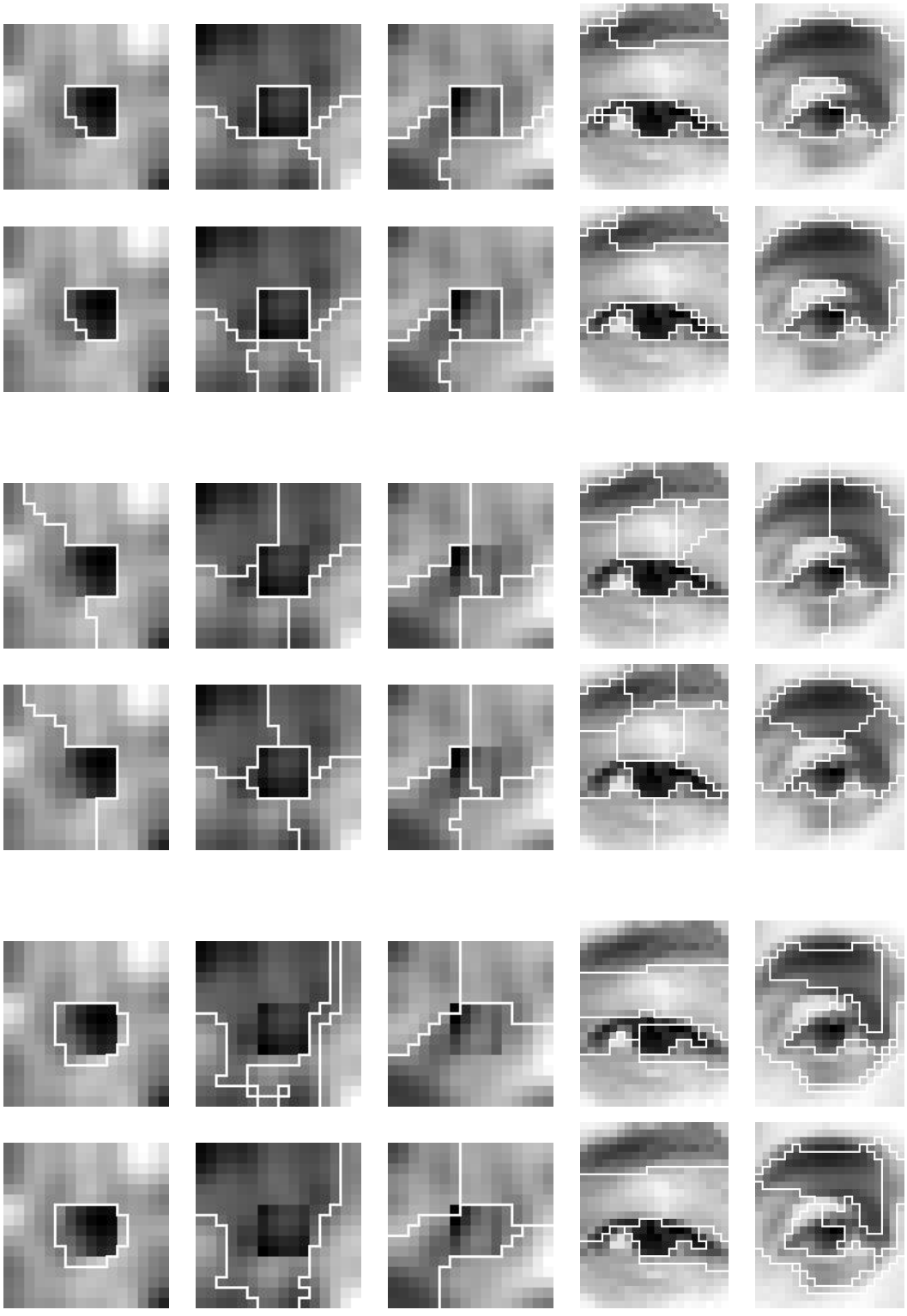

Figure 7.10: Segmentation results on the test dataset in Fig. 7.4(a-e): EIGENCUTS with $\beta_0 = 80$ (Row 1) and 60 (Row 2); K-means spectral in Rows 3 and 4; Falsenszwalb & Huttenlocher with $\tau = 70$ (Row 5) and 50 (Row 6).

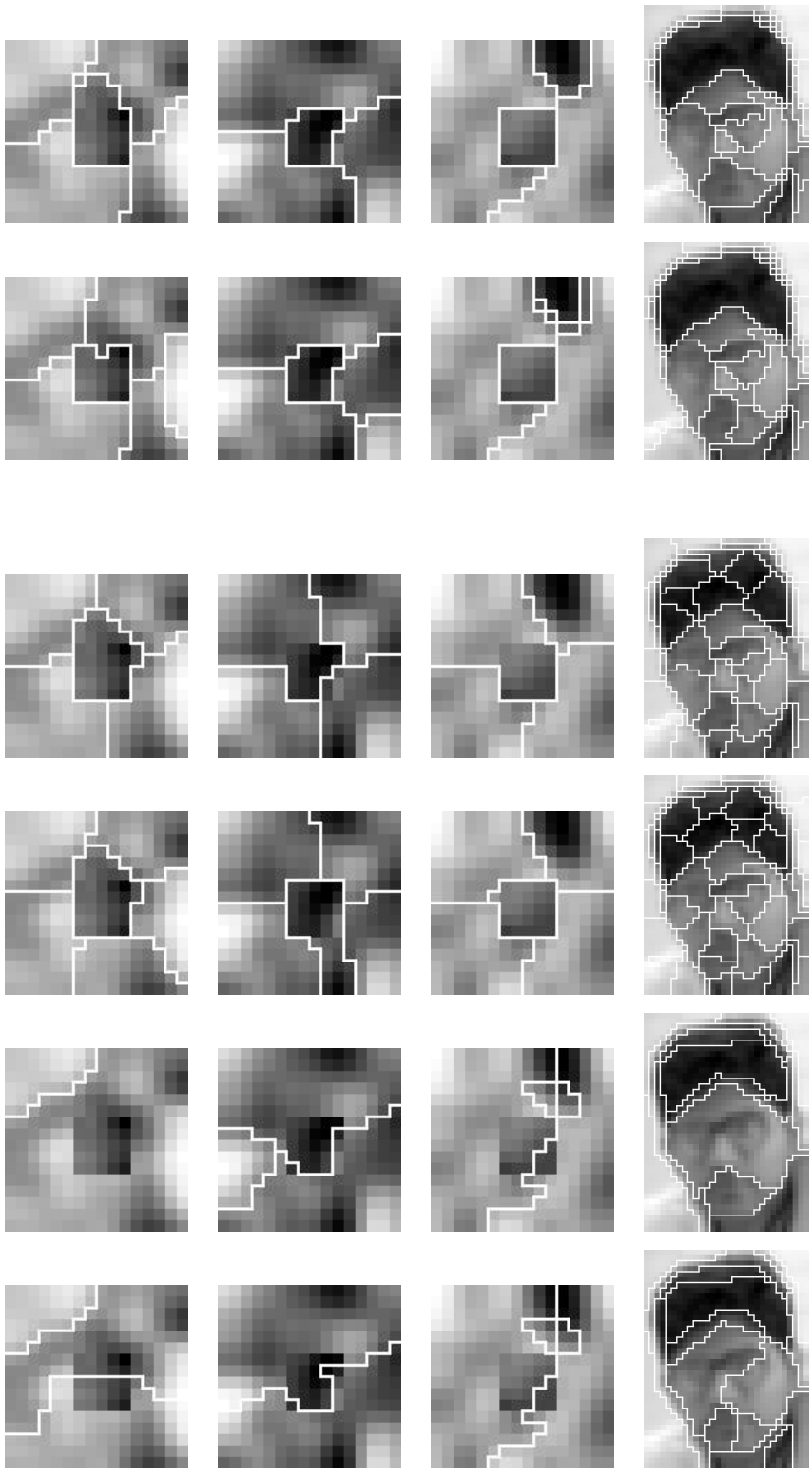

Figure 7.11: Segmentation results on the test dataset in Fig. 7.4(f-i): EIGENCUTS with $\beta_0 = 80$ (Row 1) and 60 (Row 2); K-means spectral in Rows 3 and 4; Falsenszwalb & Huttenlocher with $\tau = 70$ (Row 5) and 50 (Row 6).

Chapter 8

Hierarchical Representation of Transition Matrices

Spectral methods enable the study of properties global to a dataset, using only local pairwise similarity measurements between data points. We have studied global properties that emerge from such similarities in terms of a random walk formulation on the graph. In particular, as described in Chapter 7, we can partition the graph into clusters by analyzing the perturbations to the stationary distribution of a Markovian relaxation process defined in terms of the affinity weights. The Markovian relaxation process need never be explicitly carried out; instead, it can be analytically expressed using the leading order eigenvectors, and eigenvalues, of the Markov transition matrix.

Two issues arise in the implementation of spectral methods. First, the stochastic matrices need not be symmetric in general, and hence for reasons of numerical instability, a direct eigen decomposition step is not preferred. This problem is easily circumvented by considering a normalized affinity matrix which is related to the stochastic matrix by a similarity transformation (Eq. 7.7). By virtue of symmetry, the eigen decomposition of the normalized symmetric matrix is numerically stable (e.g., see §6.5 [118]). While the eigenvalues of the stochastic matrix remain the same as for the normalized affinity

matrix, the eigenvectors are related by a simple transformation.

The second issue is how the spectral methods scale to large datasets. In particular, the eigen decomposition can be very expensive, on the order of $O(n^3)$, where $n = |V|$. While it is possible to compute analytically the first eigenvector (see §7.2.4), the remaining subspace of vectors necessary for clustering has to be explicitly computed. A typical approach to dealing with this difficulty is to first sparsify the links in the graph, thus generating a sparse affinity matrix, and then apply an efficient eigensolver such as Lanczos [56].

In comparison, we propose in this chapter a specialized eigensolver suitable for large stochastic matrices with known stationary distributions. In particular, we exploit the spectral properties of the Markov transition matrix to generate hierarchical, successively lower-ranked approximations to the full transition matrix. The eigen problem is solved directly at the coarsest level of representation. The approximate eigen solution is then interpolated over successive levels of the hierarchy, using a small number of power iterations to correct the solution at each stage. To show the effectiveness of this approximation, we present a multi-scale version of the EIGENCUTS algorithm in the subsequent chapter.

8.1 Previous Work

One approach to speeding up the eigen decomposition is to use the fact that the columns of the affinity matrix are typically correlated. The idea then is to pick a small number of representative columns to perform eigen decomposition via SVD. For example, in the Nyström approximation procedure, originally proposed for integral eigenvalue problems [31,89], the idea is to randomly pick a small set of m columns; generate the corresponding affinity matrix; solve the eigenproblem and finally extend the solution to the complete graph [15,40]. The Nyström method has also been recently applied in the kernel learning methods for fast Gaussian process classification and regression [121]. Other sampling-

based approaches include the work reported in [1, 2, 42].

Our starting point is the transition matrix generated from affinity weights and we show how building a representational hierarchy follows naturally from considering the stochastic matrix. The work closest in spirit to our research is the paper by Lin on reduced rank approximations of transition matrices [62]. We differ in how we approximate the transition matrices, in particular our objective function is computationally less expensive to solve. While the paper by Lin suggests interpreting the reduced rank approximations directly for clustering, we embed our procedure in a graph partitioning framework. In particular, one of our goals in reducing transition matrices is to develop a fast, specialized eigen solver for spectral clustering. Fast eigensolving is also the goal in ACE [53], where successive levels in the hierarchy can potentially have negative affinities. A graph coarsening process for clustering was also pursued in [100].

8.2 Markov Chain Terminology

We first provide a brief overview of the Markov chain terminology here (for more details see §7.2). We consider an undirected graph $G = (V, E)$ with vertices v_i, for $i = \{1, \ldots, n\}$, and edges $e_{i,j}$ with non-negative weights $a_{i,j}$. Here the weight $a_{i,j}$ represents the affinity between vertices v_i and v_j. The affinities are represented by a non-negative, symmetric $n \times n$ matrix A having weights $a_{i,j}$ as elements. The degree of a node j is defined to be: $d_j = \sum_{i=1}^{n} a_{i,j} = \sum_{j=1}^{n} a_{j,i}$, while D is a diagonal matrix of degree values: $D = \text{diag}(d_1, \ldots, d_n)$. A Markov chain is defined using these affinities by setting a transition probability matrix $M = AD^{-1}$, where the columns of M each sum to 1. The transition probability matrix defines the random walk of a particle on the graph G.

For analysis, we consider a similarity transformation of the Markov matrix: $L = D^{-1/2} M D^{1/2}$. Observe L is a normalized form of the affinity matrix given by: $L = D^{-1/2} A D^{-1/2}$. As a consequence L is symmetric and hence it can be diagonalized as:

$L = U\Lambda U^T$, where $U = [\vec{u}_1, \vec{u}_2, \cdots, \vec{u}_n]$ are the eigenvectors and Λ is a diagonal matrix of eigenvalues $[\lambda_1, \lambda_2, \cdots, \lambda_n]$ sorted in decreasing order. While the eigenvectors have unit length, $\|\vec{u}_k\| = 1$, the eigenvalues are real and have an absolute value bounded by 1, $|\lambda_k| \leq 1$. Because L and M are similar we can perform an eigen decomposition of the Markov transition matrix as: $M = D^{1/2}LD^{-1/2} = D^{1/2}U\ \Lambda\ U^T D^{-1/2}$. Thus an eigenvector $\vec{u}$ of L corresponds to an eigenvector $D^{1/2}\vec{u}$ of M with the same eigenvalue λ.

The transition matrix after β iterations, namely M^β, can be represented as: $M^\beta = D^{1/2}U\Lambda^\beta U^T D^{-1/2}$. Therefore, a particle undertaking a random walk with an initial distribution $\vec{p}^0$ acquires after β steps a distribution $\vec{p}^\beta$ given by: $\vec{p}^\beta = M^\beta \vec{p}^0$. Assuming the graph is connected, as $\beta \to \infty$, the Markov chain approaches a unique stationary distribution $\vec{\pi} = \text{diag}(D)/\sum_{i=1}^n d_i$, and hence $M^\infty = \vec{\pi}\mathbf{1}^T$. Observe that $\vec{\pi}$ is an eigenvector of M as it is easy to show that $M\vec{\pi} = \vec{\pi}$ and the corresponding eigenvalue is 1. Next, we show how to generate hierarchical, successively low-ranked approximations for the transition matrix M.

8.3 Building a Hierarchy of Transition Matrices

The goal is to generate a very fast approximation, while simultaneously achieving sufficient accuracy. For notational ease, we think of M as a fine-scale representation and $\widetilde{M}$ as some coarse-scale approximation to be derived here. By coarsening $\widetilde{M}$ further, we can generate successive levels of the representation hierarchy. We use the stationary distribution $\vec{\pi}$ to construct a corresponding coarse-scale stationary distribution $\vec{\delta}$. In the process, we see how to construct a transition matrix $\widetilde{M}$ for the coarse-scale.

8.3.1 Deriving Coarse-Scale Stationary Distribution

We begin by expressing the stationary distribution $\vec{\pi}$ as a probabilistic mixture of latent distributions. In matrix notation, we have

$$\vec{\pi} = K\vec{\delta}, \tag{8.1}$$

where $\vec{\delta}$ is an unknown mixture coefficient vector of length m, K is an $n \times m$ non-negative kernel matrix whose columns are latent distributions that each sum to 1 and $m \ll n$.

For choosing the kernels K, we first diffuse the Markov matrix M using a small number of iterations to get M^β. The diffusion causes random walks from neighboring nodes to be less distinguishable. We then choose a small number of columns of M^β to be the kernel matrix K[1]. The kernel selection is fast and greedy; we defer the details to the following section.

We now show how to get a maximum likelihood approximation of $\vec{\delta}$ using an EM type algorithm [71]. To derive this we minimize the *Kullback-Liebler* distance measure [54, 55] between the two probability distributions $\vec{\pi}$ and $K\vec{\delta}$ given by

$$\begin{aligned} L &= -\sum_{i=1}^{n} \pi_i \ln \frac{\sum_{j=1}^{m} K_{i,j}\delta_j}{\pi_i}, \\ &= -\sum_{i=1}^{n} \pi_i \ln \sum_{j=1}^{m} K_{i,j}\delta_j + \sum_i \pi_i \ln \pi_i. \end{aligned} \tag{8.2}$$

Note the second term in the above expression is the negative entropy of the stationary distribution $\vec{\pi}$. Given that $\vec{\delta}$ is a probability distribution, a maximum likelihood estimating process has to find a stationary point $\left(\vec{\delta}, \lambda\right)$ for the following Lagrangian

$$\begin{aligned} E &= L + \lambda\left(\sum_{j=1}^{m} \delta_j - 1\right), \\ &= -\sum_{i=1}^{n} \pi_i \ln \sum_{j=1}^{m} K_{i,j}\delta_j + \lambda\left(\sum_{j=1}^{m} \delta_j - 1\right), \end{aligned} \tag{8.3}$$

[1] If M is a full matrix, to avoid the expense of computing M^β explicitly, random kernel centers can be selected, and only the corresponding columns of M^β need be computed.

where the negative entropy term $\sum_i \pi_i \ln \pi_i$ in L is dropped because it will have a fixed value and hence will not affect the subsequent minimization with respect to δ_j. Now, taking the derivative with respect to δ_j gives

$$\frac{\partial E}{\partial \delta_j} = \sum_{i=1}^{n} \frac{\pi_i K_{i,j}}{\sum_{k=1}^{m} \delta_k K_{i,k}} - \lambda. \tag{8.4}$$

Setting $\frac{\partial E}{\partial \delta_j}$ to zero we obtain

$$\sum_{i=1}^{n} \frac{\pi_i K_{i,j}}{\sum_{k=1}^{m} \delta_k K_{i,k}} = \lambda. \tag{8.5}$$

Multiplying both sides of the above equation by δ_j results in

$$\sum_{i=1}^{n} \frac{\pi_i \delta_j K_{i,j}}{\sum_{k=1}^{m} \delta_k K_{i,k}} = \lambda \delta_j. \tag{8.6}$$

Because the contribution made by kernel j at node i is given by $K_{i,j}$, we can define ownership of a node i by kernel j as

$$r_{i,j} = \frac{\delta_j K_{i,j}}{\sum_{k=1}^{m} \delta_k K_{i,k}}. \tag{8.7}$$

Using the ownerships $r_{i,j}$ we can rewrite Eq. 8.6 as

$$\sum_{i=1}^{n} \pi_i r_{i,j} = \lambda \delta_j. \tag{8.8}$$

By definition $\sum_{j=1}^{m} r_{i,j} = 1$ and hence we have

$$\begin{aligned} \sum_{i=1}^{n} \sum_{j=1}^{m} \pi_i r_{i,j} &= \lambda \sum_{j=1}^{m} \delta_j, \\ \sum_{i=1}^{n} \pi_i &= \lambda, \\ \Rightarrow \lambda &= 1. \end{aligned} \tag{8.9}$$

Here we use the fact that $\sum_{j=1}^{m} \delta_j = 1$ and $\sum_{i=1}^{n} \pi_i = 1$. Substituting for λ in Eq. 8.8 gives the mixing probability, which is the stationary distribution at the coarse-scale, given by

$$\delta_j = \sum_{i=1}^{n} \pi_i r_{i,j}. \tag{8.10}$$

Along with $\vec{\delta}$, we can update the latent distributions in the kernel matrix K (as in [62]). To see how notice that we can interpret the responsibility term $r_{i,j}$ in Eq. 8.10 as the conditional probability of being in the coarse-scale node j given the fine scale state i. Hence, in Eq. 8.10 we are integrating over the states at the fine-scale, each having a probability π_i, so we can obtain the coarse-scale distribution $\vec{\delta}$. Similarly, elements in the kernel matrix $K_{i,j}$ represent the conditional probability of being in fine-scale state i given the coarse-scale state j. Then using Bayes theorem the kernel matrix can be updated as follows:

$$K_{i,j} = \frac{r_{i,j}\pi_i}{\delta_j}, \tag{8.11}$$

where we use the updated coarse-scale stationary distribution values from Eq. 8.10. Thus, a EM type procedure would follow this sequence of steps:

1. *M-step*
    - Compute ownership maps $r_{i,j}$ (Eq. 8.7)
2. *E-step*
    - Estimate mixing probabilities which are the coarse-scale stationary distribution values δ_j (Eq. 8.10)
    - Estimate the kernel parameters $K_{i,j}$ (Eq. 8.11)
3. Repeat until convergence

By diffusing the Markov matrix M through a small number of iterations, as in M^β, and then choosing a small number of columns of M^β as the kernel matrix K, we facilitate a rapid convergence of the EM procedure. We initialize $\vec{\delta}$ to be uniform over the coarse-scale states.

8.3.2 Deriving the Coarse-Scale Transition Matrix

In order to define $\widetilde{M}$, we break it down into two steps. To define the random walk in the reduced space, say

$$\vec{q}^{\,k+1} = \widetilde{M}\vec{q}^{\,k}, \tag{8.12}$$

we first *expand* $\vec{q}^{\,k}$ into the fine scale using the kernels K, resulting in

$$\vec{p}^{\,k} = K\vec{q}^{\,k}. \tag{8.13}$$

Then we *lift* $\vec{p}^{\,k}$ back into the coarse scale by using the ownership probability of the j^{th} kernel for the i^{th} node on the fine grid. Computing the ownership probability is an implicit step in the EM procedure described above and is given by

$$r_{i,j} = \frac{\delta_j K_{i,j}}{\sum_{k=1}^{m} \delta_k K_{i,k}}.$$

Thus,

$$\begin{aligned} q_j^{k+1} &= \sum_{i=1}^{n} r_{i,j} p_i^{\,k}, \\ &= \sum_{i=1}^{n} r_{i,j} \sum_{t=1}^{m} K_{i,t} q_t^{\,k}, \\ &= \sum_{i=1}^{n} \left(\frac{\delta_j K_{i,j}}{\sum_{k=1}^{m} \delta_k K_{i,k}} \right) \sum_{t=1}^{m} K_{i,t} q_t^{\,k}. \end{aligned} \tag{8.14}$$

We can write the preceding equation in a matrix form,

$$\begin{aligned} \vec{q}^{\,k+1} &= \text{diag}(\,\vec{\delta}\,)\, K^T \,\text{diag}\left(K\vec{\delta}\right)^{-1} K\vec{q}^{\,k}, \\ &= \widetilde{M}\vec{q}^{\,k}, \end{aligned} \tag{8.15}$$

where the transition matrix is given by

$$\widetilde{M} = \text{diag}(\,\vec{\delta}\,)\, K^T \,\text{diag}\left(K\vec{\delta}\right)^{-1} K. \tag{8.16}$$

It is easy to see that $\vec{\delta} = \widetilde{M}\vec{\delta}$, so $\vec{\delta}$ is the stationary distribution for $\widetilde{M}$.

One critical property of the fine scale Markov matrix that we would like to preserve in the coarse scale version is that it is *precisely* similar to a symmetric matrix. It follows from the definition of $\widetilde{M}$ and its stationary distribution $\vec{\delta}$, we can generate a *scaled symmetric* affinity matrix $\widetilde{A}$ given by

$$\begin{aligned}\widetilde{A} &= \widetilde{\gamma}\widetilde{M}\text{diag}(\vec{\delta}), \\ &= \widetilde{\gamma}\left(\text{diag}(\vec{\delta})\,K^T\right)\left(\text{diag}\left(K\vec{\delta}\right)^{-1}\right)\left(K\text{diag}(\vec{\delta})\right),\end{aligned} \tag{8.17}$$

where we substitute for the transition matrix $\widetilde{M}$ from Eq. 8.16. From this equation, it is clear that the affinity matrix at coarse-scale is also symmetric. The scalar variable $\widetilde{\gamma}$ is used to fix the scale by computing

$$\widetilde{\gamma}^{-1} = \text{median}(\widetilde{d}_i), \tag{8.18}$$

where $\widetilde{d}_i$ is the degree of node i in the coarse-scale graph represented by the matrix $\widetilde{A}$ (as in step 2 of Sec. 7.4). The coarse-scale affinity matrix $\widetilde{A}$ is normalized to get

$$\begin{aligned}\widetilde{D} &= \text{diag}(\widetilde{d}_1, \widetilde{d}_2, \cdots, \widetilde{d}_m), \\ \widetilde{L} &= \widetilde{D}^{-1/2}\widetilde{A}\widetilde{D}^{-1/2}.\end{aligned} \tag{8.19}$$

which is then used for eigen decomposition.

To summarize, we use the stationary distribution $\vec{\pi}$ at the fine-scale to derive a transition matrix $\widetilde{M}$, and its stationary distribution $\vec{\delta}$, at the coarse-scale. It is obvious that this procedure can be repeated recursively. To maintain consistency, a $\widetilde{\gamma}$ factor is computed for each level of the hierarchy and the corresponding affinity matrix is scaled. Also, at successive levels of the hierarchy we sparsify $\widetilde{A}$ by zeroing out elements associated with small transition probabilities in $\widetilde{M}$.

8.3.3 Selecting Kernels

In Fig. 8.1, we show the details of kernel selection for a three-scale approximation of the transition matrix, one fine-scale and two coarse-scales. To begin with, a graph cluster-

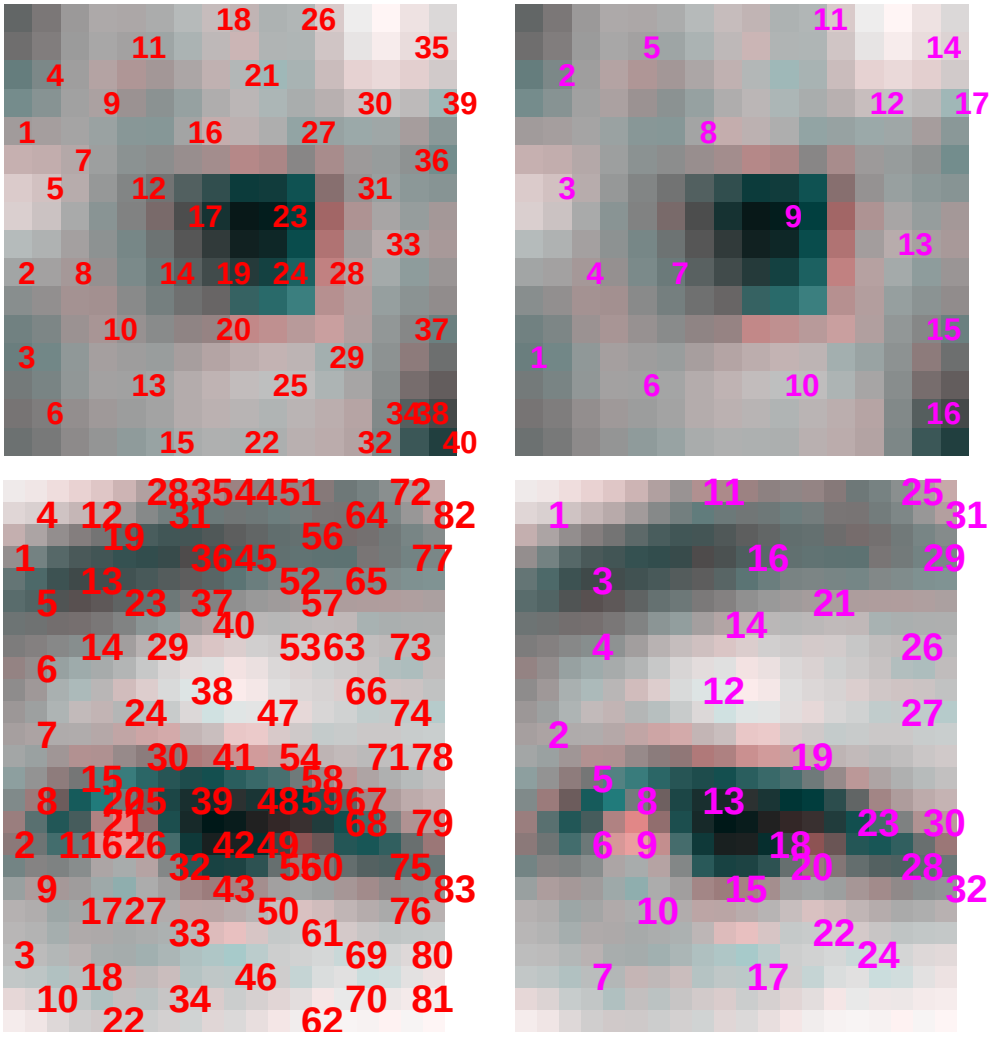

Kernel centers for scale 1 Kernel centers for scale 2

Figure 8.1: Kernel selection at levels 2 (Left Column) and 3 (Right Column) of the hierarchy. The numbers in red and magenta indicate the location of the kernel centers.

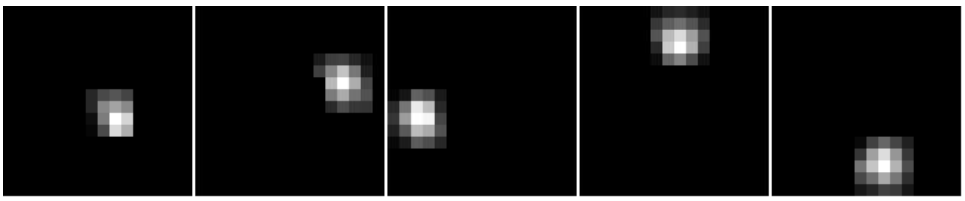

Figure 8.2: A random selection of kernels for the occluder image. These kernels carry information from fine-scale (level 1) to the first coarse-scale (level 2) of the hierarchy. The kernel matrix is of size 256×40.

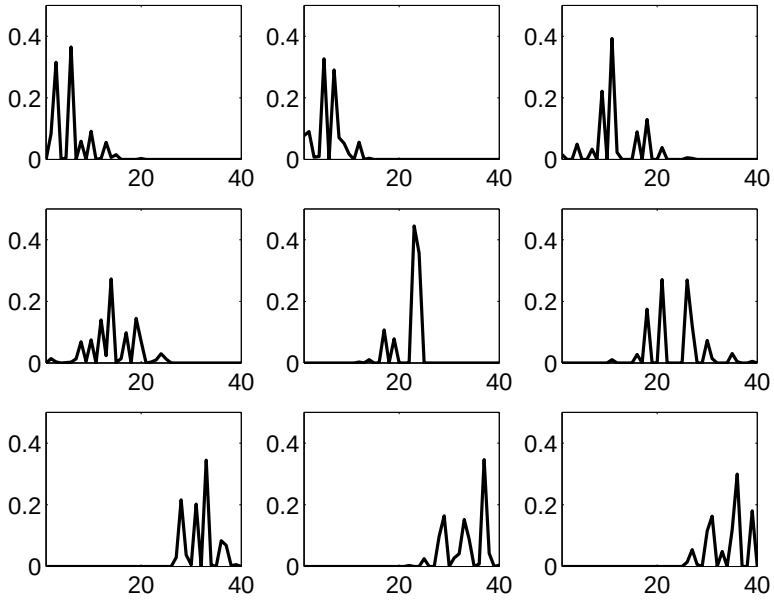

Figure 8.3: A random selection of kernels for the occluder image. These kernels carry information from level 2 to level 3 of the hierarchy. The kernel matrix is of size 40×17.

ing problem is formed for the underlying image where each pixel in the test image is associated with a vertex of the graph G. The edges in G are defined by the standard 8-neighbourhood of each pixel. For the demonstrations in this thesis, the edge weights between neighbouring vertices are simply given by a function of the difference in the corresponding intensities (as in Eq. 6.1). The affinity matrix A, with the edge weights, is then used to generate a Markov transition matrix M.

The kernel selection process we use is fast and greedy. First, the fine-scale Markov matrix M is diffused to M^β using $\beta = 4$. The Markov matrix M is sparse as we make the affinity matrix A sparse. Every column in the diffused matrix M^β is a potential kernel. To facilitate the selection process, the second step is to rank order the columns of M^β based on a probability value in the distribution

$$\vec{p} = \frac{(d_1, \cdots, d_n)}{\sum_{i=1}^{n} d_i},$$

where $\vec{p}$ is a vector of length n and d_i is the degree of node v_i in the graph. If the graph is connected, this would have been the stationary distribution of the Markov chain. Third,

the kernels (i.e. columns of M^β) are picked in such a way that for a kernel K_i all of its neighbours which are within the *half-height* of its peak value are suppressed from the selection process. Finally, the kernel selection is continued until we ensure that every pixel in the image is within a half-height of the peak value of at least one kernel.

We show results from a three-scale hierarchy in Fig. 8.1, where the left, and right, columns indicate the locations of the kernel centers for two different images at the two coarse-scales. The random occluder image is of size 16×16 pixels and the eye image is of size 25×20 pixels. These images are enlarged in Fig. 8.1 for clarity. For the random occluder image, the greedy algorithm picks 40 kernels which allow us to go from from scale 1 (fine-scale) to scale 2 (coarse-scale) of the hierarchy. The kernel centers are shown in numbers. The transition matrix $\widetilde{M}$ generated for the 40 dimensional space is then diffused to $\widetilde{M}^\beta$, again using $\beta = 4$. The greedy algorithm is applied again, this time picking 17 kernels, which allow us to go from scale 2 to scale 3 of the hierarchy. Similar results can be seen for the eye image. In Fig. 8.2, we show a random sample of kernels. The kernels are columns of the transition matrix and hence, they should be seen as conditional probability distributions. Note, at higher levels of the hierarchy, the kernel matrix begins to get less sparse. Consequently, the corresponding affinity matrix will be less sparse as well (see Fig. 8.3). We next describe how to use this representation hierarchy for building a fast eigensolver.

8.4 Fast EigenSolver

Given that our procedure is hierarchical, the eigen decomposition of the normalized affinity matrix L is done only at the "coarsest" scale. Once computed, the coarse-scale eigenvectors are interpolated using the kernel matrix to generate the fine-scale eigenvectors. For demonstration purposes, let us consider a three-scale interpolation process applied to the test image of an eye (Fig. 8.1). The first scale is the fine-scale

normalized affinity matrix L for the eye image and is of size $n \times n$ where $n = 500$. The kernel selection selection process results in a matrix K, which is of size $n \times m$ where $m = 83$ and m is typically $\ll n$. The coarse-scale representation of L at the second level of the hierarchy is $\widetilde{L}$, which is of size $m \times m$. This representation is further reduced at the third-level of the hierarchy to a matrix of size $e \times e$, which for the face image is 32×32.

A full eigen decomposition of the normalized affinity matrix is done only at the coarsest level. As discussed in the previous section the affinity matrix at the coarsest level is not likely to be sparse, hence it will need a full (as opposed to a sparse) version of an eigen solver. However it is typically the case that $e \leq m \ll n$, even in the case of the three-scale hierarchy that is under consideration. The resulting eigenvectors are interpolated to the next lower level of the hierarchy by a process which will be described next. Because the eigen interpolation process between every adjacent pair of scales in the hierarchy is similar, we will assume we have access to the leading eigenvectors $\widetilde{U}$ (size: $m \times e$) for the normalized affinity matrix $\widetilde{L}$ (size: $m \times m$) and describe how to generate the leading eigenvectors U (size: $n \times e$), and leading eigenvalues S (size: $e \times 1$), for the fine-scale normalized affinity matrix L (size: $n \times n$). There are several steps to the eigen interpolation process.

- First, the coarse-scale eigenvectors $\widetilde{U}$ can be interpolated using the kernel matrix K to generate U, an approximation for the fine-scale eigenvectors,

$$U = K\widetilde{U}.$$

- Second, interpolation alone is unlikely to set the directions of U exactly aligned with U_L, the vectors one would obtain by a direct eigen decomposition of the fine-scale normalized affinity matrix L. We update the directions in U by applying a small number of power iterations with L as in:

  for $i = 1$ to POWER_ITERS **do**

  $U \Leftarrow LU$

end for

- Third, the interpolation process and the power iterations need not preserve orthogonality in the eigenvectors in U. We fix this by Gram-Schmidt orthogonalization procedure.

- Finally, there is a still a problem with power iterations that needs to be resolved, in that it is very hard to separate nearby eigenvalues. In particular, for the convergence of the power iterations the ratio that matters is between the $(e+1)^{\text{st}}$ and e^{th} eigenvalues. So the idea we pursue is to use the power iterations only to separate the reduced space of eigenvectors (of dimension e) from the orthogonal subspace (of dimension $n-e$). We then use a full SVD on the reduced space to update the leading eigenvectors U, and eigenvalues S, for the fine-scale:

$$L_e = U^T L U,$$
$$U_e S_e V_e^T = \text{svd}(L_e),$$
$$U \Leftarrow U U_e^T,$$
$$S \Leftarrow \text{diag}(S_e).$$

In ALGORITHM 2 we present the details of this coarse to fine eigen interpolation procedure.

8.4.1 Interpolation Results

In Fig. 8.4 we compare the spectrum S obtained from a three-scale decomposition on the eye and face images (Fig. 7.4) with the ground truth, which is the spectrum S_L resulting from direct eigen decomposition of the fine-scale normalized affinity matrices L. For the direct eigen decomposition, we have used the Matlab implementation of an implicitly restarted Arnoldi method for solving large-scale eigenvalue problems [90]. Our multi-scale decomposition code is also in Matlab.

Algorithm 2 function $(U, S) = \text{CoarseToFine}(L, K, \widetilde{U})$

INPUT

$L, K \Leftarrow \{L \text{ is } n \times n \text{ and } K \text{ is } n \times m \text{ where } m \ll n\}$

$\widetilde{U} \Leftarrow \{\text{leading coarse-scale eigenvectors of } \widetilde{L}.\ \widetilde{U} \text{ is of size } m \times e, e \leq m\}$

OUTPUT

$U, S \Leftarrow \{\text{leading fine-scale eigenvectors/eigenvalues of } L.\ U \text{ is } n \times e \text{ and } S \text{ is } e \times 1.\}$

CONSTANTS

TOL $= 1.0e{-}3$; POWER_ITERS $= 25$

$U = K\widetilde{U}$ {interpolation from coarse to fine}

while not converged **do**

$U_{\text{old}} = U$ {$n \times e$ matrix, $e \ll n$}

for $i = 1$ to POWER_ITERS **do**

$U \Leftarrow LU$

end for

$U \Leftarrow \text{Gram-Schmidt}(U)$ {orthogonalize U}

$L_{\text{e}} = U^T L U$ {L may be sparse, but L_{e} need not be.}

$U_{\text{e}} S_{\text{e}} U_{\text{e}}^T = \text{svd}(L_{\text{e}})$ {eigenanalysis of L_{e}, which is of size $e \times e$.}

$U \Leftarrow U U_{\text{e}}$ {update the leading eigenvectors of L}

$S = \text{diag}(S_{\text{e}})$ {grab the leading eigenvalues of L}

innerProd $= \mathbf{1} - \text{diag}(\, U_{\text{old}}^T U\,)$ {$\mathbf{1}$ is a $e \times 1$ vector of all ones}

converged $= \max[\text{abs}(\text{innerProd})] < \text{Tol}$

end while

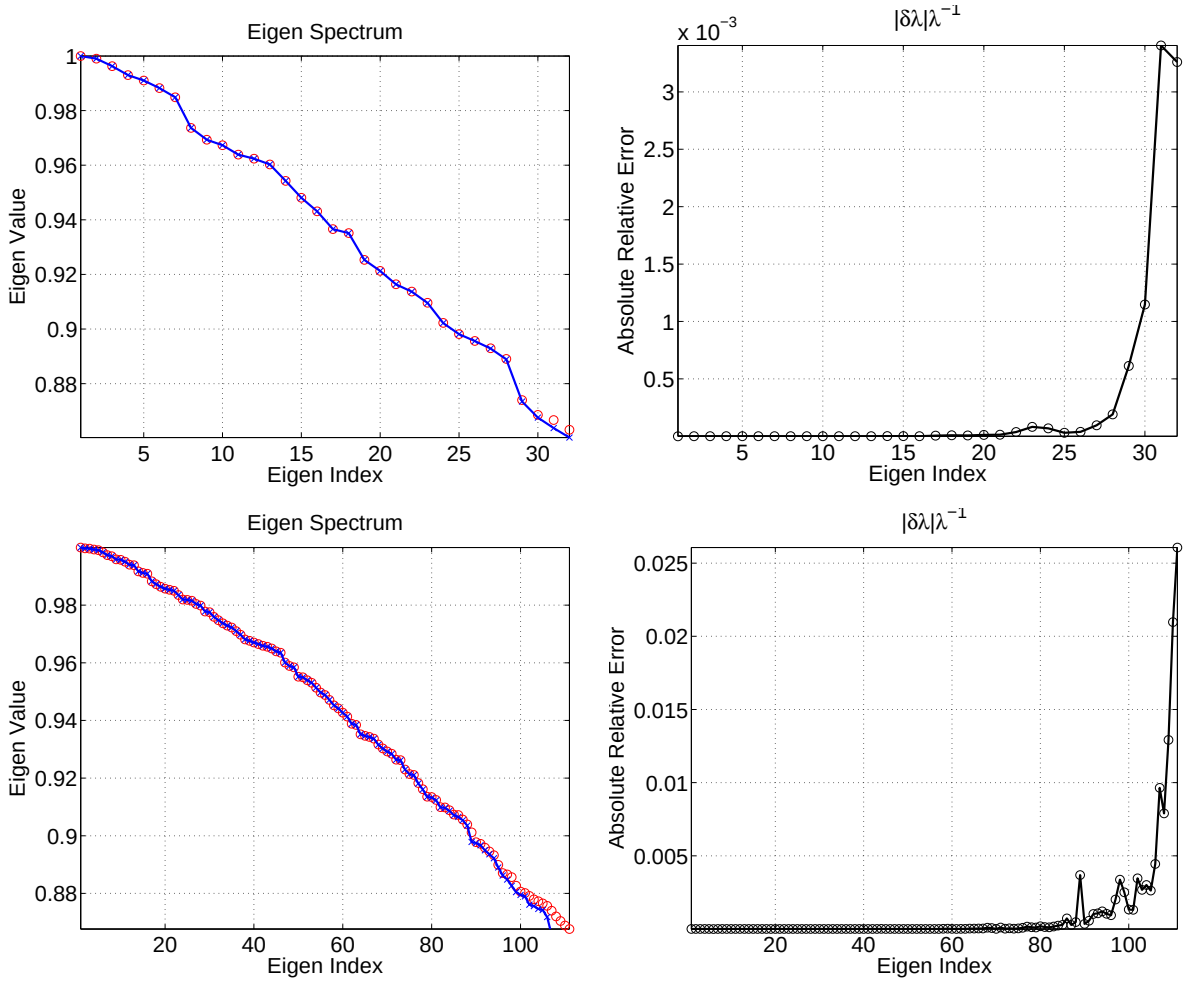

Figure 8.4: Hierarchical eigensolver applied to the eye image (TOP ROW) and the face image (BOTTOM ROW). Comparison of eigen spectra: red circles represent the eigenvalues S_L obtained by a direct eigen decomposition of the fine-scale normalized affinity matrix L; blue line with crosses are eigenvalues S obtained by a three-scale decomposition of the transition matrix built from L. Plots to the right show the relative absolute error: $\frac{|S-S_L|}{S_L}$, between the eigenvalues.

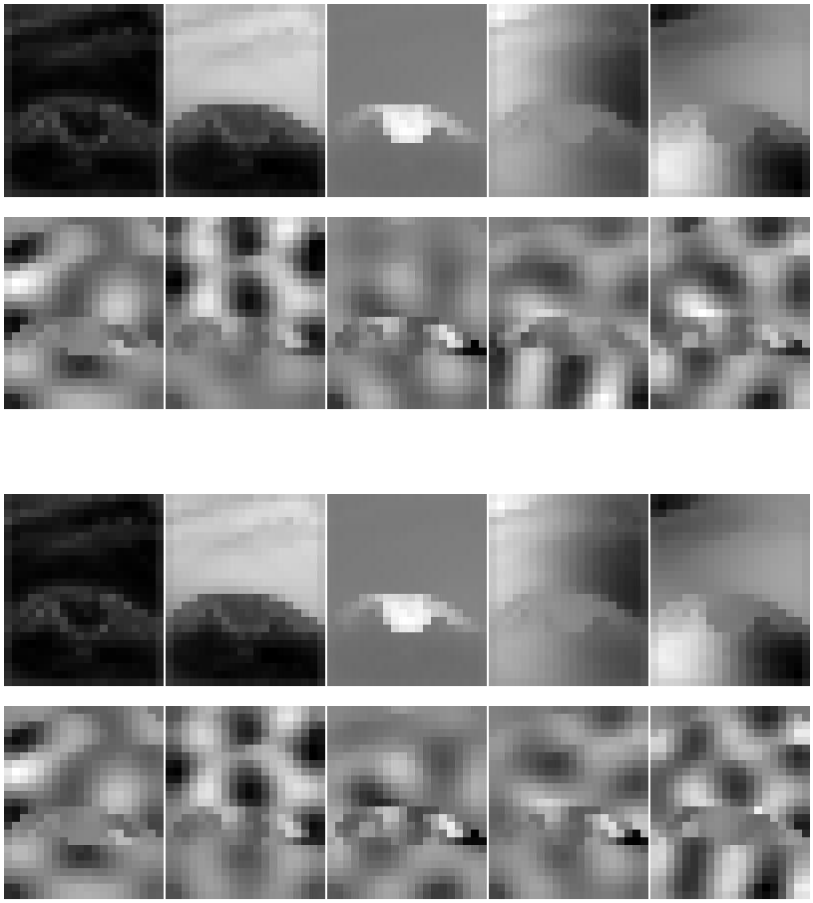

Figure 8.5: Hierarchical eigensolver applied to the eye image. Eigenvector comparison: (Rows 1 & 2) eigenvectors 1–5 and 28–32 obtained by a direct eigen decomposition of the fine-scale normalized affinity matrix L; (Rows 3 & 4) corresponding vectors obtained by a three-scale decomposition of the transition matrix built from L. Observe the slight mismatch in the last few eigenvectors, but excellent agreement in the first few eigenvectors.

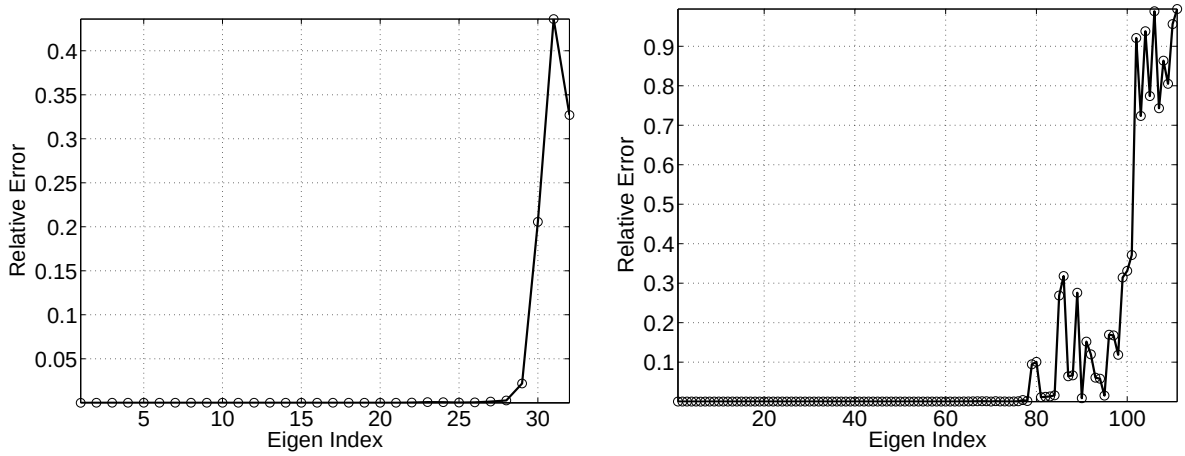

Figure 8.6: Measuring the mismatch: $\mathbf{1} - \text{diag}\left(|U^T U_L|\right)$, between the eigenvectors U derived from multi-scale approximation and the ground truth U_L for the eye image (LEFT) and the face image (RIGHT).

For the eye image, recall the original Markov matrix is of size 500×500, which is reduced to a 83×83 matrix at the second level of the hierarchy and is further reduced to a matrix of size 32×32 at the third level of the hierarchy. Hence the eigenspectrum is a 32-long vector (Fig. 8.4 TOP LEFT). To illustrate how close the multi-scale approximation is to the true eigen spectrum we show absolute relative error between the spectra: $\frac{|S-S_L|}{S_L}$ (Fig. 8.4, TOP RIGHT). The spectra agree mostly, except for the last few eigenvalues.

Similar results can be seen for the face image, where the fine-scale affinity matrix is of size 1200×1200, which is reduced to a matrix of size 252×252 at the second-level of the hierarchy and further reduced to a matrix of size 111×111 at the third-level of the hierarchy. Hence, the eigenspectrum is a 111 long vector as shown in Fig. 8.4 (BOTTOM LEFT). The absolute relative error demonstrates a close match between the multi-scale approximation and the ground truth, in the leading eigenvalues.

To further assess the mis-match between the spectra, in Fig. 8.5 we compare visually the leading eigenvectors for the eye image returned by the multi-scale approximation to the ground truth. The first two rows of the figure correspond to the first and the last

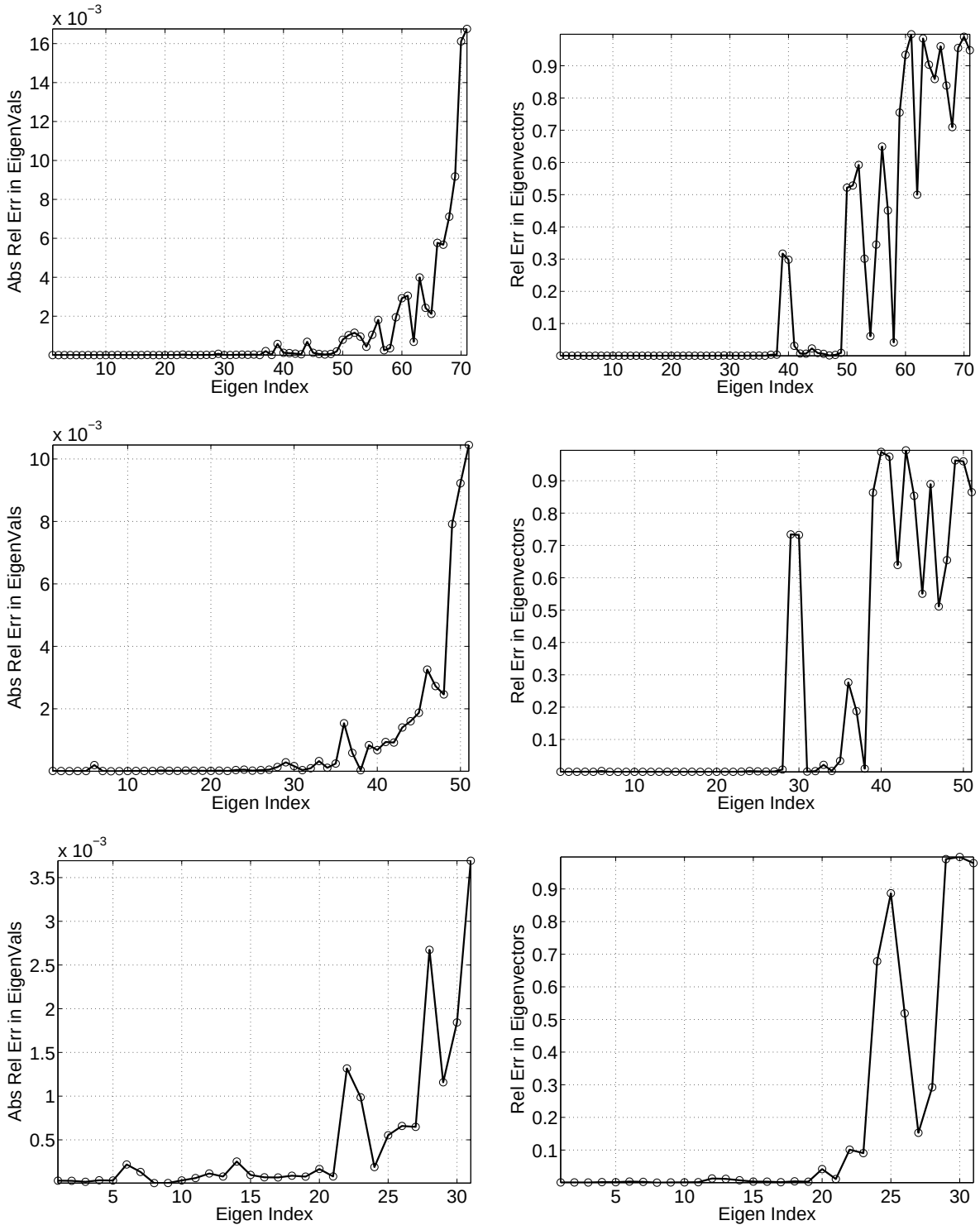

Figure 8.7: Hierarchical eigensolver on the face image for various subspace dimensions: (TOP ROW) 71, (MIDDLE ROW) 51 and (BOTTOM ROW) 31. (LEFT COLUMN) Relative absolute error: $\frac{|S-S_L|}{S_L}$, between the eigenvalues S returned by the eigensolver and the ground-truth S_L. (RIGHT COLUMN) Measuring the mismatch: $\mathbf{1} - \text{diag}\left(|U^T U_L|\right)$, between the eigenvectors U derived from multi-scale approximation and the ground truth U_L.

five eigenvectors returned by a direct eigen decomposition of the fine-scale normalized affinity matrix L. The third and fourth rows show the corresponding eigenvectors from the multi-scale procedure. Notice the last few eigenvectors exhibit a slight mismatch.

For a quantitative comparison, in Fig. 8.6 we plot the following measure to indicate how good the approximation is to the ground-truth: $\mathbf{1} - |U^T U_L|$, where $\mathbf{1}$ is a vector of all ones, U is the matrix of eigenvectors obtained by the multi-scale approximation and U_L is the ground-truth resulting from a direct eigen decomposition of the fine-scale affinity matrix L. The relative error plot demonstrates a close match in the leading eigenvector directions between the two methods. The relative error is high with the last few eigen vectors, which suggests that the power iterations have not clearly separated them from other directions.

Finally, we compare the timings of the two eigensolvers: the sparse SVD routine mentioned before [90] and our hierarchical method. In Table. 8.1 using a three-scale decomposition of the face image, we report time taken, in seconds, to compute the leading eigenbasis for a fixed size input problem. We consider the face image, where the fine-scale affinity matrix is of size 1200×1200, which is reduced to a matrix of size 252×252 at the second-level of the hierarchy and further reduced to a matrix of size 111×111 at the third-level of the hierarchy. Given the matrix size at the coarsest scale, we have an option to pick the total number of eigenbases to be interpolated down the hierarchy. So, in Table 8.1 we report the time it takes to compute the leading eigenbasis for various subspace dimensionalities. Also for each subspace selection, the sparse SVD procedure is invoked for the corresponding basis on the fine-scale sparse normalized affinity matrix. The results from the sparse SVD routine serve as the ground-truth.

Comparing the numbers in Table. 8.1, the multi-scale approach clearly outperforms the sparse SVD routine. However, as we observed before the relative error between the interpolated eigen vectors from the multi-scale procedure and the sparse SVD basis tends to be high in the last few eigen directions (see Figs. 8.6 and 8.7). The strategy we suggest

Eigen Subspace Dim	Sparse SVD	Multi-Scale Approach
11	21.1	2.9
31	55.3	3.4
51	90.4	3.8
71	127.3	4.4
91	171.1	5.5
111	220.5	6.3

Table 8.1: Comparing the timings of the two eigensolvers on a 1200×1200 Markov matrix: Sparse SVD [90] and the hierarchical approach reported in this chapter, where the size of the input problem is fixed but the the size of the leading subspace is changed. The reported time is in seconds. The code, written in Matlab, is run on a Pentium 4, 1.9Ghz, 512MB machine.

Image Size	Markov Matrix Size	Sparse SVD	Multi-Scale Approach
16×16	$[256^2 \quad 39^2]$	4.2	0.6
24×24	$[576^2 \quad 85^2 \quad 32^2]$	12.1	1.3
32×32	$[1024^2 \quad 150^2 \quad 56^2]$	28.3	4.7
48×48	$[2304^2 \quad 334^2 \quad 120^2 \quad 48^2]$	95.6	8.9
64×64	$[4096^2 \quad 573^2 \quad 213^2 \quad 71^2]$	271.9	35.0

Table 8.2: Comparing the timings of the two eigensolvers: Sparse SVD [90] and the hierarchical approach reported in this chapter, where the size of the input problem is changed but the size of the leading subspace is kept fixed to a value = 31. The second columns shows the size of the transition matrix at each level of the hierarchy. The number of stages in the hierarchy is chosen to accommodate a subspace of atleast 31 dimensions. The reported time is in seconds. The code, written in Matlab, is run on a Pentium 4, 1.9Ghz, 512MB machine.

then is to pad the required number of leading eigen basis by about 20% before invoking the multi-scale procedure. Obviously, the number of hierarchical stages for the multi-scale procedure must be chosen such that the transition matrix at the coarsest scale can accommodate the slight increase in the subspace dimensions.

Next, we measure the time it takes to compute the leading eigenbasis for various sizes of the input problem. We form images, each of size $N \times N$, by Gaussian smoothing of i.i.d noise. The Gaussian function has a standard deviation of 3 pixels. The affinities are computed as in Eq. 6.1. The affinity matrix is then normalized so that the median value for the degree d_i of any node i in the underlying graph is 1 (see Sec. 7.4 for more discussion). We fix the subspace dimensionality to 31. In Table. 8.2 the column under sparse SVD denotes the time taken by the sparse SVD routine to generate the leading 31 eigenvectors and eigenvalues. The reported time is in seconds.

We then perform a hierarchical decomposition of the Markov transition matrix. The number of hierarchical stages is selected to accommodate a minimum subspace of 31 dimensions. In Table. 8.2 the column reporting Markov matrix sizes shows the size of the transition matrix at each level of the hierarchy and also the number of stages in the hierarchy. For example, for $N = 16$ we chose only 2 levels in the hierarchy while for $N = 64$ we select 4 levels in the hierarchy. At the coarsest scale a subspace size that is at most 51 dimensional is selected for interpolation. This conforms to our earlier suggestion of padding the necessary subspace, which is 31, by a number that is 20% larger, to overcome the errors introduced by the multi-scale procedure in the last few eigen directions. Again, the multi-scale procedure outperforms the sparse SVD routine. In Table 8.2, we suspect the timings reported for $N = 64$ are an anomaly in that Matlab is probably hitting an hardware issue with paging or caching. Otherwise, the reported times for the multi-scale procedure scale linearly in N.

Chapter 9

Multi-Scale EigenCuts

9.1 Introduction

We show how to use the information in the transition matrix approximation hierarchy to build an effective multi-scale spectral clustering algorithm. In particular, we modify the basic procedure of EigenCuts for the multi-scale version. At the coarsest scale we run one iteration of the EigenCuts algorithm. Once the cuts have been identified at the coarsest scale, processing continues to the next finer scale. The eigenvectors are interpolated according to the Algorithm 2 presented in Chapter 8, the cut locations are predicted from the coarser scale and the fine scale sensitivities are computed only at these locations. We discuss the details of this multi-scale EigenCuts algorithm next.

9.2 Algorithm Details

To begin, a graph clustering problem is formed for the underlying image where each pixel in the test image is associated with a vertex on the graph G. The edges in G are defined by the standard 8-neighbourhood of each pixel. The edge weights between neighbouring vertices are simply given by a function of the difference in the corresponding intensities (as in Eq. 6.1). The affinity matrix A, with the edge weights, is then used to generate a

Markov transition matrix M.

We now illustrate the various steps of a three-scale EIGENCUTS algorithm applied to a random occluder image shown in Fig. 9.1. The image size is 16×16, but is enlarged in the figures for clarity. The fine-scale Markov matrix M is diffused to M^β using $\beta = 4$ and a greedy kernel selection process is applied (see §8.3.3). The greedy algorithm picks 40 kernels. The kernel centers are numbered in Fig. 9.1a. The transition matrix $\widetilde{M}$ generated for the 40 dimensional space is then diffused to $\widetilde{M}^\beta$, again using $\beta = 4$. The greedy kernel selection algorithm is applied again, this time picking 17 kernels. The kernel centers are shown in Fig. 9.1b.

At the coarsest scale we run one iteration of the EIGENCUTS algorithm (§7.4). The cuts identified at the coarsest scale are drawn as black lines in Fig. 9.1, where a line joining two kernels indicates a link that is highly sensitive at the coarsest scale and hence must be cut. Once the cuts have been identified at the coarsest scale, processing continues to the next finer scale. The eigenvectors are interpolated according to the ALGORITHM 2 presented in Chapter 8, the cut locations are predicted from the coarser scale and the fine scale sensitivities are computed only at these locations.

The cut locations at the fine-scale are predicted in a greedy fashion. For illustration, consider the link between kernels 11 and 18 in Fig. 9.1a, which the EIGENCUT procedure, applied at the coarse-scale, identifies as a link to be cut. The kernels will have a form shown in Fig. 8.2. The greedy method we adopt is to intersect the two kernel shapes and find pixels with non-zero transition probability between the two kernel centers. From the Fig. 9.1a, we can see that for kernels 11 and 18, there are six such pixel locations, drawn as yellow coloured crosses. These pixels (along with their links at the fine-scale) are then identified for further processing. Note, while we predict cut locations, it may be more appropriate to predict the actual links that should be perturbed at the fine scale. Instead we chose a greedy approach for this problem.

As we discussed in §8.3.2, at successive levels of the hierarchy we sparsify the affinity

matrix $\widetilde{A}$ by zeroing out elements associated with small transition probabilities in $\widetilde{M}$. The suppression can give rise to the following situation. Consider a link with a *non-zero* transition probability at the fine-scale between nodes v_i and v_j. Assume two different kernels K_r and K_s have the "maximum" ownership weights (via Eq. 8.7) for nodes v_i and v_j respectively. If on account of suppression, which happens before the EIGENCUTS procedure is run, the transition probability between coarse-scale nodes v_r^c and v_s^c is zero, then this information must be propagated to the fine-scale for further investigation. In Fig. 9.1a these links are identified by blue colored lines and they form part of the set of predicted cut locations.

The actual cuts are made only at the finest scale and the process by which this is done was already explained in Sec. 7.4.1. The weights of the links that are cut, are moved into the diagonal of the affinity matrix A at the finest scale, as is done in the basic EIGENCUTS procedure.

In Figs. 9.1 to 9.5 we show successive iterations of this multi-scale procedure. In the first iteration shown in Fig. 9.1, we see that the multi-scale EIGENCUTS algorithm eliminates large portions of the image from further analysis. Interestingly, the majority of the blue lines are at the boundary of the foreground object and this confirms our intuition that the links across the boundary are weak and hence they are being suppressed indirectly at a coarser scale. In the second iteration (Fig. 9.2), the placement of kernels is roughly the same. Notice, at the third-level of the hierarchy (Fig. 9.2b) an extra kernel (labeled '8') is placed inside the foregound object, when compared to the configuration in the previous iteration. As more links get cut, more kernels are placed inside the foreground and background regions. For the image used in this demonstration, the multi-scale algorithm converges after the fifth iteration.

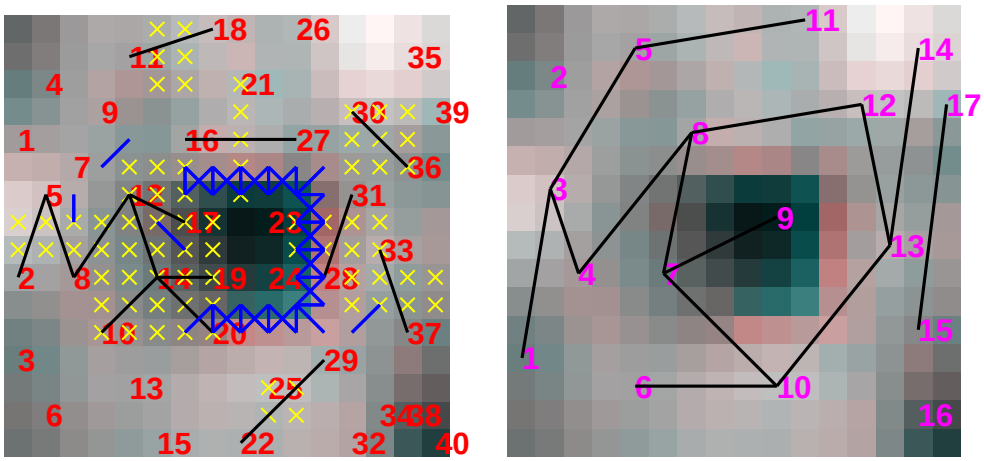

(a) (b)

Figure 9.1: Iteration 1 of the MULTI-SCALE EIGENCUTS algorithm. There are 40 kernels at the first coarse scale (kernel centers shown in red in (a)) and 17 kernels at the second coarse scale (kernel centers shown in magenta in (b)). The links that need to be cut at the coarse scales, as identified by one iteration of the EIGENCUTS algorithm, are drawn as black lines. These links are then used to predict cut locations (or pixels) at the fine scale and these are shown as yellow crosses in (a). Fine-scale sensitivities are computed only at these locations. Blue-colored lines are links with a non-zero transition probability at the fine scale, but the nodes connected to these links are "owned" by different kernels at a coarse scale that have zero transition probability between them.

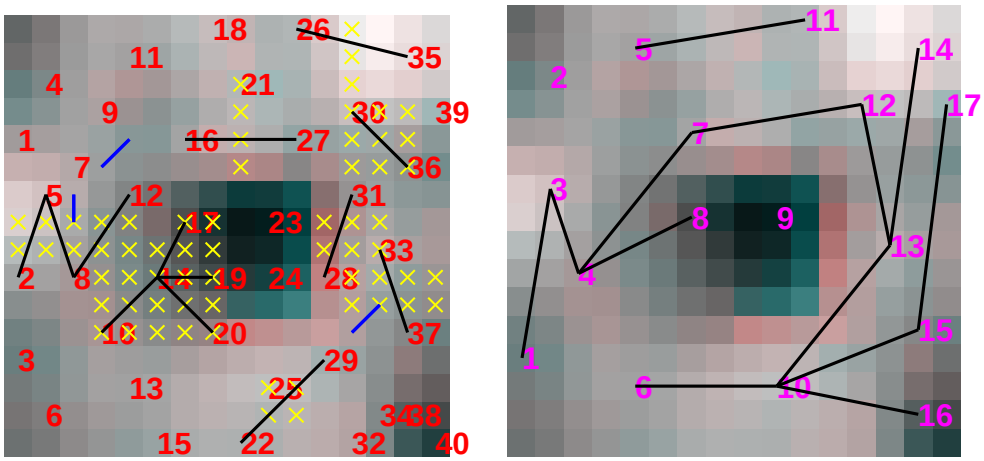

(a) (b)

Figure 9.2: Iteration 2 of the MULTI-SCALE EIGENCUTS algorithm. There are 40 kernels at the first coarse scale (kernel centers shown in red in (a)) and 17 kernels at the second coarse scale (kernel centers shown in magenta in (b)). The links that need to be cut at the coarse scales, as identified by one iteration of the EIGENCUTS algorithm, are drawn as black lines. These links are then used to predict cut locations (or pixels) at the fine scale and these are shown as yellow crosses in (a). Fine-scale sensitivities are computed only at these locations. Blue-colored lines are links with a non-zero transition probability at the fine scale, but the nodes connected to these links are "owned" by different kernels at a coarse scale that have zero transition probability between them.

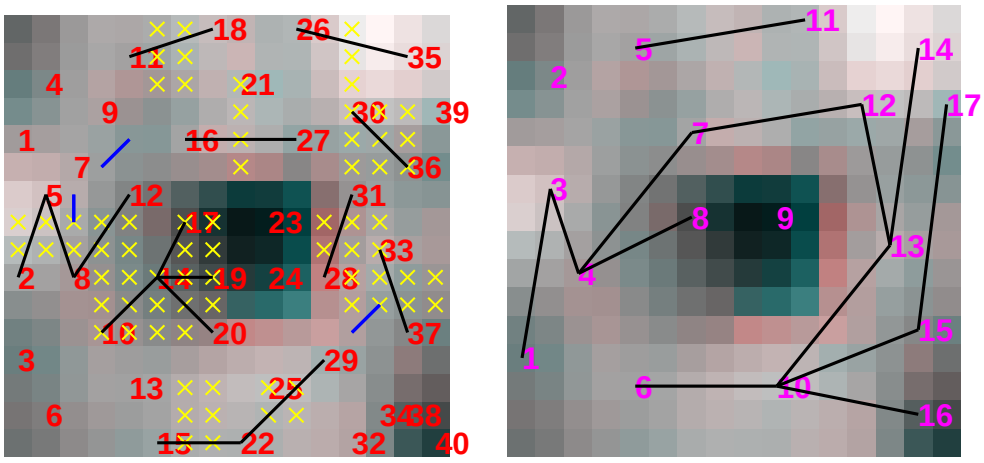

(a) (b)

Figure 9.3: Iteration 3 of the MULTI-SCALE EIGENCUTS algorithm. There are 40 kernels at the first coarse scale (kernel centers shown in red in (a)) and 17 kernels at the second coarse scale (kernel centers shown in magenta in (b)). The links that need to be cut at the coarse scales, as identified by one iteration of the EIGENCUTS algorithm, are drawn as black lines. These links are then used to predict cut locations (or pixels) at the fine scale and these are shown as yellow crosses in (a). Fine-scale sensitivities are computed only at these locations. Blue-colored lines are links with a non-zero transition probability at the fine scale, but the nodes connected to these links are "owned" by different kernels at a coarse scale that have zero transition probability between them.

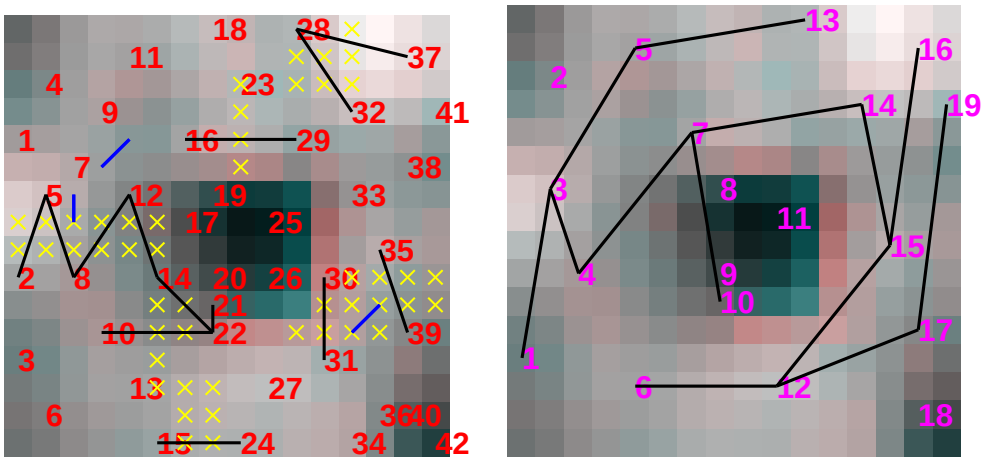

(a) (b)

Figure 9.4: Iteration 4 of the MULTI-SCALE EIGENCUTS algorithm. There are 42 kernels at the first coarse scale (kernel centers shown in red in (a)) and 19 kernels at the second coarse scale (kernel centers shown in magenta in (b)). The links that need to be cut at the coarse scales, as identified by one iteration of the EIGENCUTS algorithm, are drawn as black lines. These links are then used to predict cut locations (or pixels) at the fine scale and these are shown as yellow crosses in (a). Fine-scale sensitivities are computed only at these locations. Blue-colored lines are links with a non-zero transition probability at the fine scale, but the nodes connected to these links are "owned" by different kernels at a coarse scale that have zero transition probability between them.

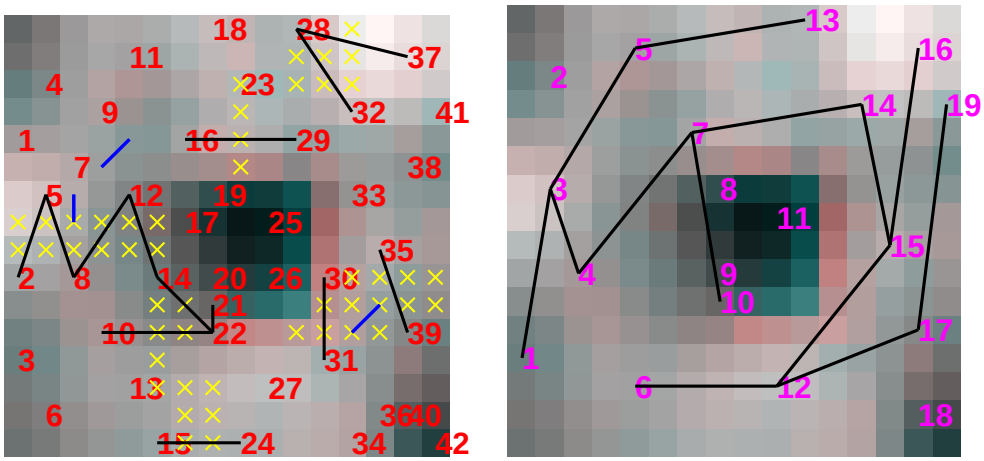

(a) (b)

Figure 9.5: Iteration 5 of the MULTI-SCALE EIGENCUTS algorithm. There are 42 kernels at the first coarse scale (kernel centers shown in red in (a)) and 19 kernels at the second coarse scale (kernel centers shown in magenta in (b)). The links that need to be cut at the coarse scales, as identified by one iteration of the EIGENCUTS algorithm, are drawn as black lines. These links are then used to predict cut locations (or pixels) at the fine scale and these are shown as yellow crosses in (a). Fine-scale sensitivities are computed only at these locations. Blue-colored lines are links with a non-zero transition probability at the fine scale, but the nodes connected to these links are "owned" by different kernels at a coarse scale that have zero transition probability between them.

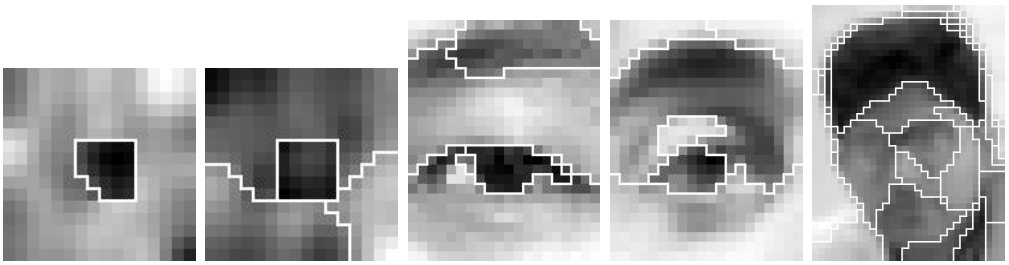

Figure 9.6: Results from Multi-Scale EIGENCUTS. The random occluder images are of size 16×16, the eye images are of size 25×20 and the face image is of size 40×30.

9.3 Results

The multi-scale method was compared to basic EIGENCUTS procedure using both a full SVD solver and a Matlab implementation of sparse SVD [90]. The eigenvalue tolerance parameters for were set to provide no more than 20% additional components over the ground truth segments returned by the full SVD procedure. This amounts to a tolerance value of 10^{-3}. The results obtained by the multi-scale procedure are shown in Fig. 9.6. The results are very similar to the segments obtained by the basic version of the EIGENCUTS procedure (see Figs. 7.10 and 7.11).

There are two points to be made with the multi-scale approach: a) how to speed up the eigensolver; and b) how to speed up the cutting. What we observed is that the hierarchical approach speeds up the eigen computation itself by about 5 times. Although the total number of links that are perturbed at the finest scale is less than the direct EIGENCUTS approach, because of the non-maxima suppression we did not see significant gains in speed in the overall algorithm. As a result we found for the face image, the multi-scale method is 8 times faster than the full eigen solver and provides a speedup of 20% over the use of sparse SVD.

Chapter 10

EigenCuts: Conclusions

We presented an algorithm EigenCuts for finding stable clusters in a dataset using their pairwise-similarities. Using a Markov chain perspective, we characterized the spectral properties of the matrix of transition probabilities, from which we derived eigenflows along with their halflives. An eigenflow describes the flow of probability mass due to the Markov chain, and it is characterized by its eigenvalue, or equivalently, by the halflife of its decay as the Markov chain is iterated. A ideal stable cluster is one with zero eigenflow and infinite half-life. The key insight in this work is that bottlenecks between weakly coupled clusters can be identified by computing the sensitivity of the eigenflow's halflife to variations in the edge weights. The EigenCuts algorithm performs clustering by removing these identified bottlenecks in an iterative fashion.

Also, in this thesis we proposed a specialized eigensolver suitable for large stochastic matrices with known stationary distributions. In particular, we exploit the spectral properties of the Markov transition matrix to generate hierarchical, successively lower-ranked approximations to the full transition matrix. The eigen problem is solved directly at the coarsest level of representation. The approximate eigen solution is then interpolated over successive levels of the hierarchy, using a small number of power iterations to correct the solution at each stage. To show the effectiveness of this approximation, we presented a

multi-scale version of the EIGENCUTS algorithm. Compared to the basic procedure, the multi-scale EIGENCUTS algorithm distributes the cutting of links across different scales and saves time in solving the underlying eigen problem.

Bibliography

[1] D. Achlioptas and F. McSherry. Fast computation of low-rank approximations. In *ACM Symposium on Theory of Computing*, 2001.

[2] D. Achlioptas, F. McSherry, and B. Scholkopf. Sampling techniques for kernel methods. In *Neural Information Processing Systems*, 2001.

[3] S. Agarwal and D. Roth. Learning a sparse representation for object detection. In *European Conference on Computer Vision*, 2002.

[4] C. Alpert and A. Kahng. Multiway partitioning via geometric embeddings, orderings and dynamic programming. *IEEE Transactions on Computer-Aided Design and Integrated Circuits and Systems*, 14(11):1342–1358, 1995.

[5] C. Alpert, A. Kahng, and S. Yao. Spectral partitioning: the more eigenvectors, the better. *Discrete Applied Mathematics*, 90:3–26, 1999.

[6] M. Alvira and R. Rifkin. An empirical comparison of snow and svms for face detection. Technical report, CBCL, MIT, A.I. Memo:2001-004, 2001. `http://www.ai.mit.edu/projects/cbcl/software-datasets/FaceData2.html`.

[7] J. J. Atick. Could information theory provide an ecological theory of sensory processing? *Network: Computation in Neural Systems*, 3:213–251, 1992.

[8] J. J. Atick and A. N. Redlich. Towards a theory of early visual processing. *Neural Computation*, 2:308–320, 1990.

[9] J. J. Atick and A. N. Redlich. What does the retina know about natural scenes? *Neural Computation*, 4:196–210, 1992.

[10] H. Barlow. Possible principles underlying the transformation of sensory messages. In *Sensory Communication*, pages 217–234, MIT Press, Cambridge, MA, 1961.

[11] H. Barlow. Unsupervised learning. *Neural Computation*, 1:295–311, 1989.

[12] M. Bartlett. *Face image analysis by unsupervised learning and redundancy reduction.* Doctoral Dissertation, University of California, San Diego, 1998.

[13] A. J. Bell and T. J. Sejnowski. The independent components of natural scenes are edge filters. *Vision Research*, 37:3327–3338, 1997.

[14] A. J. Bell and T. J. Sejnowski. The 'independent components' of natural scenes are edge filters. *Vision Research*, 37(23):3327–3338, 1997.

[15] S. Belongie, C. Fowlkes, F. Chung, and J. Malik. Spectral partitioning with indefinite kernels using the nystrom approximation. In *European Conference on Computer Vision*, pages 21–31, Copenhagen, Denmark, 2002.

[16] W. Bialek, D. L. Ruderman, and A. Zee. Optimal sampling of natural images: A design principle for the visual system? In *Neural Information Processing Systems*, pages 363–369, 1991.

[17] M. Black and A. Jepson. Eigentracking: Robust matching and tracking of articulated objects using a view-based representation. *International Journal of Computer Vision*, 26(1):63–84, 1998.

[18] R. W. Buccigrossi and E. P. Simoncelli. Image compression via joint statistical characterization in the wavelet domain. *IEEE Transactions on Image Processing*, 8(12):1688–1701, 1999.

[19] G. J. Burton and I. R. Moorhead. Color and spatial structure in natural scenes. *Applied Optics*, 26:157–170, 1987.

[20] J. Cardoso. High-order contrast for independent component analysis. *Neural Computation*, 11:157–192, 1999.

[21] P. K. Chan, M. Schlag, and J. Zien. Spectral k-way ratio cut partitioning and clustering. *IEEE Transactions on Computer-Aided Design and Integrated Circuits and Systems*, 13(9):1088–1096, 1994.

[22] S. Chen, D. L. Donoho, and M. A. Saunders. Atomic decomposition by basis pursuit. *SIAM Journal of Scientific Computing*, 20(1):33–61, 1998.

[23] Chakra Chennubhotla and Allan D. Jepson. Sparse coding in practice. In *Workshop on Statistical and Computational Theories of Vision*, July 2001.

[24] Chakra Chennubhotla and Allan D. Jepson. Sparse pca: Extracting multi-scale structure from data. In *IEEE International Conference on Computer Vision*, volume I, pages 641–647, Vancouver, CA, July 2001.

[25] Chakra Chennubhotla, Allan D. Jepson, and John Midgley. Robust contrast-invariant eigendetecton. In *International Conference on Pattern Recognition*, 2002.

[26] F. R. K. Chung. *Spectral Graph Theory.* CBMS Lecture Notes, American Mathematical Society, 1997.

[27] P. Comon. Indepedent component analysis, a new concept? *Signal Processing*, 36:287–314, 1994.

[28] J. Daugman. Complete discrete 2-d gabor transforms by neural networks for image analysis and compression. *IEEE Transactions on Accoustics Speech and Signal Processing*, 36:1169–1179, 1988.

[29] J. Daugman. Entropy reduction and decorrelation in visual cortex by oriented neural receptive fields. *IEEE Transactions on Accoustics Speech and Signal Processing*, 36:107–114, 1989.

[30] Fernando de la Torre and M. Black. Robust pca. In *IEEE International Conference on Computer Vision*, volume I, pages 362–369, Vancouver, Canada, July 2001.

[31] L. Delves and J. Mohamed. *Computational Methods for Integral Equations*. Cambridge University Press, 1985.

[32] P. A. Devijver and J. Kittler. *Pattern Recognition: A Statistical Approach.* Prentice Hall, 1982.

[33] C. Ding, X. He, H. Zha, M. Gu, and H. Simon. Spectral min-max cut for graph partitioning and data clustering. In *First IEEE International Conference on Data Mining*, pages 107–114, San Jose, 2001.

[34] D. W. Dong and J. J. Atick. Statistics of natural time-varying images. *Network: Computation in Neural Systems*, 6:345–358, 1995.

[35] P. Felzenszalb and D. Huttenlocher. Image segmentation using local variation. In *IEEE Conference on Computer Vision and Pattern Recognition (CVPR)*, pages 98–104, Santa Barbara, June 1998.

[36] D. J. Field. Relation between the statistics of natural images and the response properties of cortical cells. *Journal of Optical Society of America*, 4:2379–2394, 1987.

[37] D. J. Field. Scale-invariance and self-similar "wavelet" transforms: an analysis of natural scenes and mammalian visual systems. *Wavelets, Fractals and Fourier Transforms*, pages 151–193, 1993.

[38] D. J. Field. What is the goal of sensory coding? *Neural Computation*, 6:559–601, 1994.

[39] Francois Fleuret and Donald Geman. Coarse-to-fine face detection. *International Journal of Computer Vision*, 41(1/2):85–107, 2001.

[40] C. Fowlkes, S. Belongie, and J. Malik. Efficient spatiotemporal grouping using the nystrom method. In *IEEE Conference on Computer Vision and Pattern Recognition*, 2001.

[41] W. Freeman and E. Adelson. Design and use of steerable filters. *IEEE Transactions on Pattern Analysis and Machine Intelligence*, 13(9):891–906, 1991.

[42] A. Frieze, R. Kannan, and S. Vempala. Fast monte-carlo algorithms for finding low-rank approximations. In *IEEE Symposium on Foundations of Computer Science*, pages 370–378, 1998.

[43] R. C. Gonzalez and R. E. Woods. *Digital Image Processing.* Prentice Hall, 2002.

[44] L. Gu, S. Z. Li, and H.J. Zhang. Learning representative local features for face detection. In *IEEE Conference on Computer Vision and Pattern Recognition (CVPR)*, Hawaii, December 2001.

[45] G. F. Harpur. Low-entropy coding with unsupervised neural networks. Technical report, University of Cambridge, 1997.

[46] G. F. Harpur and R. W. Prager. Development of low-entropy coding in a recurrent framework. *Network: Computation in Neural Systems*, 7(2):277–284, 1996.

[47] J. Huang and D. Mumford. Statistics of natural images and models. In *IEEE Conference on Computer Vision and Pattern Recognition*, pages 541–547, 1999.

[48] A. Hyvrinen and R. Karthikesh. Sparse priors on the mixing matrix in independent component analysis. In *International Workshop on Independent Component Analysis and Blind Signal Separation (ICA2000)*, pages 477–452, Helsinki, Finland, 2000.

[49] I. T. Jolliffe. *Principal Component Analysis.* Springer, New York, 1986.

[50] H. F. Kaiser. The varimax criterion for analytic rotation in factor analysis. *Psychometrika*, 23:187–200, 1958.

[51] R. Kannan, S. Vempala, and A. Vetta. On clusterings–good, bad and spectral. In *41st Annual Symposium on Foundations of Computer Science*, pages 367–377, 2000.

[52] J. R. Kemeny and J. L. Snell. *Finite Markov Chains.* Van Nostrand, New York, 1960.

[53] Y. Koren, L. Carmel, and D. Harel. Ace: A fast multiscale eigenvectors computation for drawing huge graphs. In *IEEE Symposium on Information Visualization*, pages 137–144, 2002.

[54] S. Kullback. *Information Theory and Statistics.* Dover Publications, New York, 1959.

[55] S. Kullback and R. A. Leibler. On information and sufficiency. In *Annals of Mathematical Statistics*, volume 22, pages 79–86, 1951.

[56] C. Lanczos. An iteration method for the solution of the eigenvalue problem of linear differential and integral operators. In *Journal of Research of the National Bureau of Standards*, volume 45, pages 255–282, 1950.

[57] S. B. Laughlin. Retinal information capacity and the function of pupil. *Opthalmic and physiological optics*, 12:161–164, 1992.

[58] A. Lee and D. Mumford. Scale-invariant random-collage model for natural images. In *Workshop on Statistical and Computational Theories of Vision*, Fort Collins, 1999.

[59] D. Lee and S. Seung. Learning the parts of an object by non-negative matrix factorization. *Nature*, 401:788–791, 1999.

[60] M. S. Lewicki and T. J. Sejnowski. Learning overcomplete representations. *Neural Computation*, 12:337–365, 2000.

[61] Z. Li and J. J. Atick. Toward a theory of the striate cortex. *Neural Computation*, 6:127–146, 1994.

[62] J. J. Lin. Reduced rank approximations of transition matrices. In *9th International Conference on Artificial Intelligence and Statistics (AI & STATS)*, 2002.

[63] R. Linsker. Self organization in a perceptual network. *IEEE Computer*, 21(3):105–117, 1988.

[64] R. Linsker. Sensory processing and information theory. In *From Statistical Physics to Statistical Inference and Back*, pages 237–247, 2002.

[65] L. Lova'sz. Random walks on graphs: A survey. In *Combinatorics*, pages 353–398, 1996.

[66] S. B. Laughlin M. V. Srinivasan and A. Dubs. Predictive coding: A fresh view of inhibition in the retina. *Proceedings Royal Society of London, B.*, 216:427–459, 1982.

[67] D. J. C. Mackay. Maximum likelihood and covariant algorithms for independent component analysis. Technical report, University of Cambridge, 1996. `http://www.inference.phy.cam.ac.uk/mackay/ica.pdf`.

[68] J. Malik, S. Belongie, T. Leung, and J. Shi. Contour and texture analysis for image segmentation. *International Journal of Computer Vision*, 43(1):7–27, 2001.

[69] S. G. Mallat. A theory of multiresolution signal decomposition: The wavelet representation. *IEEE Transactions on Pattern Analysis and Machine Intelligence*, 11(7):674–693, 1989.

[70] S. G. Mallat. *A Wavelet Tour of Signal Processing*. Academic Press, 1999.

[71] G. J. McLachlan and K. E. Basford. *Mixture Models: Inference and Applications to Clustering*. Marcel Dekker, N.Y., 1988.

[72] M. Meila and J. Shi. A random walks view of spectral segmentation. In *8th International Conference on AI and Statistics*, 2001.

[73] C. D. Meyer. *Matrix Analysis and Applied Linear Algebra*. Society for Industrial and Applied Mathematics, 2000.

[74] John Midgley. Probabilistic eigenspace object recognition in the presence of occlusions. Technical report, Masters Thesis, Department of Computer Science, University of Toronto, 2001. `http://www.cs.utoronto.ca/~jmidgley/ut-thesis.ps.gz`.

[75] B. Moghaddam and A. Pentland. Probabilistic visual learning for object representation. *IEEE Transactions on Pattern Analysis and Machine Intelligence*, 19(7):696–710, 1997.

[76] R. Neal. *Bayesian Learning for Neural Networks.* Lecture Notes in Statistics No. 118, Springer-Verlag, 1996.

[77] A. Ng, M. Jordan, and Y. Weiss. On spectral clustering: analysis and an algorithm. In *Neural Information Processing Systems*, 2001.

[78] S. Nowlan and G. Hinton. Simplifying neural networks by soft weight sharing. *Neural Computation*, 4(4):473–493, 1992.

[79] B. A. Olshausen and D. J. Field. Sparse coding with an overcomplete basis set: a strategy employed by v1? *Vision Research*, 37(23):3311–3325, 1997.

[80] AT&T Laboratories Cambridge ORL Database.

[81] C. P. Papageorgiou, F. Girosi, and T. Poggio. Sparse correlational kernal analysis and reconstruction. In *IEEE Conference on Accoustics, Speech and Signal Processing*, pages 1633–1636, March 1999.

[82] C. P. Papageorgiou and T. Poggio. A trainable system for object detection. *International Journal of Computer Vision*, 38(1):15–33, 2000.

[83] B. Pearlmutter and L. Parra. Maximum likelihood blind source separation: A context-sensitive generalization of ica. In *Neural Information Processing Systems*, volume 9, pages 613–619, 1997.

[84] P. S. Penev. *Local Feature Analysis: A Statistical Theory for Information Representation and Transmission*. Doctoral Dissertation, The Rockefeller University, 1998.

[85] P. S. Penev and J. J. Atick. Local feature analysis. *Network: Computation in Neural Systems*, 7(3):477–500, 1996.

[86] P. Perona and W. Freeman. A factorization approach to grouping. In *European Conference on Computer Vision*, 1998.

[87] P. J. Phillips, H. Wechsler, J. Huang, and P. Rauss. The feret database and evaluation procedure for face recognition algorithms. *Image and Vision Computing*, 16(5):295–306, 1998.

[88] A. Pothen. Graph partitioning algorithms with applications to scientific computing. In D. E. Keyes, A. H. Sameh, and V. Venkatakrishnan, editors, *Parallel Numerical Algorithms*. Kluwer Academic Press, 1996.

[89] W. H. Press, W. T. Vettering S. A. Teukolsky, and B. P. Flannery. *Numerical Recipes in C: The Art of Scientific Computing.* Cambridge University Press, New York, 1992.

[90] R. J. Radke. A matlab implementation of the implicitly restarted arnoldi method for solving large-scale eigenvalue problems. Technical report, Masters Thesis, Department of CAM, Rice University, 1996. `http://www.ecse.rpi.edu/homepages/rjradke/papers/radkemathesis.pdf`.

[91] D. A. Ross and R. S. Zemel. Multiple-cause vector quantization. In *Neural Information Processing Systems (NIPS)*, 2002.

[92] S. Roweis. Em algorithms for pca and spca. In *Neural Information Processing Systems*, 1997.

[93] D. Ruderman. Origins of scaling in natural images. *Vision Research*, 37(23):3385–3395, 1997.

[94] D. Ruderman and W. Bialek. Statistics of natural images: scaling in the woods. *Physical Review Letters*, 73:814–817, 1994.

[95] T. D. Sanger. Optimal unsupervised learning in a single-layer network. *Neural Networks*, 2:459–473, 1989.

[96] S. Sarkar and K. Boyer. Quantitative measures of change based on feature organization: Eigenvalues and eigenvectors. *Computer Vision and Image Understanding*, 71(1):110–136, 1998.

[97] C. Schmid and R. Mohr. Local gray value invariants for image retreival. *IEEE Transactions on Pattern Analysis and Machine Intelligence*, 19(5):530–535, 1997.

[98] H. Schneiderman and T. Kanade. Object detection using the statistics of parts. *International Journal of Computer Vision*, 2002.

[99] G. L. Scott and H. C. Longuet-Higgins. Feature grouping by relocalization of eigenvectors of the proximity matrix. In *British Machine Vision Conference*, pages 103–108, 1990.

[100] E. Sharon, A. Brandt, and R. Basri. Fast multiscale image segmentation. In *IEEE Conference on Computer Vision and Pattern Recognition*, pages 70–77, 2000.

[101] J. Shi and J. Malik. Normalized cuts and image segmentation. *IEEE Transactions on Pattern Analysis and Machine Intelligence*, 15(12):1253–1268, 2000.

[102] E. P. Simoncelli, W. Freeman, E. Adelson, and D. Heegar. Shiftable multiscale transforms. *IEEE Transactions on Information Theory*, 38(2):587–607, 1992.

[103] L. Sirovich and M. Kirby. Low-dimensional procedure for the characterization of human faces. *Journal of Optical Society of America*, 4:519–524, 1987.

[104] K. Sung and T. Poggio. Example-based learning for view-based detection. *IEEE Transactions on Pattern Analysis and Machine Intelligence*, 20:39–51, 1998.

[105] P. Teo and D. Heeger. Perceptual image distortion. In *Proceedings ICIP-94 (IEEE International Conference on Image Processing)*, volume 2, pages 982–986, 1994.

[106] M. E. Tipping. Sparse bayesian learning and the relevance vector machine. *Journal of Machine Learning Research*, 1:211–244, 2001.

[107] M. E. Tipping. Sparse bayesian learning and the relevance vector machine. *Journal of Machine Learning Research*, 1:211–244, 2001.

[108] M. E. Tipping. Sparse kernel principal component analysis. In *Neural Information Processing Systems (NIPS)*, 2001.

[109] M. E. Tipping and C. M. Bishop. Mixtures of probabilistic principal component analysers. *Neural Computation*, 11(2):443–482, 1999.

[110] N. Tishby and N. Slonim. Data clustering by markovian relaxation and the information bottleneck method. In *Neural Information Processing Systems*, 2001.

[111] D. J. Tolhurst, Y. Tadmor, and T. Chao. Amplitude spectra of natural images. *Opthal. Physiol. Opt.*, 12:229–232, 1992.

[112] M. A. Turk and A. P. Pentland. Eigenfaces for recognition. *Journal of Cognitive Neuroscience*, 3(1):71–86, 1991.

[113] J. H. van Hateren. Theoretical predictions of spatio-temporal receptive fields of fly lmcs, and experimental validation. *Journal of Comp. Physiol. A*, 171:157–170, 1992.

[114] J. H. van Hateren. Theory of maximixing sensory information. *Biological Cybernetics*, 68:23–29, 1992.

[115] V. Vapnik. *Statistical Learning Theory.* John Wiley & Sons, 1998.

[116] J. Vermaak and P. Pe'rez. Constrained subspace modeling. In *IEEE Conference on Computer Vision and Pattern Recognition (CVPR)*, Madison, Wisconsin, June 2003.

[117] P. Viola and M. Jones. Robust real-time object detection. In *Workshop on Statistical and Computational Theories of Vision*, July 2001.

[118] D. Watkins. *Fundamentals of Matrix Computations.* John Wiley and Sons., 2002.

[119] Y. Weiss. Segmentation using eigenvectors: a unifying view. In *Seventh International Conference on Computer Vision*, 1999.

[120] M. Wertheimer. Laws of organization in perceptual forms (partial translation). In W. B. Ellis, editor, *Source book of Gestalt Psychology*, pages 71–88. Harcourt, Brace and Company, 1938.

[121] C. Williams and M. Seeger. Using the nystrom method to speed up the kernel machines. In *Neural Information Processing Systems*, 2001.

[122] P. M. Williams. Bayesian regularization and pruning using a laplace prior. *Neural Computation*, 7(1):117–143, 1995.

[123] Z. Wu and R. Healy. An optimal graph theoretic approach to data clustering: Theory and its application to image segmentation. *IEEE Transactions on Pattern Analysis and Machine Intelligence*, 11:1101–1113, 1993.